Supramoléculaire artificial water channels: from molecular design to membrane materials

Istvan Kocsis

Supramolecular artificial water channels: from molecular design to membrane materials

Présentée par Istvan KOCSIS
Le 05 octobre 2017

Sous la direction de Dr. Mihai Barboiu
Devant le jury composé de

M. Mihai BARBOIU, DR, CNRS	Directeur de thèse
Mme. Françoise BONNETÉ, CR, Institut des Biomolécules Max Mousseron	Co-encadrante de thèse
Mme. Andreea PASC, MCF, Université de Lorraine	Rapporteur
M. Pierre AIMAR, DR, Laboratoire de Génie Chimique de Toulouse	Rapporteur
M. Ion GROSU, Prof, Université Babes-Bolyai	Examinateur
M. André AYRAL, Prof, Université de Montpellier	Examinateur
M. Yves-Marie LEGRAND, IR, CNRS	Invité

UNIVERSITÉ
DE MONTPELLIER

Acknowledgements

I can only express so much my gratitude towards the people that have positively influenced both the progresses of my thesis work as well as my personal development. As a show of my appreciation I gladly offer these honourable mentions addressed to them.

First and foremost, I would like to thank my thesis director **Dr. Mihail Barboiu**, the person who gave me the chance to undergo my doctoral work. He has been a wonderful mentor, showing passion every time we discussed science and immense kindness at all occasions. His flair for finding innovative ways to tackle problems has inspired me countless times to push my own imagination and try to find new approaches and solutions for my research work. His skill in finding value in hidden details has taught me to be always perceptive when interpreting results. The experience I gained from the international collaborations and conferences the he promoted me into is invaluable. He has offered me the chance to develop my own individual research work and mentality and for this I will always be grateful. Humongous amounts of gratitude are due for **Dr. Yves-Marie Legrand**, from who I have taken up a quarter of his time on a daily basis, mainly filling his whiteboard with naive and overzealous research ideas. He has been ever present and available to help me in and out of the lab, making him a valuable advisor and a dear friend.

The roots of my passion for research have been set even before I began my thesis and I would like to thank Prof. Dr. Ion Grosu for allowing me to join his lab when I was merely a curios student in my first year of university. **Dr. Niculina Hadade** deserves special thanks as she was the one who guided my development as a young researcher and showed me the importance of initiative, integrity and teamwork in research.

Gratitude is due towards our collaborator who worked together with us on various projects, as so I would like to thank Dr. Manish Kumar, Prof. Dr. Georges Belfort, Dr. Poul Petersen, Dr. Marc Baaden and Dr. Mirco Sorci.

I would like to thank my thesis co-director Dr. Francoise Bonetté for investing time and effort into trying to find solutions for our joint research work. Also thanks to Thomas Zemb for the brainstorming meetings and suggestions made in our project. I would like to thank my current and former colleagues Yan Zang, Yuhao Li, Weixu Feng, Arnaud Gilles, Erol Licsandru, Alina Cristian, Mihai Deleanu, Maria di Vincenzo and Adina Coroaba for their involvement and for making the group a more welcoming place.

And least but not last I thank the members of the jury for accepting to be part of my thesis defense, with special thanks to Dr. Andreea Pasc and Dr. Pierre Aimar who took up the responsibility of being reviewers of this work.

Table of content

Abbreviations

ABM – aquaporin biomimetic membranes

AQP – aquaporin

ARGET – activator regenerated by electron transfer

ATR – attenuated total reflectance

ATRP – atom transfer radical polymerization

Chol – cholesterol

CNT – carbon nanotube

DLS – dynamic light scattering

DOPE – 1,2-Dioleoyl-sn-glycero-3-phosphoethanolamine

DOPS – 1,2-dioleoyl-sn-glycero-3-phospho-L-serine

EDC – 1-Ethyl-3-(3-dimethylaminopropyl)carbodiimide

FO – forward osmosis

FTIR – Fourier transform infrared

gMH – $g/m^2/h$

IP – interfacial polymerization

LCR – lipid channel ratio

LMH – $L/m^2/h$

MD – molecular dynamics

MPD – m-phenylenediamine

NHS – N-hydroxysuccinimide

OG – *n*-octyl-β-D-glucoside

PCC – 4-trans-(4-trans-Propylcyclohexyl)-cyclohexyl α-maltoside

PDA - polydopamine

PES - polyethersulfone

PET – polyester

PMDETA – N,N,N',N'',N''-Pentamethyldiethylenetriamine

PMOXA-PDMS-PMOXA - poly-(2-methyloxazoline)-poly- dimethylsiloxane)-poly-(2-methyloxazoline)

POPC – 1-palmitoyl-2-oleoyl-sn-glycero-3-phosphocholine

QCM-D – Quartz Crystal Microbalance coupled with Diffusion

RC – regenerated cellulose

RMSD – root mean square displacement

RO – reverse osmosis

SEM – scanning electron microscopy

SFG – sum frequency generation

SLB – supported lipid bilayer

SUV – small unilamelar vesicles

TAA – triarylamine

TEM – transmission electron microscopy

TFC – thin film composite

TFN – thin film nanocomposite

TMC – trimesoyl chloride

Preface

Scientific research in its purest form serves the benefit of humankind and the thirst for knowledge of the world that surrounds us. Over the decades we were faced with various treats that, when tackled with the scientific approach, were solved. If we look at research from this point of view, it almost follows an evolutionary course that adapts to the "needs" of society. The threat of bad health care prompted researchers to come up with various medications while the threat of lack of resources prompted the discovery of new and more efficient tools to satisfy needs. In this last category falls the topic of the work described in this thesis. Water scarcity, or more accurately, renewable freshwater scarcity is rising on the list of resources that are becoming insufficient for the needs of the global population. While oil shortage is concerning mainly commodity production, water is a basic necessity for survival and the lack of it has a more severe impact. One of the biggest crises in the present, the refugee flight, caused by the Syrian civil war was flared up, among other religious and socio-political tensions, by the incapability of providing for clean water by the Syrian government. But developing countries are not the only ones facing water shortage problems, a clear example being the concerns faced by the US due to prolonged drought in recent years. As a reaction to global concerns, a lot of research effort has been directed towards halting the aggravation of water shortage.

Technological advancement allowed tapping into new sources for satisfying global needs. For obtaining clean water, by far the most abundant source is represented by the Oceans, as they hold 97.5% of the total amount of water on the globe. Accordingly, desalination techniques evolved, with membrane technology developing into the most applied instrument in the field. More than a half of century has passed since the first functional membrane materials were designed, and although significant improvements have been made, the principle of these membranes remained almost the same. With the arrival of nanotechnology new approaches have also appeared. In the last decade, two branches have emerged with relative importance to the work described in this thesis: thin film nanocomposites and biomimetic membrane materials. In both cases, significant performance enhancement has been achieved, although the downside of these new generation materials is the extra high complexity in design and fabrication.

This thesis brings a new concept for the development of new desalination technology. Through the mimic of natural water transporter proteins and simple synthetic availability, self-assembled artificial water channels represent a simple tool for the development of both biomimetic and nanocomposite membranes. The work presented in this thesis covers, starting from the most basic levels of molecular design, up to the fabrication of integrated membrane materials containing artificial water channels. As this project involved an interdisciplinary research, during these three years I have successfully acquired skills in a broad scientific spectrum including supramolecular chemistry, biophysics

and material science, greatly contributing to my personal development as a researcher. The main part of the work done during these years has been described in this thesis in a "to the point" manner, avoiding non-sense discussions, examples and over detailed explanations, in an effort to keep a keen sense of the scientific discussion. Nonetheless, a self-critical point of view was used in order to be able to draw the most relevant conclusions.

Chapter I
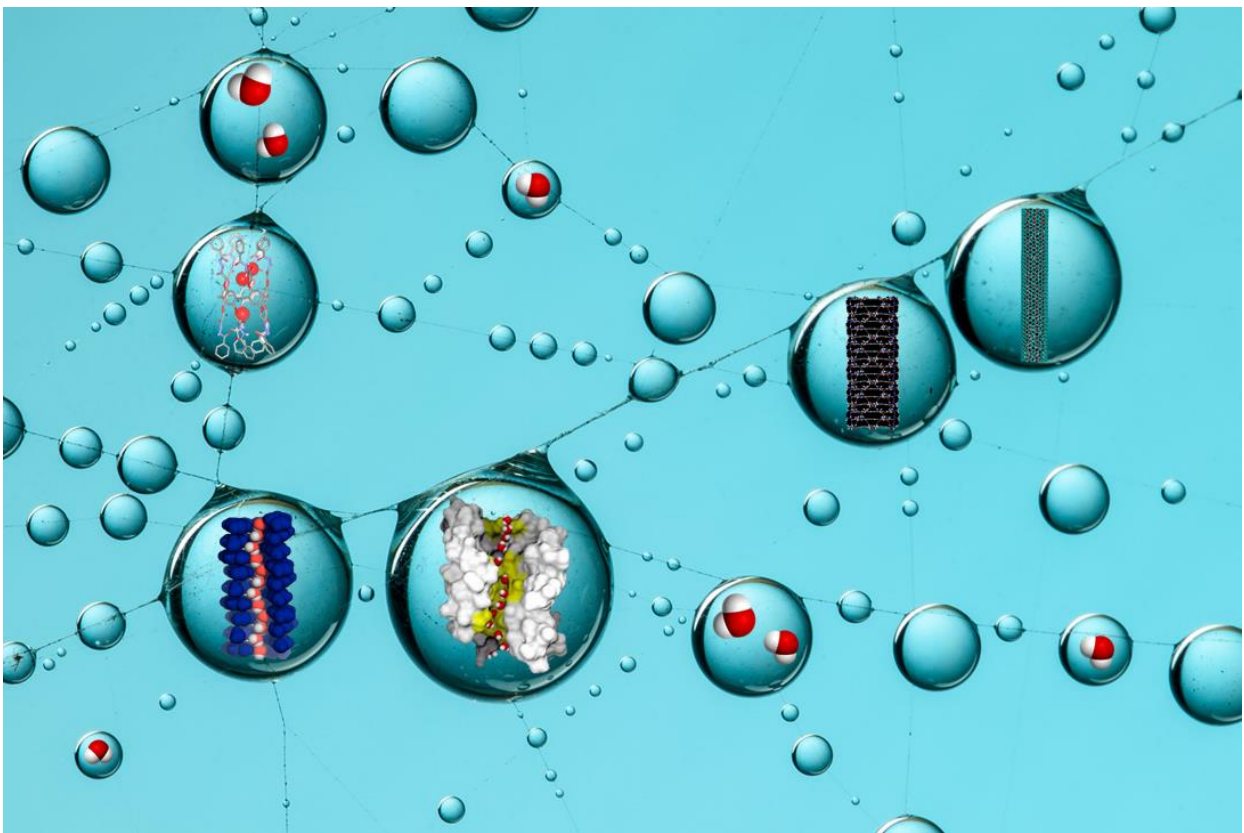
"Life is water, dancing to the tune of solids."

Albert Szent–Gyorgyi

1.1 Aquaporins and biomimetic desalination technologies

Since long chemists sought to replicate complex processes which nature can carry out with an elegant mix of complexity and efficiency. Nature inspired technology is plentiful in our current society, but most of these mimic the macroscopic side of nature.[1,2] In the last few decades scientist have dug deeper into the microscopic level of nature, uncovering, for instance, how the nano-machineries or molecular systems of biological cells function.

Aquaporins. One of these machinery, of notable importance to the project described in this thesis, is that of the proteins belonging to the aquaporin (AQP) family. Peter Agre received the Nobel prize in 2003 in chemistry for its effort in describing the function and mechanism of aquaporin-1 (AQP-1).[3] The main function of this protein is that of transporting water across the lipid bilayer membrane of the cell, (Fig. 1 A) but looking at the way this is being done brings into light a few remarkable properties that make it much more than a simple water transporter. Although the main role of the aquaporin proteins is that of the facilitated transport of water across the phospholipid bilayer of cells, only a handful of proteins from the aquaporin family is specific for water transport, other members being able to transport small solutes such as ammonia, carbon dioxide, urea or glycerol.[4] The structural determination based on simulations initially,[5] then later supported by single crystal crystallography,[6] have shown an hourglass-shaped structure that in the case of AQP-1 allowed passage of only water molecules.[7]
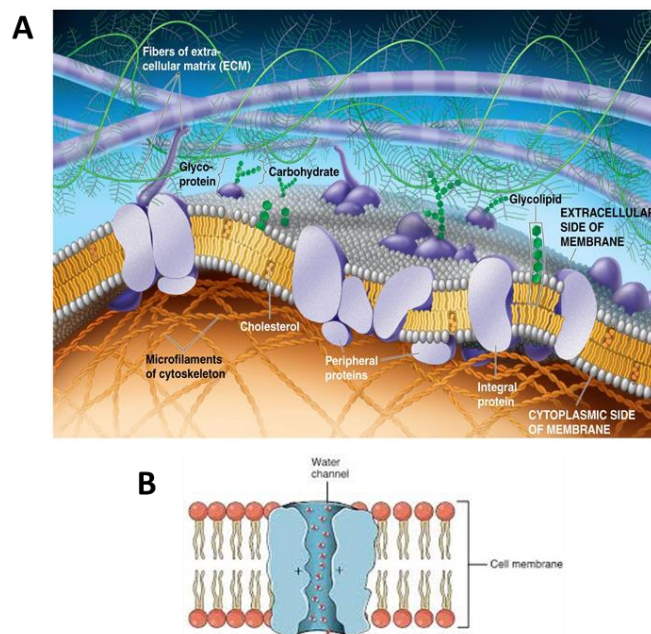
Figure 1. (A) Representation of a cellular wall (Copyright @ Pearson Education, Inc.) (B) cell membrane water channel protein.

Besides the high selectivity towards water molecules, there are three main features which make the aquaporins so effective and intriguing from a mechanistic point of view:

1) *size restriction and chemical environment allowing the passage of only a single file of water molecules.* Although water molecules have a larger volume than ionic species found the physiological solutions, the aquaporins can selectively allow the passage of only water molecules through its central pore. The average diameter of the pore itself is 3 Å, which is large enough for the water molecules to pass having themselves a diameter of 2.8 Å, but theoretically not restrictive enough to block the passage of dehydrated Na^+ or Mg^{2+} cations, with ionic radii of about 2 Å and 1.6 Å. There are two mechanisms that prohibit the passage of cations. One is related to the solvation of the cations. Both Na^+ and Mg^{2+} are larger than 3 Å with their respective hydration shells in water solutions but the structure of the pore itself doesn't favor the dehydration of the cations, leaving them too large to pass through the pore. A second "defense" mechanism against cation passage is given by the asparagine motif found close to the central pore. In physiological conditions, the asparagine is protonated acting as a repellent for any positively charged species.

2) *orientation of dipolar water molecules.* An interesting collective structuration of several water molecules is taking place in the narrowest pore region of the protein. The single file of water present there is not randomly sitting in the pocket of the pore. The water molecules have a dipole orientation from the center of the pore outwards to the mouth of the pore. The point where the inversion takes place is next to asparagines Asp 203 and 68: here a water molecule is sitting perpendicular to the pore axis. Two asparagine moieties act as hydrogen donors for the water molecules, preventing the central water molecule from receiving any extra proton that could hop along the water wire. (Fig. 2 B)

3) *no proton transport.* The result of the previously discussed water dipolar orientation inside the pore confers the ability to reject protons along the water wires. Although protons can pass from one water molecule to another through the Grotthuss mechanism[8] the inversion center in the center of the pore prohibits the proton jumping to happen in the Aquaporin thus making it impermeable for proton transport. This adds to the complexity of functions of the protein as it prevents sudden changes in pH to occur when there is a gradient across the cell bilayer, which is present almost all the time since protons are the energetic currency of cells.
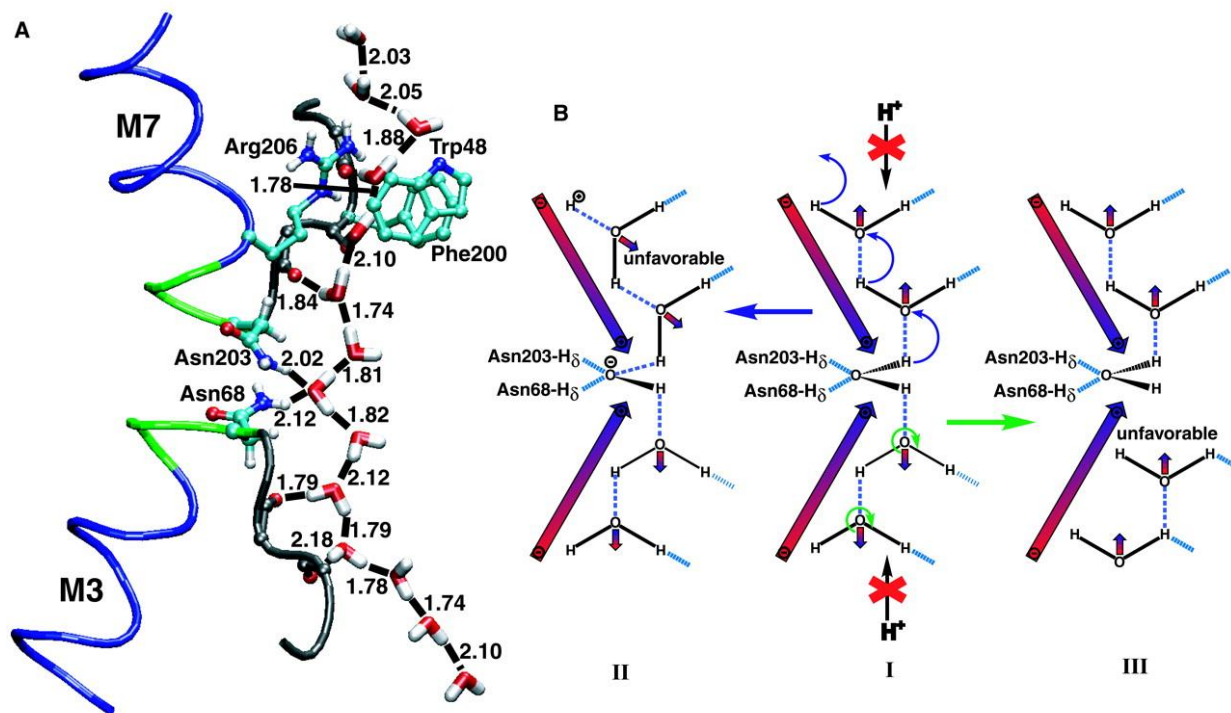
Figure 2. *(A) Structure of the aquaporin pore region (B) highlights of key features of the water channel* (image adapted from reference [7])

Synthetic bilayer vesicles. To be able to characterize more easily the proteins *in vivo* functions, scientists have developed synthetic vesicles that mimic biological cells. Using simple techniques,[9,10] small unilamellar vesicles (SUV) can be created that are much less complex than their biological counterparts. In order to quantify the water transport capabilities of the Aquaporins, a method based on light scattering modulation of a vesicle suspension was used. The details of this technique are fully described in Chapter 2. For the determination of the water transport, synthetic vesicles were made with and without aquaporin incorporated and subjected to an osmotic shock.[11]

It is important to note that vesicles composed of only lipids have also a significant permeability due to the passive diffusion of water across the bilayer, mainly caused by the flipping motion of lipids.[12] By comparing the permeability of the vesicles with and without aquaporin inserted into the bilayer one can determine the water transport specific to the proteins. However, the permeability is attributed to the bilayer and any component inserted into the bilayer. Therefore in order to calculate the permeability of single aquaporin channel, it is required to determine the actual amount of inserted proteins into the vesicle bilayer. Using this method several members of the AQP family were studied to determine their osmotic water permeability which can be as high as $\sim 10^{-14} - 10^{-13}$ cm^3/s per channel.

As water scarcity is projected to be on the rise in the next decades[13–15] development of new technologies are needed to provide affordable and sustainable production of clean water. Having been proven as high performing and selective water channel, the aquaporins

became an attractive tool to be used for the design of new materials capable of purifying water. Due to its energy efficiency, membrane systems have dominated the water purification technologies[16] and are expected to do so in the near future. As so it was an attractive option to combine the potential of the aquaporins with the currently existing technology in membrane-based water filtration.

Biomimetic Desalination Technologies. As soon as the functions of the aquaporins became known it seemed logical that in order to make use of the high selectivity and water transport, the protein needed to be used in conjunction with a membrane barrier.[17,18] This way a new branch of membrane technologies for water purification called aquaporin biomimetic membranes (ABMs) was developed. In the simplest fashion, these membranes consisted of three main components: i) aquaporin proteins ii) amphiphilic molecules in which the aquaporins are embedded and iii) a polymeric support for the mechanical resistance. The choice for the amphiphilic molecules is argued for by the fact that the Aquaporins are transmembrane proteins and their native environment is partly the hydrophobic region of the lipids found in cellular membranes, meanwhile keeping the "mouths" of the protein exposed to the water from the cytosol. As such, a reasonable direction was to fabricate membranes which had as an active barrier a lipid bilayer containing aquaporin for the enhanced water permeation. *Ding et al* demonstrated the fabrication of supported lipid bilayer (SLBs) on a polymeric support can yield functional membranes with high selectivity.[19] This was achieved through the covalent attachment of SLBs to a polydopamine-coated porous polyethersulfone. Through the use of an amine functionalized lipid, the bottom half of the lipid bilayer is attached to the free carboxylic groups that can be found on the polydopamine. (Fig. 3)
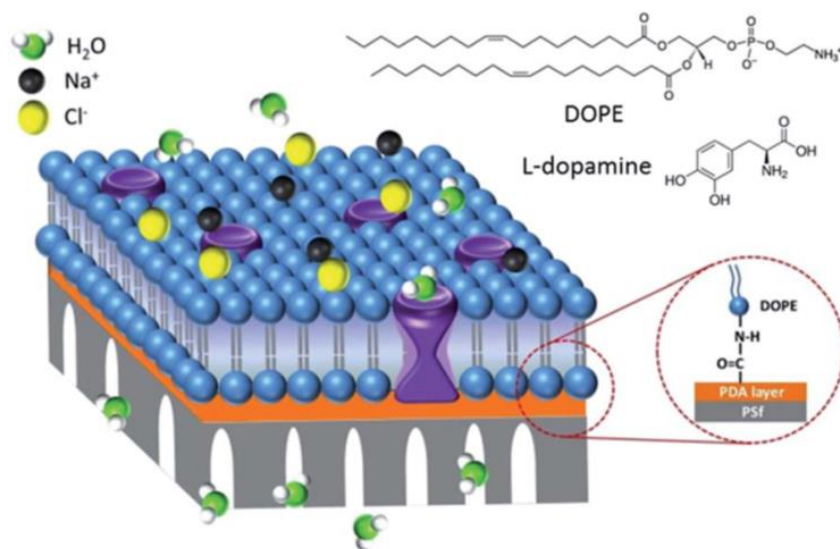
Figure 3. *Schematic presentation of the structure of the AqpZ-incorporated SLB membrane with covalent bonds; the amide bond linked 1,2-Dioleoyl-sn-glycero-3-phosphoethanolamine (DOPE) SLB is established on top of a polydopamine (PDA) layer (orange) coated porous polyethersulfone (PSf) (gray) support (image adapted from reference [20])*

The covalent link between the bilayer and the support prevents the easy desorption of the lipid matrix, offering stability to the active layer of the membrane. Nevertheless, the SLB is still prone to degradation when in contact with solutions containing detergents, which can readily disrupt the lipid bilayer. The performances of these SLB membranes are remarkable in water filtration, presenting a water flux of ~23 LMH and a reverse salt flux of 3.1 gMH when tested in a forward osmosis setup, although the reliability of these membranes remains an issue for long term applications and upscaling. To tackle this problem a different approached was needed for the amphiphilic matrix hosting the aquaporins.

In terms of flexibility and stability, the block copolymers offered a good solution. The first work to successfully incorporate aquaporins into polymer-based vesicles, called *polymersomes*, and to prove the functionality of the protein within was done by Meier.[20,21] The vesicles were made of a block copolymer with poly-(2-methyloxazoline)-poly-dimethylsiloxane)-poly-(2-methyloxazoline) (PMOXA-PDMS-PMOXA) units and were used to host Aquaporin Z, a bacterial type protein from the aquaporin family. Using the stopped flow setup it was shown that the otherwise impermeable polymersomes undergo an increase of up to 800 times in water permeability when the Aquaporins are incorporated. (Fig. 4) The activation energy for water to pass through the proteopolymersomes was comparable for that obtained in the case of native protein.
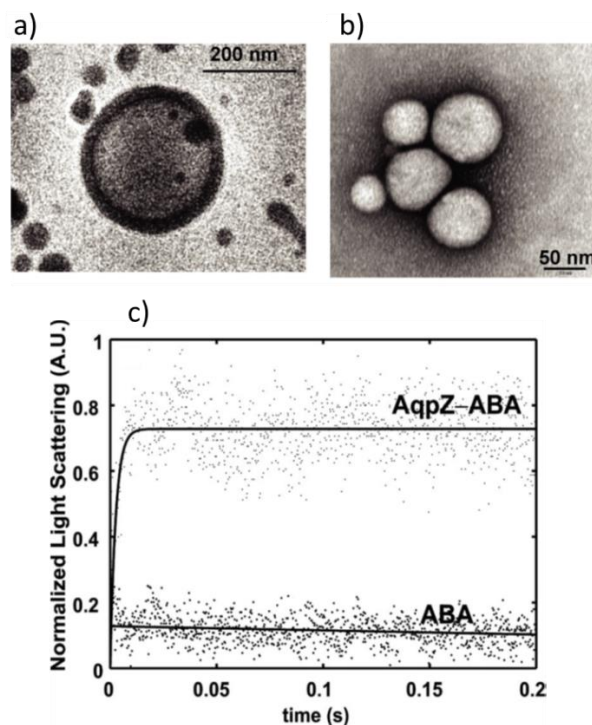
Figure 4. *Cryogenic transmission electron micrograph of a polymer vesicle b) electron micrograph of a cluster of vesicles c) Stopped-flow light-scattering experiments; increase in relative light scattering with and without reconstituted AqpZ into the polymer at 5.5°C at a molar ratio of 200:1 (polymer:protein) (image adapted from reference[21])*

12

In a compromise to obtain high stability and relatively high-performance biomimetic membranes, a different strategy was applied through the use of a mixed matrix approach.[22] *Nielsen et al* managed to trap vesicles incorporating aquaporins into traditional polyamide thin films. This way the aquaporins can achieve high efficiency having a basically native environment and at the same time keeping the composite membrane stable through the robustness of the polyamide matrix. The newly obtained hybrid membranes proved to be more permeable than their simple thin film composites (TFC) counterparts, achieving water permeability values of up to 4 LMH/bar with a salt rejection of ~97% when tested in a reverse osmosis setup, meanwhile being stable for periods relevant for industrial applications.
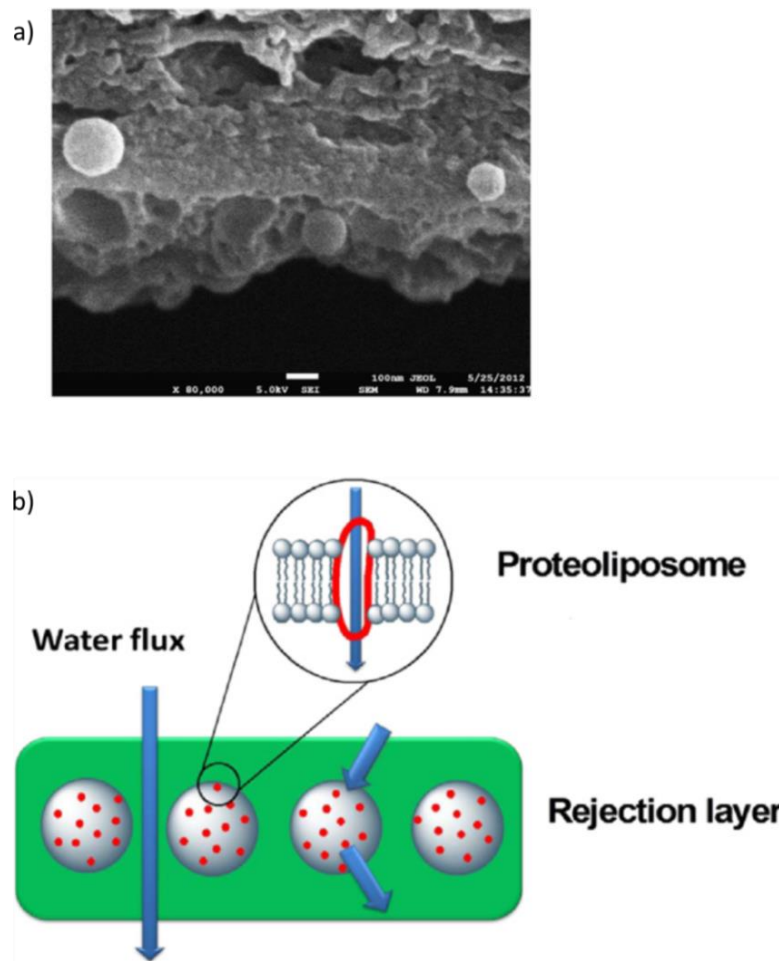
Figure 5. *a) Scanning electron microscopy (SEM) image of the cross-section of an ABM-thin film composite membrane b) Conceptual model of aquaporin proteoliposomes integrated into a polyamide rejection matrix (image adapted from reference[23])*

Most of the current designs for AQP membranes involve polymeric materials, which can make it viable for upscaling and use in industry. However, a vital part of AQP membranes and not yet a commercially available product is the AQP protein itself. Production of AQP proteins is a non-trivial task, as the purification setup still represents an expensive and time-consuming obstacle. Another limitation is the surface to channel ratio of these proteins. In

order to have one channel present, an AQP protein will take up approximately 6 nm^2 on a surface. From a chemical engineering point of view, this can pose limitations when trying to achieve highly functional membrane surfaces. As so, using Aquaporin bioassisted materials is advantageous, but in the long run, the technology might suffer from limitations that make them a less appealing options for the fabrication of desalination membranes.

1.2 Synthetic water channels

As shown in the previous sub-chapter, new emerging biomimetic technologies are being applied to tackle the increasing need of clean water. An alternative strategy for this is to develop completely synthetic water channels that are capable of selective water transport across a membrane barrier. Using artificial systems is attractive as they can offer increased stability, scalability and easier fabrication process than their protein counterparts. But in order to achieve artificial systems capable of outperforming proteins without the burden of complicated synthetic procedures, it is important that they are able to imitate the protein's key structural features and functions using a simple as possible approach. With the aim of obtaining artificial membranes for water filtration, the first and foremost important issue that is to be considered for the artificial systems is their interaction with water molecules.
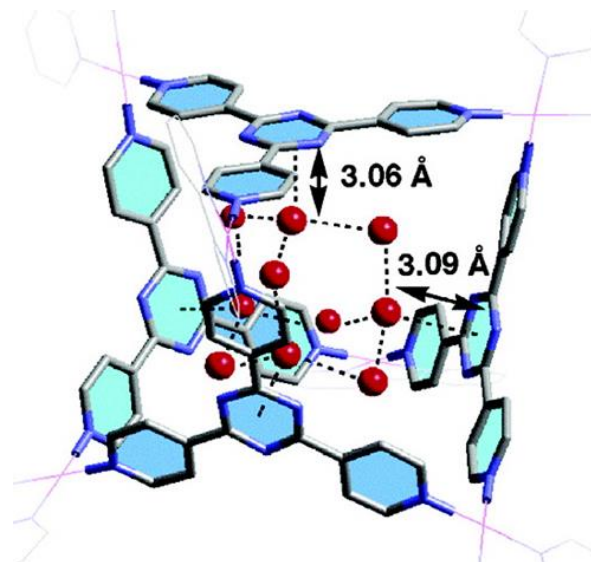
Figure 6. *"Molecular ice" in the confinement of a self-assembled cage (Image adapted from reference [24])*

Molecular encapsulation of water molecules in artificial molecular architectures such as capsules or channels offers possibilities to explore the properties and mechanistic behavior of water under conditions very close to confined water found in biological systems. This confinement can be considered a small border of the physical state of water that is between the solid and liquid state. (Fig. 6) Several water clusters have been entrapped within complex structures and they have attracted a lot of interest from the point of view of fundamental knowledge such as water structuration related to water–water or water-host interactions under confinement.[23]

Among water clusters, the one-dimensional water-wires have especially attracted a lot of interest with emphasis on their structural similarities to their biological counterparts present inside the protein channels. In order to understand and progress towards systems of

increasing functional complexity, studying the adaptive nature of water clustering when interacting with the neighboring molecular environment is important. This is especially true when considering phenomena that take place at the level of cellular processes, like for example the process of water transport. As previously described, the aquaporins are the representative protein family for the function of water transport across lipid bilayers. Although there is a rich inventory when it comes to molecular encapsulation of water,[24,25] in most cases these water host systems are highly polar which prohibits them to be used in conditions similar to the one offered by the hydrophobic bilayer of the cellular wall. As so the examples for confined water systems capable of being inserted into hydrophobic environments are scarce. Even less are the examples of systems capable of actively transporting water across the lipid bilayer. These systems that are truly capable of mimicking the function of natural water transporters have received the label of artificial water channels.

The common features of these biomimetic systems are the presence of a central pore, which is a hydrophilic or hydrophobic region that allows the passage of water and relatively hydrophobic shell that permits the insertion into the lipid bilayer. There are two main approaches when considering the structure of synthetic water channels:

i)   *single molecular systems* that can span the length of the lipid bilayer;
ii)   non covalently bound *supramolecular systems* that can self-assemble into functional water channels inside the bilayer.
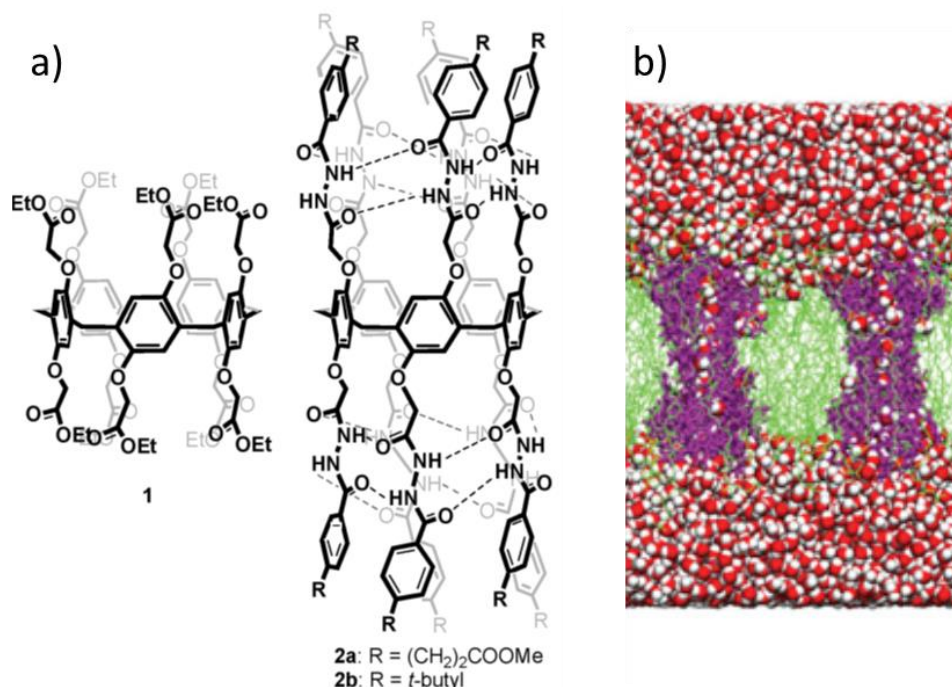

Figure 7. *a) Pillar[5]arene derivatives with tubular conformation b) molecular dynamics simulation of similar molecules place in lipid bilayers* (image adapted from references [27,28])

Single Molecular Channels. The pillar[5]arene derivatives with appending hydrazide[26,27] arms from Hou and coworkers behave as single molecular pore spanning channels (Fig. 7). Intramolecular hydrogen bonds between the arms confer robustness, keeping the channels intact when inserted into a lipid bilayer. Depending on the length of the appending arms, the water transport rates vary, having a relatively low water transport rate of up to 40 molecules of water per second per channel. Although there is no selectivity against cations, the pillar[5]arenes are impermeable to protons. The explanation for this is the impeded proton hopping through a Grotuss effect. Curiously the molecular dynamics simulation for the pillar[5]arenes imbedded into a lipid bilayer formed of POPC lipids show an oscillation between an empty and water filled state, with some protruding of lipid chains into the cavity of the channels. (Fig. 7 – B) This variation of filling is argued by the authors to happen due to the presence of alternating hydrophobic-hydrophilic regions in the pore of the channels, the benzene rings being hydrophilic and the hydrazide, respectively amide bonds being hydrophilic. This results in the formation of low-dimensional disrupted water wires within these channels, showing selectivity against protons but not a high water permeability.

Following up on these results a second generation more hydrophobic pillar[5]arene molecules containing poly-phenylalanine peptidic arms were designed. The average single channels osmotic water permeability for these is $3.5*10^8$ water molecules per second, being in the range of AQPs ($10^8 - 10^9$ water molecules per second). Nevertheless, the channels present a drawback when it comes to ionic selectivity. Having an inner pore size of approximately 5 Å, the channels are not suitable to selectively transport water. They allow the passage of cations with selectivity according to their hydration energy: $NH_4^+ > Cs^+ > Rb^+ > K^+ > Na^+ > Li^+ > Cl^-$.

A rather distinctive type of unimolecular synthetic water channels is represented by the carbon nanotubes (CNTs). It is a little ambiguous to attribute the name of single molecular channels as CNTs are basically rolled up graphene sheets into perfect cylinders and have a more nanopolymeric architecture rather than that of a well-defined molecule. Known for their wide applications in nanotechnology[28–30] recently they have attracted more attention for their applications in nanofluidic devices for translocation and separation. Until recently the main advantages of using CNTs as transport devices was their mechanical and electric properties. With the narrowing of the pore sizes of synthesized CNTs, a new discovery was made regarding the mass-transfer behavior across CNTs with pore sizes approaching the range of one nanometer. Simple diffusion or Newtonian flow doesn't apply when water clusters are broken down on entering the nanotubes (Fig. 8). Between 1.25 nm and 1.39 nm, the water suffers a transition from bulk phase water into solid-like organized water. Under 0.9 nm water adopts a single file structure very similar to the one found in the Aquaporins. The change in structuration in the confinement of the pore causes water molecules to pass through with enhanced speed due to a boundary slip mechanism.[31,32]
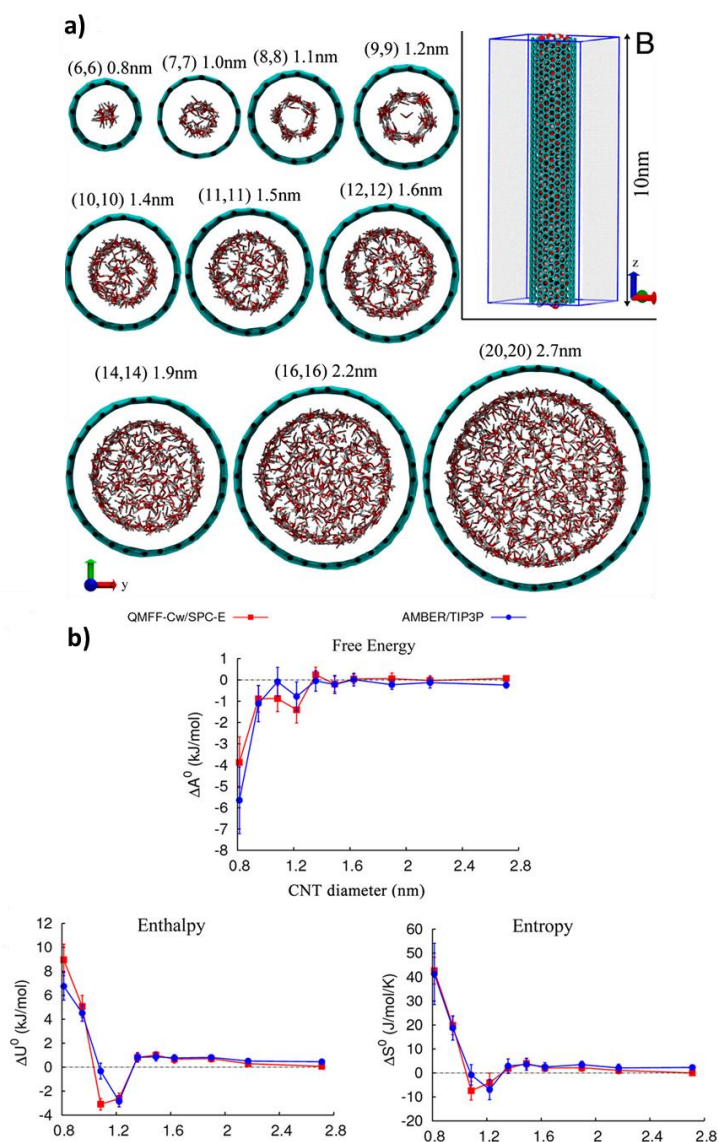
Figure 8. *a) Water structuration in a 10 nm long CNT with varying pore sizes obtained through equilibrium molecular dynamics b) variation of free energy, enthalpy and entropy of water confined in CNT pores of varying size using two different simulation models (image adapted from reference [33])*

CNTs have been proved to easily self-insert themselves into both biological and synthetic lipid bilayer membranes.[33,34] Recently, *Noy et al* conducted several studies on the permeability and selectivity of small porosity CNTs when inserted into lipid environments. [35–37] Vesicles containing short CNTs in the range of 5-20 nm length were prepared and examined in various transport experiments. It was demonstrated that the ion transport rates are strongly related to the level of ionic strength of the solutions and the hydration shell radii of the cations. (Fig. 9 A) A special behavior towards proton transport was observed when the diameter of the tubes is in the range of 0.8 nm. As argued by the authors, the rate of the proton transport is enhanced by the organization of the water molecules, reaching values of one order of magnitude higher than for bulk water. (Fig. 9 B)
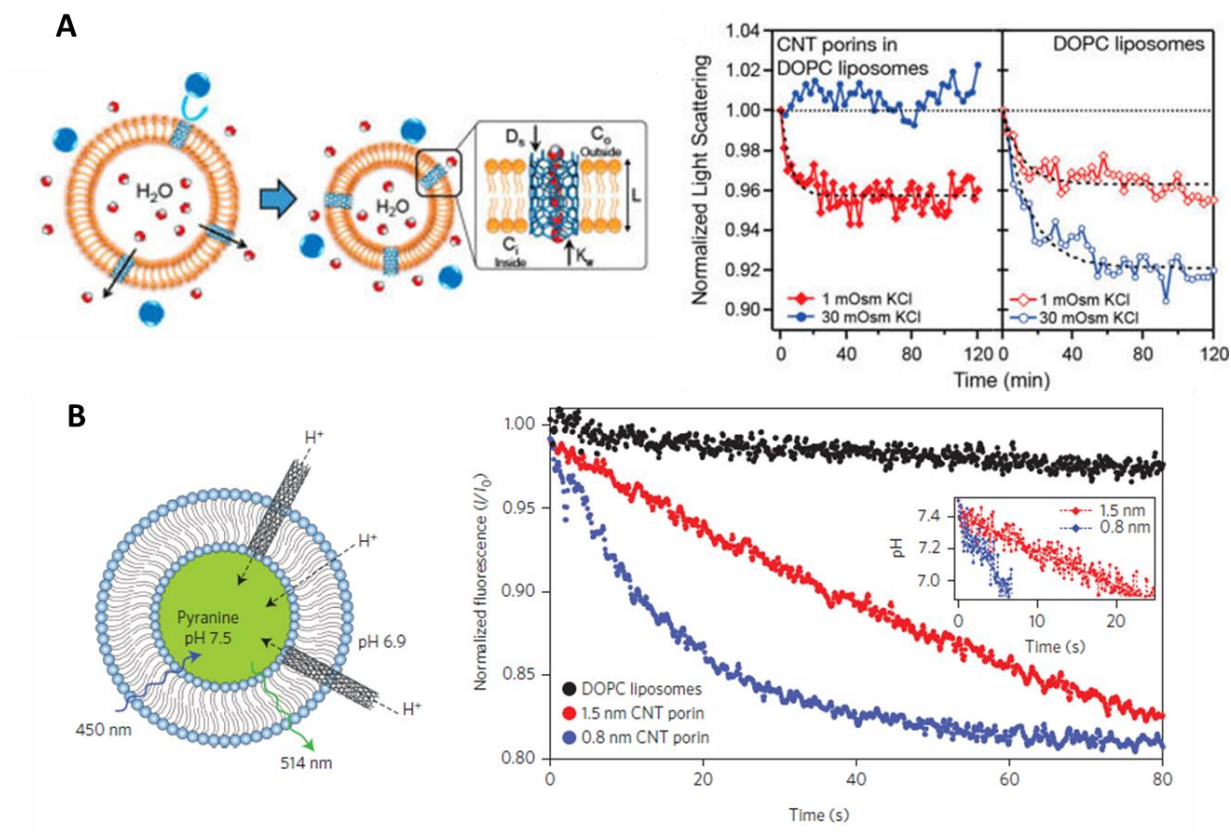
Figure 9. *CNTs in vesicular systems: (A) water and ion transport through a 1.5 nm diameter CNT and (B) proton through 0.8 nm and 1.5 nm CNT (Image adapted from references [36,37]*

Molecular dynamics simulation show that in order to achieve total rejection of hydrated cations, uncharged carbon nanotubes need to have a diameter of approximately 0.4 nanometer,[38] although in theory a rejection rate of 95% can be achieved when using (7,7) CNTs with a diameter of approximately 1 nm.[39] So far functional membranes have been prepared (Fig. 9) using 1.6 nm CNTs[40,41] presenting a water flux of $9*10^8$ water molecules per second per channel.

Although impressive in performance, there is still the issue of producing low polydispersity CNTs capable of high salt rejection and to further upscale the technology for desalination applications. Nonetheless, CNTs represent a very attractive tool for obtaining robust filtration membranes with tailored selectivity through pore size variation.
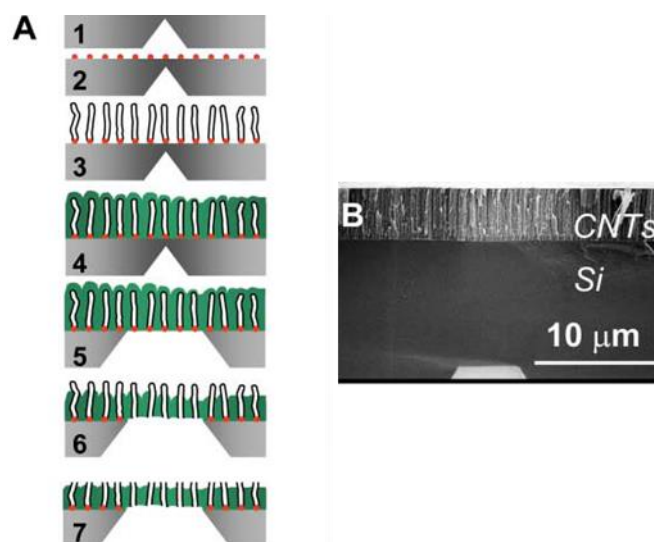
Figure 9. *(A) CNT membrane fabrication: 1) silicon support micro etching 2) catalyst deposition 3) nanotube growth 4) gap filling with chemical vapor deposition 5) membrane area etching 6) ion etching to expose nanotubes and remove catalyst nanoparticles 7) nanotube uncapping (B) SEM cross-section of the CNT membrane (Image adapted from reference [30])*

Self-assembled supramolecular channels. The second category of synthetic water channels uses a strategy based on the principles of supramolecular chemistry. Although the concept of supramolecular chemistry was initially developed more than a century ago by Hermann Emil Fischer who proposed the "lock and key" concept[42] for the functioning of enzymes, synthetic supramolecular chemical systems were developed much later and their importance received recognition initially through the Nobel Prize in chemistry awarded to Jean-Marie Lehn, Charles J. Pederson and Donald J. Cram in 1987.[43] Their work was focused on the development of cation binding small organic molecules, such as crown ethers[44] and cryptands.[45] It became clearer what the importance of non-covalent interactions is in the constitution of a chemical system. In short, the creed of supramolecular chemistry is that the total of a system is more than the sum of its parts. This put the highlights on synthetic supramolecular chemistry and was followed by an intensified focus of research in this area. Later, much more complex systems emerged from exploiting the principles of supramolecular chemistry and yet another Nobel Prize was awarded in 2016 to the pioneers of supramolecular machines[46–48]: Jean-Pierre Sauvage, J. Fraser Stoddart and Bernard L. Feringa.[49]

One particular concept that derived from supramolecular chemistry was the property of small organic molecules to self-assemble into supramolecular architectures that often have properties that are not predictable and differ completely from that of their building blocks.[50] Supramolecular self-assembly works through non-covalent interactions between relatively small organic molecules. Based on the information embedded into the molecules

through different chemical moieties, one can obtain self-assembled structures which translate into various macroscopic properties, through cooperative effect.[51,52]

Basically, the design of self-assembled artificial water channels makes use of self-assembly to produce functional supramolecular entities that act as water transporters. By embedding the building block with chemical information, one can influence the outcome of the resulting architecture formed through self-assembly. Based on this concept *Zeng et al* designed oligopyridine amide foldamers which are able to self-assemble into a functional water channel.[53] (Fig. 10)
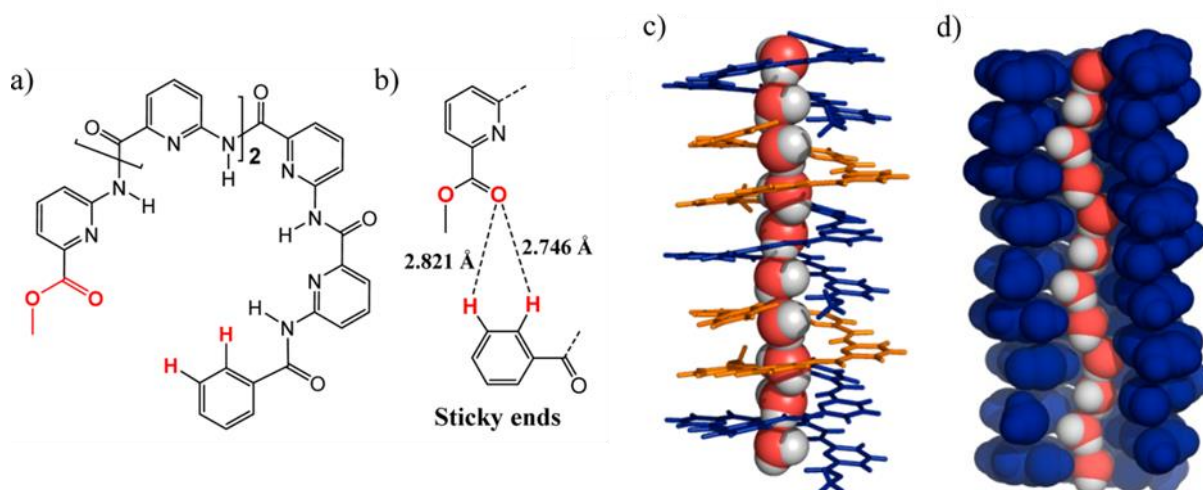
Figure 10. *a) Building block of the synthetic water channels; b) "sticky ends" motif for self-assembly guidance; c) crystal structure and d) representation of a single water channel (image adapted from reference [53])*

Using a "sticky ends" strategy the relatively small olygopyridine molecules are able to self-assemble into helical structures with a pore of approximately 2.8 Å, approaching the pores size of the restrictive narrowest region in AQPs. The nanopore contains a single file water molecule. Water transport experiments were run using a simple dynamic light scattering (DLS) setup, thus it is not possible to report an actual osmotic water permeability value for these channels. Interestingly when water permeability tests were performed the channels showed no water transport under salt-induced osmotic pressure, but when under proton gradient the helical stacks effectively transported water. This underlines the dependence between the chain-like confinement of the water inside the pore and translocation capabilities of the channel. The channels showed no transport of Na^+ and K^+ cations when tested using the vesicular fluorescent dye assay, making them a viable option for desalination applications. However, these systems have a few drawbacks also, as the synthetic route is tedious and the global yield is relatively low.

With a similar approach, *Gong et al* have synthesized a series of macrocycles capable of self-assembling into one-dimensional tubular channels.[54] Through the combination of pi-pi stacking and hydrogen bonding, macromolecules bearing ethynylene bridged phenyl rings

as core and amide-linked alkyl chains as a shell are proposed by the authors to form columnar nanoporous assemblies with a porosity under 2 nm. (Fig. 11)
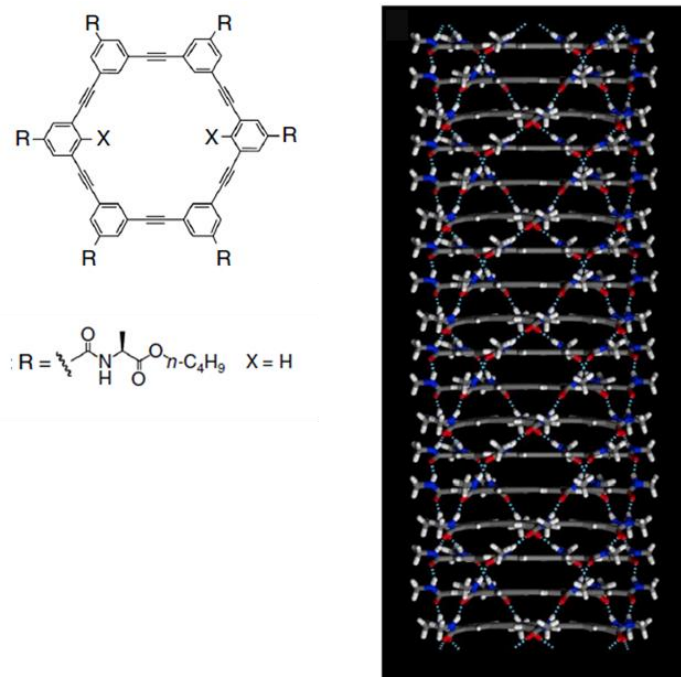

Figure 11. *Simulated structure of ethynylene-arylene based channels (image adapted from reference [54])*

Although the size of the pore of 4-5 Å would normally offer little selectivity, the self-assembled tubes present a hydrophobic cavity forcing water to adopt specific conformations when passing through and thus inducing selectivity when considering hydrated cations. Remarkably the channels can selectively transport K^+ cations across a lipid bilayer but they are rejecting the passage of both Li^+ and Na^+. The transport of water occurs in a similar fashion as the one observed in the case of CNTs, a hoping of water molecules between voids having no specific binding to the walls of the pore. The determined osmotic water permeability of these hydrophobic channels is approximately $4.9*10^7$ water molecules per second per channel.

Barboiu et al have previously reported that alkylureido-imidazole organic molecules can be used as scaffolds for the self-assembly of imidazole quartets (I-quartet) mutually stabilized by water wires.[55] Through the use of a urea-urea, Imidazole-Imidazole and Imidazole-water hydrogen bonding network, induced organization into tubular quartet architectures are present in the solid state, including water wires in the confinement of the formed channels. (Fig. 12) The obtained crystal structures showed similar structural features as found in the pores of the aquaporins. The imidazole based water channels showed a central pore of approximately 2.6 Å, close to the 3 Å provided by the AQP channel, with the water molecules adopting a specific organization. The water molecules inside the I-quartet form a single molecular wire structure adopting a dipole orientation. Encouraged with the

Aquaporin mimicking power of these supramolecular entities a new project was proposed to study the water transport capabilities. Thus, this became the main topic of the project described in this work.
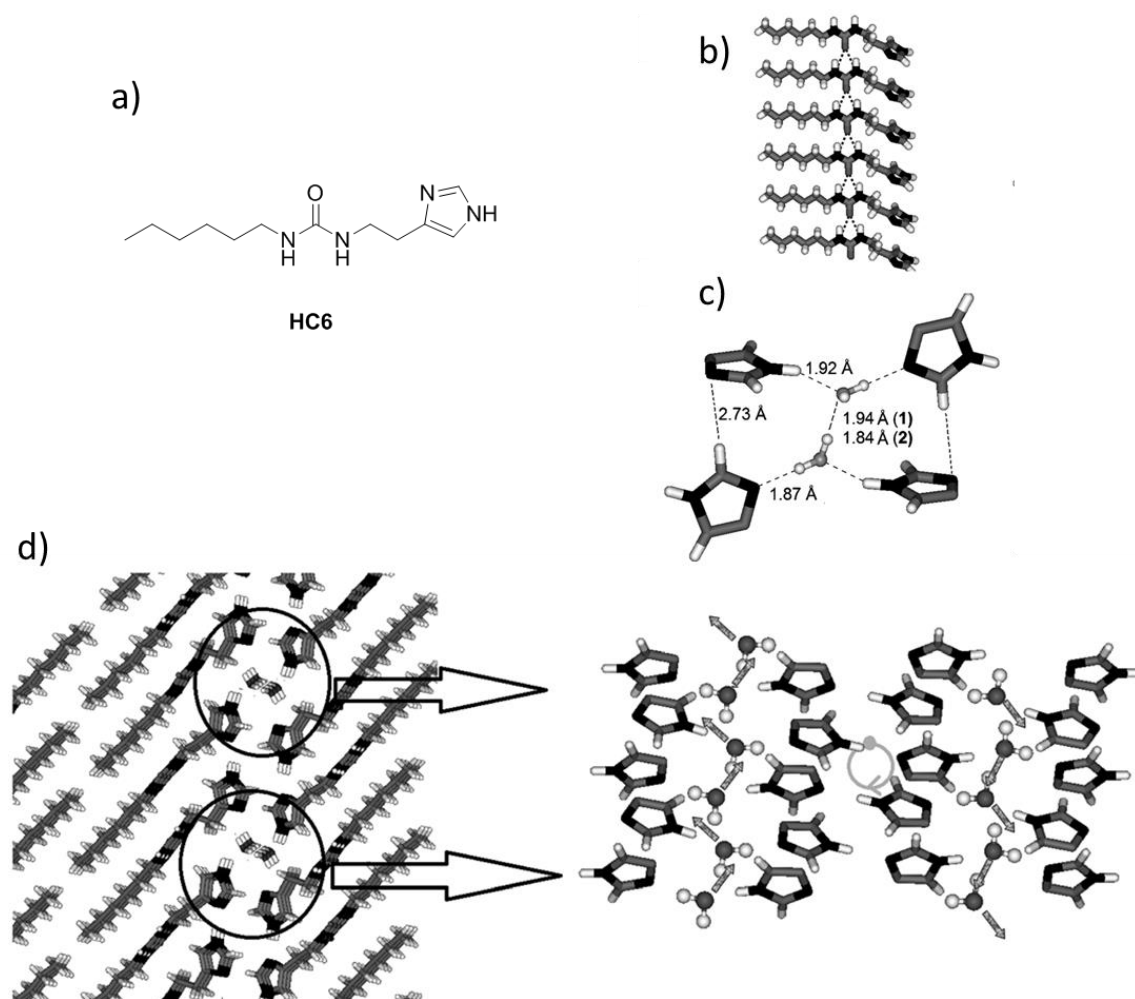
Figure 12. *a) Molecular structure of hexyl-ureido ethylimidazole; Single crystal structure featuring: b) H-bonding through urea ribbons c)* I-quartet *containing two bound water molecules d)* I-quartet *channel structure (top view) and dipole orientation of water molecules along the pore of the channel (side view)(image adapted from reference [55])*

1.3   Objectives and strategy

The three main objectives of the project described in this thesis were as follows:

i) the assessment of water transport and selectivity, description of the functioning and structural existence/stability of I-quartet artificial water channels in lipidic systems;
ii) expanding the artificial water channel family by exploring different design approaches by synthesizing new molecules for the construction of novel supramolecular self-assembled water channels;
iii) incorporation of artificial water channels into polymeric matrixes to obtain functional materials for water desalination experiments.

The strategy of the work development was initially put in place based on the previously obtained results. The first and most important task was to establish if, and how these imidazole based channels will behave when assessed for water transport. Due to their inherent amphiphilic nature, the channels were eligible for insertion into lipid environments. As so, the option to study the imidazole channels inside vesicular systems was chosen, as it offers the possibility to determine whether or not the compounds are capable of water transport across the lipid bilayer of the vesicles. The first step was to extend the library of imidazole compounds through the synthesis of simple variation of the hydrophobic tail and obtain solid state structural information through X-ray crystallography. It followed to describe the water channels transport capabilities and structure/performance relationship of water transport across lipid bilayers.

After establishing that the channels are indeed capable of water transport, we started to enquire about the mechanism of water movement through the confinement of the channels inside lipid bilayers. In this idea, we started a collaboration with Marc Baaden (Institut de Biologie Physico-Chimique Paris), an expert in molecular dynamics. We proposed to study through molecular dynamics simulations the structural behavior of the initial solid state like structures of the channels when placed in a lipid environment.

Following the encouraging results from the simulations we proposed to further prove the physical existence of the channels inside the bilayer and in an effort to elucidate the effect of chirality on the channels performance we initiated a collaboration with Poul Pedersen (Cornell University) and Georges Belfort (Rensselaer Polytechnic Institute, Troy), and studied the artificial channels inserted into single lipid bilayers through sum frequency generations experiments.

In the meanwhile, as a second objective, we proposed the design and synthesis of functional organic molecules that could self-assemble into functional channels in a similar fashion as the imidazole compounds. We proposed the synthesis of new building blocks mainly through the modification of the functional head of the amphiphilic compounds to

obtain similar small organic compounds capable of self-assembling into water channels like in the case of the I-quartets. The compounds were studied for their ability to form water channels in solid state and tested for water transport in the same fashion as for the I-quartet channels.

As a self-imposed objective at the end of the second year of the project, the third significant objective was to make the transition from molecular and nanometric level studies and transfer the artificial water channels onto the macroscopic level. Thus the design of membrane materials containing artificial water channels for water desalination was proposed. Two different approaches were attempted for I-quartet channels and analogous channels, having obtained functional integrated membrane materials.
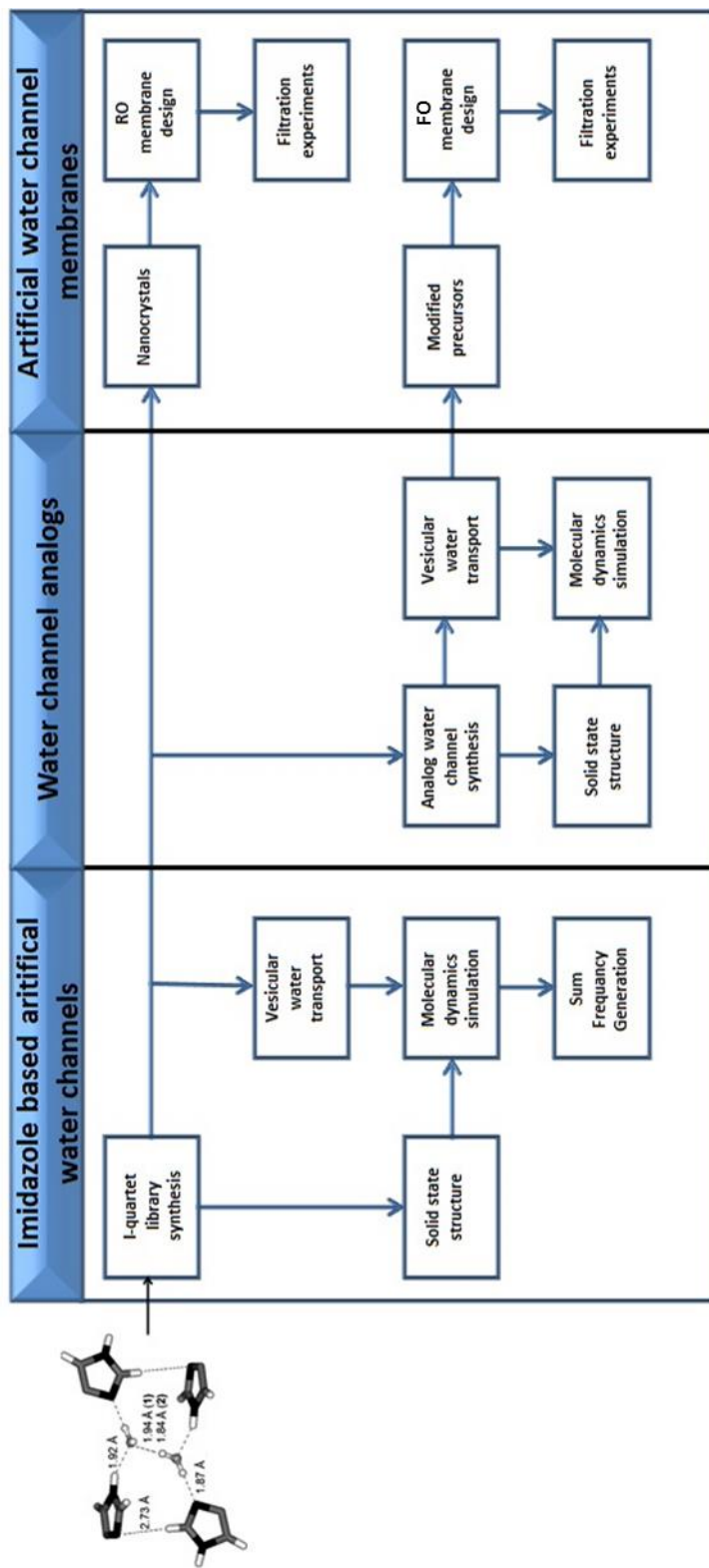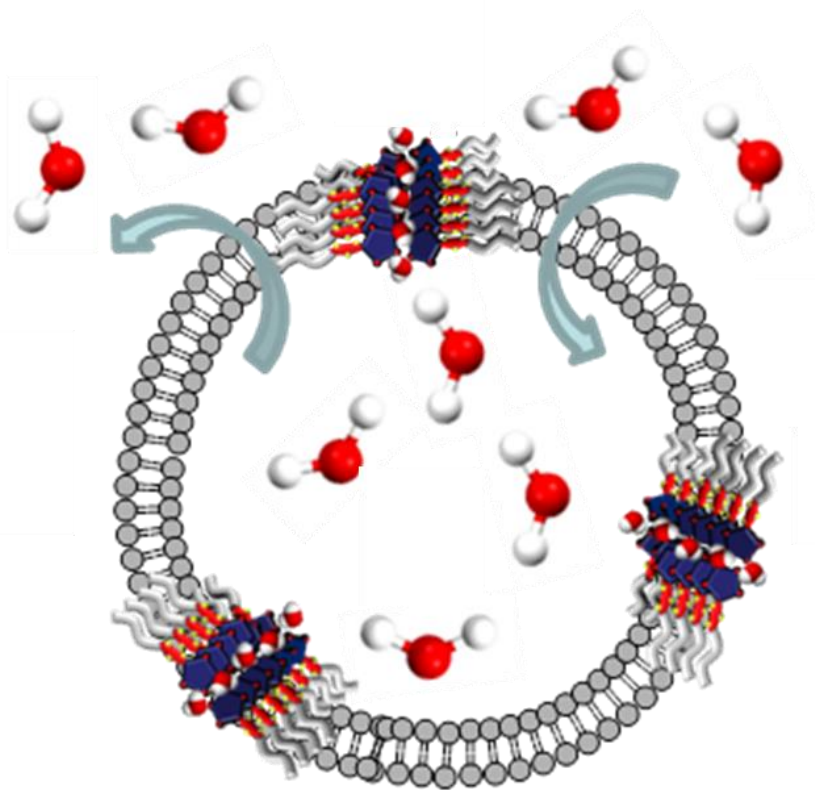
Figure 13. *Work strategy*

Chapter II

–Imidazole quartet artificial water channels–

"When nature finishes to produce its own species, man begins using natural things in harmony with this very nature to create an infinity of species."

Leonardo da Vinci

2.1 Context

Interactions at the molecular level and hydrodynamics within biological systems are of crucial relevance in understanding the structural behavior of biomolecules and in controlling important biological functions.[56,57] Central to the properties of water is the structure and dynamics of the hydrogen-bonded network. The collective interactions of water with biomolecular surfaces and channel inner-structures render its structure different from bulk water, as it can be seen in the changes to the strength of the hydrogen bonded network of such "Biological water".[58–61] Imposing examples are the selective transport of water or ions from membrane potential gradients across biological pores like AQPs[3] or Gramicidin A.[62] In this context, it has previously been shown that natural AQPs can be mimicked using structurally much simpler artificial compounds.[55]

The alkylureido-imidazole compounds previously reported by our group, self-assemble to form I-quartet water channels that present structural similarities to AQPs pore structure concerning the ability to confine structured water molecules in a single file water wire, while having also a dipole orientation. So far, the hydrogen bonded network of oriented water confined within artificial water channels has eluded physical characterization. The use of synthetic scaffolds for mimicking natural protein functions pave the way for better understanding the underlying mechanism responsible for their high functional efficiency.

In this chapter, a family of alkylureido-ethylimidazoles was studied, focusing on describing their solid state supramolecular structures through X-ray crystallography, water transport properties through stopped-flow experiments, in lipid behavior through molecular dynamics (MD) simulations and physical characterization of channel confined water molecules through sum frequency generation (SFG) spectroscopy. Special attention was accorded to the octylureaido-ethyl imidazole and its chiral *S-octyl* and *R-octyl* isomers in an effort to elucidate the effect of chiral translation on water structuration and translocation.

2.2 Design, synthesis and X-ray single crystal structures

Synthetic Design. The design of the alkylureido-imidazole compounds was made bearing in mind both the envisaged functions –selective water conduction- and final superstructures – lipid membranes embedded channels - of the potential self-assembled artificial water channel systems.

The building blocks contain 3 main structural features:

i)   hydrophilic moiety for the function of specific water binding;
ii)   a moiety capable of inducing self-assembly along a specific direction;
iii)   hydrophobic components allowing the insertion into lipid bilayers. (Fig. 14)

hydrophobic chains   self-assembly motif   hydrophilic head group
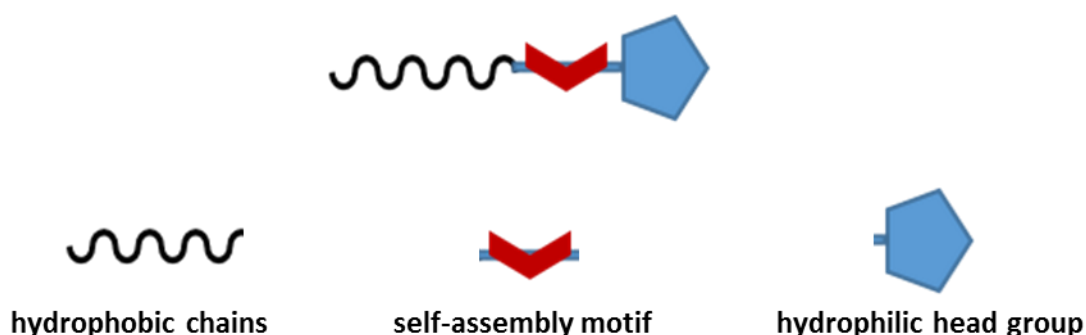
Figure 14. *Structural design for water channel building blocks*

The choice for the **hydrophilic head group** was made based on the capacity to form hydrogen bonds with the water molecules. In this idea a moiety with both donor (NH) and acceptor (N:) H-bonding groups were preferred. Among the essayed hydrophilic groups, interesting results have been obtained previously using amino-triazole groups forming self-assembled helical channels with a pore of about 5 Å diameter and a supramolecular architecture that resembles that of the natural cation channel Gramicidin.[63] The functional group that provided an ideal environment for selective water confinement was obtained when imidazole head group was used.

Choosing a **self-assembling moiety** that can offer the molecule's potential to self-organize along a specific direction was quite straightforward. We know from the literature examples that ureas induce assembly through hydrogen bonded linear ribbons and that is ideal for obtaining directional architectures.[64–66]

The choice of the **hydrophobic part**, on the other hand, was not as obvious. For the obtaining of the solid state structures almost any hydrophobic group, in conjunction with the urea, contributed positively to the formation of single crystals suitable for X-ray crystallography, mainly through the hydrophobic pressure exercised during the process of

the crystal formation. A first step was to screen the structure/functionality relationship of different imidazole-based compounds, keeping in mind the need for compatibility with the lipid bilayer for later water transport experiments. With this reasoning, a family of alkyureido-imidazole-based compounds using varying lengths and geometries of alkyl chains was synthesized. (Fig. 15)
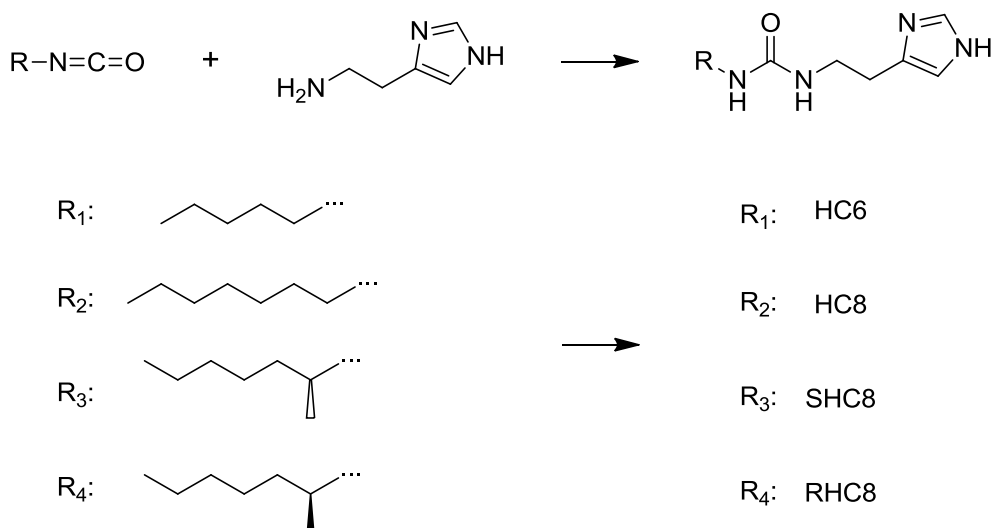

Figure 15. *Synthesis of imidazole-based compounds*

Synthesis: The synthesis of the compounds is relatively simple. It involves a one-step reaction between the respective alkyl isocyanates and histamine. The previously reported method[55] has been improved by reducing the temperature reaction and using a single solvent media instead of a mixture, simplifying the workup step of the synthesis. The new method consists in using only THF as a solvent and is described in detail in the experimental part. Depending on the length of the alkyl tail, we used the terminology of HC_x, where X represents the number of carbon atoms in the alkyl chain. The compounds' affinity to water is making them highly hygroscopic, exposure to wet atmospheric conditions will cause the adsorption of water molecules.

Single crystal X-ray structures. High affinity to water allowed the easy crystallization from water/solvent miscible solutions. Most of the compounds can be readily solubilized in polar solvents such as methanol, ethanol or dimethyl sulfoxide. When injected from a solution of such solvents into the water in volume ratios lower than 2:1 solvent: water, the compound will instantly precipitate as small crystalline aggregates. If kept soluble in water solutions, slow evaporation of the polar solvent will cause the formation of larger single crystals suitable for X-ray crystallography. As was expected from the design, the solid state structures present linearly stacked molecules through the hydrogen-bonded network of the urea groups and under the hydrophobic effect of the alkyl tails, imposing a planar conformation on the urea ribbon. With the exception of **HC4**, The crystal structures reveal a homomeric association between urea–urea and imidazole–imidazole/imidazole–water of hydrogen bonding sites. The imidazole-water-imidazole association is forming a basic

30

repeating unit we call imidazole quartets (I-quartet) that stack to form tubular structures, forming a supramolecular water channel. (Fig. 16)
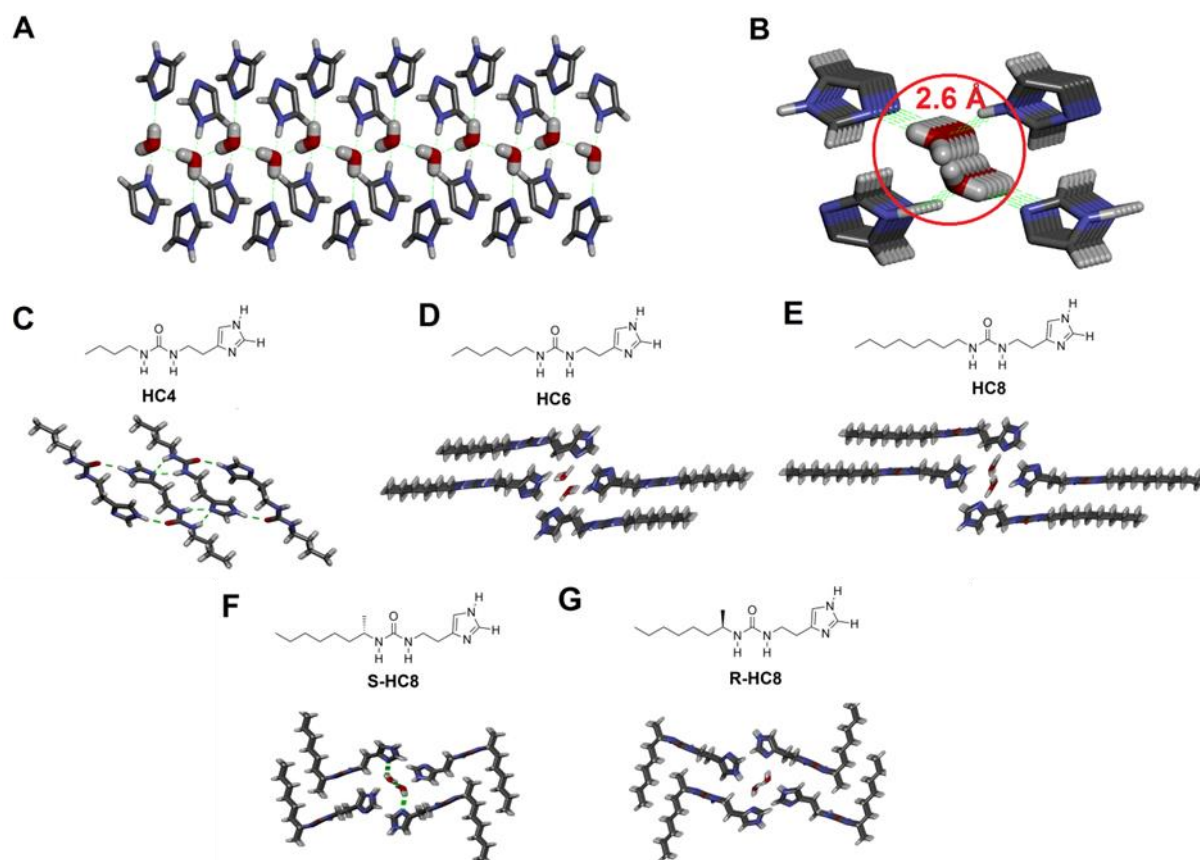

Figure 16. *I-quartet artificial water channels. A. Side and B. top views of I-quartet water/proton channels that self-assemble into tetrameric- tubular architectures (~ 2.6 Å diameter) confining dipolar oriented water-wires. Top views in stick representation (N, blue, C, gray, O, red, H-white) of the water confined I-quartet X-ray single crystal structures of C. Butylureido-ethylimidazole **HC4**, D. Hexylureido-ethylimidazole **HC6**, E. Octylureido-ethylimidazole **HC8**, F. S-Octylureido-ethylimidazole **S-HC8** and G. R-Octylureido-ethylimidazole **R-HC8**.*

The pore diameter of the I-quartets is approximately 2.6 Å, each perfectly accommodating two alternating water molecules. These confined water molecules form hydrogen bonds between themselves and the walls of the channels, adopting a single file structure along the axis of the pores. Importantly, the structuration of the water wires is not random, having a unique dipolar orientation in each of the individual channels. This feature, together with the narrow pores size, make for an artificial mimetic of the AQP water channels, thus having received the name of artificial water channels. Analysis of crystal structures of **HC8** and **R-HC8** or **S-HC8** further reveals unexpected H-bonding –C-H---N motifs ($d_{N\cdots HC}$ of 2.7-2.8 Å) between two orthogonally disposed imidazole moieties, resulting in the formation of imidazole dimers reminiscent with the structures observed for His[37]-quartet proton gate of the Influenza A M2 protein.[67,68] The oxygen atom of each water molecule is

simultaneously and strongly H-bonded to both imidazole N-H groups ($d_{O \cdots H}$ of 1.9 Å) and the vicinal water molecules ($d_{O \cdots H}$ of 1.8 Å).

In an effort to essay the effect of chirality upon the structure of the water channels and the water wires, alkyl chains with chiral centers were used for the building blocks. The *R* and *S* isomers of n-octylisocyante precursors were used to obtain their chiral compounds **S-HC8** and **R-HC8**. The structural differences when comparing the solid state structures of the achiral HC8 with its chiral isomers are quite remarkable. (Fig. 17)
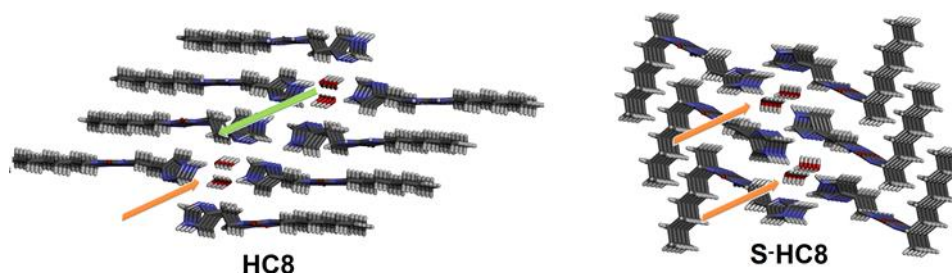
Figure 17. *Alternating and unidirectional dipolar orientation of water wires in **HC8** channels and **S-HC8** channels*

Similar patterns can be observed in the solid state channel structures of the two chiral isomer compounds: they consist of a hydrophobic external region, urea stacking ribbons and water confinement in the cylindrical imidazole quartets. The most important difference between the achiral and chiral compounds is in the hydrophobic region, where the presence of the methyl group in the alpha position from the urea group is inducing a kink in the alkyl chain. This makes the relative position of the alkyl chains of the chiral compounds **S-HC8** and **R-HC8** to be perpendicular on the urea ribbon, rather than collinear like in the case of **HC8**. Second, the occupancy state of alternating imidazole quartets changes. For the **HC8** channels, we observe filled-empty states of alternating quartets, with the empty channels forming hydrogen bonds between the imidazole heads. Meanwhile, for the chiral channels, each successive channel is filled with water wires. The last and most important difference is the orientation of the water molecules in the confinement of the channels. In all cases, the water molecules are highly orientated with a unique dipole orientation in each filled channel. For the **HC8** channels, however, the presence of an inversion center causes the water channel dipoles to be orientated in opposite directions in alternating channels. In the case of the **S-HC8** and **R-HC8** channels, water molecules in successive channels are all oriented in the same directions, the structures showing a unique dipole orientation for all the water channels. This display of unidirectional water systems is reminiscent of an electric dipole system, where the passage of current can only happen in one direction. In this idea, we can consider the chiral channels with total water orientation as a primitive scaffold for a water diode system.

Crystallization experiments in a lipid bilayer environment. In an effort to reproduce the channel structures in a lipid environment, we proposed to co-crystalize the compounds in the presence of lipid-like compounds. Our aim was to directly detect the functional water channels superstructures in a lipid bilayer membrane environment. For this, we used two different techniques that were developed for protein crystallization: i) lipidic mesophase crystallization and ii) micellar crystallization. Arguing that the channel assemblies would have a similar behavior in the lipid bilayer, crystallization was attempted using the work methods applied for proteins. The first technique involves the use of the lipid phase transitions. (Fig. 18)
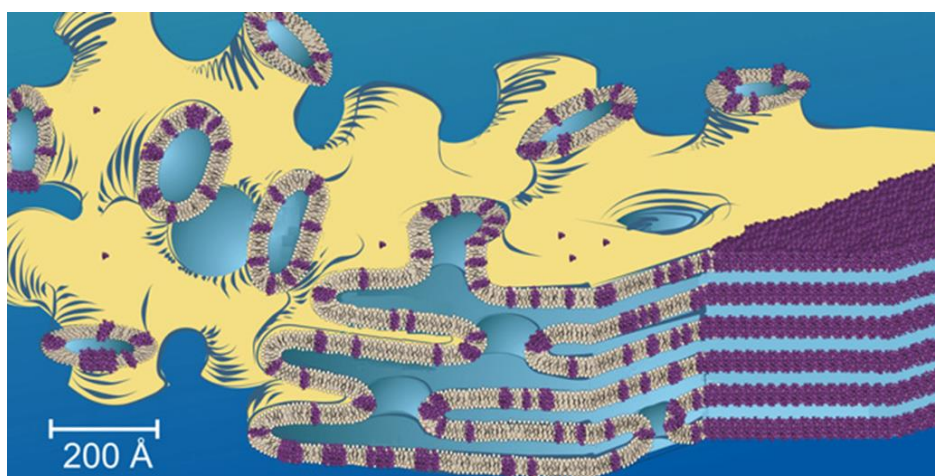
Figure 18. *Crystallization of protein (purple) from a lipid bilayer in cubic mesophase (image adapted from reference [69])*

Lipidic mesophase crystallization. The proteins are first reconstituted into the bilayer of cubic aqueous mesophase and later crystallized by the addition of a precipitant that causes nucleation and crystallization.[69–71] The protein loaded cubic mesophase lipid bilayer is obtained by mixing a melted lipid with an aqueous solution of the protein. In our case, we used Monoolein (1-Oleoyl-rac-glycerol) as lipid bilayer constituent and a solution of **HC6** or **HC8** in water. After obtaining the mesophase, the viscous mix is portioned out into wells and covered with a precipitating solution. A variation of 48 precipitating solutions has been tried, containing different mixes of high concentration inorganic and organic compounds with various pH. The systems were then left to crystallized, checking periodically for the formation of crystals using a polarized light microscope. Although managing to obtain crystals from the lipid mix, (Fig. 19) as soon as the crystals were removed from their respective solution they started melting/dissolving, not being suitable for X-ray structure determination.
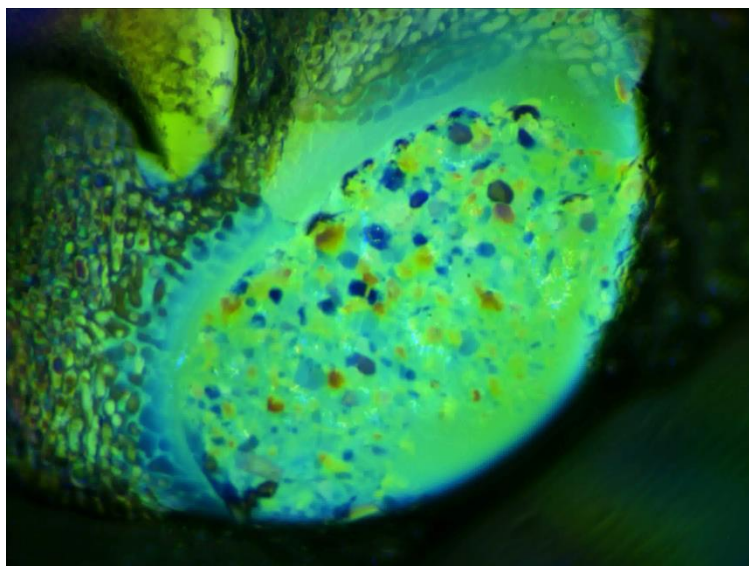
Figure 19. *Image of crystals (regular shaped blue and purple particles) from the **HC8** mesophase system under polarized light*

Micellar crystallization. The second technique is based on the use of a surfactant compound capable of forming micelles in water above a critical concentration.[72–74] We argued that, with the HC_x compounds being liposoluble, the formed channels would be integrated into the formed micelles in aqueous solutions. Then, through a similar mechanism as in the case of in meso experiments, the addition of a precipitating agent would induce the crystallization of the channels. For our experiments, we used 4-trans-(4-trans-Propylcyclohexyl)-cyclohexyl α-maltoside (PCC) as a surfactant. We obtained crystals for both **HC8** and **HC6** but the obtained structures did not form the expected water channels. (Fig. 20)
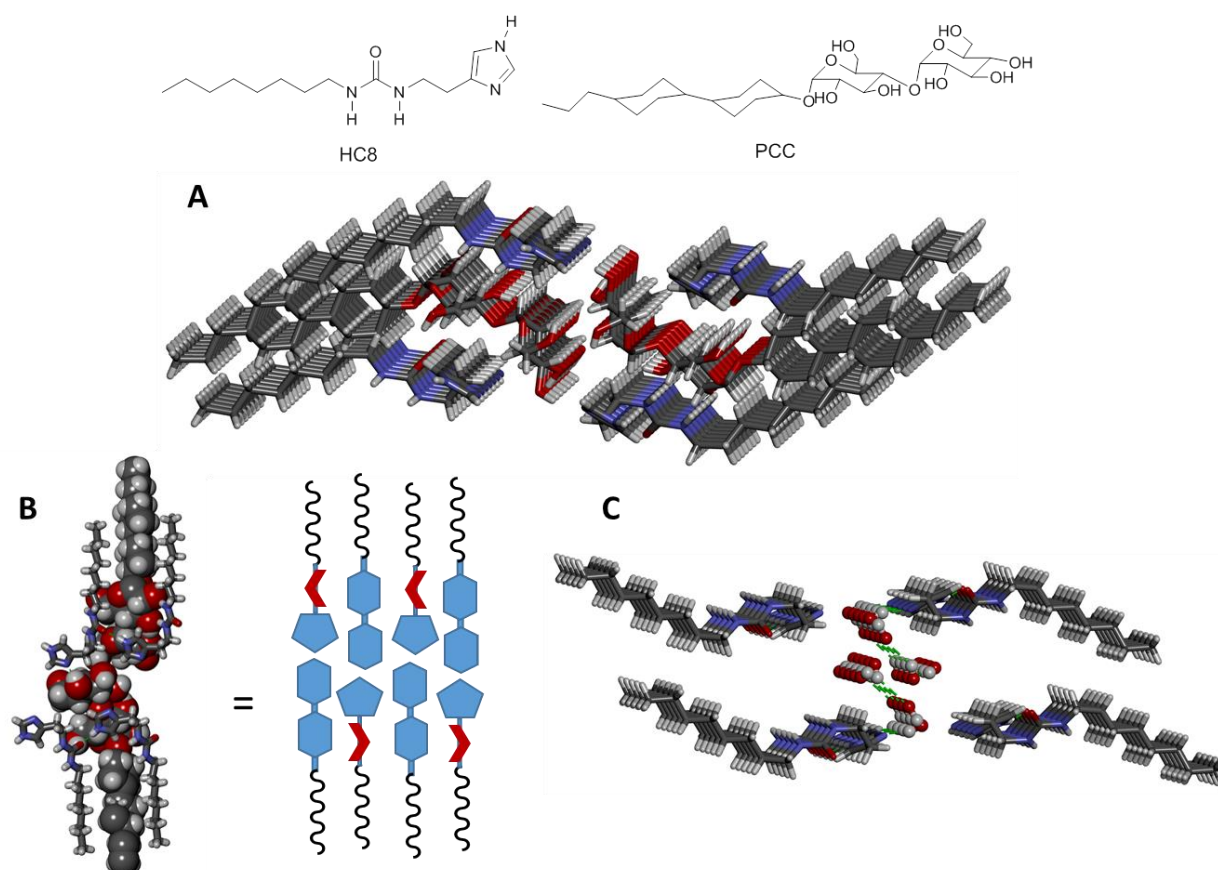
Figure 20. *(A) X-ray single co-crystal structure of* **HC8** *and PCC; (B) Schematic representation of the crystal packing of the co-crystallized components; (C) Sugar-Hydroxyls binding pattern in the crystal structure (PCC backbone omitted)*

The two compounds crystallized in an almost identical fashion. The quartets are not present anymore in this structures showing an intercalated packing of maltoside and of imidazole heads, resulting in the formation of alternative layers of PCC and ureidoimidazole molecules (Fig. 20 B) The urea ribbons are also distorted and are no longer providing a linear stacking ribbon, preferring to form hydrogen bonding networks via the N-H groups with the hydroxyls present in their vicinity, while the carbonyl group is H-bonded to a vicinal imidazole of another neighboring molecule. Although there is no water present in the system, the imidazole headgroups are still binding the hydroxyls from the PCC in a fashion that is reminiscent of the H-bonded water wires water channels (Fig. 20 C) The same network of the donor-acceptor-donor-acceptor binding motif is present between adjacent imidazole moieties and the intercalated sugar groups.

35

2.3 Water transport experiments

Following up on the description of structural details and self-assembly behaviors of the I-quartets solid state structures, we rationalized that due to their amphiphilic nature the channels could be tested as artificial channels for water transport through synthetic lipid vesicles. Lipids are the main constituent of the bilayer in biological cells and they act both as a barrier for intra and extracellular media and as supporting matrix for proteins. Depending on their nature and the working conditions, lipids can self-assemble into different structures ranging from micelles and bilayer sheets up to single or multiwall liposomes. (Fig. 21)
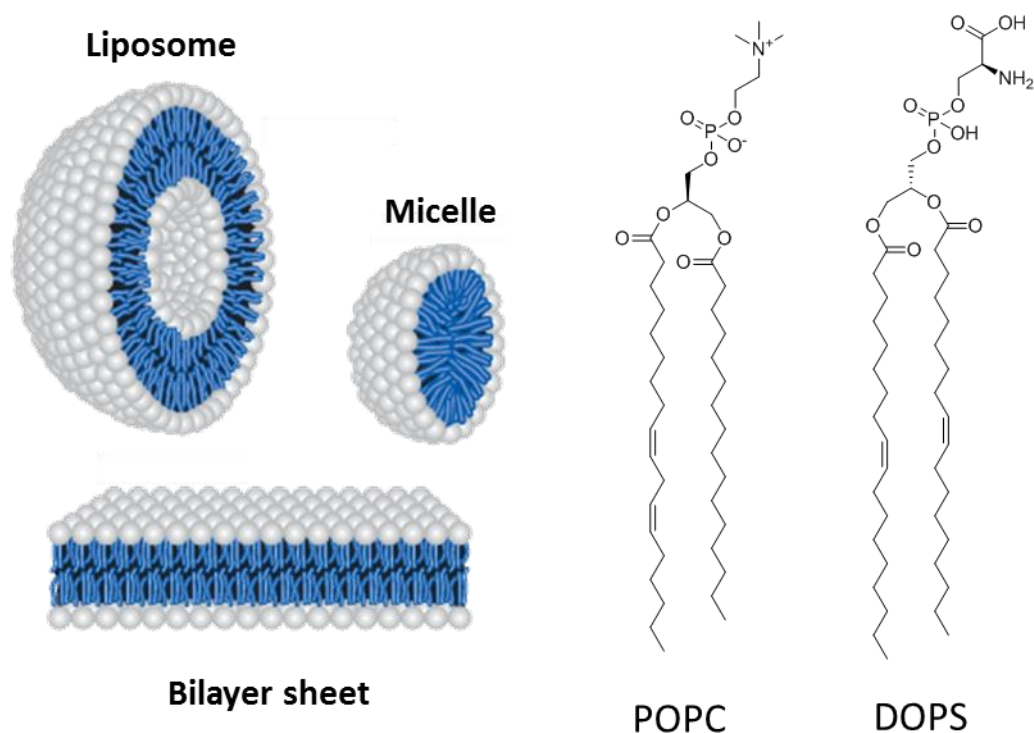
Figure 21. *Lipid structures and most often used lipids*

The biological cells can easily be mimicked in a synthetic fashion by using lipids. For our studies, we mainly used lipids from the phosphatidylcholine and phosphatidylserine class in conjunction with bilayer rigidifying molecules such as cholesterol (Chol). Using synthetic liposomes is advantageous as they offer a more simplified version of the biological cells while keeping its bilayer functions.[75,76]

The principle for using liposomes to determine the water permeability of the artificial channels is based upon using the lipid bilayer of liposomes as an osmotic barrier as well as being the host for the channels themselves. Under an osmotic pressure between the intravesicular and extravesicular solutions, the vesicles will undergo a shrinking/swelling process due to the system's tendency to reach chemical potential equilibrium.[12] (Fig. 22)
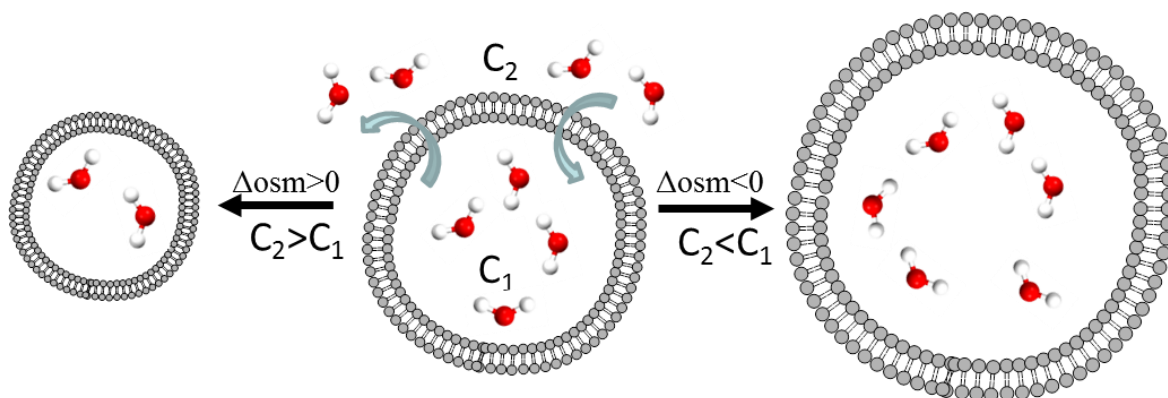
Figure 22. *Lipid vesicle shrinking/swelling under different exterior osmotic gradient*

This change in vesicle size can be quantified by irradiating the solution and following the change in light dispersion intensity. The rate at which the vesicles shrink or swell to change in size under osmotic pressure will be determined by the speed of water translocation across the bilayer, directly influencing the change in scattered light intensity. In the absence of any pore-forming elements, water will diffuse only passively through the bilayer. When the artificial channels are incorporated into the bilayer, the shrinking/swelling will happen faster due to the facilitated transport of water. To experimentally determine the water permeability a stopped flow machine was used. The setup consists of at least 2 pump syringe chambers with digitally controlled injection system connected to a mixing chamber. By connecting a light source and a detector to the mixing chamber it allows the real-time measurement of the light dispersion of the mixed solution.[77] (Fig. 23)
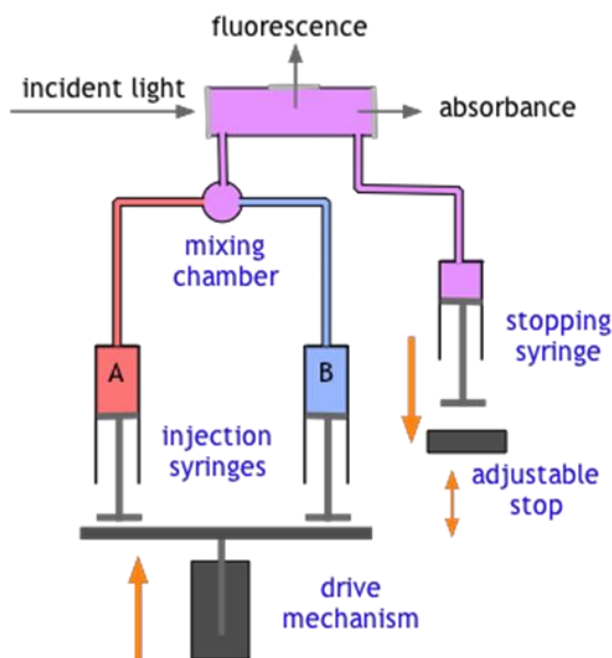
Figure 23. *Stopped-flow setup used for water permeability determination experiments(Image adapted from Stephen Lower – Chem1 Virtual Textbook)*

In collaboration with Prof. Manish Kumar from Penn State University, we prepared vesicles with and without channels incorporated through the rehydration method. This method allows us to capture in the intravesicular media a solution of a certain concentration. By exposing the vesicles to a solution of the same solute but at a different concentration and following the light scattering intensity variation in real time, we generate stopped-flow traces which can be correlated to the water permeability of the vesicles. (Fig. 24)
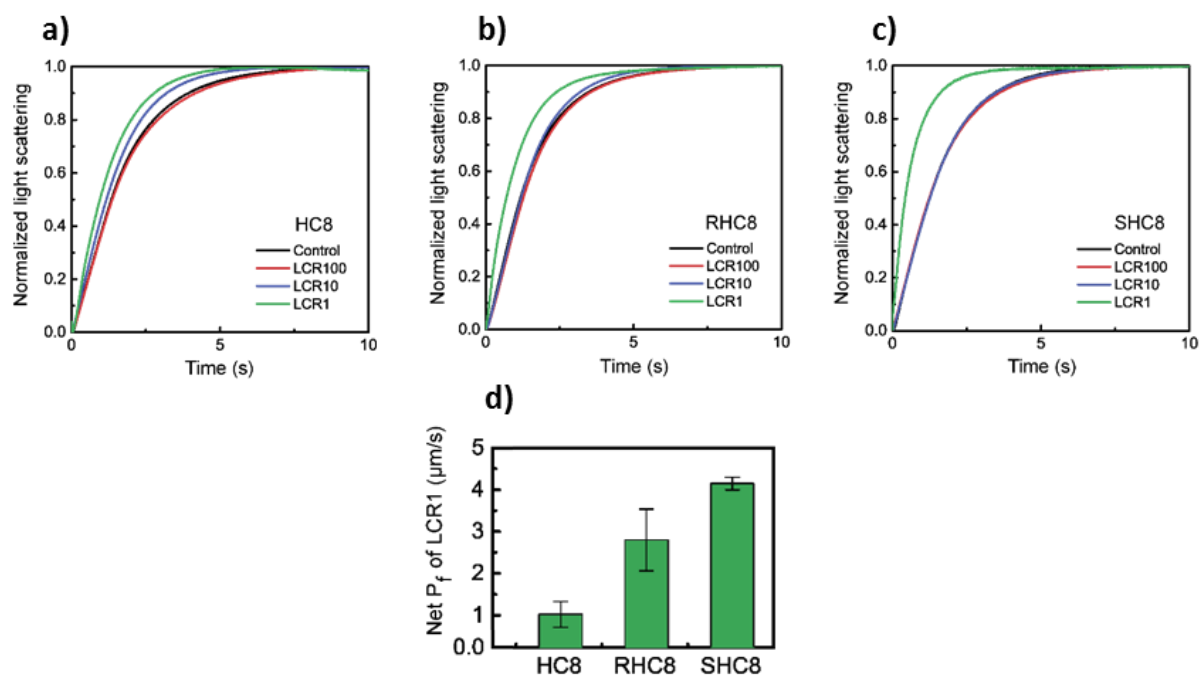
Figure 24. *(a-c) Stopped-flow traces from experiments on liposomes with different weight lipid to channel ratios (LCRs: 1, 10 and 10). All the liposomes were abruptly exposed to a hypertonic solution of 200 mM NaCl. (f) The net permeability of the channels assembled by different imidazole compounds at LCR of 1.*

The obtained value of permeability is attributed to the entire vesicular system. We obtain the net permeability specific for the channels by subtracting the permeability value of vesicles alone from that of the vesicle/channels system. The net permeabilities of **HC8** and its chiral isomers **R-HC8** and **S-HC8** channels at a weight lipid to channel ratio of 1 (LCR1) are 0.989 ± 0.306 µm/s, 2.771 ± 0.738 µm/s, and 4.120 ± 0.152 µm/s, respectively. In order to determine the permeability of a single water channel, information is needed on the amount of inserted compounds into the bilayer, as well as the number of molecules forming a single channel. For the first issue, we underwent experiments to determine the insertion rate, described later in this chapter. For the structure of the channel in the bilayer, we made a rationalized approximation based on the solid state structures. Considering that the length of a lipid bilayer cross-section is around 3.5 nm, we considered that the length of a water channel would be that of 10 stacks of imidazole quartets which have approximately the same length in the solid state structures as the bilayer. This way we have a single water

channel formed out of 40 molecules. Since the distance between two planes of I-quartets is not changing when the alkyl tails are varied, we assumed that all compounds use more or less the same amount of molecules to form a bilayer spanning water channel.

In order to determine the amount of inserted channels into the vesicles, we developed a method based on the UV absorption experiments. The building blocks of the water channels present an absorption band at around 230 nm, mainly due to the imidazole headgroup. Due to their amphiphilic nature, we presumed that there will be a distribution between the aqueous phase and the hydrophobic environment offered by the lipid bilayer, with the main factors contributing to the insertion into the bilayer being the hydrophobic pressure exercised by the alkyl tails, as well as the stabilizing effect of the self-assembly process. (Fig. 25)
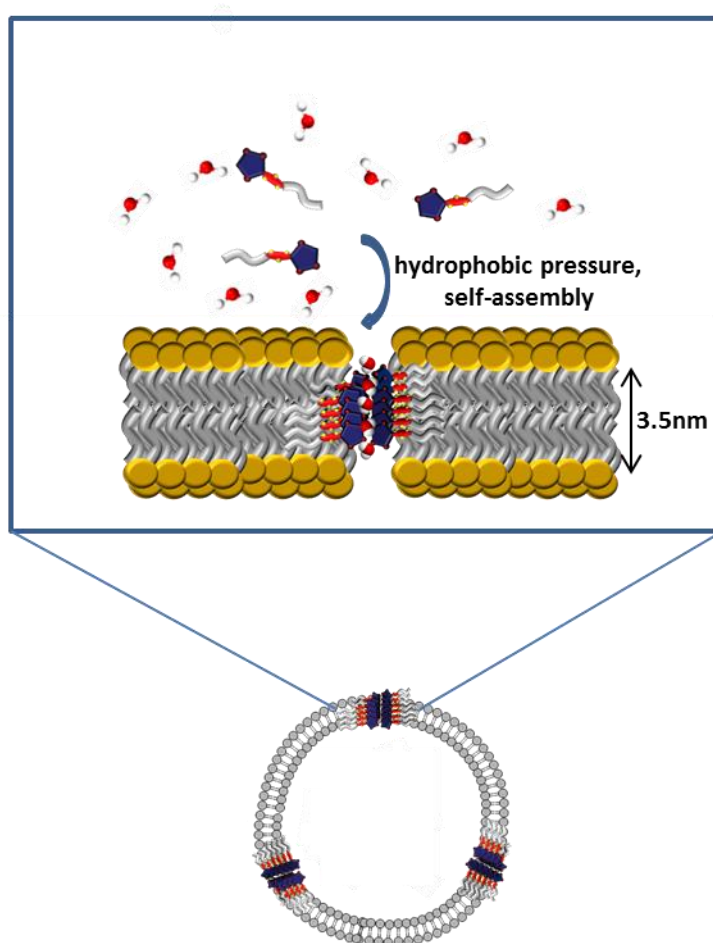
Figure 25. *Channel insertion and self-assembly in lipid bilayer*

Different lipid to channels ratios (LCRs) was assayed. Due to solubility differences and saturation issues of the lipid bilayer the insertion rate varies significantly at different ratios between the compounds. Using a fluorescence experiment we obtained insertion rates of 63%, 52% and 60% for **HC8**, **R-HC8** and **S-HC8** when having an LCR of 10. Based on the determined insertion efficiency and the permeability results from the sopped-flow experiments we were able to determine the water permeability of the artificial channels. We

calculated the single-channel permeability of each channel type based on the insertion, actual lipid concentration, and channel configuration in the lipids. In the shrinking mode, **HC8**, **R-HC8**, and **S-HC8** had permeabilities of $1.4\pm0.4\times10^6$, $7.9\pm2.1\times10^5$ and $1.5\pm0.1\times10^6$ water molecules per second per channel, respectively, which are only 2 orders of magnitude lower than that of AQPs ($\sim10^8-10^9$ water molecules per second per channel).

As seen in the first chapter, the selectivity of artificial channels is as important as their water permeability. In order to determine the selectivity of the imidazole-based water channels, we determined their permeability using NaCl and glucose as solutes for inducing the osmotic shock while keeping the osmotic pressure identical in both cases. (Fig. 26) If the vesicle shrinkage is happening only through the transport of water across the bilayer, then the two determined permeability should be identical. If either component of the solutes is being transported then the concentrations equilibrate without the induced shrinkage not generating any stopped-flow trace.
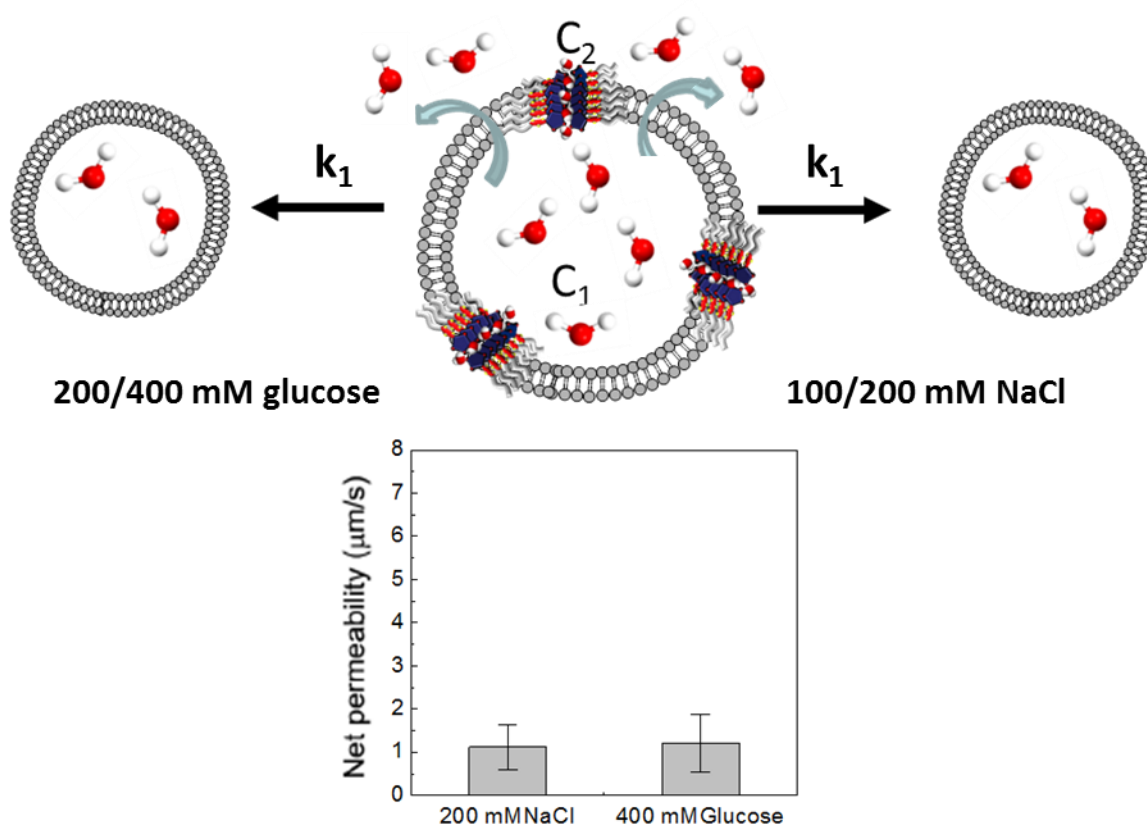
Figure 26. *Permeability determination of **HC8** vesicles using intra/extravesicular solutions of 200/400 mM glucose and 100/200 mM NaCl*

Having obtained almost identical permeabilities in both cases, we concluded that the imidazole-based artificial water channels are completely selective for water molecules

against Na$^+$ and Cl$^-$ ions. This remarkable feature makes **these channels the first reported artificial water transporters capable of total salt rejections.**

The increased efficiency of certain I-quartets can be synergistically attributed to the enhanced hydrophobic stabilization of the channels within the bilayer membrane environment. This is mainly based on an optimal molecular packing of the hydrophobic tails. The length of these tails seems to be optimal for the octyl chains, while the chiral packing is favored with a special emphasis for the S-isomer, probably more compatible with the natural chiral L-lipids. At the same time, the directional water-dipolar orientation present within the chiral I-quartets most probably plays a role of its own. This underpins the obtained higher permeability in the case of the chiral compounds for which the X-ray crystal structures show a unique orientation within all the channels, while in the non-chiral channels there is a 50/50% distribution of directionality of the oriented water molecules.

2.4   Vibrational spectroscopy of SLBs

Vibrational spectroscopy has a long history of being an important tool for describing molecular bonds and structures in gas, liquid or solid state. In the last few decades, a nonlinear technique has been developed called *Sum Frequency Generation* (SFG). This technique is especially suited for the analysis of molecules found at interfaces.[78] In a typical SFG experiment, an interface is irradiated by tunable laser and infrared beams. When passing through non-centrosymmetric environments, the two beams generate a third one specific to the nature of the chiral material. (Fig. 27) Briefly, a non-resonant visible photon and a resonant infrared photon induce a nonlinear polarization in the sample at the interface that emits a detected photon at the sum frequency of the two.
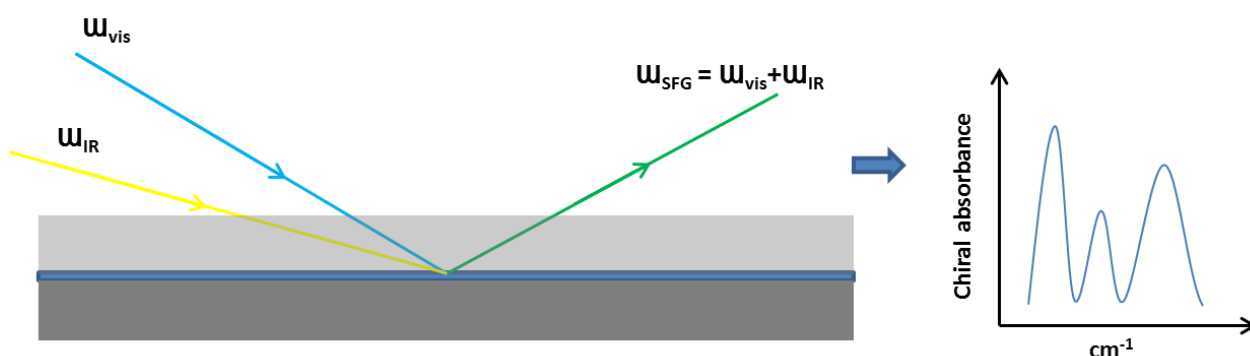
Figure 27. *SFG experiment principle*

Since the method is only generating a signal for the oriented molecules at the interface, only the close layers of molecules that feel the effect of the interface will be probed. This has proved highly efficient in describing the behavior of water molecules at different interfaces. [79,80]

Objective. Using the SFG technique we presumed that the structuration and the dipolar orientation of water inside the artificial water channels in their active state can be measured and detected when the channels are inserted into the lipid bilayer. For this, we envisaged an interfacial system composed of a single lipid bilayer containing the water channels, deposited on a silica surface. This work was part of a joint research project with Prof. Georges Belfort from Rensselaer Polytechnic Institute and Prof. Poul Petersen from Cornell University. (Fig. 28)

Quartz Crystal Microbalance experiments. In order to track the formation of the SLB on the silica surface, we used a Quartz Crystal Microbalance coupled with Diffusion (QCM-D). We know that the I-quartet channels are spontaneously inserted into lipid bilayers.[81] Among the various methods which can be used to analyze the interactions between the I-

quartets and a SLB, the QCM-D technique[82,83] was deemed suitable as it allows detection of mass changes at the sensor surface on the basis of the reciprocal piezoelectric effect.
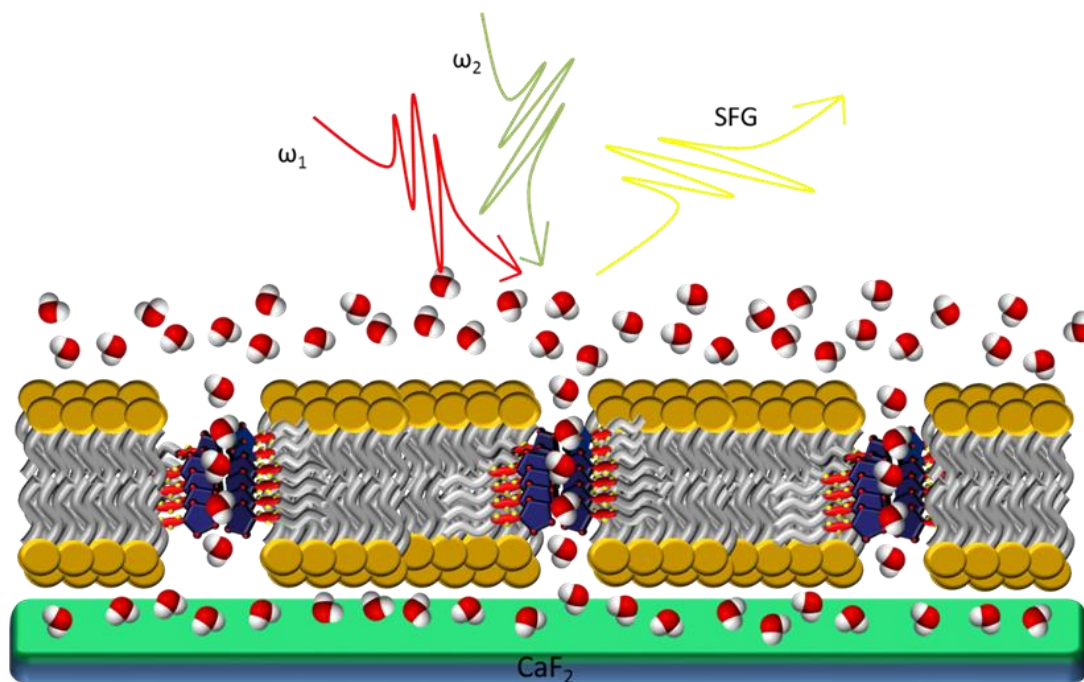
Figure 28. *SFG experiment set up with imidazole channel loaded lipid bilayer deposited on silica coated CaF$_2$ prism*

Previous studies showed that the formation of the SLB from SUVs follows a two steps mechanism: (i) fast adsorption of the SUVs to the QCM-D silica crystal with increased mass (i.e. decreased ΔF, frequency) and increased layer flexibility (i.e. increased ΔD, dissipation coefficient), because floppy SUVs were deposited on the QCM-D sensor) and (ii) SUVs rupture and fusion into SLBs (ΔF minimum and ΔD maximum). A final buffer wash is included to allow complete annealing of the SLB.[84,85] In our particular case, for the molar composition of 4:1/PC:PS and **HC8** a ΔF of -25.3 Hz was observed, corresponding to a total mass of 352 ng (i.e. mLipids = 217 ng, mHC8 = 54 ng, m_{H2O}hydration layer = 79 ng and m_{H2O}channel = 1.8 ng), which demonstrated the formation of a stable SLB on the QCM-D surface. (Fig. 29)
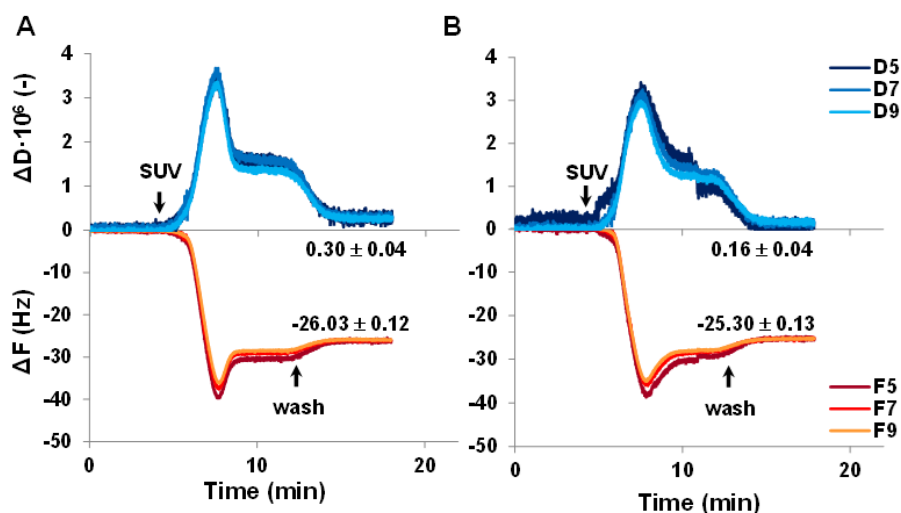
Figure 29. *Incorporation of **HC8** I-quartets in 4:1=POPC:DOPS SLB. Experimental QCM-D frequency, ΔF [Hz] and dissipation coefficient, ΔD [-] shifts associated with the SLB formation on silica QCM-D sensors via fusion of small unilamellar vesicles (SUVs) of mixtures of lipids: (A) POPC:DOPS, 4:1 mol:mol, and (B) POPC:DOPS, 4:1 mol:mol + HC8. The two arrows indicate (i) SUVs injection at 4 min and (ii) the washing step with 10 mM phosphate buffer pH 6.4 after 12 min. Data of the 5th, 7th and 9th overtones are shown for ΔF (F5, F7 and F9) and ΔD (D5, D7 and D9).*

The calculations were based on the total insertion of **HC8** into the vesicles. The formation of a SLB, with or without **HC8**, was also tested for 4:1/POPC:DOPS + 20% w/w cholesterol and POPC alone. While the addition of cholesterol did not affect the formation of a SLB, the POPC alone SUVs failed to form a SLB. Additionally, based on the ΔF values the addition of **HC8** caused a decrease of the bilayer thickness from 4.61 nm (i.e. 4:1=POPC:DOPS alone) to 4.48 nm (4:1=POPC:DOPS with **HC8**). This demonstrated the formation of a more compact structure and the partial contraction of the SLB when **HC8** was incorporated. A more compact structure compared with the pure SLB only was probably is most likely the result of global SLB stabilization via supplementary phospholipid head–groups/imidazoles electrostatic interactions and hydrophobic contact between the lipid and alkyl tails towards the bilayer aggregation. About 4% of the total mass of the SLBs comprise of water wires in the system. Taken all together, these results demonstrate the incorporation of I-quartet channels into supported 4:1/POPC:DOPS SLB, that was selected for SFG experiments.

Sum frequency generation spectroscopy. In order to understand the structure of the water wires under confinement, we collected the SFG spectra of the achiral **HC8** and chiral **S-HC8** I-quartets inserted in SLB together having as reference the SLB without channels. Waveplates and polarizers control the polarization of each of the three beams (sum frequency, visible, and infrared) to be parallel (p) or perpendicular (s) relative to the plane of incidence of the visible and infrared beams on the sample. Polarizations are listed in

descending order of photon frequency (e.g., an ssp experiment indicates s-polarized SFG, s-polarized visible, and p-polarized IR). We measured four different pure polarization combinations: the achiral combinations ppp and ssp (Fig. 30 A,B), and the chiral combinations psp and spp (Fig. 30 C, D). Measuring two different polarization combinations for the achiral and chiral combinations provides information on the alignment of the vibrations (perpendicular to or with a shallow angle with respect to the surface) depending on the symmetry of the functional group.

We examined the spectral region 2600-4000 cm^{-1} covering the strong OH and NH stretches, with very weak CH stretches observed in the 2800-3000 cm^{-1} range. For the lipid bilayer without channels, we observe in Fig. 3 the typical 3200 (yellow) and 3450 (green) cm^{-1} bands observed for aqueous interfaces in both achiral ppp and ssp polarization combinations. For the water-bilayer interface, the two features could be due to specific subpopulations of bulk-like water molecules oriented in the field of the charged headgroups, and water molecules directly interacting with the lipid headgroups, respectively. The overall distribution of vibrational frequencies reflects the breadth of hydrogen-bonding interactions at the water-bilayer interface.
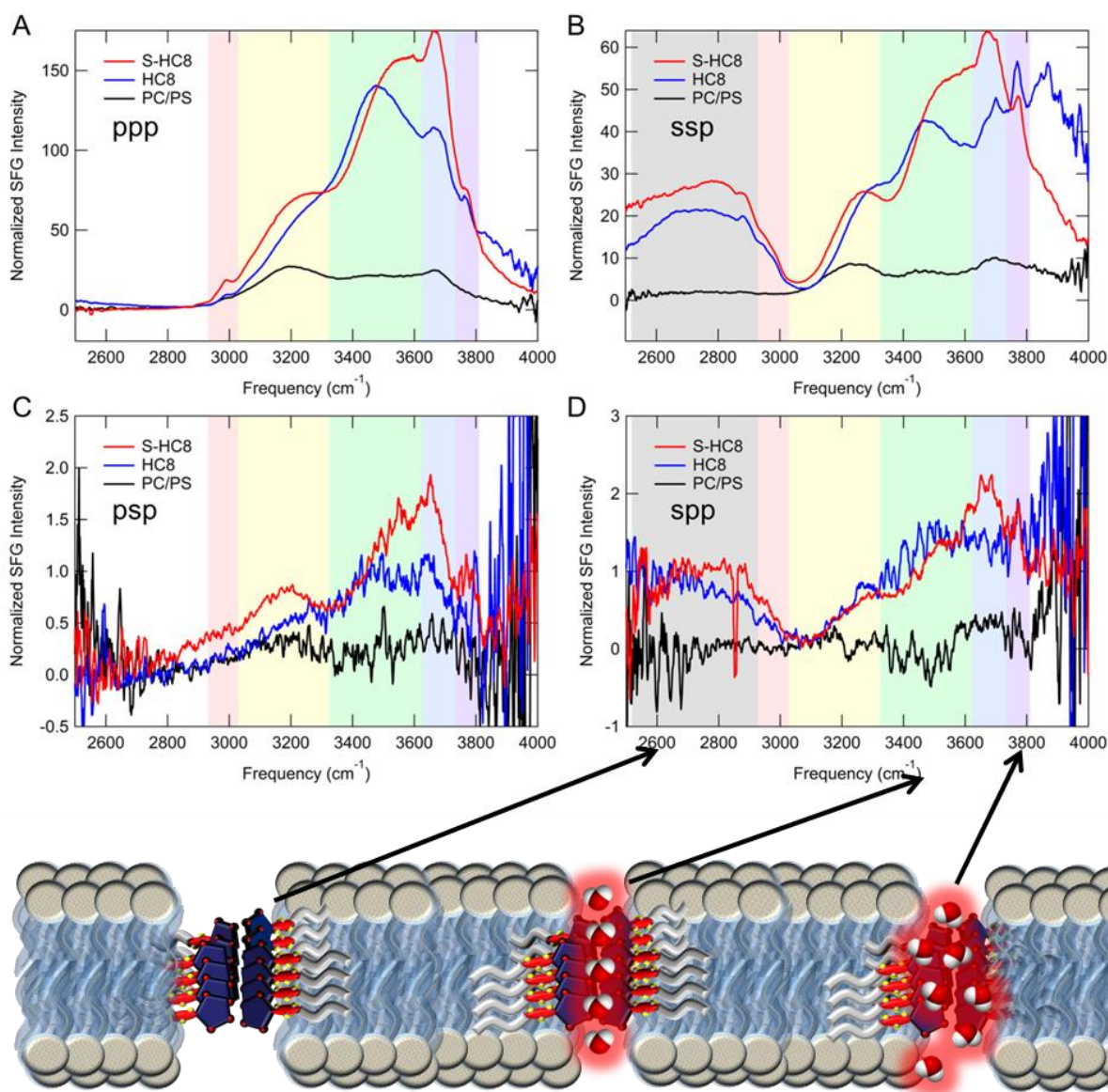
Figure 30. *SFG spectra of 4:1=POPC:DOPS SLB (reference), **HC8** and **S-HC8** I-quartets in 4:1=POPC:DOPS SLB determined for pure achiral (A) ppp or (B) ssp, and pure chiral (C) psp and (D) spp polarization combinations.*

For both samples with the artificial channels inserted into the supported lipid bilayer, we observe a large increase in the SFG intensity across the whole spectral region. In particular the 3450 cm^{-1} band increases, which is consistent with chain-like water-wires molecules inside the channel. In addition to three bands observed for the bilayer, we observed an additional sharp feature at 3750 cm^{-1} (violet) in both ppp and ssp. This sharp feature is due to non-hydrogen-bonded OH group, attributed to a sub-population of the singular water molecules inside the channel (Fig. 30). Furthermore, we observe a broad feature at 2800 cm^{-1} in ssp but not in ppp. This feature we attribute to the imidazole groups of the water channels. That the feature is observed in ssp but not ppp validates that the I-quartet channels are highly ordered perpendicular to the lipid bilayer. Overall, the very large

46

increase in the SFG intensity across the OH spectral region confirms that the insertion of the channels do not disrupt the order of the bilayer but rather prove that the hydrogen-bonded structure of the water molecules inside the channels is highly orientated with a strong dipolar alignment.

The large SFG response further shows that the dipolar ordered water-wires inside the channels are aligned in the same direction. If alternate channels have opposite orientations, as one would expect for a free-standing bilayer, the achiral SFG signal would vanish due to cancelation. Given the large SFG intensity, the silica surface must induce a preferential ordering of the water wires with respect to the water surface. This is collaborated by the similar achiral SFG strengths of the **HC8** and **S-HC8** channels, which show that the dipolar alignment of the water-wires in the supported bilayers is similar, where it is known not to be the case for free standing bilayers.

In the psp chiral SFG polarization combination (Fig. 3D), we observe a weak but non-zero chiral signal for the lipid bilayer without channels. This is caused by the chiral headgroups of the lipids inducing a chiral-polarized arrangement of water molecules near to the polar region of the bilayer. The chiral SFG responses of the OH features in the bilayers with the **HC8** and **S-HC8** channels in both psp and spp are much stronger compared to the bilayer without channels. This proves that not only are the water dipoles aligned inside the channels but that they furthermore form a chiral water super-structure templated by the I-quartet channel. While the chiral psp response is stronger for S-**HC8**, as expected, the psp response of **HC8** is significant and in spp the chiral SFG responses for both channels are similar. This is perhaps initially surprising. However, we know that each individual **HC8** channel is chiral in the solid crystal structures and successive enantiomeric channels of opposite chirality are separated by water-free I-quartets. When **HC8** is embedded in the bilayer membrane, the chiral polar region of lipids at the surface induces the amplification for one orientation that would preferentially form one chirality over another. In contrast, the non-centrosymmetric structures of chiral **S-HC8** show a unique dipolar orientation for all water-filled channels and correspondingly the chiral response of the **S-HC8** channels is larger compared to the achiral HC8 channel. This proves again the translation of chirality towards water organization inside in confinement of the artificial water channels.

2.5   Molecular dynamic simulations

Most of the published research results on artificial self-assembled channels are concentrating their rationale on transport activity measurements without really knowing the functional structure that is doing the job.   A second case is the results presenting a structure but nobody knows if this structure is the functional one or not. Thus in cooperation with Marc Baaden from Institut de Biologie Physico-Chimique Paris, an expert in molecular dynamics, we proposed to study through molecular dynamics simulations the functional stability of the initial X-ray single crystal structures when placed in a lipid environment.

Stability of the channels depending on applied lateral pressure. Based on the determined X-ray structures we embedded ca. 3 nm wide I-quartet channel patches in a mixed POPC/DOPS/Chol lipid bilayer environment. We used the Mercury 3.5.1 software to fill the crystallographic unit cell with missing molecules, then replicate it keeping 2, 6 and 8 slices in x, y and z-axis directions, respectively, resulting in a 96 molecule patch. The four: **HC6**, **HC8**, **R-HC8**, and **S-HC8** systems include respectively 2, 6 and 6 water channels that we inserted in a pre-equilibrated triclinic membrane patch containing a 5/4/1 ratio of Chol/POPC/DOPS molecules. We deleted overlapping water and lipid molecules and added a concentration of roughly 50 mM Na^+Cl^- to the solvent, as well as an excess of Na^+ ions to neutralize the system charge induced by the negatively charged PS lipids.

Having various too many unpredictable variables related to the nature of the active aggregate water channels, a precise model could not be set from the beginning. In order to explore the properties of these systems, simple assemblies were studied initially in order to set the basis of the models.

We, therefore, started our investigation on an 8x8 imidazole **HC6** molecules system, WC4, forming 2 channels and 12x8 imidazole **HC6** molecules system, WC6, with 4 channels under varying conditions. We use a simple model lipid membrane composition of ca. 5 cholesterol: 4 POPC: 1 DOPS molecules. (Fig. 31)
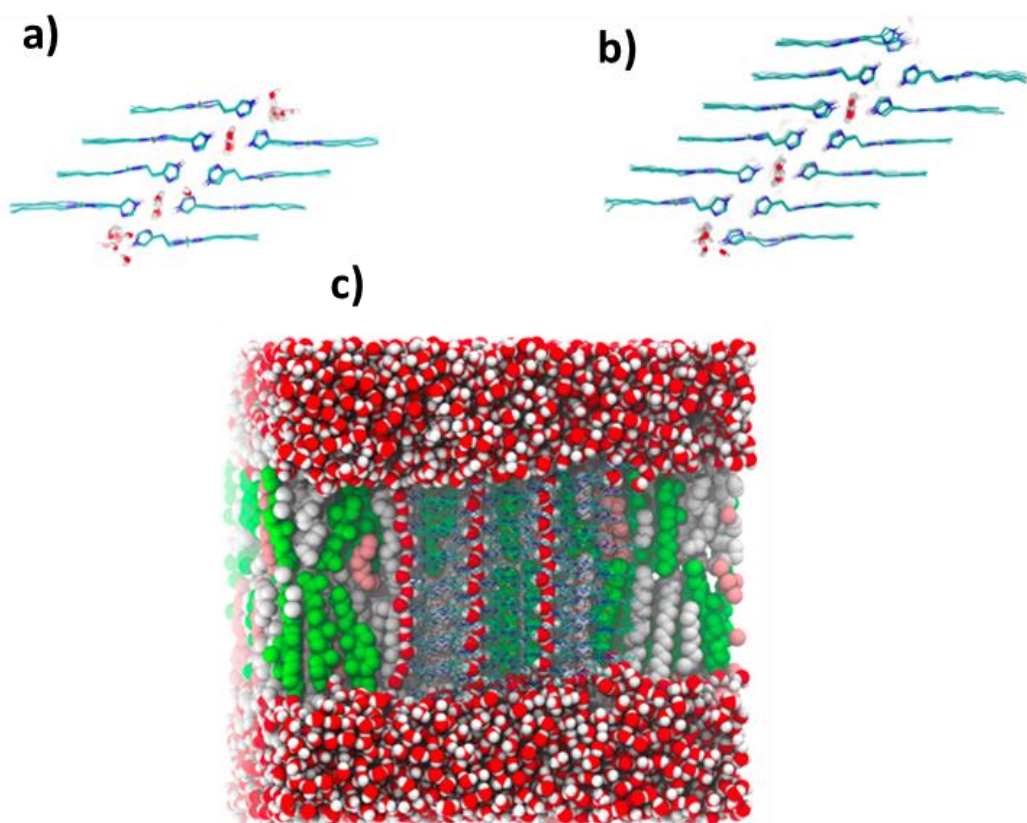
Figure 31. *Schematic top and side views of the a) WC4 system and the b) larger 12x8 WC6 system used as starting point for all simulations; c) membrane packing and water filling in the simulation box*

From the analysis of the WC4 simulation, we noticed that the membrane exposed I-quartets are clearly less stable compared to the central ones. This is documented by the structural drift RMSD (root mean square displacement) and the disruption of the existing water strings exposed to the membrane. They disappear after ~20 ns. The central water strings become discontinuous after 25 ns. To remediate these issues, two more imidazole **HC6** slices were added to shield the two water pores from the membrane. (Fig. 32).

49
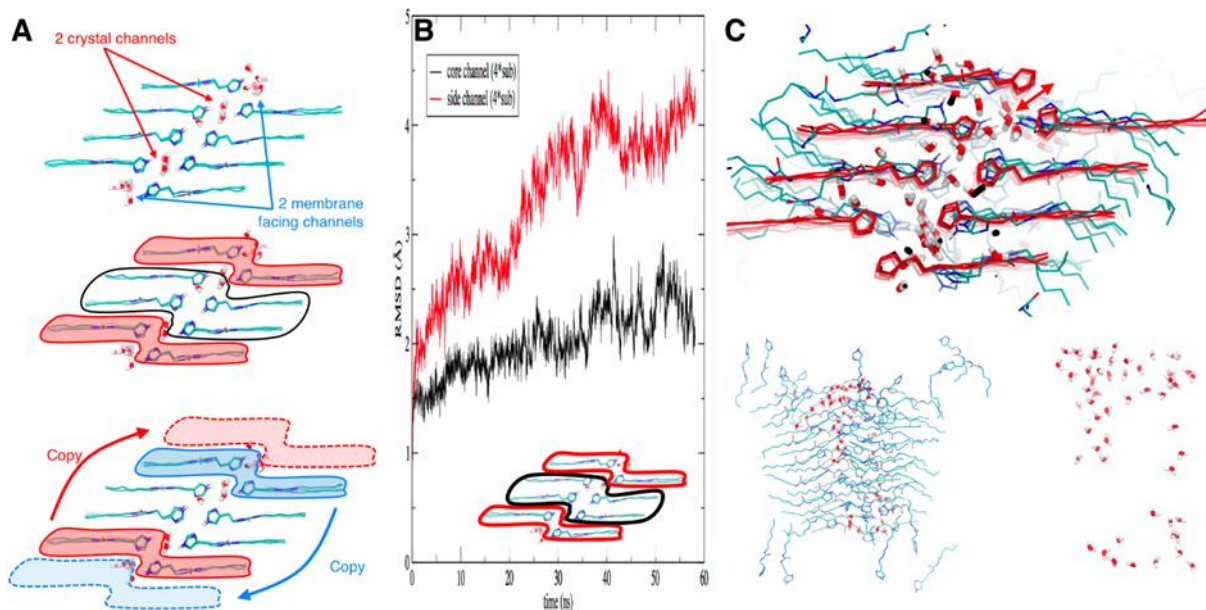
Figure 32. *(A) Membrane facing and interior crystal channels in the WC4 system. At the bottom is shown how the WC6 systems were constructed. (B) The structural drift of the membrane facing (red) versus interior (black) IMID aggregates. (C) Simulation snapshots illustrating the structural drift of the unclustering molecules after 50 ns of simulation. Discontinuities in the water strings are shown.*

Analysis of the WC6 simulation also showed that initial cholesterol placement is important, as cholesterol binds and potentially stabilizes the membrane facing channels. Having observed this we proposed that the lateral pressure in the lipid bilayer would play an important role in stabilizing the water channel structures. As so, several experiments with varying lateral pressure were conducted. Visual inspection shows that initial water channels of **HC6** I-quartets are lost after around 90, 103 and 109 ns at -10, 1 and 10 atm, respectively, while at 100 atm the I-quartets are much better preserved, one is fully intact at the end of the simulation (250 ns), the other has started to disassemble and loose some of its water. (Fig. 33)

Although the channels have increased stability when 100 atm is applied, we observed that also water movement across the channels is "frozen". We, therefore, chose 10 atm for subsequent simulations, to stabilize the aggregate structures, yet to preserve the possibility of water transport at the simulation timescale of ca. 1 microsecond.
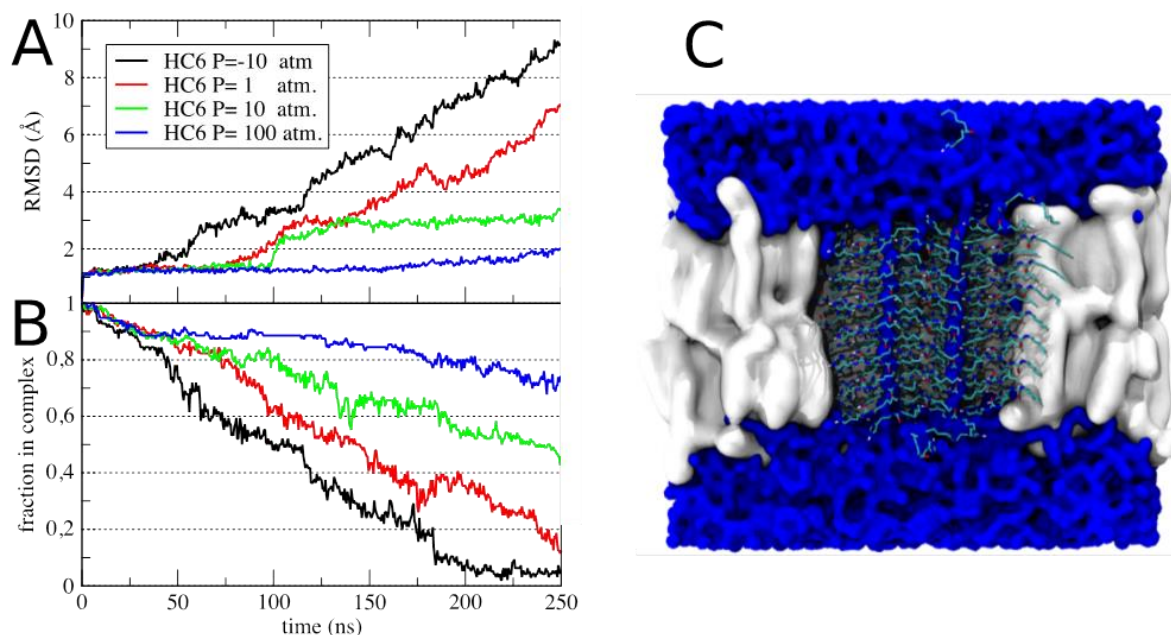
Figure 33. *Pressure dependent evolution in time of channel structure quantified through (A) RMSD and (B) fraction of molecules present in the channel; (C) Cross section structure of HC6 channels held together by the lipid bilayer (gray)*

Having a preset model from the HC6 simulations we moved on to octyl C8 series water channels. The longer alkyl chains in the **HC8**, **R-HC8** and **S-HC8** systems favor a more pronounced superstructure and more stable water wires. Initial and final snapshots at 50 and 500 ns of these I-quartet systems are shown in Fig. 34, with an emphasis on highlighting the water wire.

The difference between HC6, where water wire structuring is clearly lost, and the chiral **S-HC8** and **R-HC8** superstructures maintaining a strong ordering of the wires is marked. By construction, the water wires at the right-most and left-most positions – in direct contact with the lipid environment – are structurally more labile. The difference between **HC8** and **R-HC8** or **S-HC8** is again very apparent and even differences among channels are clearly visible. Not only are these wires clearly structured in the chiral systems, but their orientation is tightly controlled as well. The chiral systems undergo a twist of the superstructure. The structural drift is quantified in Fig. 35, the **R-HC8** system being the most stable one, followed by **S-HC8**, whereas **HC8** is more stable than **HC6** on longer timescales (>250 ns) in terms of RMSD. The analysis of the radius of gyration of the superstructure confirms this trend.
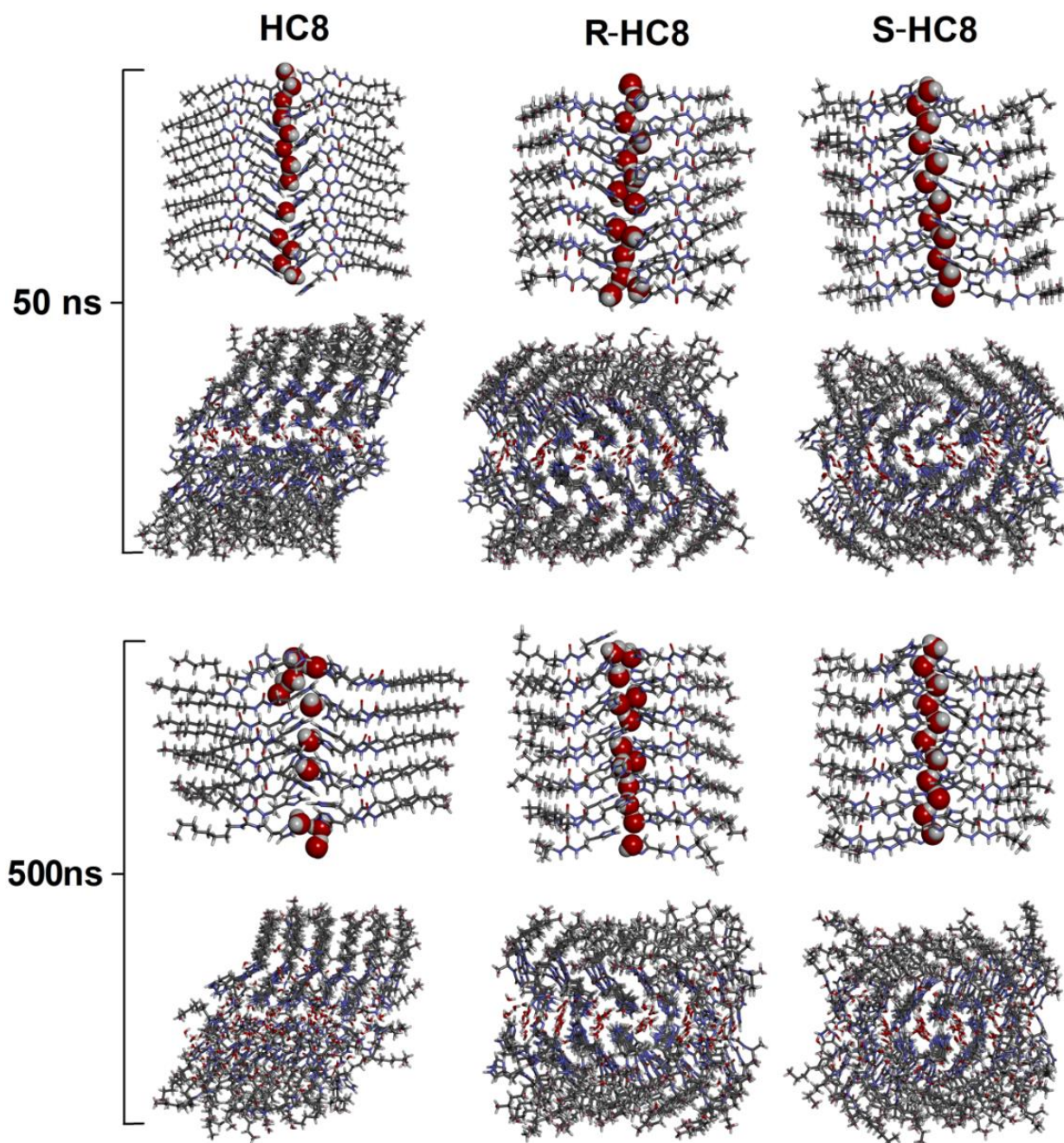
Figure 34. *I-quartet channels structures in stick representation, water CPK representation (top row) and their molecular packing (bottom row) obtained after 50 ns (top) and 500 ns (bottom) molecular dynamics simulations at 10 atm of the **HC8, R-HC8** and **S-HC8** X-ray crystal structures embedded in the bilayer membrane environment.*
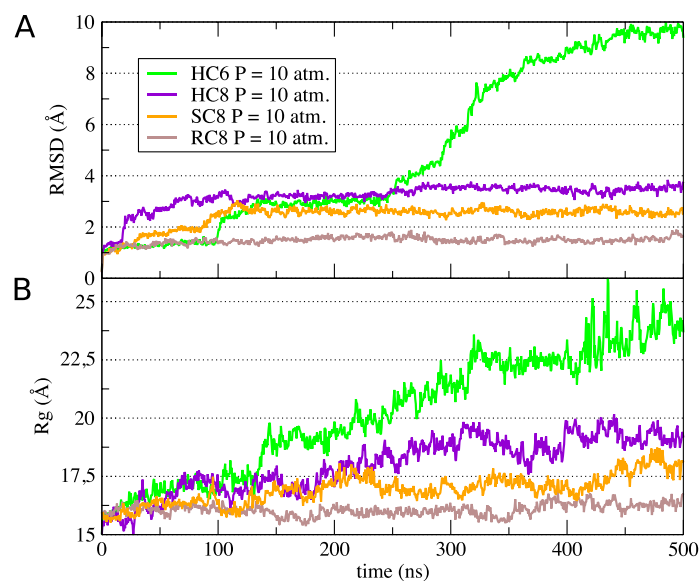
Figure 35. *Time series of the structural drift of **HC6, HC8, R-HC8, S-HC8** I quartet channels, measured as (A) RMSD or as (B) radius of gyration of the imidazole nitrogen atoms at 10 atm.*

Water translocation. We characterized water transport first globally, through counting the overall passage of water molecules through the membrane in either direction (Fig. 36). A more nuanced picture, separating the membrane-exposed lateral channels from the central two well-shielded channels reveals that structured water wire transport is observed for the **R-HC8** system in particular.
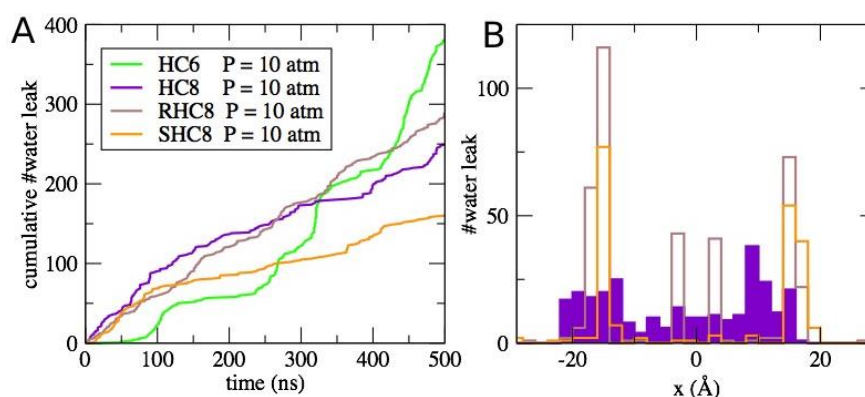
Figure 36. *(A)The water transport activity time series of the I-quartet channels is shown as the cumulated passage of water molecules across the membrane, in either direction (B) shows the count of permeation events for each water wire along the membrane width (x-axis).*

By comparing the stability and water transport activity of the channels we see that there is a trade-off between the lifetime of the channels and the flux of water molecules. In order to have functional channels over longer time intervals the stability becomes the main issue to consider and in this case, we have observed that the **HC8** series performs quite well

with the remarkable translation of the chiral information from the backbone of the chiral building blocks as observed by the adopted helical structures of the channel assemblies. In a new set of experiments, we focused especially on this series with more emphasis on the channel/lipid interactions and the hydrogen bonding network of the water wires. The number of water molecules within the membrane region at the end of 500 ns simulation is similar for the **R-HC8** and **S-HC8** constructs, 68 and 65, respectively, and is significantly higher than for the **HC8** system featuring 39 waters. (Fig. 37)

|	HC8	RHC8	SHC8	Bulk	Memb. Interface
Channel					
H$_2$O num	39 ± 6	68 ± 3	65 ± 4		
# Hbonds:					
H$_2$O↔H$_2$O	0,5 ± 0,4	1,3 ± 0,2	1,3 ± 0,2	3,2 ± 0,1	2,5 ± 0,3
H$_2$O→Imid.	1,2 ± 0,3	1,0 ± 0,1	1,0 ± 0,1		
H$_2$O←Imid.	0,5 ± 0,3	0,7 ± 0,1	0,7 ± 0,1		
H$_2$O↔Lipid	0 ± 0	0 ± 0	0 ± 0	0 ± 0	0,9 ± 0,1
Total	2,2 ± 0,6	3,0 ± 0,2	3,0 ± 0,3	3,2 ± 0,1	3,4 ± 0,4
Imid.↔Imid.	3,6 ± 0,3	4,3 ± 0,2	4,3 ± 0,2		
Imid.↔Lipid	0,7 ± 0,4	0,5 ± 0,2	0,6 ± 0,2		
Imid.↔Water	3,8 ± 1,0	3,3 ± 0,3	3,3 ± 0,3		
Total	8,1 ± 1,1	8,1 ± 0,5	8,1 ± 0,5		
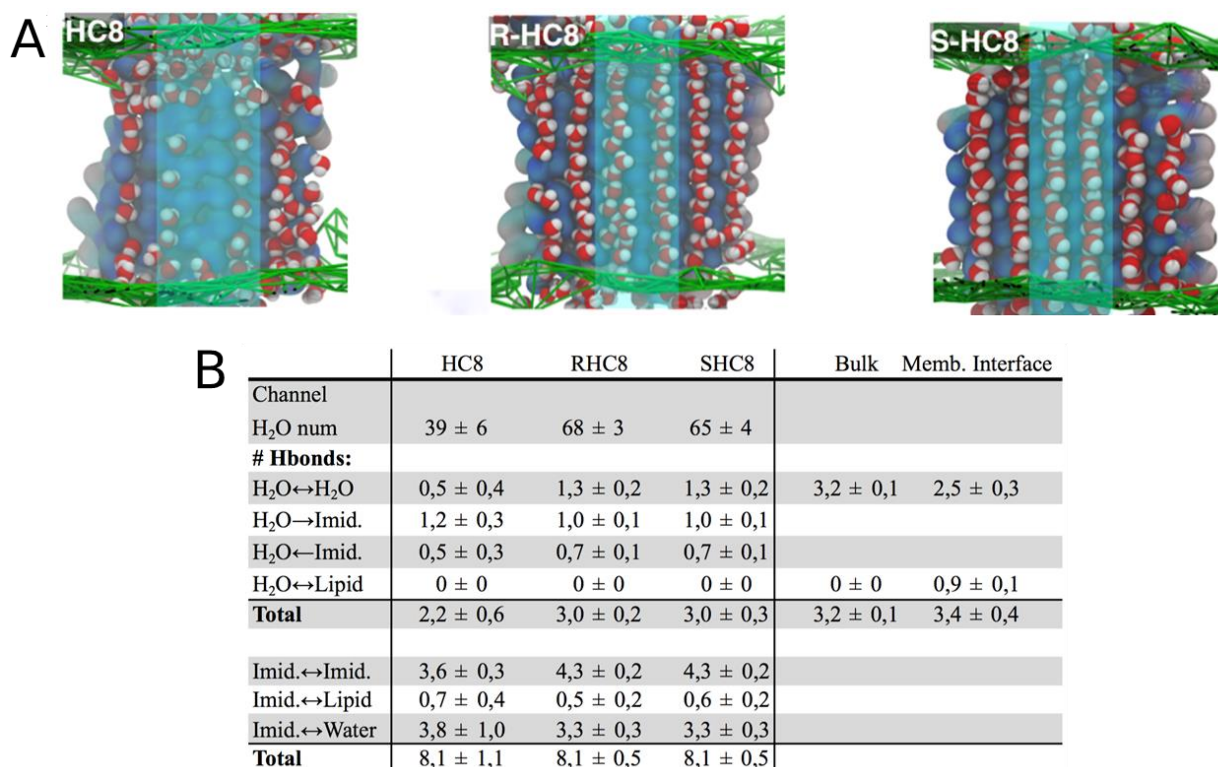
Figure 37. *(A) cross-sectional view of the **HC8**, **R-HC8** and **S-HC8** channels (B) hydrogen bonding details in the system*

The hydrogen bonding patterns were analyzed in terms of water-water hydrogen bonds, water(donor) to imidazole(acceptor) hydrogen bonds, imidazole(donor) to water(acceptor) and water with lipid ones (fig hydrogen bonds). **R-HC8** and **S-HC8** constructs have comparable patterns with 1.4 and 1.6 hydrogen bonds on average connecting the pore waters and 1.9/1.8 hydrogen bonds linking them to the imidazoles. With 0.9 water-water hydrogen bonds on average, the water cohesion is significantly lower for the HC8 system. The anchoring to the imidazoles is also of lower magnitude. Hydrogen bonds with lipids are not observed for these channels. Looking at the overall number of hydrogen bonds for the water molecules, compared to a reference value of 3.2 for bulk solvent, we notice that water in the **R-HC8** pore is unperturbed and for the **S-HC8** pore even stabilized, reaching up to 3.2 and 3.4 hydrogen bonds, respectively, whereas the HC8 system lacks almost an entire hydrogen bond.

We analyzed the strength of the hydrogen bonds for each water molecule in a cylindrical selection around the two central channels. Fig. 38 depicts the hydrogen bond energy difference compared to the bulk water hydrogen bond energy taken as reference projected along the membrane normal direction. The **S-HC8** system exhibits a strong and constant stabilization of the water molecules of almost 20 kJ/mol for the two central channels. For **R-HC8**, the stabilization varies from a maximum of about 13 kJ/mol down to 0 kJ/mol as in bulk water, which is due to an increased mobility - and hence destabilization - of the channel water molecules on one side of the membrane. For **HC8**, the hydrogen bond energy is fluctuating with a global tendency to be slightly less stable than in bulk water. For comparison, the hydrogen bond energies averaged over the central membrane-inserted waters from about z=-1.2 to 0.8 nm are +17.6, +4.6 and -1.3 kJ/mol stabilization of **S-HC8**, **R-HC8** and **HC8** compared to bulk, respectively.
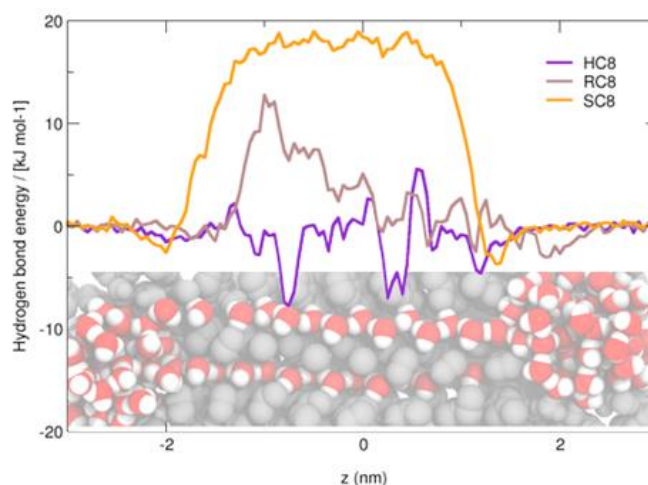
Figure 38. *Hydrogen bonds strength in function of the distance from the centre of the bilayer*

There are several factors that play together when efficient water transport is considered across the imidazole water channels. According to the molecular dynamics simulations, the stability of the channels is well influenced by the nature of the hydrophobic backbone and this is in a synergistic relationship with the ordering of the water molecules inside the channels as well the dipole structuration. The result of these interactions leads to the final energetic state of water in the confinement of the channels. Spending relatively small amounts of energy in the transition from bulk water to confinement translates in the end to a low-energy-cost system that could be a viable scaffold for highly efficient water purification materials.

2.6 Experimental

2.6.1 Synthesis and structural characterization

All reagents were obtained from commercial suppliers and used without further purification. All of the compounds have been synthesized following the general scheme is shown in Chapter 2.1. In a general synthesis, 10 mmol of histamine have been suspended in 10 ml THF. The solution was brought to boiling point and 1 equivalent of the respective isocyanate was added, leaving it to react for 3h under reflux. The solution is left to cool down to room temperature and the obtained white precipitate is filtered and washed with 3 aliquots of 5 ml THF. The precipitate is then dried under low-pressure vacuum to afford the respective compounds as a white flaky compound. The average yield varies between 90-99% with slightly lower yields for the chiral compounds **S-HC8** and **R-HC8**.

NMR spectroscopy and MS spectrometry

^{1}H NMR spectra were recorded on an ARX 300 MHz Bruker spectrometer in DMSO-d6 with the use of the residual solvent peak as reference. Mass spectrometric studies were performed in the positive ion mode using a quadrupole mass spectrometer (Micromass, Platform 2+). Samples were dissolved in DMSO and were continuously introduced into the mass spectrometer at a flow rate of 10 mL/min through a Waters 616HPLC pump.

1-(2-(1H-imidazol-4-yl)ethyl)-3-octylurea, HC6 : RMN^{1}H (DMSO-d6, 300 MHz) δ (ppm) = 0,86 (br, 3H) ; 1,25-1.34 (m, 8H) ; 2,58 (t, *J* = 6 Hz, 2H) ; 2,95 (q, *J* = 6 Hz, 2H) ; 3,21 (q, *J* = 6 Hz, 2H) 5,74 (t, *J* = 6 Hz, 1H) ;5.82 (t, *J* = 6 Hz, 1H) ; 6,76 (s, 1H) ; 7,52 (s, 1H). ESI-MS: M$^+$=239.1;

1-(2-(1H-imidazol-4-yl)ethyl)-3-octylurea, HC8 : RMN^{1}H (DMSO-d6, 300 MHz) δ (ppm) = 0,86 (br, 3H) ; 1,25-1.34 (m, 12H) ; 2,58 (t, 2H) ; 2,95 (q, 2H) ; 3,21 (q, *J* = 6 Hz, 2H) 5,74 (t, *J* = 6 Hz, 1H) ;5.82 (t, *J* = 6 Hz, 1H) ; 6,76 (s, 1H) ; 7,52 (s, 1H). ESI-MS: M$^+$=267.1;

(R)-1-(2-(1H-imidazol-4-yl)ethyl)-3-(octan-2-yl)urea, R-HC8: RMN1H (DMSO-d6, 300 MHz) δ (ppm) = 0,85 (br, 3H); 0,97 (d, *J* = 6 Hz, 3H); 1,24-1.30 (m, 10H); 2,57 (t, *J* = 6 Hz, 2H); 3,20 (q, *J* = 6 Hz, 2H); 3,53 (m, 1H); 5,67-5.69 (m, 2H); 6,75 (s, 1H); 7,51 (s, 1H); ESI-MS: M$^+$=267.1;

(S)-1-(2-(1H-imidazol-4-yl)ethyl)-3-(octan-2-yl)urea, S-HC8 : RMN1H (DMSO-d6, 300 MHz) δ (ppm) = 0,85 (br, 3H) ; 0,97 (d, *J* = 6 Hz, 3H) 1,23-1.30 (m, 10H); 2,57 (t, *J* = 6 Hz, 2H) ; 3,20 (q, *J* = 6 Hz, 2H); 3,49 (m, 1H); 5,66-5.69 (m, 2H); 6,75 (s, 1H); 7,51 (s, 1H); ESI-MS: M$^+$=267.1.

Crystal structure (X-ray diffraction)

X-ray data for the structures were collected on a Rigaku Oxford Diffraction Gemini-S S1diffractometer with a Sapphire3 detector. Mo-*K*α radiation was used with a graphite monochromator and a fiber-optics Mo-Enhance collimator for HC8. The data for S-HC8 and R-HC8 were collected with synchrotron radiation (λ = 0. 0.78965 Å) at the CRYSTAL beamline of Soleil, France. Data were corrected for absorption with *CrysAlis PRO* and the structures were solved by iterative charge-flipping methods with *Superflip*.[86] The structure refinements were carried out with *CRYSTALS*[87] and all non-hydrogen atoms were refined by full-matrix least squares on *F* using reflections with *I* > 2σ(*I*). (**Table 1**).

|	HC8	R-HC8	S-HC8
formula	$C_{28}H_{54}N_8O_3$	$C_{14}H_{28}N_4O_2$	$C_{14}H_{28}N_4O_2$
moiety	$2(C_{14}H_{26}N_4O),H_2O$	$C_{14}H_{26}N_4O,H_2O$	$C_{14}H_{26}N_4O,H_2O$
T (K)	175	150	150
Space group	$P2_1/c$	$P2_1$	$P2_1$
Crystal system	monoclinic	monoclinic	monoclinic
a (Å)	30.180(2)	12.8000(3)	12.766(4)
b (Å)	4.5911(2)	4.5826(2)	4.5679(11)
c (Å)	23.9057(14)	28.8266(11)	28.756(7)
α (º)	90	90	90
β (º)	107.482(6)	96.488(3)	96.47(2)
γ (º)	90	90	90
V (Å³)	3159.33(19)	1680.05(6)	1666.3(4)
Z	4	4	4
ρ (g·cm⁻³)	1.158	1.124	1.134
M_r (g·mol⁻¹)	550.79	284.40	294.40
μ (mm⁻¹)	0.614	0.077	0.077
R_{int}	0.044	0.058	0.070
Θ (º)	44.967	32.958	32.937
N_{tot} (measured)	4509	23942	19206
N_{ref} (unique)	2516	4503	4373
N_{ref} (I>2σ(I))	2085	3300	2999
N_{ref} (least-squares)	2085	3300	2999
N_{par}	352	361	349
R_1 (I>2σ(I))	0.1115	0.1540	0.0921
wR_2 (I>2σ(I))	0.0831	0.1687	0.1078
R_1 (all)	0.1250	0.1762	0.1262
wR_2 (all)	0.0916	0.2064	0.1501
GOF	0.9692	1.0674	1.0833
$\Delta\rho$ (eÅ⁻³)	-0.55/0.52	-0.61/1.25	-0.48/0.62
crystal size (mm³)	0.01x0.05x0.40	0.02x0.04x0.05	0.05x0.08x0.12

Table 1. X-ray data collection and refinement details.

The crystals of **HC8** were tiny and scattered only weakly as a diffracting crystal. Despite ~60 hours of prolonged measurement, no observable data was observed beyond 1.05 Å. Having acceptable data up to 0.83 Å would have required a measurement of several weeks and therefore a data strategy up to 1.0 Å only was employed. The crystal structure displayed acceptable atomic displacement ellipsoids so the relatively low data resolution does not appear to have an influence on the structure quality.
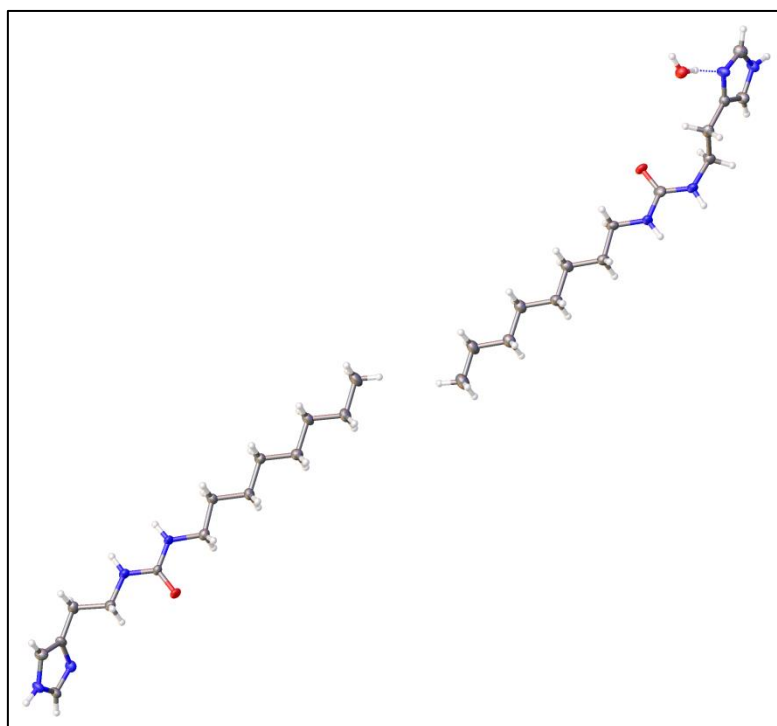
Figure 39. *Atomic displacement ellipsoid plot of the structure of **HC8** at the 50% probability level*

For the structures of **S-HC8**, the terminal imidazole ring of both independent molecules appeared to be disordered over two independent positions, which also implies that two different sets of water molecules are present in the channels. The relative occupancies of the positional disordered imidazole rings were approximately 0.8/0.2 in both cases. A number of distance and vibration restraints were used in order to keep an acceptable geometry of the rings and reasonable atomic displacement parameters.
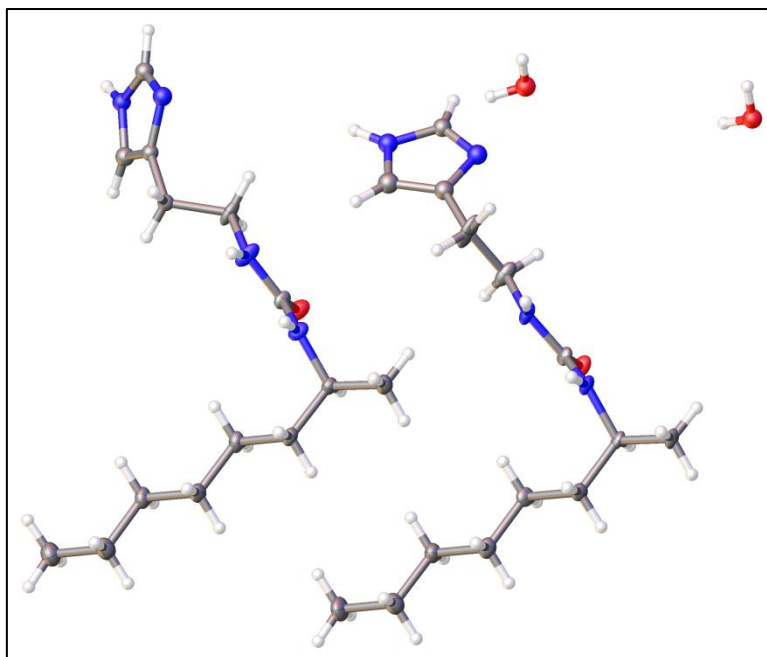
Figure 40. *Atomic displacement ellipsoid plot of the structure of **S-HC8** at the 50% probability level. Only the major disorder component (at 80% occupation probability) is shown*
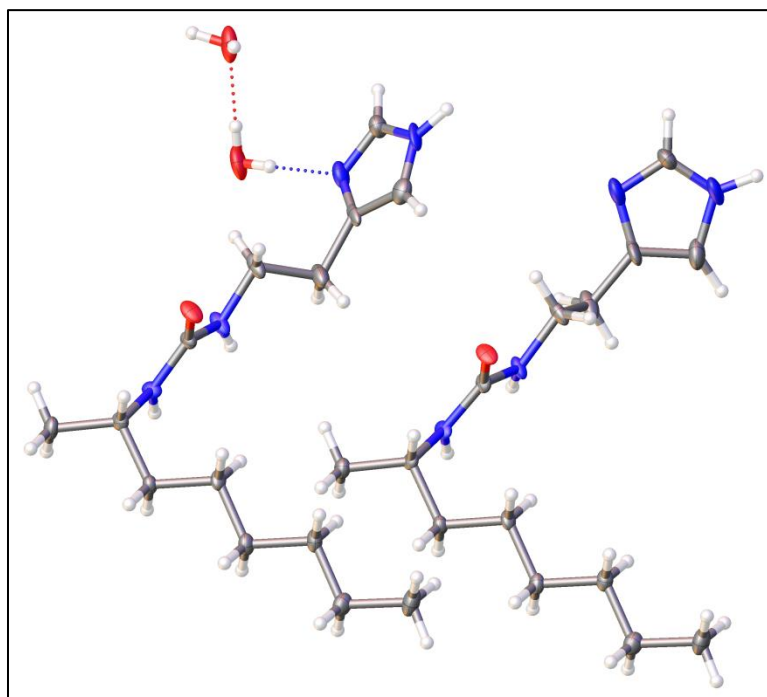
Figure 41. *Atomic displacement ellipsoid plot of the structure of **R-HC8** at the 50% probability level*

2.6.2   Stopped-flow experiments

Vesicle permeability determination

Phosphatidylcholine (chicken egg, POPC) and phosphatidylserine (porcine brain, DOPS) were purchased from Avanti Polar Lipids. Cholesterol (Chol) was obtained from Sigma. They were used without further purification. Liposomes were prepared using the film rehydration method (S1). The imidazole compounds, in chloroform/methanol mixture ($CHCl_3$/MeOH,v/v: 1/1) were added to the 1 mg POPC/DOPS/Chol mixture with a molar ratio of 4/1/5. The solution was dried on a rotary evaporator and subsequently under high vacuum to remove residual solvent. After rehydration with 1 ml buffer containing 10 mM Hepes (pH=7), 100 mM NaCl and 0.01% NaN_3, the suspension was incubated with stirring at 4 °C for 24 h and extruded through 0.2 μm track-etched filters for 10 times (Whatman, UK) to obtain monodisperse unilamellar vesicles, the size of which was characterized by dynamic light scattering (Zetasizer Nano, Malvern Instruments Ltd., UK). The water permeability tests were conducted on a stopped-flow instrument (SF-300X, KinTek Corp., USA). Exposure of vesicles to hypertonic osmolyte (10 mM Hepes, 300 mM NaCl, 0.01% NaN_3 and pH=7) resulted in the shrinkage of the vesicles due to an outwardly directed osmotic gradient. The abrupt decrease of the vesicle size leads to the increase in the light scattering at 90° according to the Rayleigh-Gans theory applied to this system (S2). The changes in light scattering caused by vesicle shrinkage were recorded at a wavelength of 600 nm.

For the determination of the water transport, synthetic vesicles were made with and without compounds incorporated and subjected to an osmotic shock. By plotting the change in intensity against time we obtain a graph that can be fitted to an exponential decay equation as shown in equation 1, where Y is the intensity of light scattering signal, A is a negative constant, t is the duration of recording, and k is the initial rate constant.

$$Y = A\exp(-kt) \qquad (1)$$

The constant of this equation basically represents the rate of swelling/shrinking of vesicles and can be used to determine the water transport taking place through the vesicle bilayer using equation 2, where P_f is the osmotic permeability, where V_0 is the vesicle initial volume, S is the vesicle surface area, V_w is the partial molar volume of water (18 cm^3), and $Δ_{osm}$ is the osmolarity difference that drives the change in the size of the vesicles.

$$P_f = \frac{k}{\left(\frac{S}{V_0}\right)V_w\Delta_{osm}} \qquad (2)$$

Channel concentration calibration

200 μL imidazole channels solutions (from 0 mg/L to 0.5 mg/L), in 10 mM Hepes (pH=7), 100 mM NaCl, 0.01% NaN$_3$ and 8% *n*-octyl-β-D-glucoside (OG), were mixed with 200 μL control liposomes. The control liposomes were first prepared using the film rehydration method in the same buffer without OG, containing 1 mg/mL PC/PS/Chl lipids with a molar ratio of 4/1/5. The liposomes were further extruded through 0.2 μm track-etched filters for 10 times (Whatman, UK) to obtain monodisperse unilamellar vesicles. The obtained solutions (final channels' concentration: 0 mg/L to 0.25 mg/L) were scanned on a UV-Vis spectrophotometer (Nanodrop 2000c, Thermo Fisher Scientific Inc., IL). We found all channels solutions had specific UV absorbance around 230 nm. For vesicles used for water transport studies, the channels were incorporated into bilayers during the film rehydration. 200 μL monodisperse vesicles after extrusion were mixed with 200 μL the same Hepes buffer containing 8% OG and the absorbance were measured at 230 nm. The insertion efficiency of the channels was calculated based on the calibration curves.
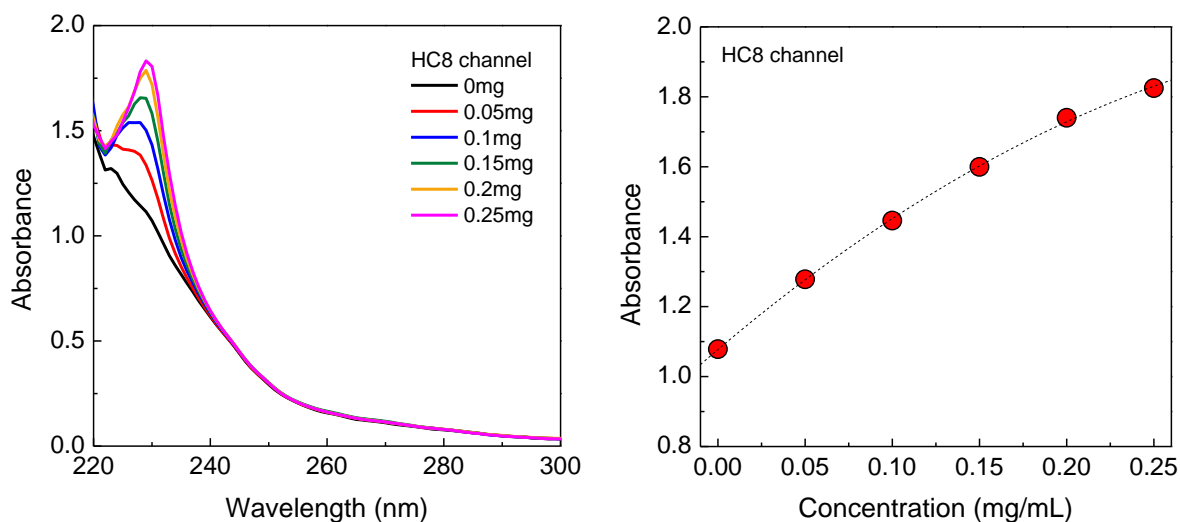
Figure 41. *Calibration curve and absorbance of SUVs with various amounts of* **HC8**

HC8	Final concentration (mg/mL)	Initial concentration (mg/mL)	Insertion efficiency
LCR10	0.063	0.1	63%
LCR1	0.131	1.0	13.1%

Table 2. *HC8 insertion efficiency*

Figure 42. *Calibration curve and absorbance of SUVs with various amounts of **R-HC8***

RHC8	Final concentration (mg/mL)	Initial concentration (mg/mL)	Insertion efficiency
LCR10	0.052	0.1	52%
LCR1	0.668	1.0	66.8%

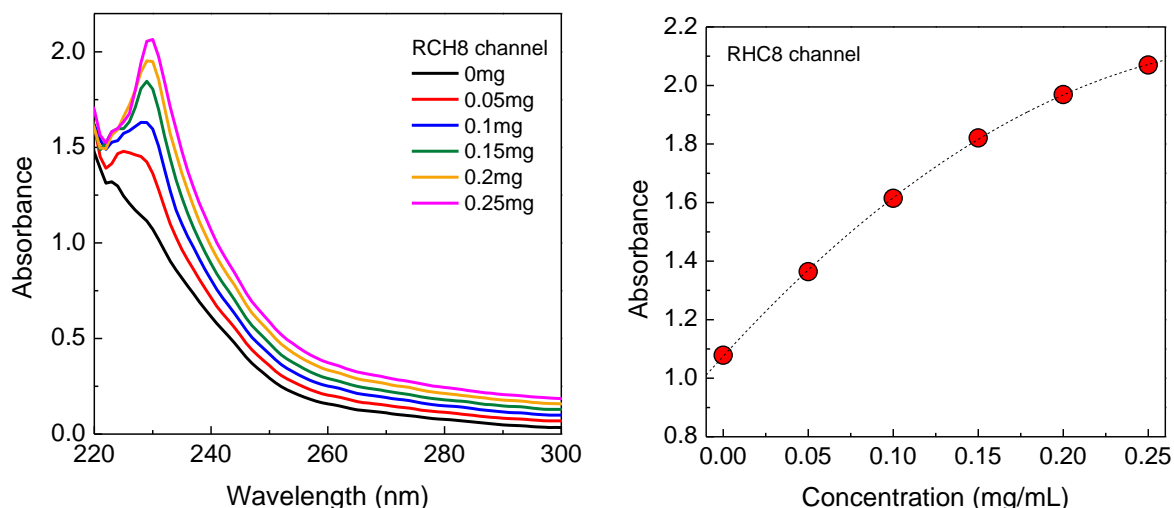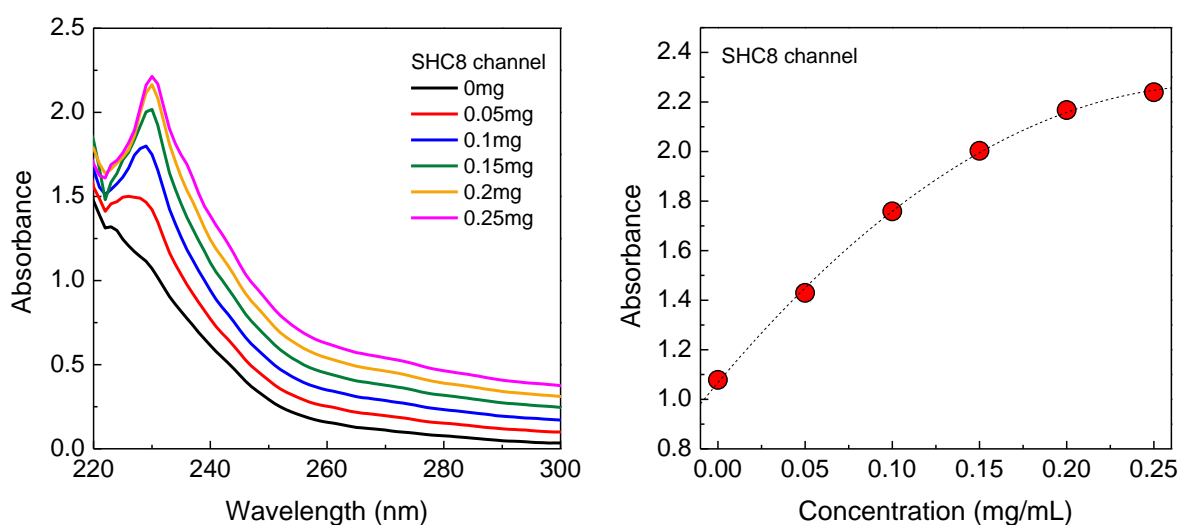**Table 3.** RHC8 insertion efficiency

Figure 43. *Calibration curve and absorbance of SUVs with various amounts of **S-HC8***

SHC8	Final concentration (mg/mL)	Initial concentration (mg/mL)	Insertion efficiency
LCR10	0.06	0.1	60%
LCR1	0.56	1.0	56%

Table 4. *SHC8 insertion efficiency*

Lipid concentration calibration

POPC/DOPS/Chol lipids solutions (from 0 mg/L to 1.0 mg/L) with a molar ratio of 4/1/5 were prepared in buffer containing 10 mM Hepes (pH=7), 100 mM NaCl, 0.01% NaN$_3$ and 4% n-octyl-β-D-glucoside (OG). The solutions were scanned on a UV-Vis spectrophotometer and we found the UV absorbance of the lipid solutions increased with the concentrations. We chose 280 nm and the absorbance at this wavelength was proportional to the concentration. When the extruded liposomes (initially 1 mg/mL) were measured at this wavelength, the actual concentration was 0.78 mg/mL.
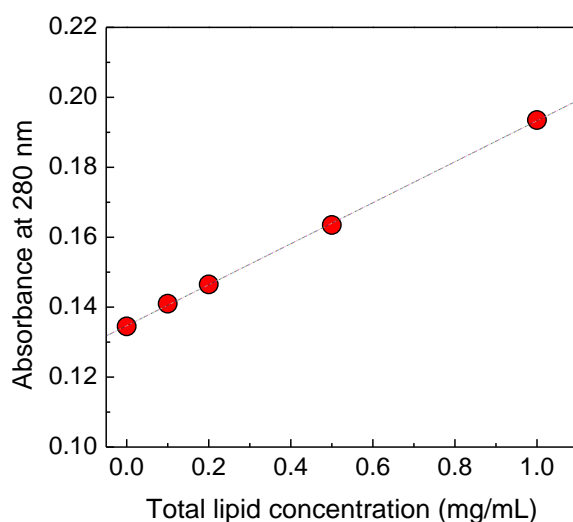
Figure 44. *Lipid concentration calibration curve*

Single channel permeability

The single-channel permeability was calculated based on the imidazole channel insertion, actual lipid concentration and channel configuration in lipids. Take one LQR1 sample of **HC8** as an example, the sum of outer and inner surface areas was $\pi/4 \times d^2 + \pi/4 \times (d-5)^2$ =123,308 nm^2, assuming that the bilayer thickness was 5 nm. The average cross-sectional area of a lipid in average was 0.287 nm^2 (POPC/DOPS/Chol lipids with a molar ratio of 4/1/5: the cross-sectional areas of PC and PS were ~0.35 nm^2 and that of cholesterol was 0.223 nm^2). The initial mass ratio of lipids/channel was 1/1. Provided 78% of lipids and only 13.1% of the HC8 channels remained in the purified the vesicles, the real mass ratio of lipids/channel was ~6. The average molecular weight of lipid is 484 Da and the molecular weight of the channel quartet is 12,768 Da (48 **HC8** molecules assembled as a channel). The molar lipids to channel ratio is 130.2. The insertion number of the channel was ~1,618 per vesicle. If the overall net permeability by channels in liposomes was 0.96 μm/s, the single-channel permeability was 3.19×10^{-17} cm^3/s and 1.35×10^6 water molecules/s.

Channel	Single channel permeability (H_2O/s)
HC8	$1.4\pm0.4\times10^6$
RHC8	$8.4\pm2.2\times10^5$
SHC8	$1.5\pm0.1\times10^6$

**Table 5.** *Single channel permeability*

2.6.3   SLB experiments

Formation of the supported lipid bilayer

QCM-D was used to track deposition of SLB formed at the QCM silica electrode surface *via* fusion of small unilamellar vesicles (SUVs) of mixtures of phosphatidylcholine (chicken egg, POPC), phosphatidylserine (porcine brain, DOPS) and cholesterol (Chol). Different lipid compositions have been tried in an effort to find the SLB that had an optimal composition with a molar ratio POPC/DOPS of 4/1, while still incorporating 20% w:w ratio of compound **HC8** and allowing a more easy interpretation of the QCM and SFG experiments. Lipid vesicles concentration was 0.2 mg/mL. Flowrate was kept constant at 100 uL/min

According to Cho et al., 2010,[82] a SLB is characterized by:

- ΔF (F = Frequency ~ Mass) = ~-25 Hz, depending on the lipid system used;

- ΔD (D = Dissipation ~ Layer rigidity, i.e. high D = floppy layer, low D = rigid layer) = 0.2-0.3.

Hence a SLB is a rigid layer coupled to the QCM-D sensor. Visually, a rigid layer is characterized by the overlapping of multiple overtones, like in Fig. 45 for the 5th, 7th and 9th overtones. For a floppy layer (i.e. the vesicles), the overtones would spread apart.
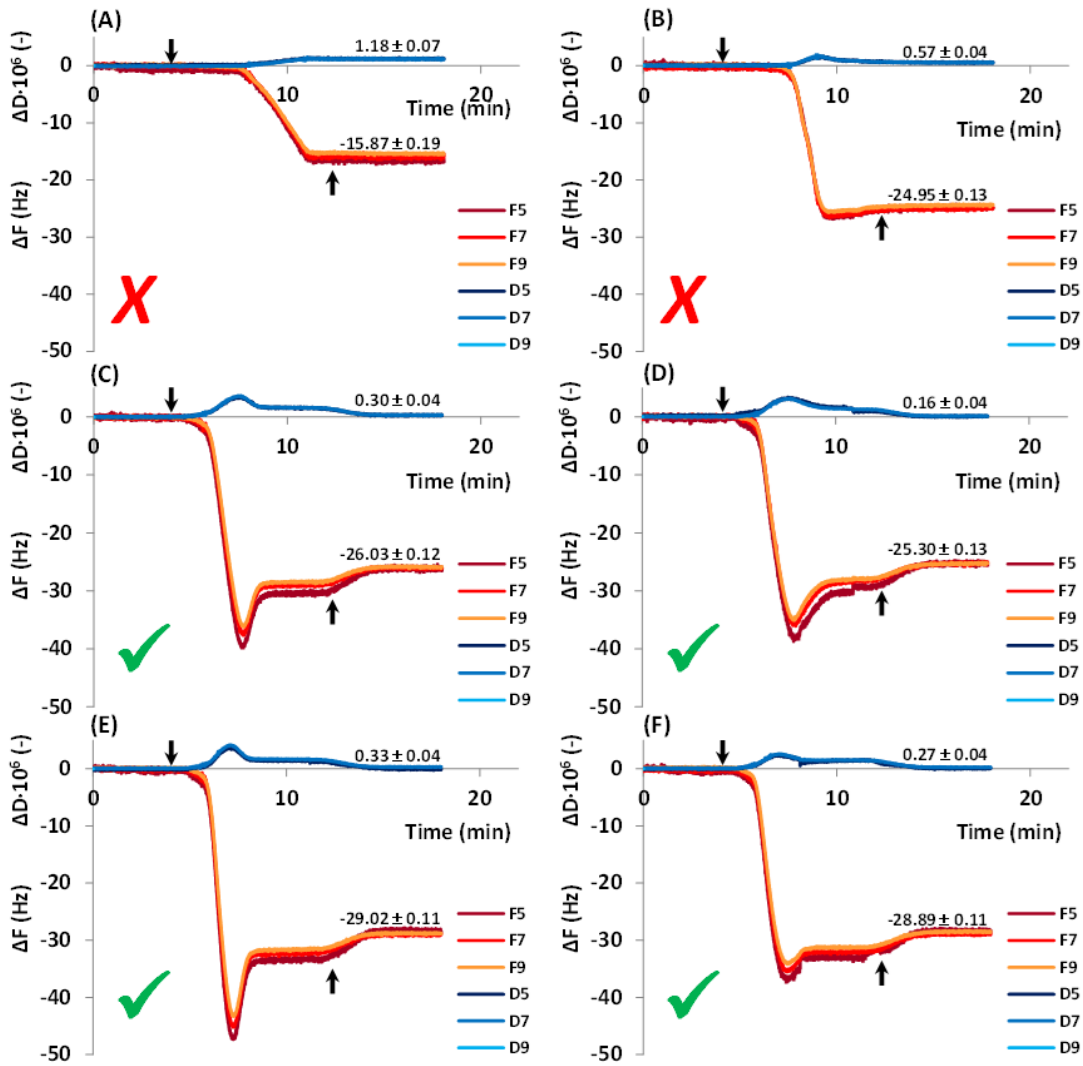
Figure 45. *Lipid vesicles deposition for (A) POPC, (B) POPC + **HC8**, (C) 4:1=POPC:DOPS, (D) 4:1=POPC:DOPS + **HC8**, (E) 4:1=POPC:DOPS, 20% w/w Chol and (F) 4:1=POPC:DOPS, 20% w/w Chol + **HC8**. The two arrows indicate (i) lipid vesicles injection and (ii) washing step with 10 mM phosphate buffer pH 6.4*

Estimate of lipids, HC8 and H$_2$O quantity in the SLB

For the 4:1=POPC:DOPS + **HC8** we obtained a $\Delta F = -25.3 \pm 0.13 \; Hz$, where the ΔF is directly proportional to the total mass per unit area,[82] m", coupled to the QCM-D sensor:

$$m^{"} = \frac{m}{A} = -C \cdot \frac{\Delta F}{n} = -17.7 \cdot (-25.3) = 447.81 \; ng/cm^2$$

The diameter, d, of the QCM-D sensor is 1 cm, hence the area, A:

$$A = \pi \cdot \frac{d^2}{4} = \pi \cdot \frac{(1)^2}{4} = 0.785 \; cm^2$$

The total mass, m, coupled to the QCM-D sensor is:

$$m = 453.12 \cdot 0.785 = 351.7 \; ng$$

→ This is the total mass coupled to the QCM-D sensor, **m$_{tot}$ = m$_L$ + m$_{HC}$ + m$_W$ = 351.7 ng** where:

    m$_L$ = mass of the lipids forming the SLB;

    m$_{HC}$ = mass of the HC8 incorporated into the SLB;

    m$_W$= mass of H$_2$O from (i) the hydration layer, (ii) molecules within the **HC8** channels and

LIPIDS

The average molecular weight, $\overline{MW}$, of the 4:1=POPC:DOPS can be calculated:

$$MW_{PC} = 770 \frac{g}{mol}$$

$$MW_{PS} = 824 \frac{g}{mol}$$

$$\overline{MW} = 0.8 \cdot 7770 + 0.2 \cdot 824 = 780 \frac{g}{mol}$$

HC8

$$MW_{HC8} = 266 \frac{g}{mol}$$

    A ratio of 20% w/w of **HC8** to lipids was used for the lipid preparation. Accordingly in 100 mg of lipid:**HC8** mixture we would have 80 mg lipids(0.103 mmol) and 20 mg of **HC8** (0.075 mmol). That would make a molar ratio of lipids:HC8 = 1.36. That would make an approximate of 73.4 **HC8** molecules for every 100 molecules of lipids.

H2O

There are 2 contributions:

(i) Hydration layer:

    $\delta_{W(i)} = 10\ A$

    $m_{W(i)} = \rho_W \cdot V_{W(i)} = 1000 \cdot (1 \cdot 10^{-9} \cdot 0.785 \cdot 10^{-4}) = 7.85 \cdot 10^{-11} kg = 78.5\ ng$

(ii) Molecules within the HC8 channels: each quartet contains 2 water molecules

$$\begin{cases} m_{tot} = m_L + m_{HC8} + m_{W(i)} + m_{W(ii)} = 351.7\ ng \\[2ex] \dfrac{m_L}{0.8} = \dfrac{m_{HC8}}{0.2} \\[2ex] m_{W(i)} = 78.5\ ng \\[2ex] m_{W(ii)} = n_{W(ii)} \cdot MW_W = \dfrac{n_{HC}}{2} \cdot MW_W = \dfrac{m_{HC}}{2} \cdot \dfrac{MW_W}{MW_{HC}} = \dfrac{1}{2} \cdot \dfrac{18.015}{266} \cdot m_{HC} \\ \qquad\qquad = 0.0339\ m_{HC8} \end{cases}$$

Solving this system of 4 equations in 4 variables:

$$m_L = 217.1\ ng$$
$$m_{HC} = 54.3\ ng$$
$$m_{W(i)} = 78.5\ ng$$

$$m_{W(ii)} = 1.8 \, ng$$

Structural information of the bilayer

<u>SLB thickness</u>

From the total mass coupled to the QCM-D sensor, we could estimate the layer (= lipids+HC8+water) thickness, given the layer density. The average SLB density, ρ_{SLB} is ~ 900-1,000 kg/m³, based on MD simulations on a 3:1=POPC:POPG SLB.[88] Assuming an average layer density, ρ of 1,000 kg/m³, we obtain:

$$\delta = \frac{V}{A} = \frac{m}{\rho \cdot A} = \frac{m''}{\rho} = \frac{-C \cdot \frac{\Delta F}{n}}{\rho} = \frac{-17.7 \cdot \left(\frac{\Delta F}{n}\right)}{\rho} = \frac{\ldots \, ng/cm^2}{1,000 \, kg/m^3}$$

Without HC8, $\Delta F = -26.03 \, Hz$, hence $\delta = 4.61 \, nm$
With HC8, $\Delta F = -25.30 \, Hz$, hence $\delta = 4.48 \, nm$

<u>Surface coverage</u>

Solving the same set of equations as in paragraph C., for the 4:1=POPC:DOPS SLB without the HC8 compound (i.e. m_{HC} = 0 ng and $m_{W(ii)}$ = 0 ng), we obtained:

$$m_{tot} = m_L + m_{W(i)} = 361.9 \, ng$$

$$m_{W(i)} = 78.5 \, ng$$
$$m_L = 283.4 \, ng$$

We can calculate the total number of lipid moles, n_L, covering the QCM-D surface:

$$n_{lipid} = \frac{m_{lipid}}{MW} = \frac{283.4}{780.8} = 0.363 \, nmol$$

Note: Because it is a bilayer, the single layer would have half number of moles
The area that the single lipid molecule occupies on the surface is:

$$\frac{\frac{n_{lipid}}{2} \cdot 6.023 \cdot 10^{23}}{A} = \frac{0.363/2 \cdot 10^{-9} \cdot 6.023 \cdot 10^{23}}{0.785 \cdot 10^{16}} = 0.014 \, \frac{molecule}{\text{Å}^2} = 1 \, \frac{molecule}{\mathbf{71.9 \text{Å}^2}}$$

This value corresponds to a value of 0.96 nm in diameter. This is in good agreement with reported values.[89]

Sum-frequency generation experiments

Samples for SFG experiments were formed on 10 mm CaF2 equilateral prisms coated with ~100 nm SiO¬2 layer deposited according to the previously published procedure. (cite Aliyah) Half of the prism face was also coated with 150 nm Au for use as a reference. To form the bilayers, 25 µL vesicle solution was added to 1 mL of aqueous 0.1 M PBS solution containing 0.2 M NaCl. A flow cell was formed by the CaF2 prism, Teflon o-ring,

and Teflon backplate with Teflon tubes as input and output ports connected to two syringes. The vesicle PBS mixture was added to one syringe and manually passed back and forth between syringes across the CaF2 surface. The solution was then stationary for about 10 minutes to completely form the bilayer. After, excess PBS solution was used to rinse off any remaining vesicles.

The laser system used for the SFG experiments has been described previously[refs]. Briefly, a Ti:Sapphire amplifier (Coherent Legend Elite Duo), seeded by a Ti:Sapphire oscillator (Coherent Micra-5), provides 5 mJ, 25 fs duration, 800 nm pulses at a repetition rate of 1 kHz. One portion of the output is spectrally narrowed with a Fabry-Perot etalon (TecOptics, Inc.) to form the "visible" upconversion beam, while another portion is used to generate tunable broadband infrared pulses in a commercial optical parametric amplifier (Coherent OPerA Solo). The visible beam (10 μJ, 792.8 nm, FWHM 10 cm^{-1}) and infrared beam (18 μJ, center frequencies of 3070 cm^{-1}, 3230 cm^{-1}, and 3670 cm^{-1}, FWHM ~300 cm^{-1}) are focused onto the prism-liquid interface at 60° and 65°, respectively, with respect to the surface normal. The 2500-4000 cm^{-1} frequency range was covered by setting the OPerA at 3 central positions. The SFG field was generated in reflection, dispersed on a diffraction grating and imaged onto a liquid nitrogen-cooled CCD (Princeton Instruments). The polarization of the individual beams was controlled with the combination of a waveplate and polarizer. All data were normalized to the nonresonant Au signal obtained in ppp-polarization combination (polarization of the SFG, visible, and IR beams, respectively) collected immediately before vertically translating the flow cell to the sample.

### 2.6.4 Molecular dynamics simulations

Simulation conditions

Simulations were performed using the CHARMM-36 force field (J. B. Klauda, et al. J. Phys. Chem. B, 114, 7830-7843, (2010)) for lipid molecules and the TIP3P model (W. L. Jorgensen, J. Chem. Phys. 79, 926-935 (1983)) for water. To represent the HC8, R-HC8 and S-HC8 molecules, and generate their topologies, we used the CHARMM General Force Field (CGenFF) (K. Vanommeslaeghe et al. J. Comput. Chem. 31, 671-690, (2010)) together with the paramchem web service (K. Vanommeslaeghe et al. J. Chem. Inf. Model., 52, 3155-3168 (2012)). The GROMACS 4.6 software (B. Hess et al. J. Chem. Theory Comp. 4, 435–447, (2008)) was used to run the simulations with virtual interaction sites allowing a 5 fs integration time step. All bonds were constrained using the LINCS algorithm. Particle mesh Ewald electrostatics was used with a 10 Å cutoff with the Verlet buffer scheme for non-bonded interactions, the neighbor list was updated every 20 steps. Three baths (imidazoles, lipids, water, and ions) were coupled to a temperature of 310 K using the Bussy velocity rescaling thermostat with a time constant τ = 0.1 ps. As previously determined, we chose a lateral pressure of 10 atm to maintain aggregate structuring and achieve reasonable sampling on a 500 ns timescale. The pressure in the x/y dimensions was scaled isotropically with a Berendsen weak barostat and the z dimension was coupled independently to a

reference pressure of 1 bar, τ = 5.0 ps and compressibility of $4.5*10^{-5}$ bar^{-1}. All systems were minimized for 10.000 steps with the steepest descent algorithm and equilibrated for 20 ns, using position restraints of 1000 kJ*mol^{-1}*nm^{-2} on heavy atoms, with the crystal structure as a reference. Production runs were finally computed for 500 ns without any position restraints.

| Acronym	Composition (Imid./Chol./POPC/POPS/water)	Atom number	Pressure (atm)	Sim. time (ns)
HC6_P1	96/148/111/28/8442	58496	1	1000
HC6_P-10	96/148/111/28/8442	58496	-10	250
HC6_P10	96/148/111/28/8442	58496	10	500
HC6_P100	96/148/111/28/8442	58496	100	500
HC8	96/155/114/32/8534	60780	10	1000
S-HC8	96/148/119/32/8608	61154	10	500
R-SC8	96/147/119/32/8589	61023	10	500

Table 6. *Simulation systems overview*
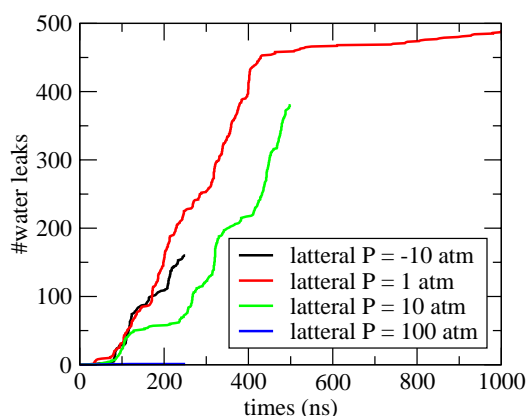
Figure 46. *The water transport activity time series of the **HC6** channels under increasing lateral pressure, from -10 atm to 100 atm is shown. Cumulated transport of water molecules across the membrane, in either direction, is shown.*
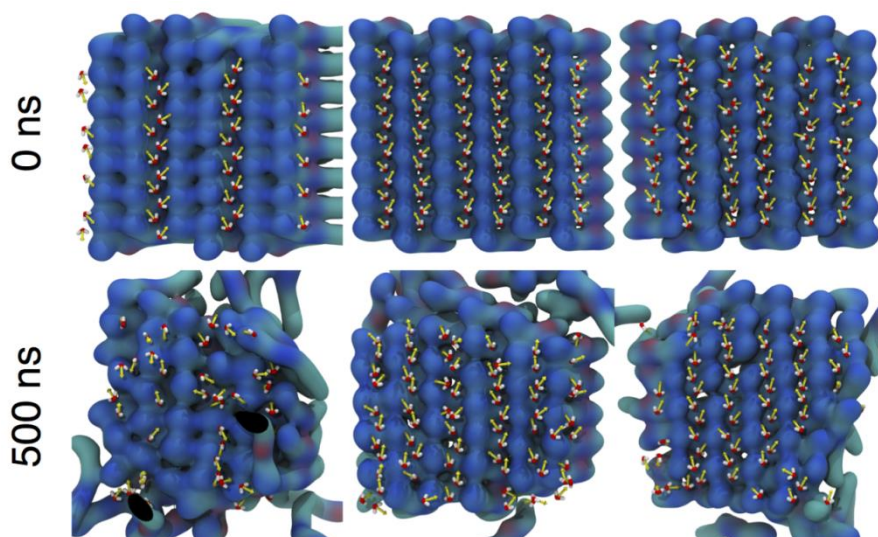
Figure 47. *Final water-wire (red/white sticks) and dipole (yellow arrows) orientations within the I-quartet **HC8**, **R-HC8** and **S-HC8** channels (bluish surface).*
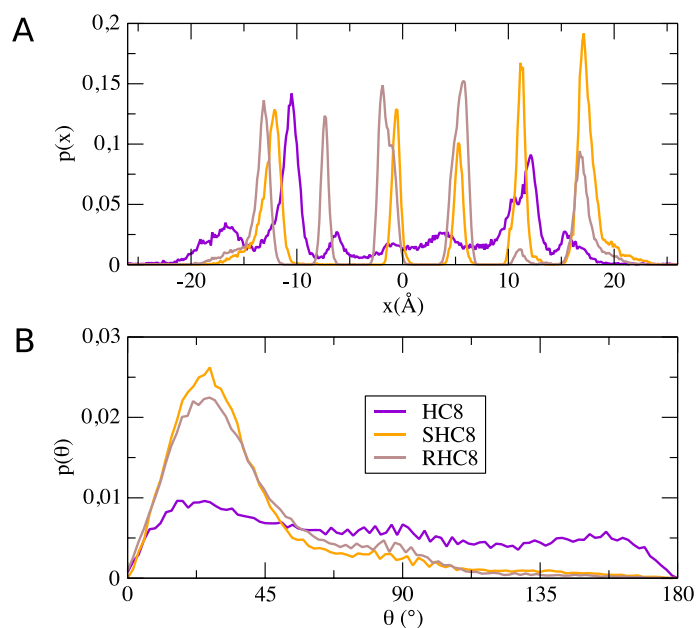
Figure 48. *A. One-dimensional water density profile for crossing water averaged for the simulations of the **HC8**, **R-HC8** and **S-HC8** channels at 10 atm. B. Water dipolar moment orientation with respect to the z-axis perpendicular to the membrane – only channel water is used for this calculation.*

The hydrogen bonding patterns were analyzed in terms of water-water hydrogen bonds, water(donor) to imidazole(acceptor) hydrogen bonds, imidazole(donor) to water(acceptor) and water with lipid ones (Fig. 49). As can be seen, **R-HC8** and **S-HC8** constructs have identical patterns with 1.3 hydrogen bonds on average connecting the pore waters and 1.7 hydrogen bonds linking them to the imidazoles. With 0.5 water-water hydrogen bonds on average, the water cohesion is significantly lower for the **HC8** system.

The anchoring to the imidazoles is of the same order of magnitude but with a slightly higher donation from water to imidazoles. Hydrogen bonds with lipids are not observed in these systems. Looking at the overall number of hydrogen bonds for the water molecules - compared to a reference value of 3.2 for bulk solvent, we notice that water in the R-HC8 and S-HC8 pores is almost unperturbed, reaching up to 3.0 hydrogen bonds, whereas the HC8 system lacks 1 hydrogen bond. Data on water at the membrane interface is provided for reference as well.
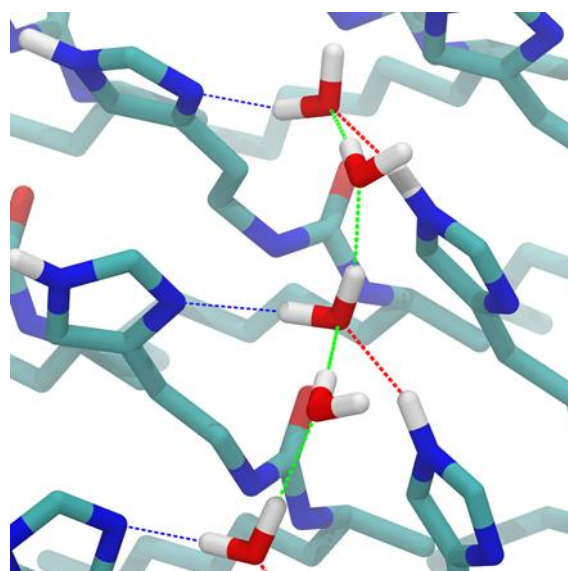

Figure 49. *Illustration of the H2O↔H2O (green dotted lines), H2O→Imid. (blue dotted lines) and H2O←Imid. (red dotted lines) hydrogen bonds formed by water molecules in the membrane region*

	HC8	RHC8	SHC8
# Central:	27 ± 7	27 ± 2	25 ± 1
$H_2O \leftrightarrow H_2O$	0,9 ± 0,7	1,4 ± 0,3	1,6 ± 0,3
$H_2O \rightarrow$Imid.	0,8 ± 0,3	1,1 ± 0,1	1,0 ± 0,1
$H_2O \leftarrow$Imid.	0,5 ± 0,2	0,8 ± 0,1	0,8 ± 0,1
$H_2O \leftrightarrow$Lipid	0,1 ± 0,1	0 ± 0	0 ± 0
Total	2,3 ± 0,8	3,2 ± 0,3	3,4 ± 0,3
# Lateral:	22 ± 5	44 ± 3	41 ± 4
$H_2O \leftrightarrow H_2O$	0,5 ± 0,5	1,2 ± 0,3	1,1 ± 0,3
$H_2O \rightarrow$Imid.	1,1 ± 0,4	1,0 ± 0,1	1,0 ± 0,1
$H_2O \leftarrow$Imid.	0,3 ± 0,2	0,6 ± 0,1	0,6 ± 0,1
$H_2O \leftrightarrow$Lipid	0,1 ± 0,1	0 ± 0	0 ± 0
Total	2,0 ± 0,6	2,9 ± 0,3	2,8 ± 0,3

Table 7. *Statistics of central channel water molecules within the lipid bilayer region*

Chapter III

–Novel Artificial Water channels –
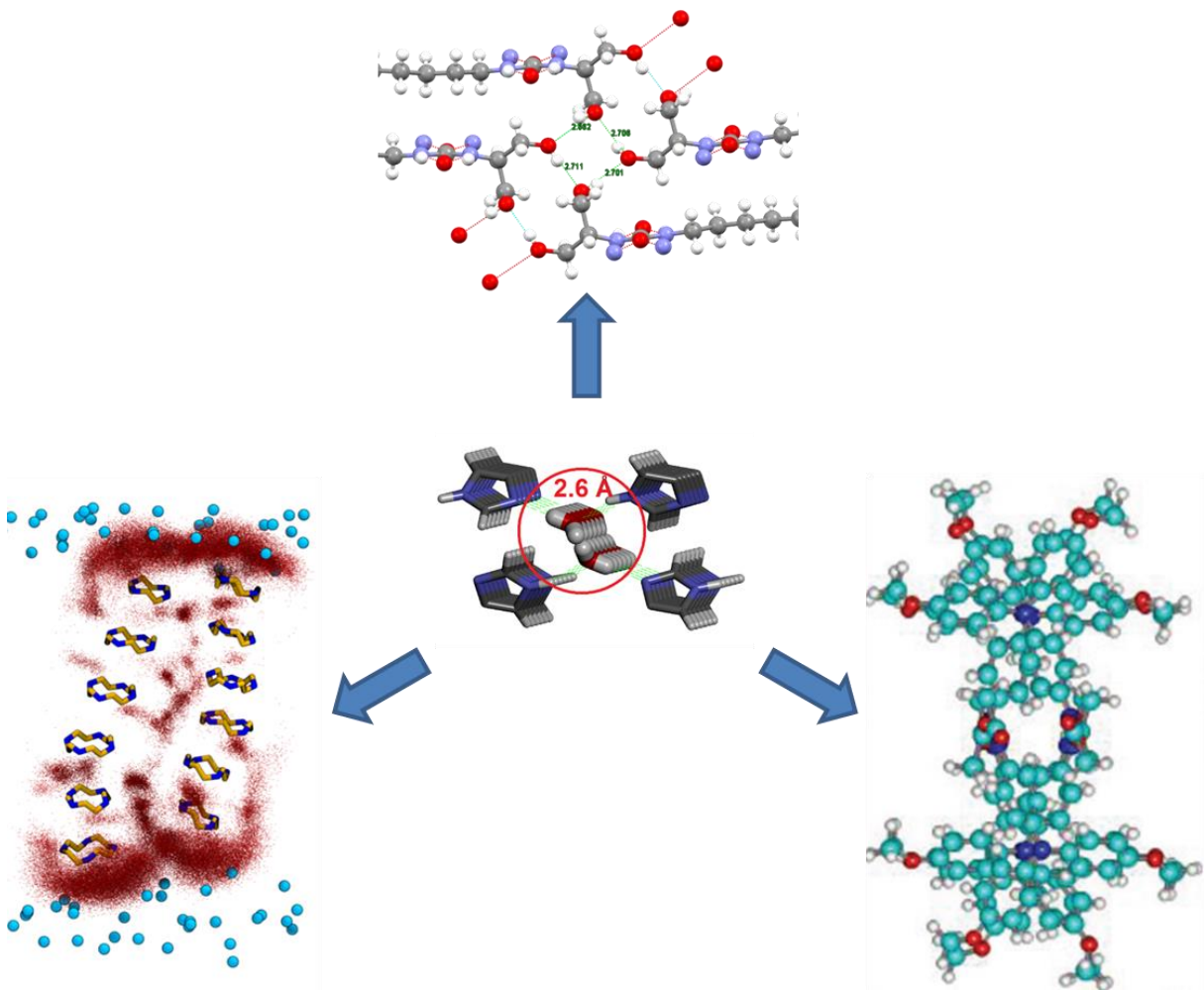

¨Originality is nothing but judicious imitation"

Voltaire

3.1 Context

We know from the literature that there are several synthetic systems capable of water transport, having various structural similarities.[90] In general, there were identified two main translocation mechanisms of water in selective filter channels working on a size restriction. They are related to:

i) *hydrophobic pores* in which very few or no H-bonding are occurring between the water molecules and the inner surface of the channels;

ii) *hydrophilic pores* that specifically bind water, resulting in the formation of water clusters .

In the first case, the design is fairly straightforward; the size of the hydrophobic pore is needed to be less than 4 Å to block the passage of hydrated ions. The difficulty lies in the synthetic route for obtaining hydrophobic channels with low porosity, while not using any moieties that might induce the dehydration of the ions. In the second case, the structural features of the channel pores are more complex. Whilst the size restrictions are still necessary, water specific binding is needed for selectivity. This can be obtained through the combination of hydrogen bonding donor-acceptor moieties. (Fig. 50) In both cases the transport of ions is prohibited due to the energy penalty that would be incurred from the dehydration of the ions and the unfavorable interactions with the channel walls, mainly leading to the selectivity of the water transport in competition with other ions.
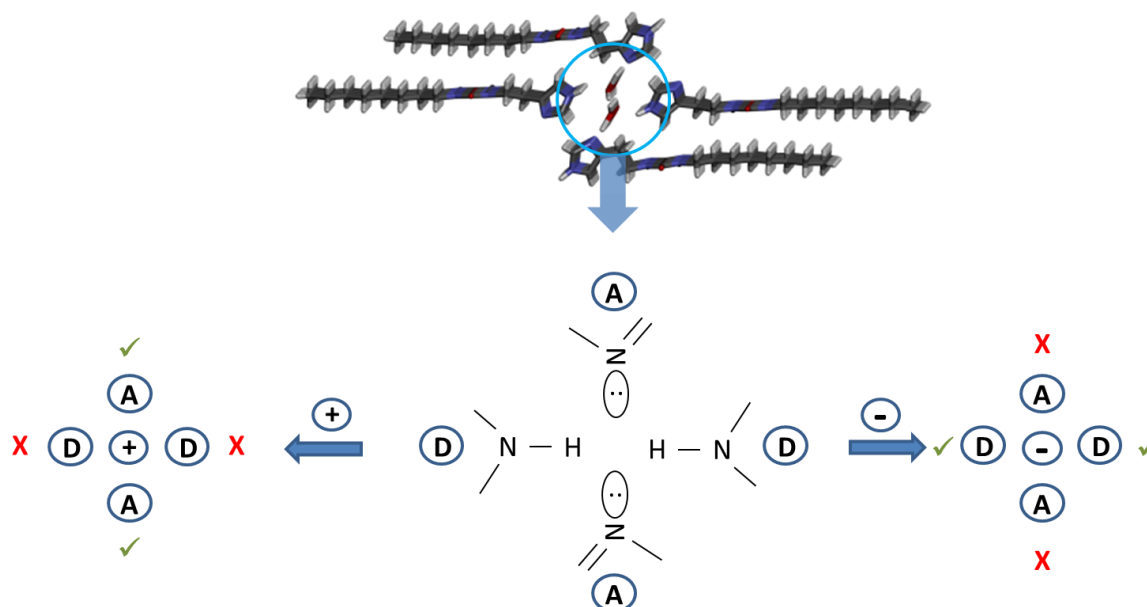
Figure 50. *Donor-acceptor-donor-acceptor H-bonding N: and N-H groups of I-quartets; incompatible with the binding of both cations (left). and anions (right).*

In the case of the imidazole I-quartet water channels described in the previous chapter, we had a system of specific water binding composed of alternating donor-acceptor-donor-acceptor H-bonding domains through the nitrogen atoms in the imidazole headgroup. We believe that this alternation of hydrogen bonding capacity is responsible for the systems selective transport properties. Having both types of domains present, cations as well as anions are energetically unfavorable to bind to the pocket due to repulsive forces from either the protons, in the case of cations, or the pair of electrons, for anions.

In an effort to find new efficient water specific channels we proposed to vary mainly the moieties responsible for specific water binding, by exploring new moieties which could provide different combinations of similar donor-acceptor systems. (Fig. 51)
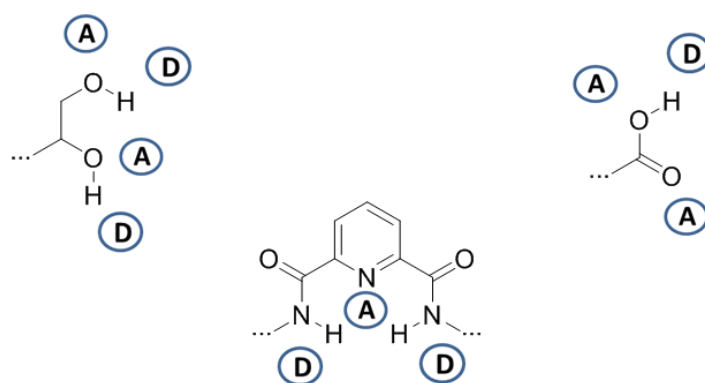

Figure 51. *Proposed donor-acceptor H-bonding systems for water binding*

Several designs were set in place for obtaining new building blocks for the construction of novel hydrophilic self-assembled water channels, with donor-acceptor water "amphiphilic" H-bonding sites. The general strategy remained similar to the one established in Chapter 2, retaining the 3 components (hydrophobic region for the bilayer membrane insertion, stacking motif for the directional self-assembly and hydrophilic region for water binding) essential for the formation of the channels.

In a first attempt, we closely followed the imidazole channel models, maintaining the backbone the same while modifying the headgroup by using various diols as hydrophilic moieties and potential water binders. (Fig. 52 A)

In an effort to increase the stability of the self-assembled channels we rationalized the design to introduce additional stacking motifs into the structure of the building blocks. In this idea, we proposed the geometry of so-called "U-shaped" molecules with pending arms containing each a stacking motif while having as water binding group the pyridine moiety. (Fig. 52 B) The choice of pyridine was not arbitrary as it is known that pyridine based foldamers are capable of binding specifically water molecules in their cavities.[53]

To further increase the stability of the potential water channels we proposed to synthesize a series of macrocyclic compounds with various hydrophilic cavities and stacking motifs. (Fig. 52 C)
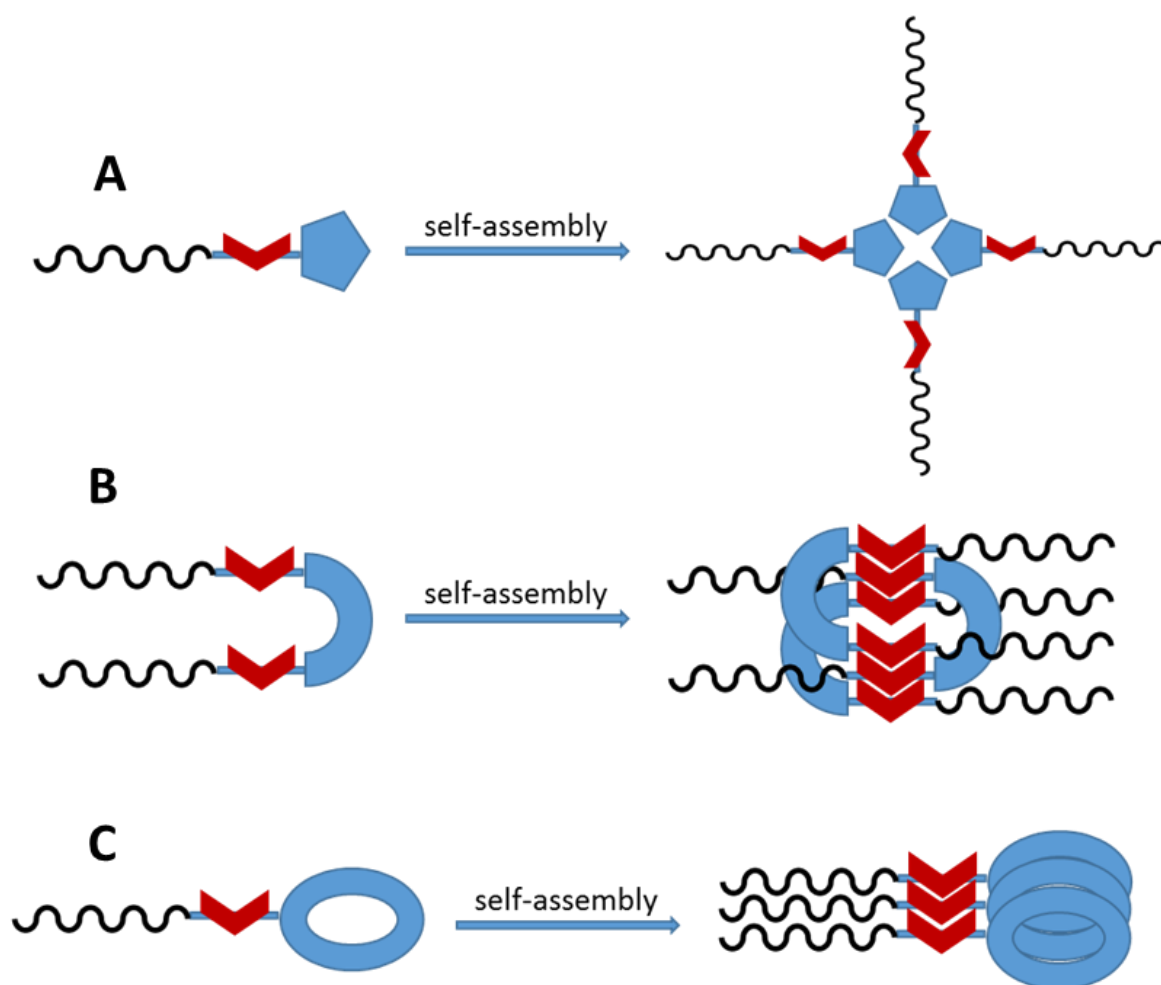
Figure 52. *General design schematics proposed for the self-assembly of water channels*: A) classic hydrophobic-stacking-hydrophilic model for quartet channel formation; B) "U-shaped" molecules with water binding pocket, self-assembly and hydrophobic motifs C) hydrophilic macrocycles with stacking motif and hydrophobic tails

This chapter is focused on the novel self-assembled water channels systems, describing the compounds starting from synthesis up to water and ion transport experiments, including other relevant results such as molecular modeling and dynamics. As this part of the project is still under incipient development, this chapter focuses mainly on the synthetic and crystal structures of the compounds, and some emphasis on the water transport properties of the synthesized systems.

3.2 Alkylureido-diols

Synthetic Design. The synthetic route for the diol based compounds is based again on a single step reaction using isocyanate and amine starting materials. (Fig. 53)

R_1:
- *n-hexyl*
- *n-octyl*
- *(S)-octyl*
- *(R)-octyl*

R_2:
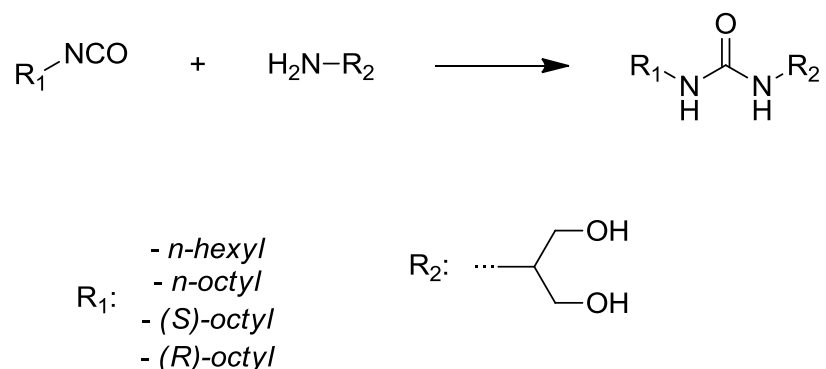
Figure 53. *Synthetic scheme for obtaining alkylureido-diols*

We rationalized that the hydroxyl groups could act as donor-acceptor moieties for water molecules. Having observed that hexyl and octyl chains are the most suitable for water transport experiments in the case of the imidazole channels, we insisted on this series of compounds, trying to correlate again chiral information translation into transport behavior. The nomenclature for the diol compounds is as follows: DCx for the achiral molecules, SDCx and RDCx for the molecules with chiral alkyl chains.

Single crystal X-ray structures. Obtaining single crystal structures was not trivial, having suitable crystals for X-ray analysis for only one of the obtained compounds. Crystallization occurred from a highly concentrated DMSO solution containing 5% water. The crystal structures present hydrophobic/hydrophilic domains linked together through the urea bonds. (Fig. 54) The single cell unit is presented in the experimental part.
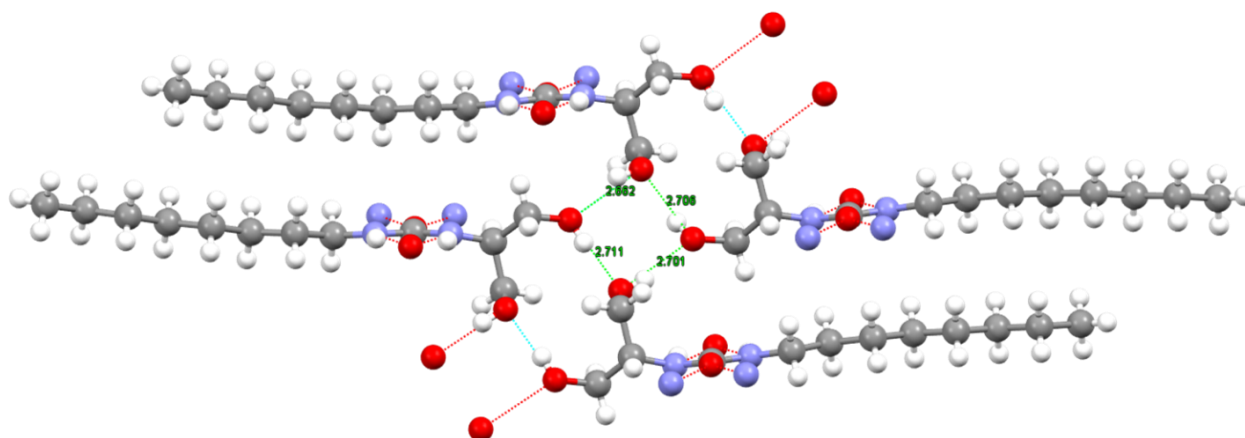

Figure 54. *View along the a axis in the single crystal structure of **DC8***

Interestingly the structures present no water molecules in interaction with the hydrophilic regions provided by the hydroxyl head-groups. However, the same organization takes place as in the case of the imidazole compounds. The diols are forming a quartet structure through the same donor-acceptor-donor-acceptor network of hydrogen bonds, excluding the water molecules. One hydroxyl arm from each molecule is contributing towards the formation of a square hydrophilic pocket with an average length of the sides of 2.7 Å. This pocket repeats itself with adjacent diol quartets on the *bc* axes, while being perfectly superposed with quartets on the *a* axis. The alkyl chains are parallel and linear, with a slight disorder on the terminal methyl group. Again we find the same hydrophobic regions made of the alkyl tails from two adjacent rows of stacked molecules, as was the case in the imidazole-based water channels.

Arguing that the alkyl chains will provide insertion into a lipid bilayer and the hydroxyl-rich group could act as a binder for water molecules, we tested the compounds for water transport across vesicle bilayers.
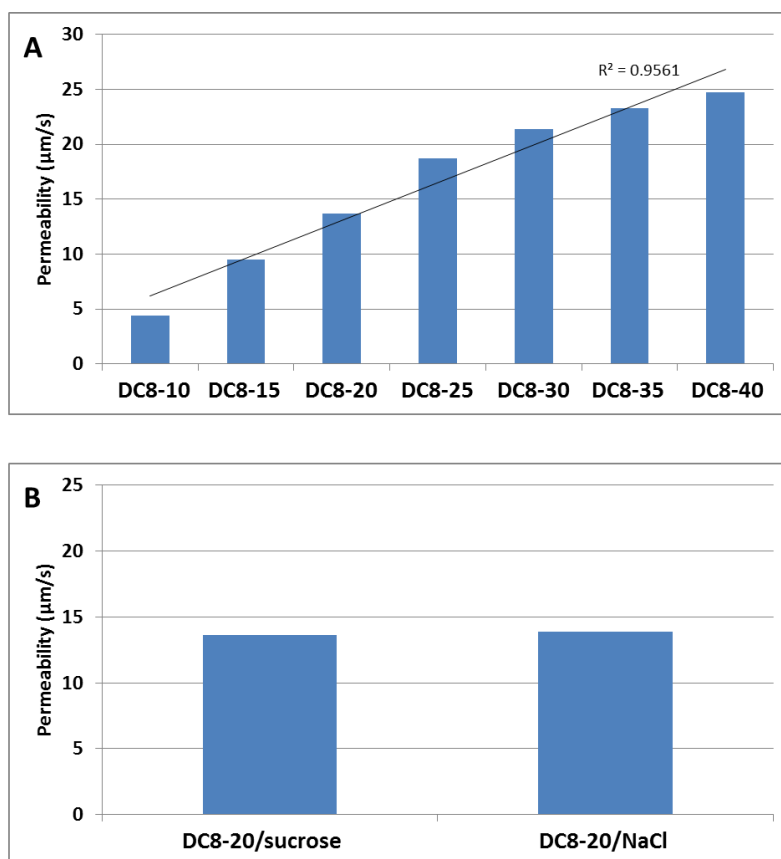
Figure 55. *(A)The average water permeability of liposomes with different concentrations of injected* **DC8** *(x axis); (B) Net permeability obtained from exposing the same liposomes to 400 mM sucrose and 200 mM NaCl solutions*

Water transport activity. Although there were no classical water channels including water molecules, present in the solid state structures, the compounds have been tested for water transport experiments using the light-scattering/stopped-flow setup. We have

obtained observable permeability increase only in the case of **DC8**. (Fig. 55) It is not farfetched to assume that through a slight relaxation of the diol quartets, water molecules can flow through the hydrophilic pocket along the stacked molecules. In the lipid bilayer, this practically provides and easy passage for water molecules, while the structure is kept stable through the hydrophobic compatibility between the alkyl tails of the compounds and the lipids.

We observed a linear response in vesicle permeability increase in function of the concentration of the injected **DC8** compound into the vesicle solution, obtaining net permeabilities for the vesicles containing **DC8** up to 23 μm/s.

In order to determine if the compounds are selective for water, the transport experiments were done under an identical osmotic pressure with the use of NaCl and sucrose as osmolytes. Having obtained almost the same permeability values in both cases proves that the vesicle undergoes a change in size only under the effect of water transport. Insertion rate has not been determined for this compound, as so actual permeability per channel cannot be attributed.

Proton transport activity. We were interested in further testing the specificity of the compound by testing it for proton transport. We use a classical HPTS assay. In short, a pH sensitive dye loaded vesicle is subjected to a proton gradient. The rate of the proton transfer across the bilayer can be tracked by the absorption/emission changes of the dye in function of the pH change. (Fig. 56)
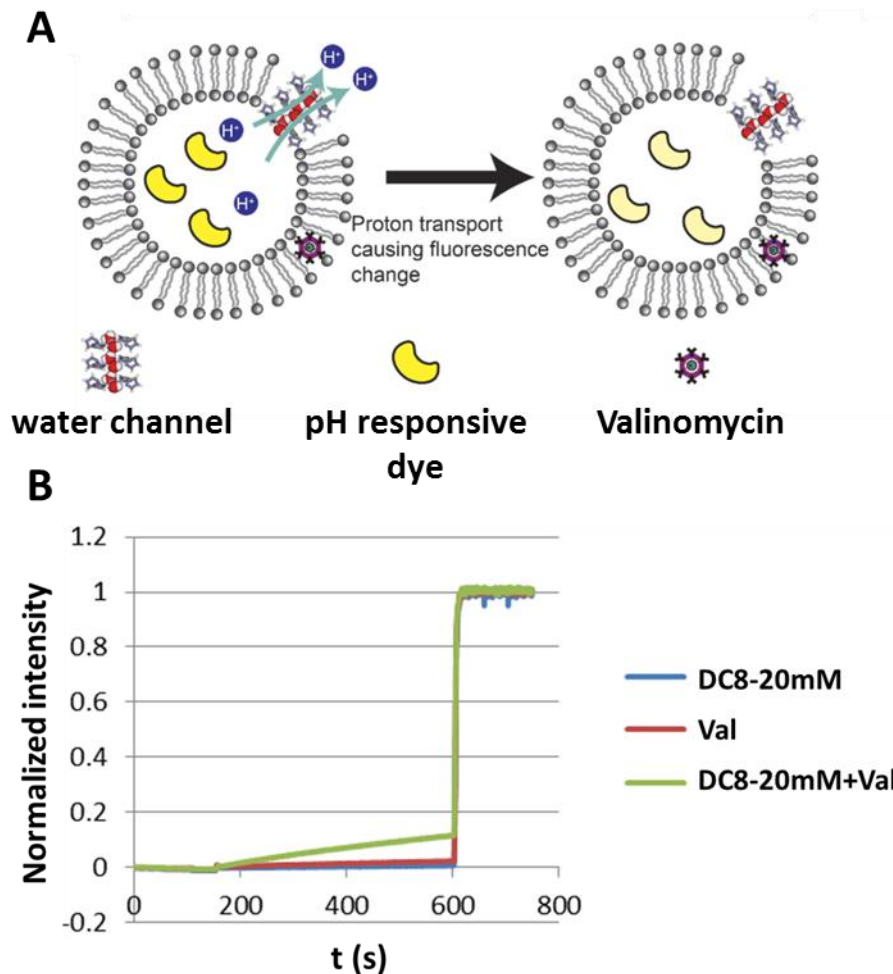
Figure 56. *(A) Vesicular proton transport schematic in lipid vesicles; (B) proton transport rate for **DC8***

The results show us that even at relatively high concentrations, the compound induces negligible proton transport in comparison to the water permeability. As a positive reference for the dose responsive experiment, we used carbonyl cyanide-p-trifluoromethoxyphenylhydrazone (FCCP), an artificial proton transporter. (see chapter 3.5)

Since we already know that DC8 is transporting water molecules, we can assume that this low proton transport efficiency is not due to a Grothuss transport mechanism, but more likely to a hydronium facilitated translocation. Since compound DC8 is not easily protonated in pH conditions used, we also exclude proton hopping along the hydroxyl groups from as a possible mechanism. Having relatively low proton transport, correlated with the obtained water transport results, makes the **DC8** compound the first artificial water channels that are exclusively transporting water molecules, making it the closest mimic of the natural AQP.

3.3   Pyridine-based "U-shaped" molecules

Synthetic Design. The design for the U-shaped molecules was based on previously reported foldamers containing functionalized pyridines.[53] Seeing that pyridine is forming a pocket for binding water, we rationalized to synthesize pyridine based molecules with pending arms that could facilitate the formation of water channels and also allow insertion into lipid bilayers. Synthetic procedures were relatively simple with either one or two step reactions, starting from two separate pyridine precursors. (Fig. 57)
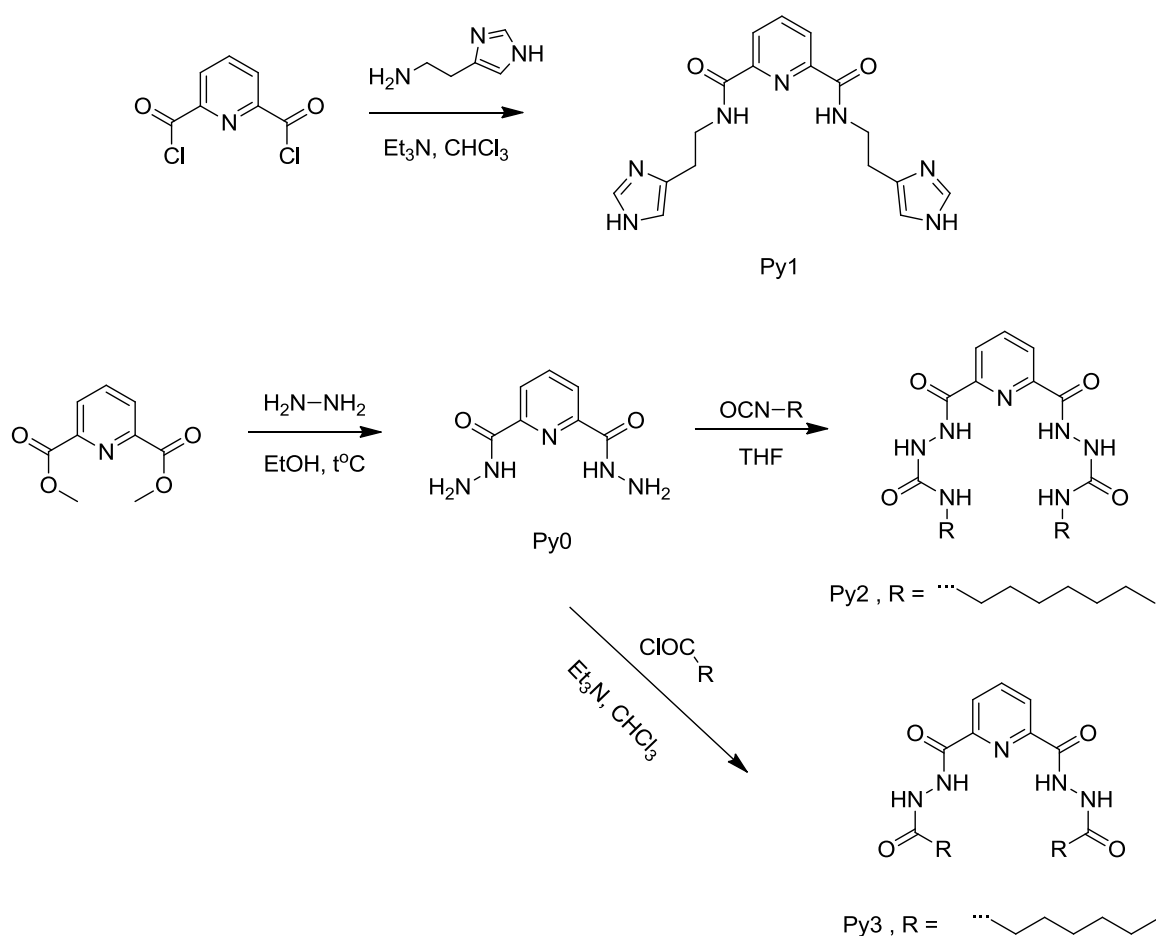
Figure 57. *Synthetic routes for obtaining pyridine based "U-shaped" compounds*

We managed to obtain a single crystal structure for compound **Py1** and indeed the assembly presented a channel-like structure. (Fig. 58)
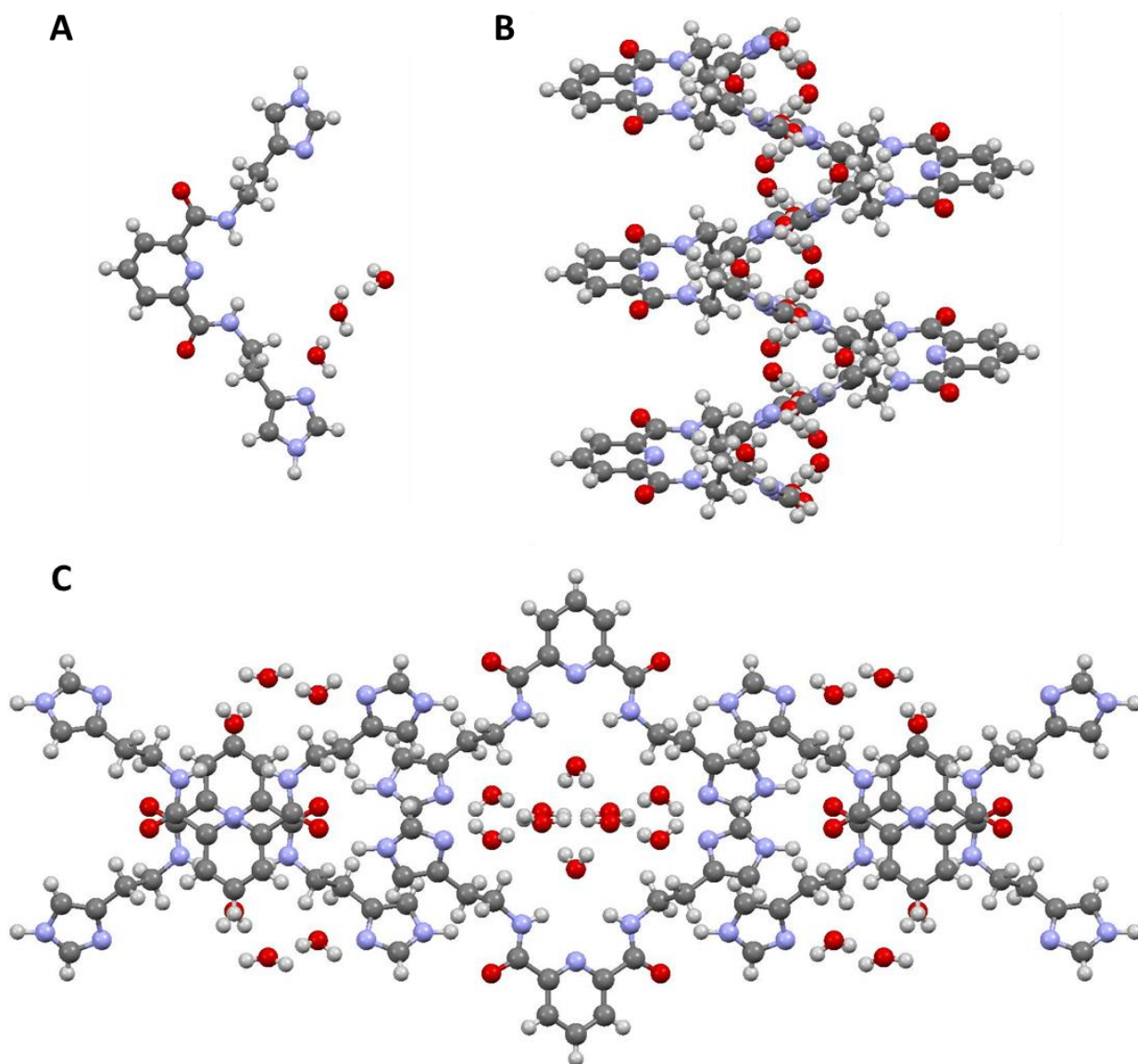
Figure 58. *Single crystal structure of **Py1**: (A) Cell unit, (B) channel-like structure and (C) packing along axis c*

Single crystal X-ray structures. As observed from the solid state structure the water molecules are bound in the pocket formed by the pyridine and the appending imidazole arms. The channels are somewhat intertwined as we can see that the pyridine rings from adjacent channels are protruding into each other, without participating in any hydrogen bonding. Inside the pocket, the water molecules are forming more of a cluster stricter, rather than a water wire, with some disorder being present as one of the water molecules has 2 different hydrogen bonding networks in alternating planes. The crystals were obtained from both pure water solutions and salt solutions. The absence of ion binding confirms that a favorable donor-acceptor network can induce selective binding towards water molecules.

The other U-shaped molecules didn't produce any crystals suitable for X-ray crystallography. This could be mainly due to the presence of the alkyl chains which can be the cause of the disorder.

Although the compounds were tested for water transport using the stopped flow setup, none of the compounds proved to be functional when integrated into vesicles. In the case of compounds **Py1**, this can be explained by the fact that the molecule is too hydrophilic, making it incompatible with the lipid environment of the bilayer. As for the compounds with alkyl arms, we encountered difficulties when tried for insertion as the compounds seem to prefer forming aggregates rather than insert into the bilayer.

3.4 Tetraazadodecane compounds

Synthetic Design. Following up on a similar strategy of using nitrogen-based adducts, we proposed the use of macrocyclic molecules capable of self-assembling into channel-like structures in the presence of hydrophobic environments such as lipid bilayers. 1,4,7,10-tetraazadodecane tetraacetic acid based compounds have been used as contrast MRI agents, especially when binding lanthanides, [91–93] but have never been tested for their transport capabilities across lipid bilayers. The compounds were obtained through a one-pot reaction by conducting a simple amide formation reaction between the azadodecane acid and the respective amine. (Fig. 59)
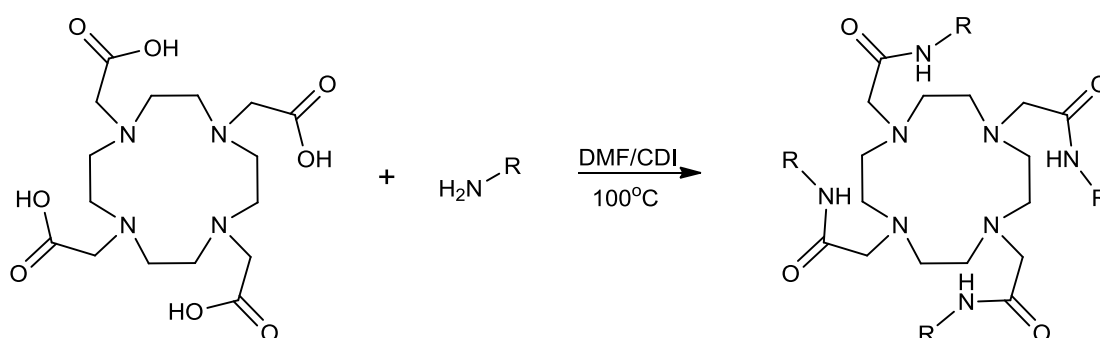
DOTA4, R = butyl
DOTA6, R = hexyl
DOTAs6, R = *s*-hexyl
DOTA8, R = octyl

Figure 59. *Reaction scheme for obtaining DOTA4-8 compounds*

The design of the molecules includes three different functional sections. Starting from a tetra aza crown as core adduct for water binding, followed by a lateral/peripheral section rich in amidic bonds to provide self-assembly H-bonding motifs and having a surrounding hydrophobic shell, the molecules possess all required structural motifs to mimic a protein in a lipid bilayer. The chosen nomenclature for this series of compounds is based on the central cyclododecanetetraza core, using the terminology of DOTA$_x$, with X representing the length of the alkyl chains. Where chiral chains were used, the denominator R or S are used, denoting the respective chirality of the alkyl chains.

Single crystal X-ray structures. The compounds have a remarkable tendency to crystallize, obtaining single colorless crystals by slow evaporation from CHCl$_3$ and DMF solutions or overnight from a sealed solution of DMSO. Regardless of the solvent, the obtained crystal structures of **DOTA4**, **DOTA6** and **DOTAs6** show a quasi-helical stacking of the molecules on one axis, while **DOTA8** is showing a parallel arrangement with hydrogen bonding along a single axis. (Fig. 60 C) In the case of butyl and hexyl chains, we observe a

wrapping of the molecules which basically generates columns of stacked molecules with alternating hydrophobic/hydrophilic sides. The stacks stacked structure then aligns on the hydrophilic side through lateral hydrogen bonds, creating parallel hydrophobic layers. (Fig. 60 F) Hypothesizing that an amplified chiral organization at the supramolecular level could be obtained, we synthesized **DOTAs6** by using chiral arms for the hydrophobic chains. Although no significant changes could be observed, the chiral information translated into the solid state packing by producing antiparallel stacking along the a axis in the single crystal structures. The single cell units are presented in the experimental part.
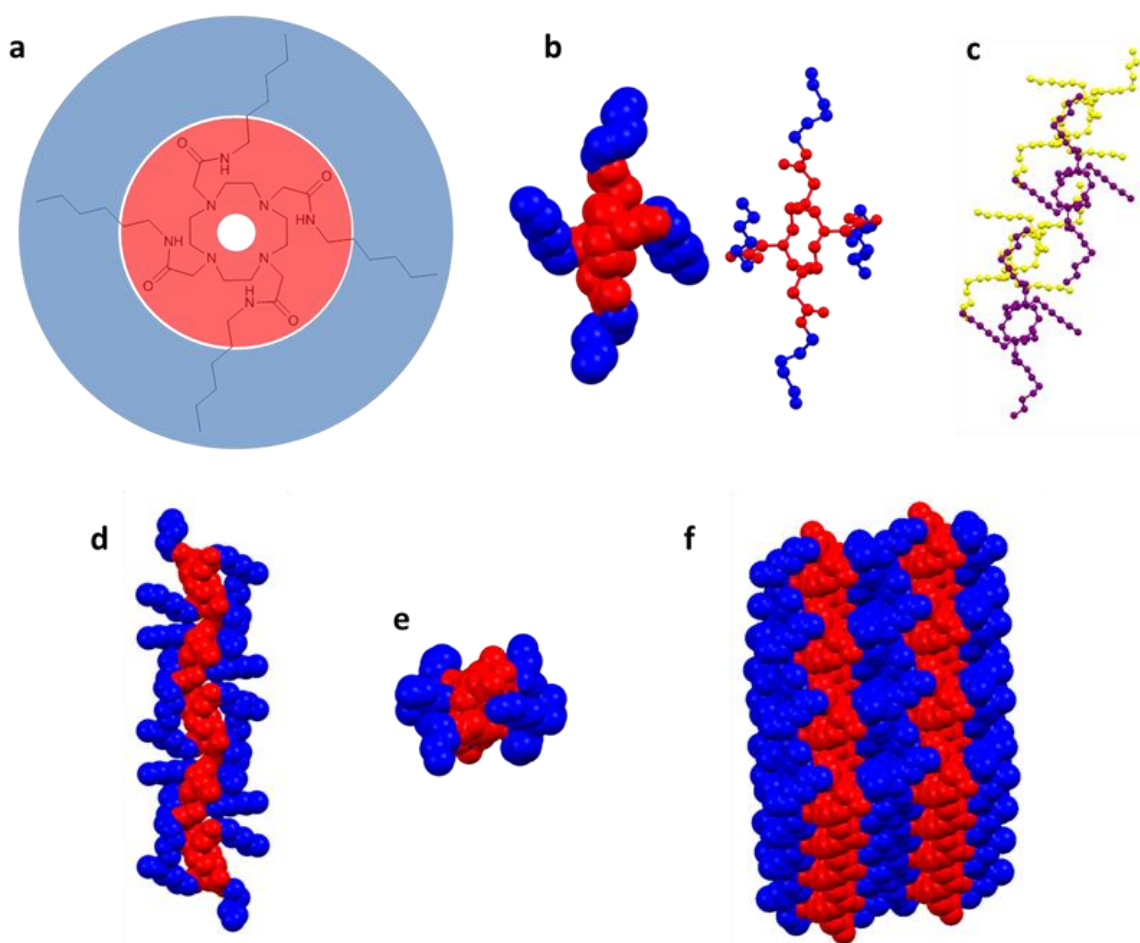
Figure 60. *a) hydrophobic core (blue)/hydrophilic shell (red) of **DOTA6** b) crystal structure of single molecule represented via space fill and ball and stick c) quasi-helical coiling of alternating molecules d) stacking of molecules along the c axis e) view along the b axis f) packing of alternating hydrophobic layers (hydrogen atoms are omitted for clarity)*

NMR experiments. To describe the compounds and monitor the behavior of the molecules in solution, we studied the DOTA molecules using solution NMR experiments. By analyzing **DOTA6** in CDCl3 we found that depending on the concentration, different sets of signals were present in the NMR spectra. (Fig. 61) Starting from a high concentration we can observe only a single set of signals for all protons of the compound. As successive dilutions

were applied the signals specific to the amidic protons, the protons from the methylene group adjacent to the crown as well as the protons from the crown itself start decreasing while a similar set of signals start to appear at a higher field. After reaching a sufficiently diluted solution the first set of signals disappears entirely. This is suggesting the presence of two different states of the molecule, with the high probability that at high concentration there is an intermolecular interaction present causing the organization of the molecules in a certain way, while at low concentration the molecules are most probably present in a monomeric state. Interestingly the signals given by the protons on the alkyl chains are not shifting at all. This could suggest that the interactions are taking place only at the level of the amidic bonds, likely producing tubular assemblies which would also explain the shift of the signals for the protons on the crown as they become more shielded inside the assembled tube.
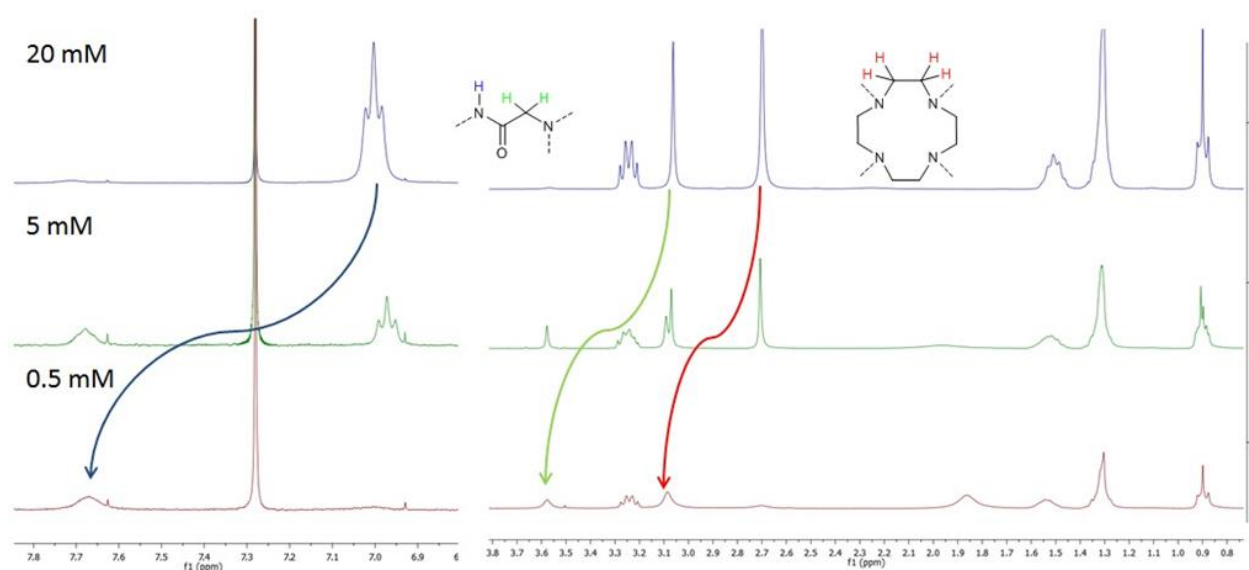
Figure 61. ^1H NMR in CDCl3 of **DOTA6** at different concentrations

Water transport activity. In order to assess the water transport ability of the compounds across lipid bilayer as a model system, we monitored the size change of lipid vesicles by Light scattering/ Stopped flow experiments. Vesicles with a mean diameter of 100 nm were prepared from a mixture of POPC:DOPS:Chol = 4:1:5 molar ratio. The hydration of the vesicle was done with a 200 mM sucrose solution while the hyperosmotic shock was induced by mixing with an equal volume a 400 mM sucrose solution. Prior to each 20 μL DMSO solution of the compounds was added to 2 ml of vesicle solution followed by mixing with a hyperosmotic solution. When comparing the compounds we found that **DOTA6** was the most efficient, while **DOTA4** and **DOTA8**, the first one having a shorter and the other a longer alkyl chain, were not as efficient. (Fig. 62) This suggests that the hydrophobic chain length plays in an important role in the stability and the optimal insertion of the assemblies in the lipid bilayer. A too short chain may not be sufficient for the insertion while a long chain may cause sterical hindrance and disorder when in the presence of the lipids.
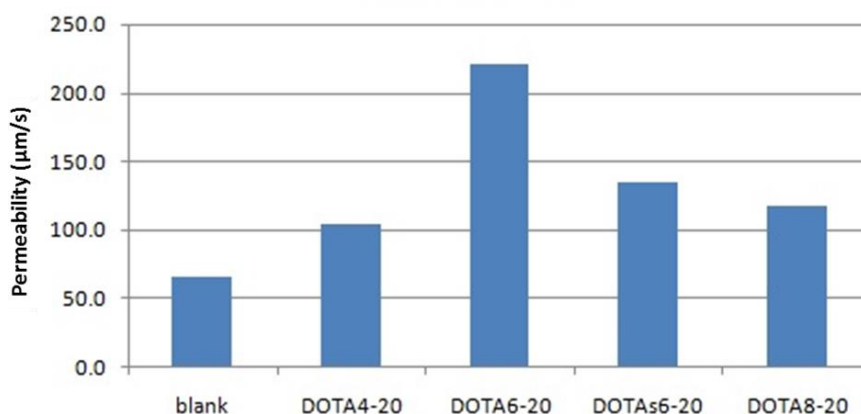
Figure 62. *Permeability of the lipid bilayer in presence DOTA compounds at 20 mM concentration*

When different concentrations of **DOTA6** were used for the insertion into the vesicules we noticed an extremely interesting behavior. At low concentrations, the vesicules went through a consecutive shrinking and swelling process, while at higher concentrations the increase in permeability became exponential (Fig. 63).
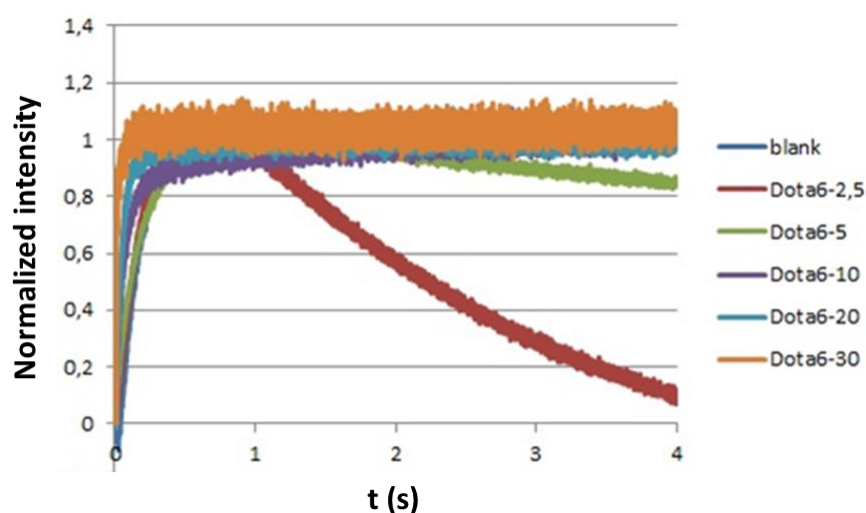
Figure 63. *Light scattering traces of vesicles in the presence of a positive osmotic shock when using different concentrations (mM) of **DOTA6***

This is suggesting that the formation of the channels is highly concentration dependent. The fact that at low concentrations there is a swelling of the vesicles means there is a transport of sucrose back into to vesicles. This behavior was observed in previously reported results on stopped flow experiments with modified aquaporins.[94] As for the higher concentrations, the permeability of the vesicles increases over 10 folds with increasing the concentration of the injected compounds solution from 20 to 30 mM, achieving astonishing permeability of up to 3695 µm/s without observing the re-swelling effect.

Patch-clamp experiments. Considering that re-swelling phenomenon happens only at low concentrations we proposed that, possibly when bellow the critical concentration

limit needed for the compounds to form channels across the lipid membrane, the compounds act as disruptors for the bilayer, creating large pores allowing the passage of sucrose back into the vesicles. For this, bilayer clamp study was performed in order to gather insight into the transport behaviors and pore formation. Briefly, a bilayer patch-clamp experiment consists in a 2 chamber setup, separated by a wall containing a single micro-scale pore (150 µm). (Fig. 64) A single lipid bilayer is painted on one side of the pore. The chambers contain electrodes and various electrolyte solutions. By applying a difference in potential between the chambers, the flow of current can be followed across the bilayer. In the absence of an electrolyte transport, there is no registered current flow.
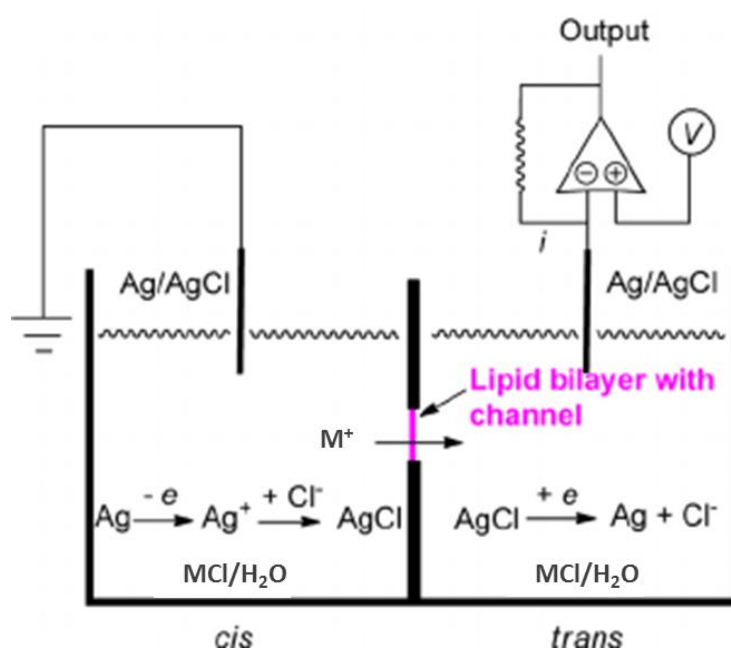
Figure 64. *Schematic of a bilayer patch clamp setup*

Experiments were done using potassium chloride as an electrolyte. After formation of the bilayer and 15 to 20 min membrane resistance test, 5 µL of a 20mM solution of **DOTA6** was added. After 10 minutes, in the absence of any activity, 10 µL of the same solution was added. After the later addition, bilayer broke and was reformed by dipping. We believe that this dipping manipulation helped the compound to get within the bilayer since it was followed, after 3 minutes, by an onset of activity. Activity begins with long-lived clear top-square openings and is rapidly mixed with multimodal activity. (Fig. 65)
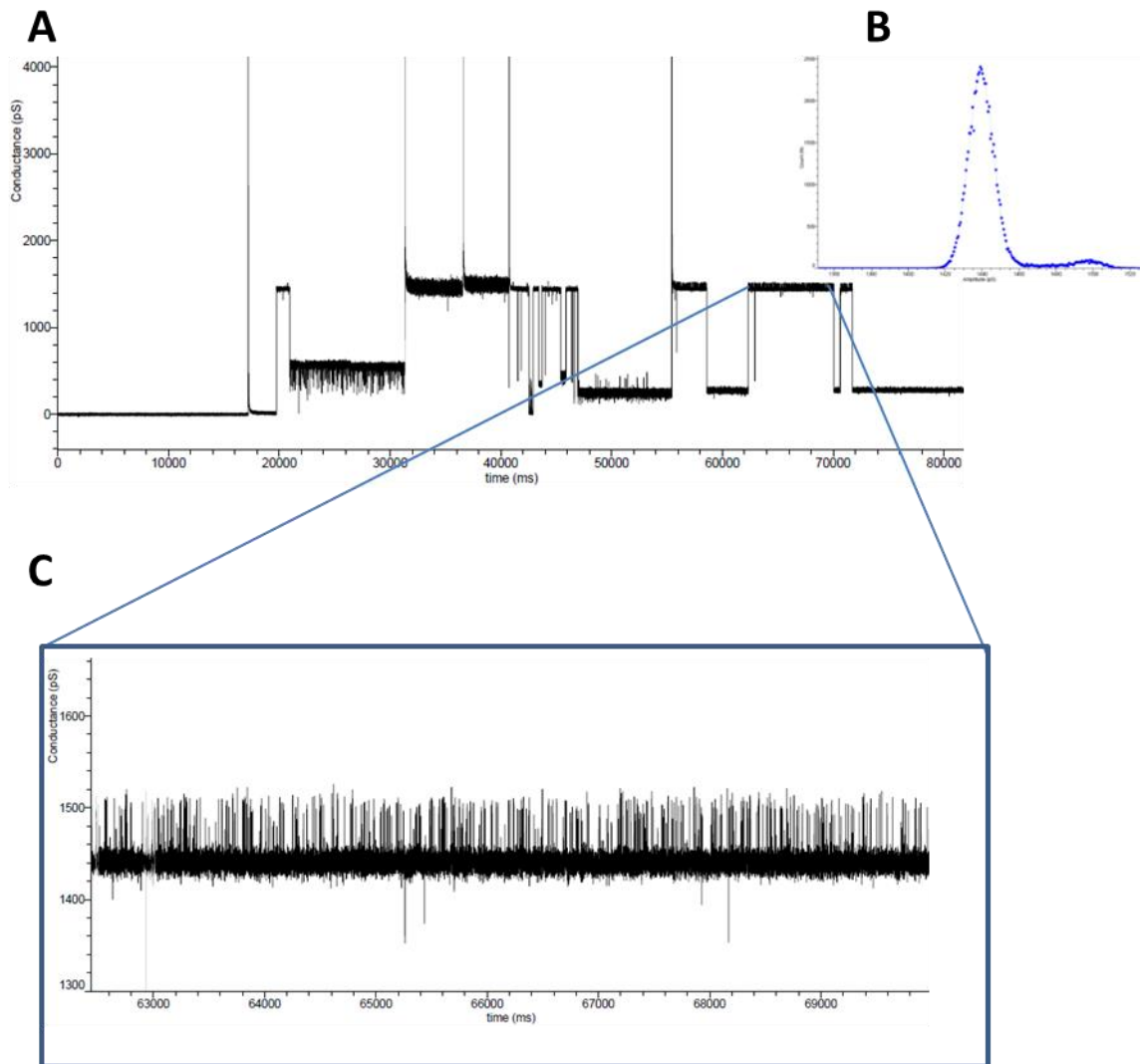
Figure 65. *Registered conductance variation across flat sheet lipid bilayer under addition of Dota6. (A) Multimodal behavior; (B) conductance histogram and narrow Gaussian fit; (C) Flickering activity between two open states*

These experiments revealed that there are multiple conductance levels, supporting the multimodal behavior. All of these conductance levels are quite narrow. Our hypothesis is that the different opened or closed states are highly influenced by the incorporation or ejection of one or more molecules, which make the pore larger or narrower, respectively. Thus, a large variety of high conductance levels has been detected, ranging from 300 pS up to 2500 pS for the stable channels. But the most observed channels were around 1000 pS. These channels were mostly long living opened states, from 30 ms for the shorter ones (rare) to 5 minutes. The average opening time lies between 5 to 10 seconds. Besides, flickering activity was detected in almost all opened states (Fig. 65) and is probably linked to morphological fluctuations of these large pores, since these fluctuations are only detected among large opening states. The detectable flickering activity was between 1 to 10 milliseconds opened (or closed) state with a conductance level of ca. 55 pS.

According to the conductance levels of these large pores, the corrected Hille equation[95] gave pore diameter ranging from 9 to 28 Å. Most of these pores have a diameter around 20 Å. If the flickering activity is a change in channel conformation, then that means there is a change in diameter between 0.4 and 2.4 Å and correspond to a variation in diameter of 2 to 20 % (calculated from the initial pore size to the final pore size). If this activity is coming from a real open or closed pore, then the diameter of this pore would be around 3.8 to 7.3 Å: this would be unlikely, considering that this flickering activity only happened when bigger pore are in their opened state, and thus would be linked with their morphological fluctuations.

Following all these results we proposed a self-assembly mechanism for the formation of the pores. As the molecules assemble, following a lateral hydrogen bonding, the most probable structure adopted in the lipid bilayer is a tubular shape which can easily be adopted from the parallel hydrophobic sheets that are present in the crystal structures. Adopting such a structure will be highly preferential for a better compatibility of the hydrophobic region of the assemblies with the hydrocarbon chains of the lipids in the bilayer. (Fig. 66) This mechanism is also in good agreement with bilayer clamp studies that shows that this "adaptable" superstructure has a preferential conformation/ composition (top square activity is representative of well-defined and stable structures), but is also slightly adapting its structure (incorporation or rejection of molecules) in order to remains as stable as possible. This last behavior is highlighted by the flickering and also the multiple conductance levels observed during bilayer clamp experiment.
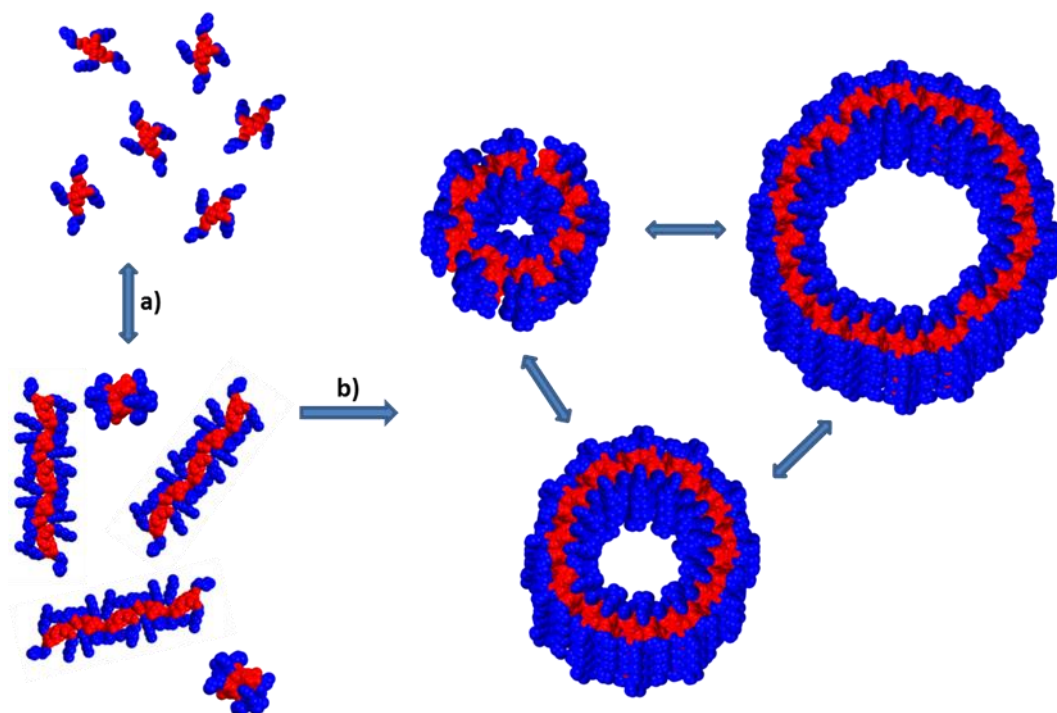
Figure 66. *Proposed self-assembly processes: a) stacking initiation after injection into water solutions b) pore formation after insertion into the lipid bilayer*

Molecular dynamics simulations. Analysis of self-assembling molecular dynamic simulations starting from fully random mixtures of DOTA8/POPC/water/ions revealed the formation of DOTA aggregates in phospholipid membrane environments. It was clear that DOTA molecules preferred to "stay together" but still, with no phase separation. Stacks of two DOTA molecules could be identified which seems to strongly interact as they move together as a whole (i.e. the central ring and the nearby -NH-CO- moieties of the adjacent molecules display collective motions). The central cycles were arranged in a parallel orientation and the inter-molecular interaction was strengthened by H-bonds formed between -N-H groups of one DOTA molecule and the -C=O group of the next molecule (Fig. 67).
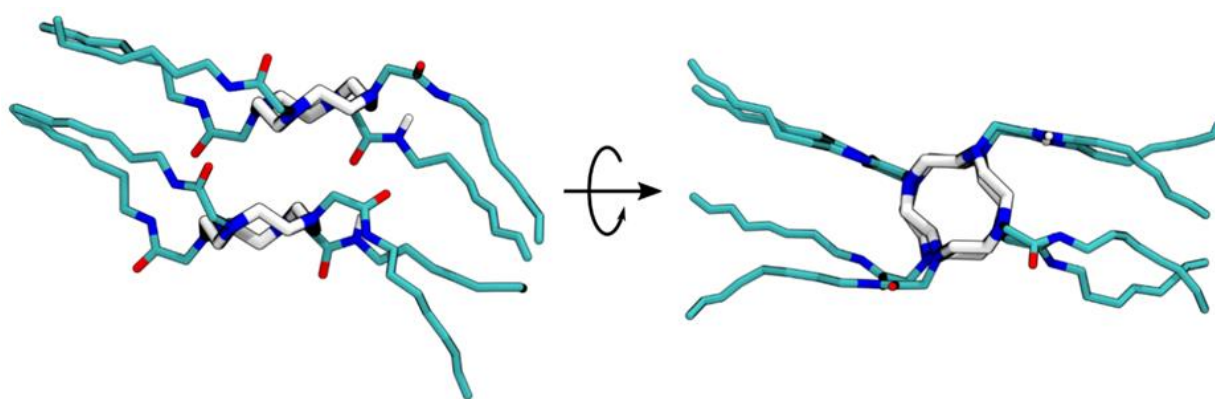
Figure 67. *Self-assembly of two **DOTA8** molecules in a POPC membrane, extracted from the simulations of random mixtures of DOTA/POPC, lipids were removed for clarity.*

This stable arrangement may favor the formation of stacks composed of several DOTA molecules with a proper dimension to completely cross the membrane from one face to the other. This could provide a pathway for water permeation. In order to study the stability of such assemblies and water passage along them we constructed stacks of 6 DOTA8 molecules and inserted them in POPC membranes. The number of DOTA molecules had been chosen on the basis of a hydrophobic match between the POPC bilayer core and the stack. (Fig. 68)
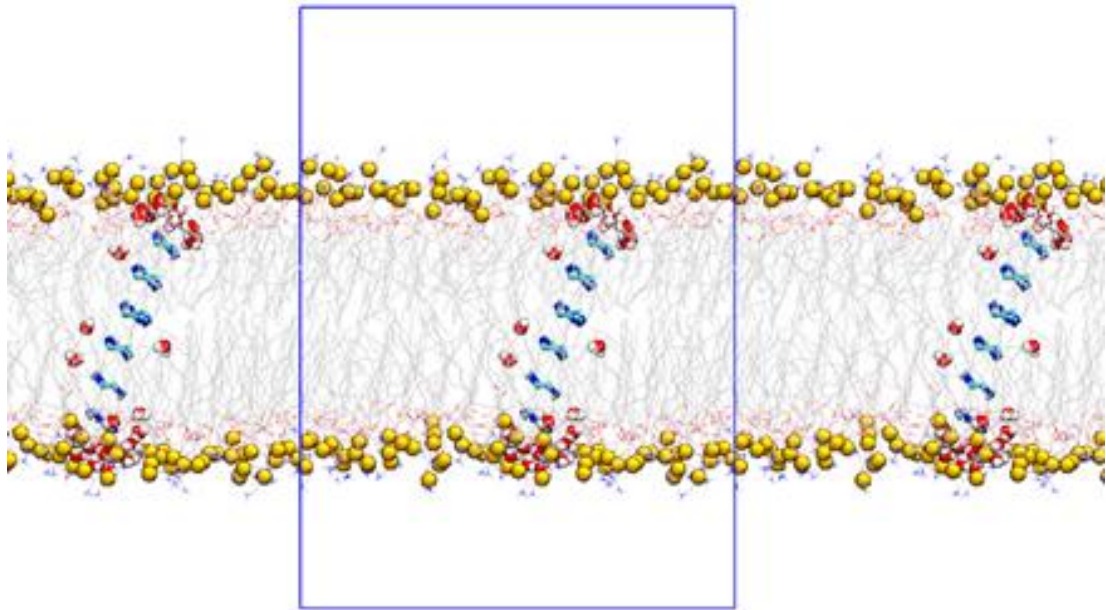
Figure 68. *Snapshot of the simulated system at the end of a 1 μs simulation for which stacks of 6 **DOTA8** molecules were inserted in POPC; the alkyl tails of **DOTA8** molecules were removed for clarity; phosphorus atoms of POPC have been represented as yellow spheres*

Very good conservation of the stacked configuration could be observed even after 1 μs of simulation within the membrane environment. Alkyl tails of DOTA prefer to align in a parallel configuration and also parallel to the membrane plane. (Fig. 69)
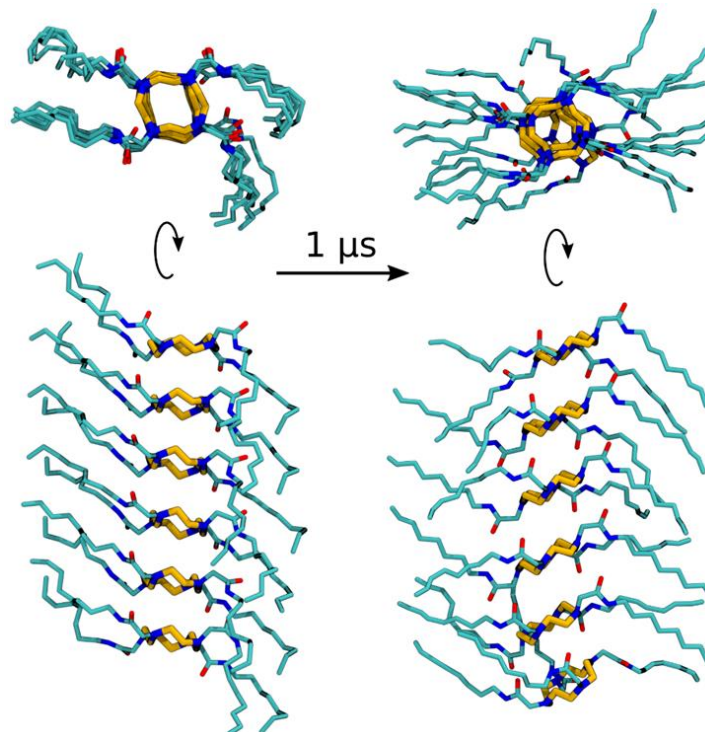
Figure 69. *Snapshots of the 6 **DOTA8** stack at the beginning and at the end of the simulation.*

Some water molecules can be found in the vicinity of the central ring of the DOTA molecules. The water density map shows that the molecules are not forming a connected

network across the bilayer. (Fig. 70) They are rather localized around the hydrophilic moieties of the **DOTA8** compounds, although jumping from DOTA ring to another has been observed.
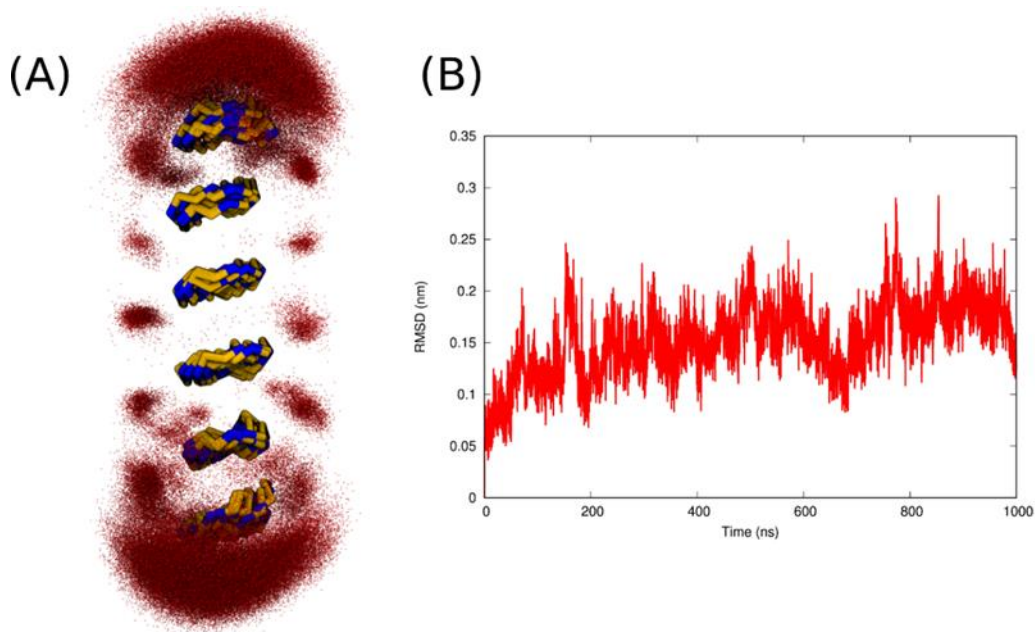
Figure 70. (A) - *Water density around the DOTA central ring stack. Water oxygen atoms were represented as red dots overlaid for multiple frames during simulation. (B) – RMSD of DOTA stack with respect to the starting configuration.*

In order to see if an increase in water translocation could be achieved, two columns of **DOTA8** stacks were placed in the bilayer in close vicinity. A 300 µs long simulations have shown that the stacks remain parallel towards each other and create a channel like structure within the space between the two stacks. (Fig. 71)
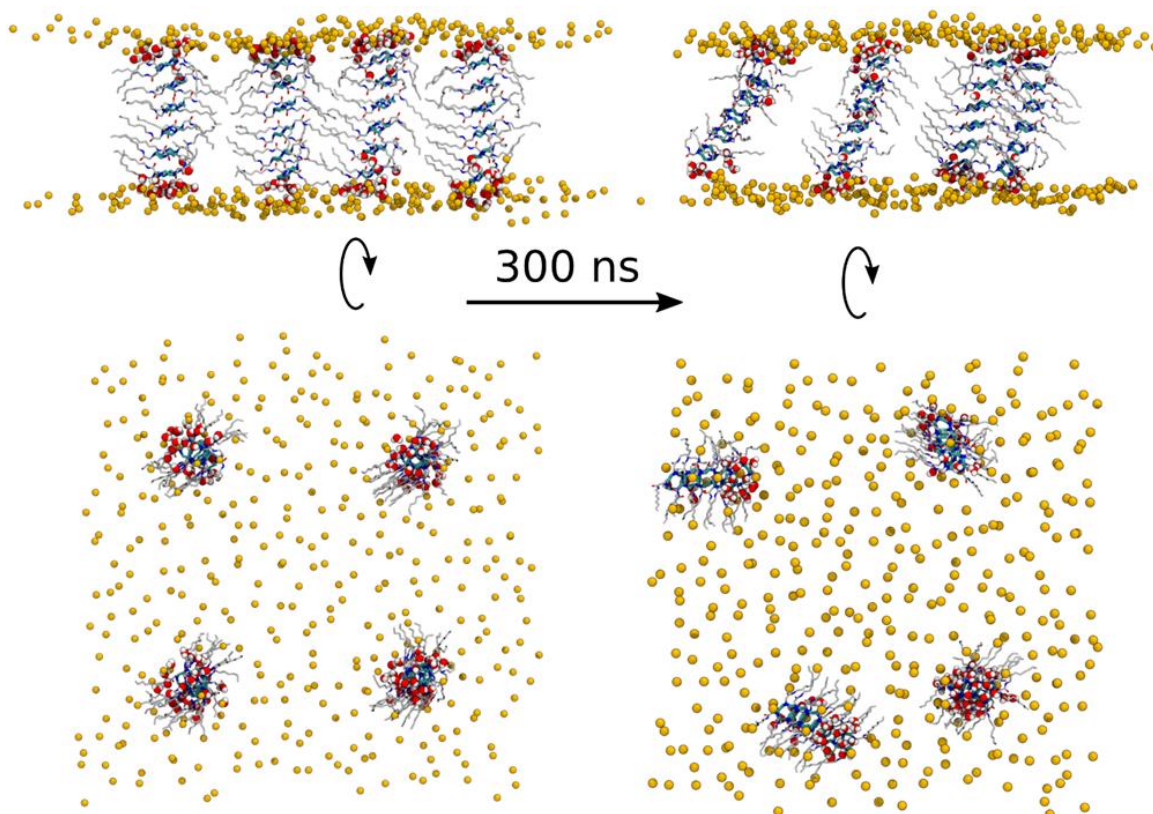
Figure 71. *Snapshots of the **DOTA8** stacks at the beginning and at the end of the simulation.*

Very good conservation of the individual stacked configurations could be seen after 300 ns of simulation within the membrane environment. When having two adjacent stacks water diffuses more freely from one side of the bilayer to the other, being in an interconnected hydrogen bonding network. (Fig. 72)
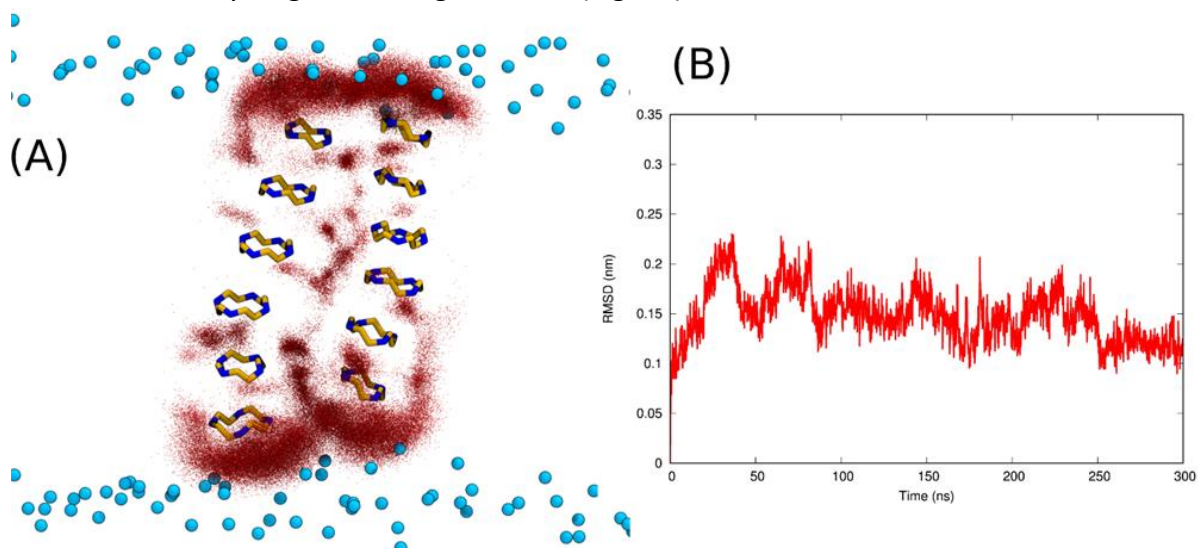
Figure 72. (A) *Water density around the **DOTA8** stack in simulation 2DOTA. Water oxygen atoms were represented as red dots overlaid for multiple frames during simulation; phosphorus atoms of POPC colored in light blue. (B) – RMSD of DOTA stack aggregate with respect the starting configuration.*

Curiously the simulations have shown no salt transport in these channels formed between the stacks. This is in disagreement with the results obtained from the patch clamp experiments which proved that there is indeed ion transport in the presence of the compound. An explanation for this could be that the two stacks system used for the simulation may not be complex enough to undergo the formation of a pore-like structure in the lipid bilayer. Increasing the number of stacks present next to each other is a proposed experiment for future simulations, and it is expected to shed more light on the formation of more complex channels.

3.5 Triarylamine compounds

In the framework of a collaboration with Prof. Nicolas Giuseppone from Institut Charles Sadron, a rather special design was proposed based on the use of triarylamines (TAAs) as stacking motifs and the use of carboxyl groups as hydrophilic headgroups. Triarilamines have been shown to form interesting supramolecular structures and physical properties.[96–98] TAAs possess a rather interesting supramolecular behavior. When correctly functionalized, molecules with TAA cores are capable of self-assembling into columnar nanowire architectures. (Fig. 73)
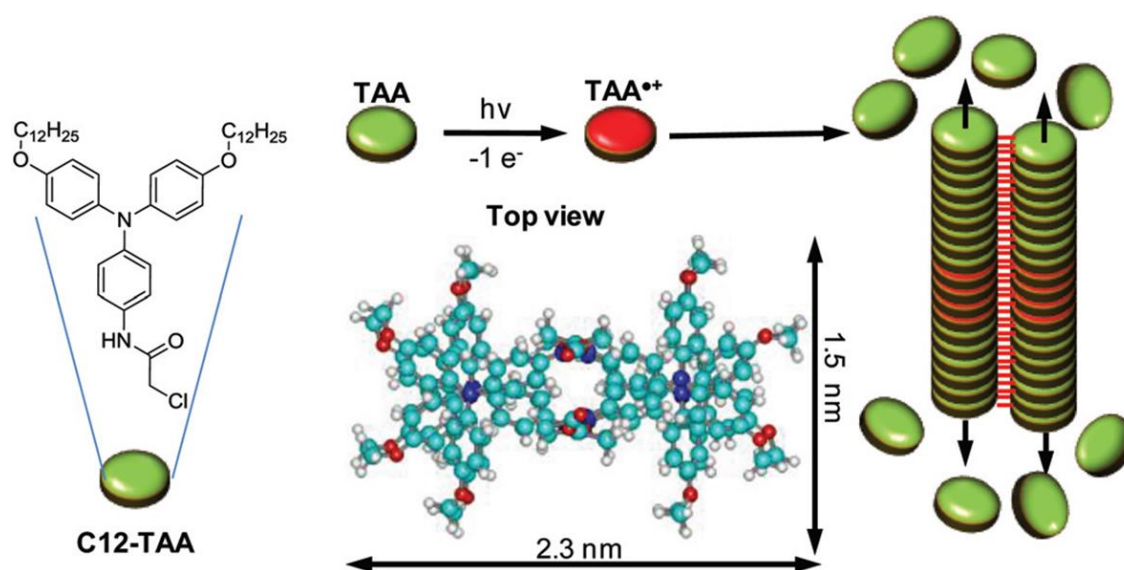
Figure 73. *Simplified supramolecular polymerization process of triarylamine nanowires (alkyl chains omitted for clarity)Image adapted from reference* [98]

TAA molecules are susceptible to oxidation by light irradiation in chlorinated solvents. The formation of a positively charged TAA leads to a nucleation/growth mechanism of the self-assembly in which TAA radical cations stack with their neutral counterparts to produce double columnar fibrils that contain charge transfer complexes. A top view of the characteristic molecular packing between 4 TAA molecules is represented to illustrate the dimensions of a fibril section.

Design. With this collaboration, we proposed to exploit the easily formed columnar stacks of TAA compounds and use them as a scaffold for the formation of bilayer spanning channels. The strategy for the design of the molecule was based on the dimeric nature of the stacked columns. We intended to preserve the dimerized nature of the supramolecular assembly but at the same time, a moiety capable of hydrogen bonding with water was necessary. Thus we proposed to use carboxyl functionalized TAAs. The synthesis of the compound is according to a previously reported method[96] and was done by our collaborators. (Fig. 74)
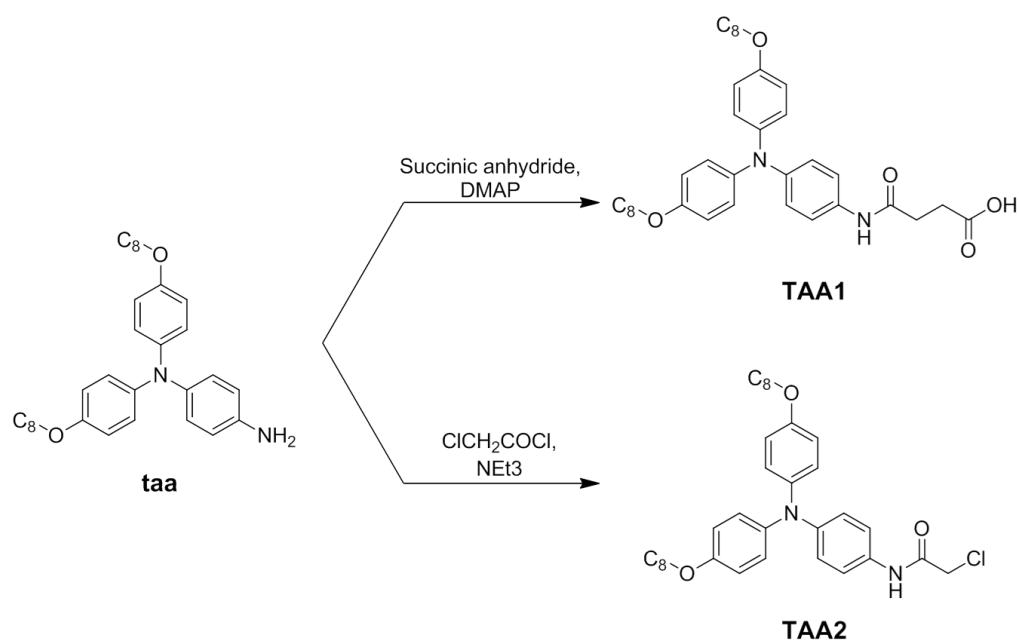
Figure 74. *Synthetic routes for obtaining TAA compounds*

Self-assembly studies. The self-assembly nature of the compound **TAA1** was proved through ^{1}H-NMR and UV-VIS experiments. The self-assembly can be followed by the disappearance of the aromatic and adjacent signals in the NMR spectra of the compound when exposed to visible light irradiation in a $CDCl_3$ solution. (Fig. 75)
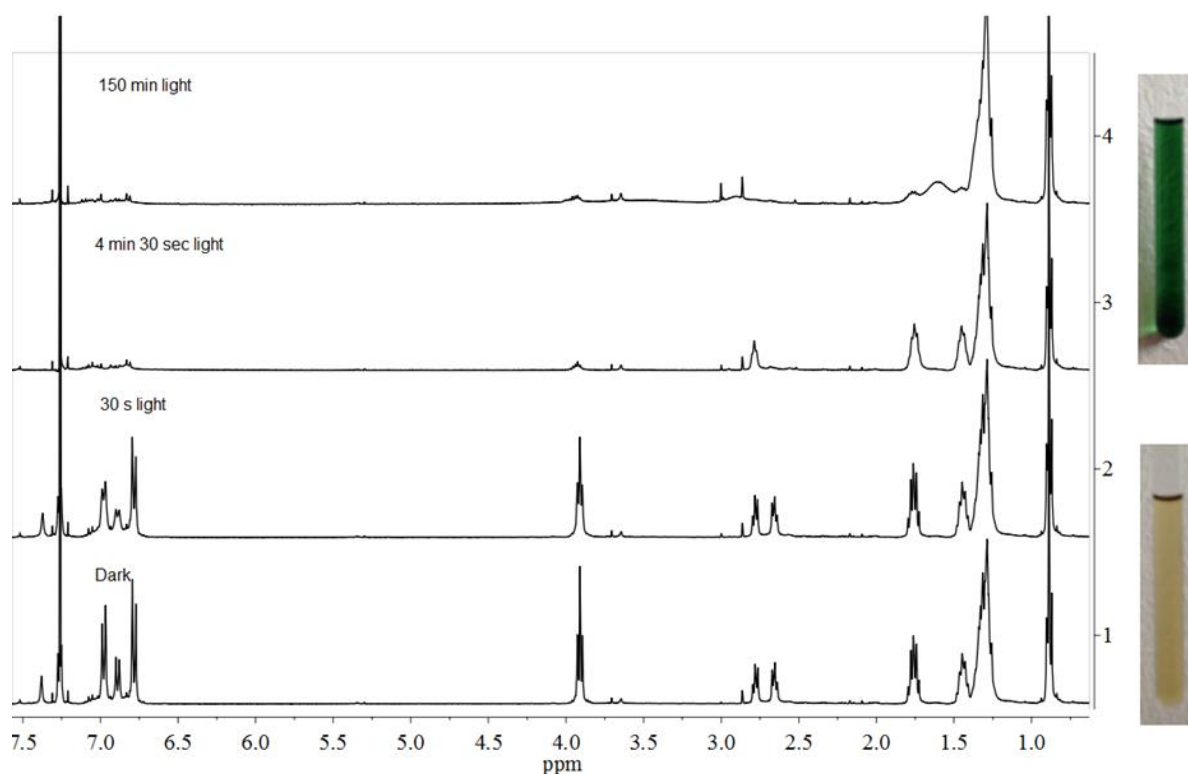
Figure 75. *Change in ^{1}H-NMR during light irradiation of a 1mM $CDCL_3$ solution of compound **TAA1**.*

The disappearance of the signal is mainly due to the self-association/delocalization process that takes place when the columnar assemblies start to form. The self-assembled structures are stable indefinitely in chlorinated solutions, even when kept in dark. In order to induce dissociation, the solution needs to be heated at $60^{\circ}C$ overnight in dark. When assessed if the structures remain stable in non-chlorinated solvents, we found that the supramolecular structures disassemble after approximately 2h. The induced change in color can be followed through the change in UV-Vis absorption of the $CDCl_3$ solution. (Fig. 76)
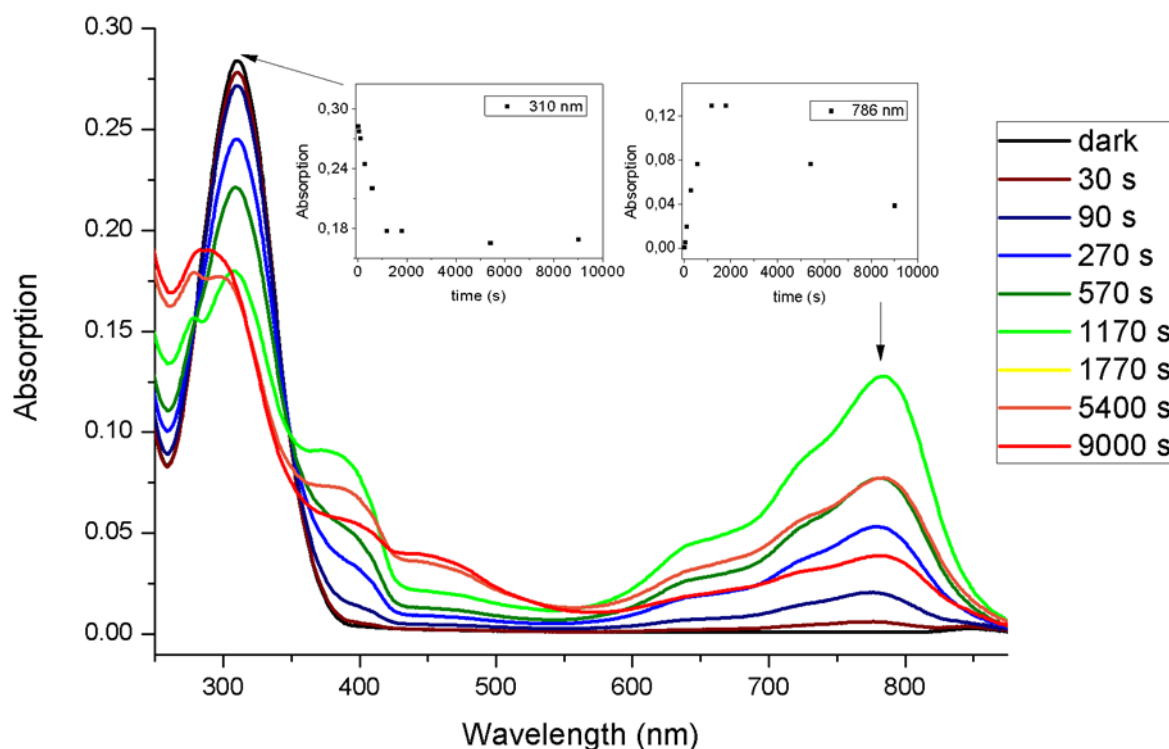
Figure 76. *UV-Vis spectra during light irradiation of a 0.1 mM chloroform solution of TAA1*

Water transport activity. Hoping to observe a water transport based on light activation, we prepared vesicles and injected **TAA1**, exposing the solutions to visible light irradiation and measuring the permeability. What we observed was that the compound did indeed induce an increase in permeability of the vesicles in time, but control experiments proved that the increase is independent of irradiation. (Fig. 77)
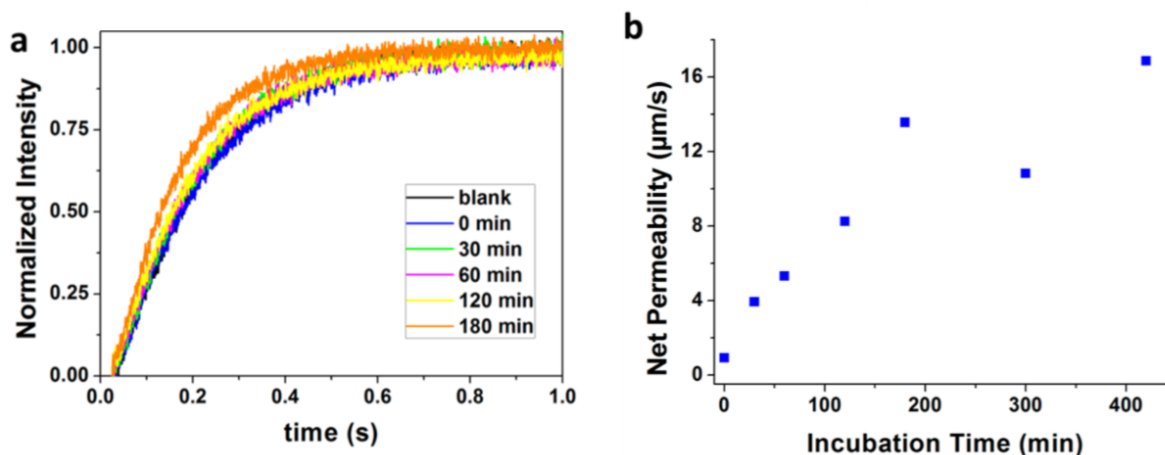
Figure 77. *(A) stopped flow traces for **TAA1** at various incubation times; (B) net permeability variation in function of incubation time*

Until 180 min of incubation, net permeabilities increase almost linearly, reaching permeability values about 13 μm/s, which is approximately a 25% increase of the permeability compared to the background transport of vesicles in the absence of **TAA1** and a 15 times larger permeability in the case of using **TAA1** but without incubation. When incubated for longer times, the permeability goes as high as 17 μm/s. This suggests that the evolving channel formation might be related to a relatively slow self-assembly process within the bilayer membrane. The fact that permeabilities change slightly between 180 and 420 min might be attributed to the fact that the channels reach a stabilized form. As a negative control, we tested **TAA2** but could not observe any induced permeability up to 420 min of incubation. This suggests that the carboxylate groups are responsible for the transport phenomena. Unfortunately, crystallographic data is unavailable for this compound. The presence of long alkyl chains causes a lot of disorder when crystallizing the compound, making it difficult to obtain single crystals from the compound.

In summary, we have proved that TAA cores can be used as scaffolds for the design of lipid bilayer spanning channels that induce water translocation. Although the mechanism remains a mystery, the use of TAA cores remains an option for future designs of water channels.

3.6   Experimental

3.6.1   Synthesis and structural characterizations

General synthesis for DCx compounds

In a general synthesis, 10 mmol of amine bearing compound has been suspended in 10 ml THF. The solution was brought to boiling point and 1 equivalent of the respective isocyanate was added, leaving it to react for 3h under reflux. The solution is left to cool down to room temperature and the obtained white precipitate is filtered and washed with 3 aliquots of 5 ml THF. The precipitate is then dried under low-pressure vacuum to afford the respective compounds as a white flaky compound. The average yield varies between 95-99%.

1-(1,3-dihydroxypropan-2-yl)-3-hexylurea - DC6: ^{1}H NMR (300 MHz, DMSO): δ (ppm) = 0.87 (br, 3H,); 1.24-1.35 (br, 8H,); 2.95 (q, 2H, J=6 Hz,); 3.41 (m, 4H,) 3.48 (m, 1H,) ; 4.62 (t, 2H, J=6 Hz,) 5.62 (d, 1H, J=6 Hz,) ; 5.99 (t, 1H, J=6 Hz,); ESI+-MS: MS: m/z (%): 219.6 (100) [DC6 + H], 241.6 [DC6 + Na], 460 [2*DC6 + Na].

1-(1,3-dihydroxypropan-2-yl)-3-octylurea - DC8: ^{1}H NMR (300 MHz, DMSO): δ (ppm) = 0.86 (br, 3H,); 1.25-1.35 (br, 12H,); 2.95 (q, 2H, J=6 Hz,); 3.41 (m, 4H,); 3.48 (m, 1H,); 4.62 (t, 2H, J=6 Hz,); 5.60 (d, 1H, J=6 Hz,) ; 5.95 (t, 1H, J=6 Hz,); ESI+- MS: m/z (%): 247.6 (100) [SDC8 + H], 269.7 [SDC8+ Na], 516.2 [2* SDC8+ Na].

(S)-1-(1,3-dihydroxypropan-2-yl)-3-(octan-2-yl)urea - SDC8: ^{1}H NMR (300 MHz, DMSO): δ 0.86 (t, J=6 Hz, 3H), 0.97 (d, J=6 Hz, 3H), 1.17-1.28 (m, 10H), 3.34-3.56 (m, 6H), 4.62 (t, J=6 Hz, 2H), 5.56 (d, J=6 Hz, 1H), 5.84 (d, J=9 Hz, 1H) ppm; MS: m/z (%): 247.6 (100) [SDC8 + H], 269.7 [SDC8+ Na], 516.2 [2* SDC8+ Na].

(R)-1-(1,3-dihydroxypropan-2-yl)-3-(octan-2-yl)urea - RDC8: ^{1}H NMR (300 MHz, DMSO): δ 0.86 (t, J=6 Hz, 3H), 0.97 (d, J=6 Hz, 3H), 1.19-1.32 (m, 10H), 3.34-3.56 (m, 6H), 4.62 (t, J=6 Hz, 2H), 5.56 (d, J=6 Hz, 1H), 5.84 (d, J=9 Hz, 1H) ppm; MS: m/z (%): 247.6 (100) [RDC8 + H], 269.7 [RDC8 + Na], 516.2 [2* RDC8+ Na].

Py0 synthesis

Dimethyl 2,6-pyridinedicarboxylate (1g) was suspended in 5 ml of 1:1 EtOH/NH2-NH2 v:v ratio. The solution was stirred under reflux for 12h. The obtained white precipitate as filtered and washed with EtOH, followed by drying to afford Py0 with an average yield of 95%.

Py1 synthesis

2,6-Pyridinedicarbonyl dichloride (1 Eq) was dissolved in $CHCl_3$ and cooled to 5^oC. Triethylamine (2 Eq) and the histamine (2Eq) were added to the solution and left to stir for 1h. The solution was then left to warm up to room temperature. The solution was then washed using a saturated $NaHCO_3$ solution and the organic solvent evaporated. The obtained powder was then triturated with EtOEt to afford the final product. Average yield 50-60%.

Py2 synthesis

Py0 (1 Eq) was then suspended in THF and octylisocyanate (2 Eq) was added. The solution was left to stir under reflux for 12h. The organic solvent was then evaporated and the obtained solid was washed with EtOH and AcCN then dried to afford the final product. Average yield 45-50%.

Py3 synthesis

Py0 (1 Eq) was then suspended in $CHCl_3$ and cooled to 5^0C. Triethylamine (2 Eq) and octanoylchloride (2 Eq) was added. The solution was then left to warm up to room temperature. The solution was then washed using a saturated $NaHCO_3$ solution and the organic solvent evaporated. The obtained powder was then triturated with EtOE to afford the final product. Average yield 50%.

pyridine-2,6-dicarbohydrazide – Py0: ^{1}H NMR (300 MHz, DMSO): δ (ppm) = 4.62 (br, 4H,); 8.3 (br, 3H); 10.63 (br, 2H)ESI+-MS: MS: m/z (%): 195.08 (100) [Py0 + H].

N,N'-bis[2-(1H-imidazol-4-yl)ethyl]pyridine-2,6-dicarboxamide - Py1: ^{1}H NMR (300 MHz, DMSO): δ (ppm) = 3.05 (t, *J*=6 Hz, 4H,); 3.67 (q, *J*=6 Hz, 4H); 7.53 (s, 2H); 8.15 (br, 3H,); 8.95 (s, 2H); 9.91 ESI+-MS: MS: m/z (%): 354.16 (100) [Py1 + H]

2,2'-(pyridine-2,6-dicarbonyl)bis(N-octylhydrazinecarboxamide) – Py2: ^{1}H NMR (300 MHz, DMSO): δ (ppm) = 0.86 (br, 6H,); 1.25 (br, 20H,); 1.36 (br, 4H); 3.01 (m, 4H); 6.49 (t, *J*=6 Hz, 2H); 7.96 (br, 2H); 8.21 (br, 3H); 10.90 (br, 2H) ESI+-MS: MS: m/z (%): 505.34 (100) [Py2 + H].

N'2,N'6-dioctanoylpyridine-2,6-dicarbohydrazide – Py3: ^{1}H NMR (300 MHz, DMSO): δ (ppm) = 0.86 (br, 6H,); 1.29 (br, 16H,); 1.62 (br, 4H); 2.22 (t, *J*=6 Hz 4H,); 8.24 (br, 3H); 9.97 (br, 2H); 10.98 (br, 2H) ESI+-MS: MS: m/z (%): 447.2 (100) [Py3 + H].

General synthesis for DOTAx compounds

Carbonyldiimidazole (8 Eq) and 1,4,7,10-tetraazacyclododecane-1,4,7,10-tetraacetic acid (1Eq) were suspended in of N,N-dimethylformamide (DMF) under N2 atmosphere. The mixture was stirred at 100oC until the solution became a clear orange solution. The respective amine (8.8 Eq) dissolved in a small amount of DMF is then added dropwise and the mixture is left to stir overnight at room temperature. DMF is evaporated using low pressure distillation and the resulting oil is recrystallized using diethylether to afford the product as a white powder. Average yield 55-70%.

2,2',2'',2'''-(1,4,7,10-tetraazacyclododecane-1,4,7,10-tetrayl)tetrakis(N-butylacetamide) - DOTA4 ^{1}H NMR (300 MHz, DMSO) δ (ppm): 0.86 (br, 12H); 1.20-1.37 (m, 8H); 1.30-1.41 (m, 8H); 2.62 (br, 16H) 2.96 (s, 8H); 3.07 (q, 8H, *J*=6 Hz); 7.87 (t, 4H, *J*=6 Hz); MS: m/z (%): 626.20 (100) [DOTA4 + H], 648.19 (70) [DOTA8+Na].

2,2',2'',2'''-(1,4,7,10-tetraazacyclododecane-1,4,7,10-tetrayl)tetrakis(N-hexylacetamide) - DOTA6: ^{1}H NMR (300 MHz, DMSO) δ (ppm): 0.85 (br, 12H); 1.24-1.39 (m, 32H); 2.61 (br, 16H) 2.95 (s, 8H); 3.05 (q, 8H, *J*=6 Hz); 7.88 (t, 4H, *J*=6 Hz); MS: m/z (%): 738.35 (100) [DOTA6 + H], 369.91 (60) [(DOTA6 + 2H)/2], 760.27 (30) [DOTA6+Na].

2,2',2'',2'''-(1,4,7,10-tetraazacyclododecane-1,4,7,10-tetrayl)tetrakis((S)-(hexan-2-yl)acetamide) - DOTAs6: ^{1}H NMR (300 MHz, DMSO) δ (ppm): 0.85 (br, 12H); 1.04 (d, 12H, *J*=6 Hz); 1.23-1.38 (m, 24H); 2.61-2.71 (m, 16H) 2.97 (s, 8H); 3.77 (quint, 4H, *J*=6 Hz); 7.59 (d, 4H, *J*=6 Hz); MS: m/z (%): 738.35 (100) [DOTAs6 + H], 369.78 (80) [(DOTAs6 + 2H)/2], 760.34 (30) [DOTAs6+Na].

2,2',2'',2'''-(1,4,7,10-tetraazacyclododecane-1,4,7,10-tetrayl)tetrakis(N-octylacetamide) - DOTA8: ^{1}H NMR (300 MHz, DMSO) δ (ppm): 0.86 (br, 12H); 1.24-1.41 (m, 48H); 2.61 (br, 16H) 2.95 (s, 8H); 3.05 (q, 8H, *J*=6 Hz); 7.86 (t, 4H, *J*=6 Hz); ESI+-MS: MS: m/z (%): 425.26 (100) [(DOTA8 + 2H)/2], 849.64 (10) [DOTA8+H].

Concentration dependent NMR studies for **DOTA6** were performed through the successive dilution of a 20 mM solution in CDCl3 at 25°C. (Fig. 78)
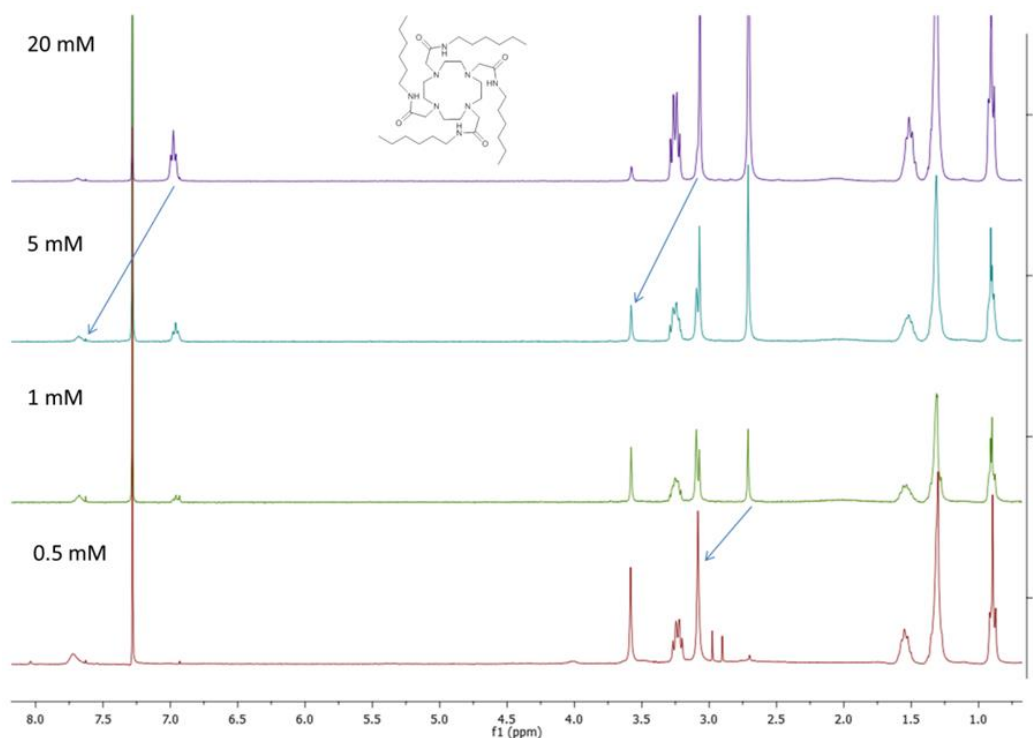
Figure 78. *^{1}H NMR in CDCl$_3$ of **DOTA6** at 0.5 mM, 1 mM, 5 mM and 20 mM*

Synthesis of TAAx compounds

Synthesis for **taa** and **TAA2** have been previously reported.[96]

TAA1: Compound **taa** (1 eq., 200 mg, 0.387 mmol) was reacted in the microwave with succinic anhydride (5.42 eq., 210 mg, 2.1 mmol) and DMAP (7.61 %, 3.6 mg, 0.0295 mmol) in a mixture of toluene (9 mL) and dimethylformamide (1 mL) for 3 hours at 120°C. The solvent was evaporated and the crude mixture was purified in the absence of light by column chromatography over silica gel with DCM/MeOH (39/1) with 1% acetic acid as the eluent. The product was obtained as a grey powder in 80% yield.

4-((4-(bis(4-(octyloxy)phenyl)amino)phenyl)amino)-4-oxobutanoic acid – TAA1 ^{1}H NMR ^{1}H NMR (400 MHz, THF-d8) 0.94 – 0.86 (m, 6H); 1.42 – 1.24 (m, 16H,); 1.53 – 1.41 (m, 4H); 1.80 – 1.68 (m, 4H); 2.63 – 2.45 (m, 4H); 3.90 (t, J = 6.4 Hz, 4H); 6.79 – 6.73 (m, 4H); 6.86 – 6.80 (m, 2H); 6.96 – 6.87 (m, 4H); 7.47 – 7.38 (m, 2H); 8.95 (s, 1H); ^{13}C NMR (101 MHz, THF) δ = 174.32, 169.99, 156.20, 145.22, 142.57, 134.94, 126.40, 123.31, 120.82, 115.98, 68.88, 32.99, 32.35, 30.54, 30.53, 30.43, 29.65, 27.25, 23.73, 14.61;). ESI-MS: M$^+$=616.3

Stability of **TAA1** assemblies was followed by dissolving the compound in CHCl$_3$ followed by light irradiation for 2h. The solvent was evaporated by low pressure distillation and immediately resolved in deuterated DMSO. (Fig. 79)

102
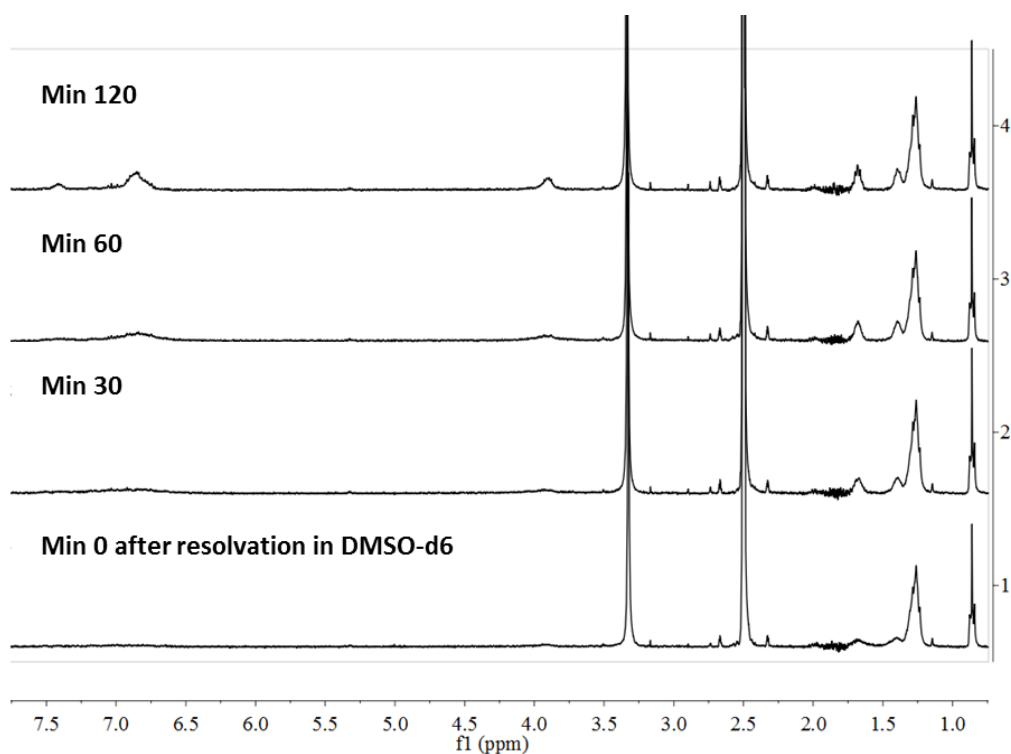
Figure 79. *Stability of self-assembly of compound **TAA1** in (CD$_3$)$_2$SO.*

Crystal structures (X-ray diffraction)

X-ray data for the structures were collected on a Rigaku Oxford Diffraction Gemini-S S1diffractometer with a Sapphire3 detector. Mo-*K*α radiation was used with a graphite monochromator and a fiber-optics Mo-Enhance collimator. Data were corrected for absorption with *CrysAlis PRO* and the structures were solved by iterative charge-flipping methods with *Superflip*.[86] The structure refinements were carried out with *CRYSTALS*[87] and all non-hydrogen atoms were refined by full-matrix least squares on *F* using reflections with *I* > 2σ(*I*). **(Table 7).**

	DOTA4	DOTA6	DOTA8	DOTAs6	DC8
formula	$C_{32}H_{64}N_8O_4$	$C_{40}H_{80}N_8O_4$	$C_{48}H_{96}N_8O_4$	$C_{40}H_{80}N_8O_4$	$C_{12}H_{26}N_2O_3$
moiety	$C_{32}H_{64}N_8O_4$	$C_{40}H_{80}N_8O_4$	$C_{48}H_{96}N_8O_4$	$C_{40}H_{80}N_8O_4$	$C_{12}H_{26}N_2O_3$
T (K)	175	175	175	175	175
spacegroup	$P2_1/c$	$P2_1/c$	P-1	$P2_12_12_1$	P-1
crystal system	monoclinic	monoclinic	triclinic	orthorhombic	triclinic
a (Å)	10.9001(4)	13.451(3)	9.4352(9)	9.7785(4)	4.6667(4)
b (Å)	17.9419(6)	17.021(4)	10.1858(11)	17.4694(9)	34.5950(17)
c (Å)	9.4220(3)	9.6996(15)	15.1723(11)	26.5271(15)	38.7306(11)
α (º)	90	90	98.479(7)	90	90.308(3)
β (º)	90.272(3)	97.313(15)	94.011(7)	90	90.668(5)
γ (º)	90	90	116.192(10)	90	91.085(6)
V (Å^3)	1842.63(6)	2202.6(3)	1279.05(10)	4531.5(3)	6251.16(17)
Z	2	2	1	4	18
ρ (gcm^{-3})	1.126	1.111	1.103	1.080	1.178
M_r (gmol^{-1})	624.91	737.12	849.33	737.12	246.35
μ (mm^{-1})	0.075	0.072	0.546	0.552	0.084
R_{int}	0.028	0.046	0.033	0.047	0.049
Θ_{max} (º)	29.036	26.749	51.561	44.723	27.933
resolution (Å)	0.73	0.92	0.98	1.10	0.92
N_{tot} (measured)	11512	7593	4850	5147	42651
N_{ref} (unique)	4005	3768	2803	3089	24260
N_{ref} ($I>2\sigma(I)$)	3043	2383	2451	2403	11457
N_{ref} (least-squares)	3043	2383	2451	2403	11457
N_{par}	205	260	277	209	1486
$<\sigma(I)/I>$	0.0394	0.0690	0.0407	0.0621	0.0677
R_1 ($I>2\sigma(I)$)	0.0712	0.1108	0.0753	0.1516	0.0731
wR_2 ($I>2\sigma(I)$)	0.0850	0.1085	0.0993	0.1799	0.0713
R_1 (all)	0.0915	0.1528	0.0822	0.1801	0.1482
wR_2 (all)	0.0924	0.1357	0.1019	0.2285	0.1103
GOF	0.9773	0.9370	1.0081	1.0543	1.0911
$\Delta\rho$ (eÅ^{-3})	-0.39/1.42	-0.41/0.58	-0.56/0.65	-1.11/0.80	-0.41/0.35
crystal size (mm^3)	0.15x0.40x0.45	0.25x0.35x0.50	0.07x0.18x0.23	0.02x0.05x0.10	0.05x0.30x0.40

Table7. Crystallographic data for obtained structures
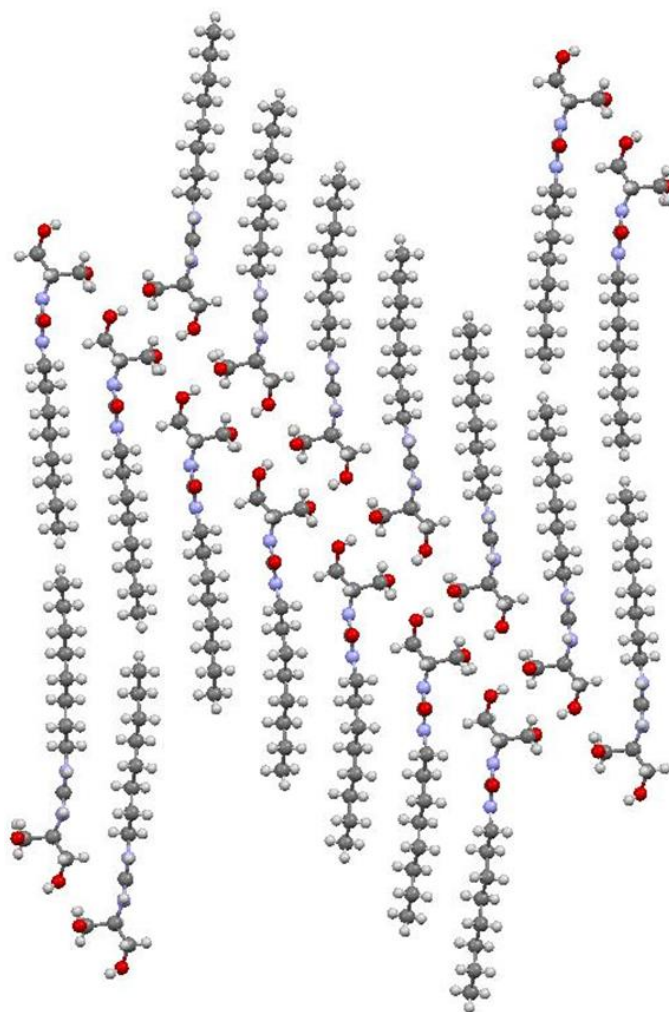
Figure 80. *Crystal structure of **DC8** with crystal packing along the a axis*
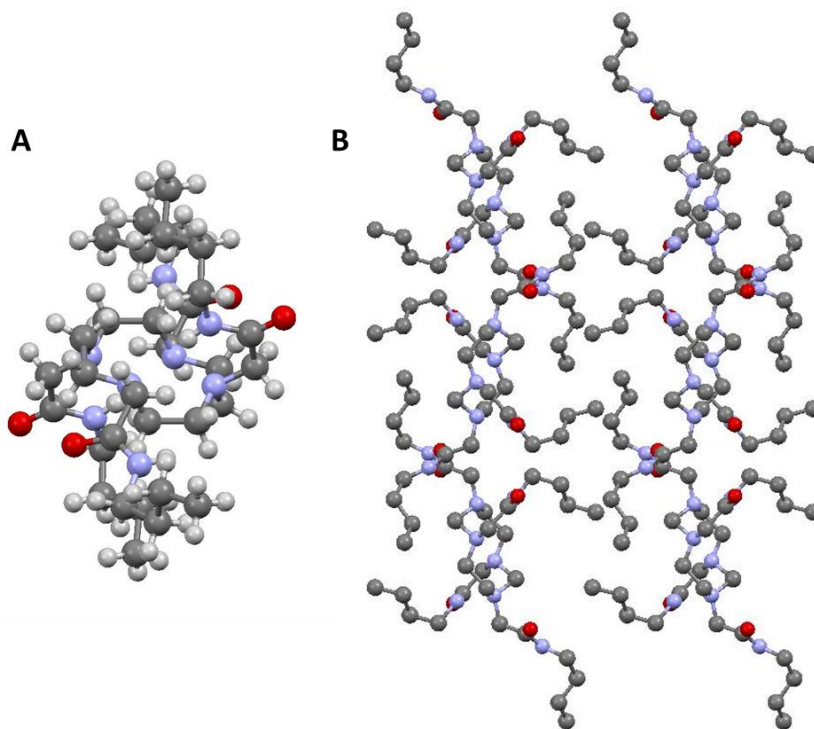
Figure 81. *Crystal structure of **DOTA4**; (A) unit cell and (B) crystal packing along the c axis (hydrogen atoms omitted for clarity)*
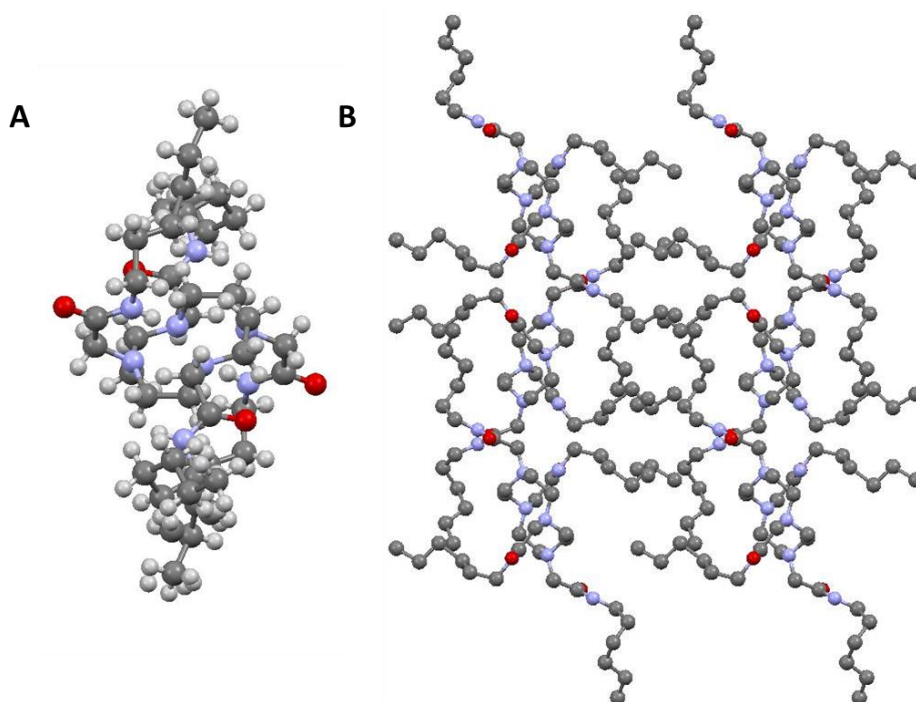
Figure 82. *Crystal structure of **DOTA6**; (A) unit cell and (B) crystal packing along the c axis (hydrogen atoms omitted for clarity)*
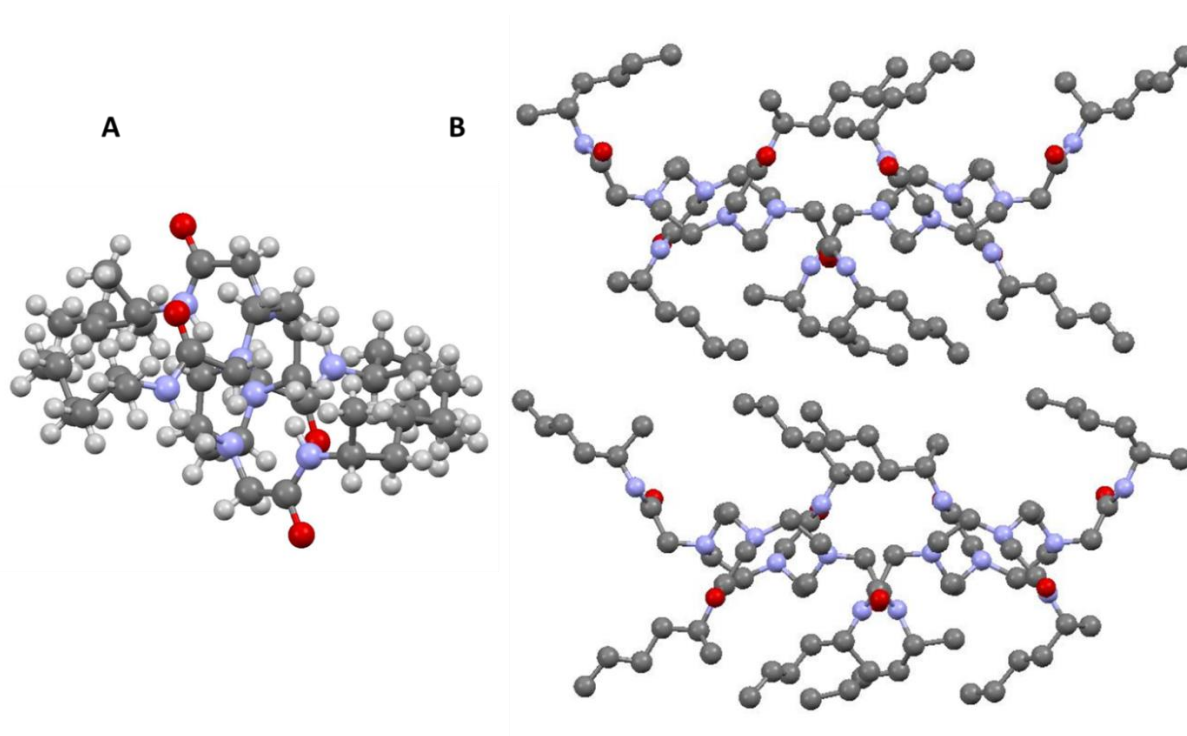
Figure 83. *Crystal structure of **DOTAs6**; (A) unit cell and (B) crystal packing along the a axis (hydrogen atoms omitted for clarity)*
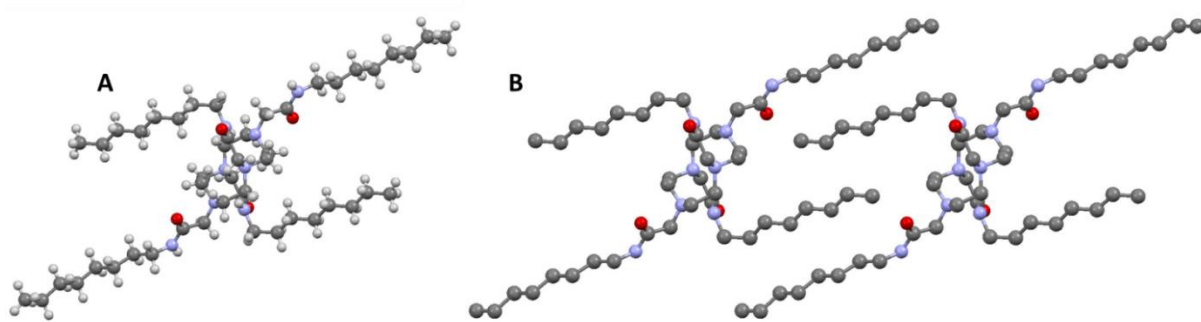
Figure 84. *Crystal structure of **DOTA8**; (A) unit cell and (B) crystal packing along the b axis (hydrogen atoms omitted for clarity)*

3.6.2   Lipid membrane transport experiments

Proton transport experiments

Egg yolk L-α-phosphatidylcholine (EYPC chloroform solution, 600 μL, 790μmol) was dissolved in a CHCl₃/MeOH mixture, the solution was evaporated under reduced pressure and the resulting thin film was dried under high vacuum for 2 h. The lipid film was hydrated in 1.2 mL of phosphate buffer (10 mM sodium phosphate, pH = 6.4, 100 mM NaCl) containing 10 μM HPTS (pyranine, 8-hydroxypyrene-1,3,6-trisulfonic acid trisodium salt) for 40 min. During hydration, the suspension was submitted to at least 5 freeze-thaw cycles

(liquid nitrogen, water at room temperature). The large multilamellar liposome suspension (1mL) was submitted to high-pressure extrusion at rt (21 extrusions through a 0.1 µm polycarbonate membrane afforded a suspension of LUVs with an average diameter of 100 nm). The LUV suspension was separated from extravesicular dye by size exclusion chromatography (SEC) (stationary phase: Sephadex G-50, mobile phase: phosphate buffer) and diluted with the same phosphate buffer to give a stock solution with a lipid concentration of 11 mM (assuming 100% of lipid was incorporated into liposomes).

100 µL of HPTS-loaded vesicles (stock solution) was suspended in 1,9 ml sodium phosphate, pH = 6.5 with 100 mM KCl and placed into a fluorimetric cell. The emission of HPTS at 510 nm was monitored with excitation wavelengths at 403 and 460 nm, using a PerkinElmer LS55 fluorescence spectrometer. During the experiment, 20 µL of a 0-40 mM DMSO solution of the compounds **X** was added at t = 50 s. followed at t=100sec by 20 µL of 1.2 µM valinomycin (Val) solution in DMSO. At t=150 s, 29 µL of 0.5 M NaOH is added. For the reference proton transport experiment, 1.2 µM of proton transporter carbonyl cyanide-4-(trifluoromethoxy)phenylhydrazone (FCCP) is added together with the valinomycin. Maximal possible changes in dye emission were obtained at t = 600 s by lysis of the liposomes with detergent (40 µL of 5% aqueous Triton X100). The pH values were calculated for each point from the HPTS emission intensities according to the calibration equation

$$(3)\ pH = 1.1684 \cdot \log(I_o/I_1) + 6.9807$$

where I_o is the emission intensity with excitation at 460 nm and I_1 is emission intensity with excitation at 403 nm. At the end of the experiment, the aqueous compartment of liposomes was equilibrated with extravesicular solution by lysis of liposomes with a detergent (40 µL of 5% Triton X100).
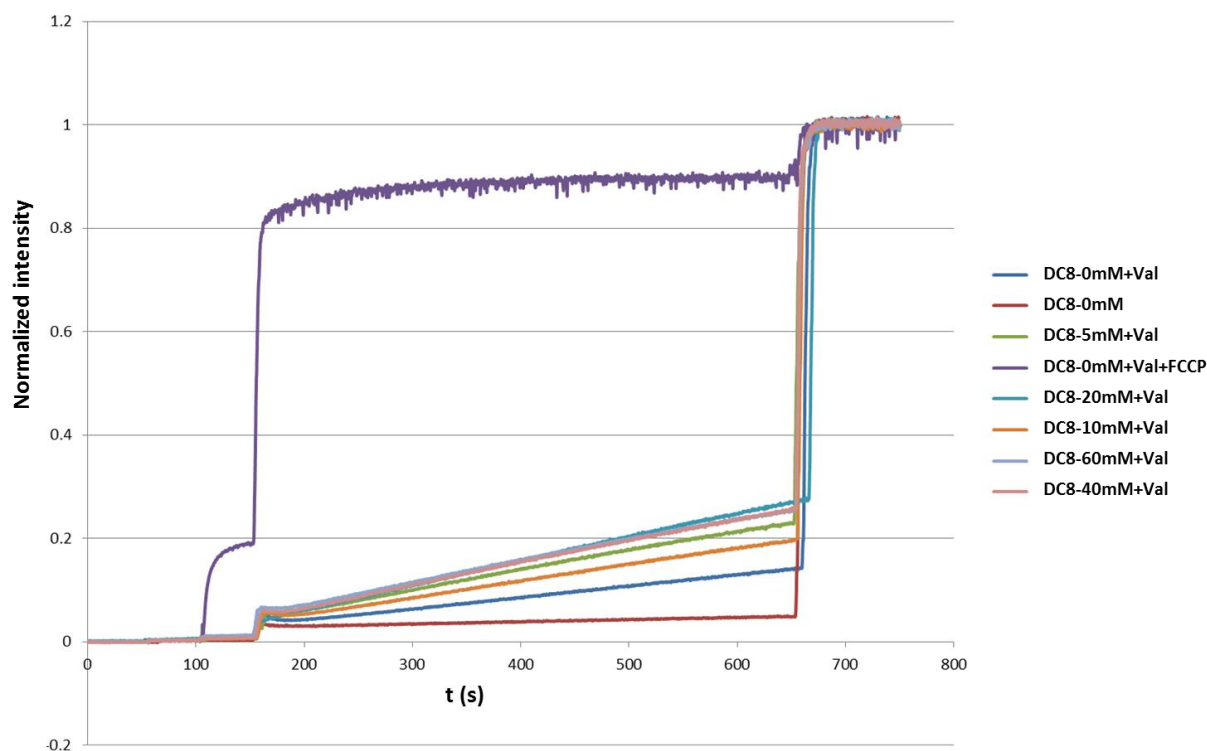
Figure 85. *Proton transport dose response for **DC8***

Water transport

Liposomes were prepared using the same film rehydration method as above. A POPC/DOPS/Chl mixture with a molar ratio of 4/1/5 was dissolved in chloroform/methanol mixture (CHCl$_3$/MeOH,v/v: 1/1). The solution was dried on a rotary evaporator and subsequently under high vacuum to remove residual solvent. After rehydration with 1 ml buffer containing 200 mM sucrose / 10 mM PBS buffer solution (pH=6.4), the suspension was extruded through 0.1 μm track-etched filters for 21 times (Whatman, UK) to obtain monodisperse unilamellar vesicles, the size of which was characterized by dynamic light scattering (Zetasizer Nano, Malvern Instruments Ltd., UK). The aliquot of the compounds dissolved in DMSO have been added to the liposome solution and left to equilibrate. The water permeability tests were conducted on a stopped-flow instrument (SFM3000 + MOS450, Bio-Logic SAS, Claix, France). Exposure of vesicles to hypertonic osmolyte (400 mM sucrose/ 10 mM PBS buffer solution, pH=6.4) resulted in the shrinkage of the vesicles due to an outwardly and inwardly directed osmotic gradient. The changes of light scattering were recorded at a wavelength of 345 nm. For salt rejection, the same experiment was done using a 100 mM inside/ 200 mM outside NaCl solutions. Permeability (P$_f$) was calculated using the same equations (1) and (2) as in chapter 2.6.2.

LUV type	net Pf 1	net Pf 2	net Pf 3	avg net Pf
DC8-10	7.75	4.77	0.581481	4.3654321
DC8-15	11.36	9.67	7.525926	9.51975309
DC8-20	11.17	14.21	15.58148	13.6555556
DC8-25	21.08	18.84	16.22963	18.717284
DC8-30	20.43	18.29	25.48889	21.4024691
DC8-35	25.62	21.99	22.24815	23.2851852
DC8-40	18.67	26.43	29.00741	24.7049383

Figure 86. *Average net permeability of vesicles with varying concentrations of injected **DC8** solutions*

LUV type	d_{LUV} /µm	S/V0	ΔO /mOsm	k	P_f /µm.s^{-1}
blank	0.1	60	100	7.1	65.7
DOTA6-10	0.1	60	100	15.85	146.8
DOTA6-20	0.1	60	100	23.79	220.3
DOTA6-30	0.1	60	100	399.16	3695.9

Figure 87. *Average net permeability of vesicles with varying concentrations of injected **DOTA6** solutions*

LUV type	d_{LUV} /µm	S/V0	ΔO /mOsm	k	P_f /µm.s^{-1}
blank	0.1	60	100	7.1	65.7
DOTA4-20	0.1	60	100	11.29	104.5
DOTA6-20	0.1	60	100	23.79	220.3
DOTAs6-20	0.1	60	100	14.56	134.8
DOTA8-20	0.1	60	100	12.76	118.1

Figure 88. *Average net permeability of vesicles with various DOTAx compounds at 20mM injection concentration*

Patch clamp experiments

A model BC-535A bilayer clamp (Warner Instrument Corp.) was used for all planar bilayer experiments. All data were hardware filtered at 1kHz (8-pole Bessel filter), digitized (Axon 1440a) and recorded in a survey mode using the Gap-free protocol and processed (ClampEx and ClampFit 10.3.1.5). Chambers were made of Delrin holding a polystyrene cup with an aperture of 250 µm. The lipid was diphytanoylphosphatidylcholine (diPhyPC) (Avanti Polar Lipids). A stock solution of 25 mg/mL lipid in CHCl3 (100 µL) was dried under N2 and then re-suspended in 100 µL decane. The electrolyte used was 1M KCl, in 10 mM HEPES, 10 mM TRIS, pH 7. The aperture was primed with 0.5-1 µL of decane/lipid, excess solvent was removed by blowing N2 over the aperture. The cup was then placed into the electrolyte-filled holding cell, consisting of 4mL and 3mL chambers, and salt bridges (KCl/Agar) and

electrodes (Ag/AgCl) were attached. Bilayers were formed by brushing on 1-1.5μL of the decane/lipid mix over the aperture and were monitored for stability, capacitance and resistance for at least 20 minutes before test compound was added. The compound was added by injection from an organic solution (typically 5 or 10μL of a 10mM or 20mM DMSO solution). Bilayers were tested repeatedly for capacitance and resistance.

3.6.3   Molecular dynamics simulations

In order to determine the mechanism through which DOTA molecules create water channels in a lipid bilayer, 6 DOTA molecules were stacked and inserted in a lipid bilayer consisting of 130 POPC molecules using 'membed' algorithm from the GROMACS 5.1 software. The insertion led to the deletion of 8 POPC molecules to a final count of 122. The system was hydrated with 7027 water molecules. The following parameters were set for the simulation:

- tcoupling : V-rescale
- Cutoff-scheme: Verlet
- integration step: 5fs
- rcoulomb: 1.2 nm
- tau_t: 2.5   2.5 ps
- tau_p: 5.0 ps
- ref_p: 1.0   1.0 bar

- simulation length: 1 μs
- pcoupling: Berendsen semiisotropic
- rlist: 1.2 nm
- rvdw: 1.2 nm
- ref_t: 298 298 K
- compressibility: 4.5e-5 4.5e-5 bar-1
- coulombtype: PME

Chapter IV

–Towards artificial water channel integrated membranes for desalination –
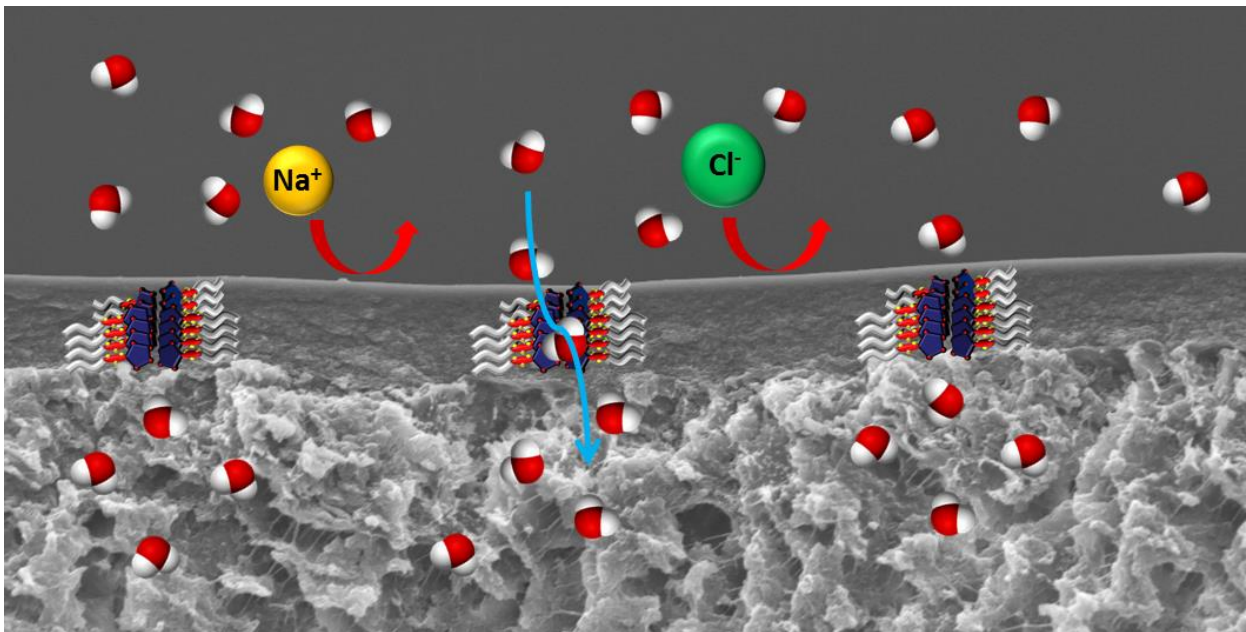
¨We take ideas from other people…we stitch them together into new forms, we create something new. That's when innovation really happens"

Steven Johnson – Where good ideas come from

4.1   Context

In order to capitalize on the functionality of the artificial water channels, and to transfer the water transport properties observed at a nanometric level within bilayer membranes, we intended to make the transition to macroscopic functional materials and membranes for desalination.

The proposed materials design for this was based on the use of hybrid matrixes of organic polymers and artificial water channels. The most simple and accessible option for this was to use existing materials used in desalination membrane technology and combine them with the compounds capable of self-assembling into water channels. Currently, semipermeable membranes are being used in two main processes for water purification: forward osmosis (FO) and reverse osmosis (RO). There are several differences between the two processes, the most important being the driving force for the separation. (Fig. 89)
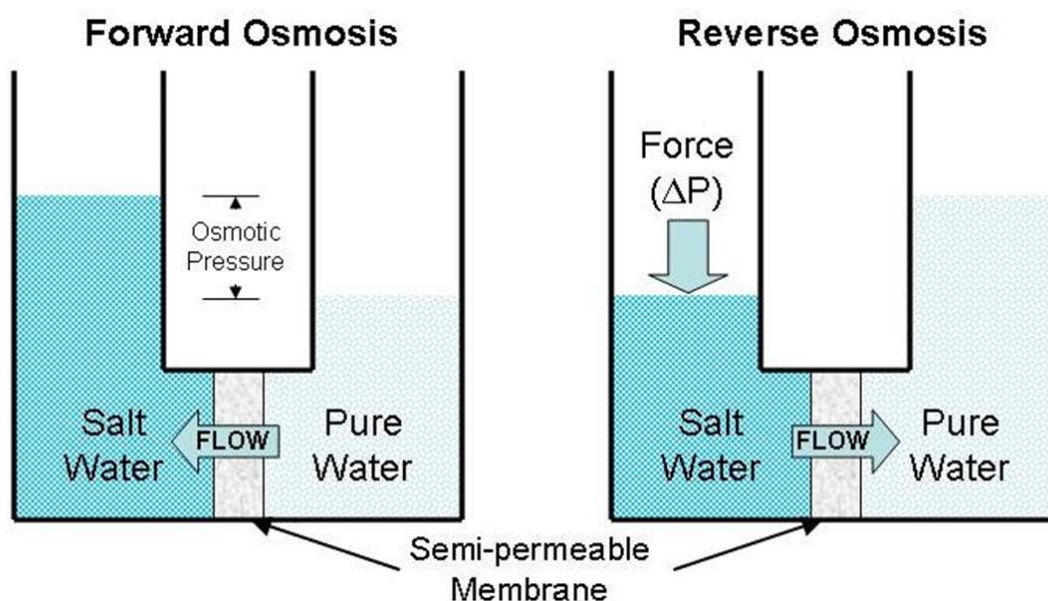
Figure 89. *Water flow in forward osmosis and reverse osmosis*

Separation in forward osmosis is driven by osmotic pressure. The purification includes two main steps. The first one is the separation of pure water by using a chemical draw solution of higher concentration than the water aimed to be purified, followed by a second step where the high concentration draw solution is regenerated to be used again for separation. In comparison to the simple one-step process of RO, this step causes extra energy expenditure and is what makes FO less efficient from an energy consumption point of view.[99] The main benefit of using FO is that the membranes used are less prone to fouling, as the mechanical pressure on the surface of the membranes is much lower than in the case of RO filtration. A lot of research has been made towards obtaining more efficient materials

113

and new draw solutes[100–102] that would make FO more attractive in separation processes. Even with the latest developments, FO seems to be most effective when used in conjunction with RO setups [103] where FO can be used as a replacement for chemical pretreatment and to reduce the cleaning costs.

Reverse osmosis works on the basis of an applied pressure in order to overcome the osmotic pressure of the solution that needs to be purified. Since the first developed membrane at the beginning of the 1960s, RO practically became the dominant technology used in desalination.[104,105] Improvements have been made in creating new materials with higher fluxes and rejections,[104] the membranes available today being practically impermeable to ions. The main research effort is currently directed towards the reduction of operating costs. Since pressure is needed to "push" water through the membranes, the main energy consumption comes from passing the osmotic pressure threshold that allows for water to go through the membranes. Consequences of using high pressure are the effect of fouling and concentration polarization that happens mainly at the surface of the membranes.

We envisaged that the previously described imidazole and diol based self-assembling water conducting channels could be integrated into semipermeable organic polymer networks, with hopes of observing enhanced performance with the presence of the channel-forming compounds. Two different strategies were proposed: i) the formation of thin film nanocomposites (TFNs) based on polyamides integrating nanocrystals of water channels ii) chemical grafting of brush copolymers on ultrafiltration membrane supports. (Fig. 90)
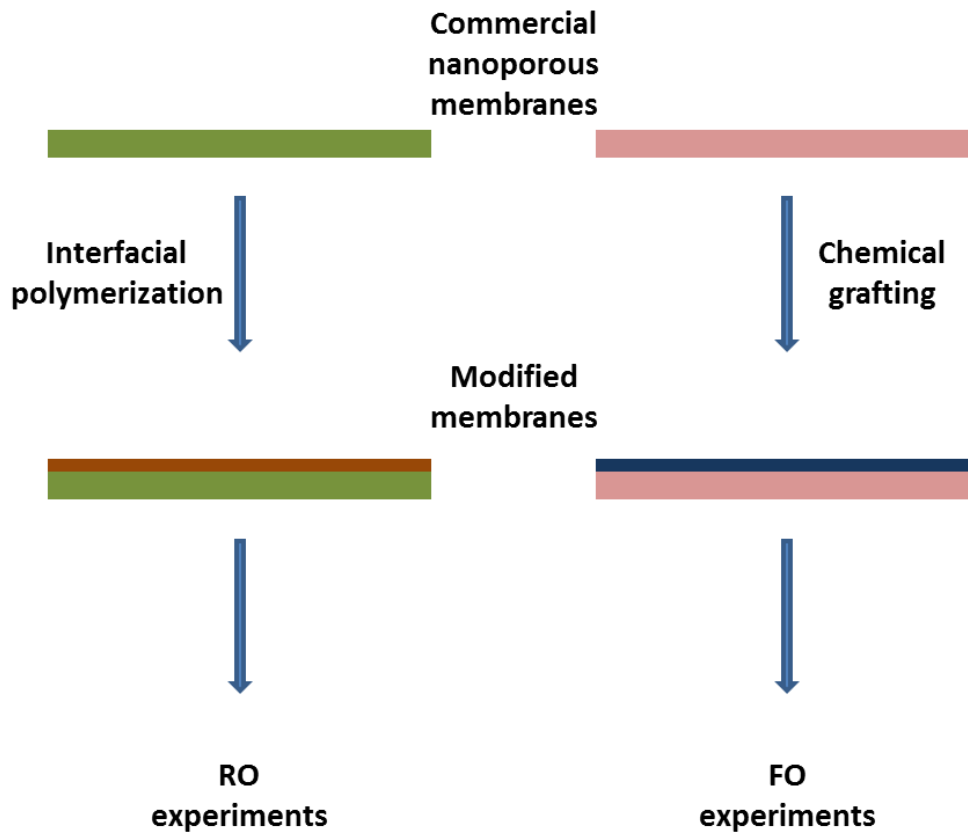
Figure 90. *Strategy for RO polyamide and FO brush copolymeric membranes development*

The TFN membranes were developed for RO filtration, having been tested using a dead end filtration setup, while the chemically modified membranes were assessed experimentally in a FO setup.

4.2   Polyamide/I-quartet thin film nanocomposite membranes

Thin film composites (TFCs) are currently dominating the water desalination industry with around 90% of membranes used in reverse osmosis/nanofiltration being based on this technology.[104] The principle of these membranes is based on the use of a multi-layer membrane design.[106] (Fig. 91)
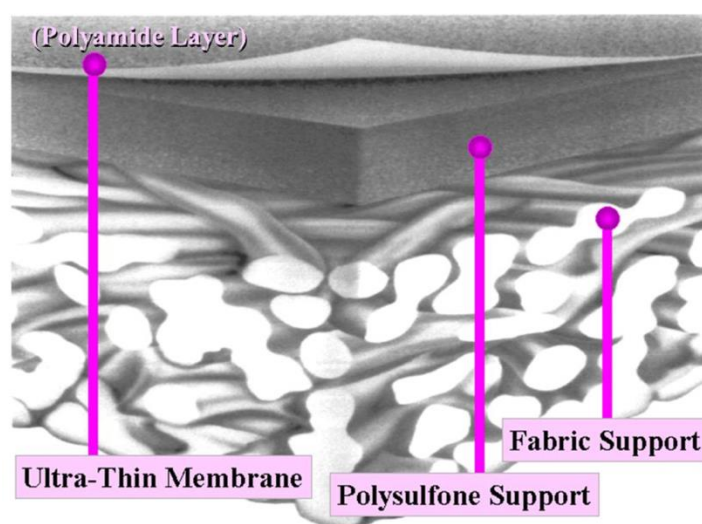
Figure 91. *TFC membrane design showing a hierarchical organization of three layers of very different porosity and thickness (image adapted from reference [106])*

A composite RO membrane is a layered material formed by a two-step process. This composite membrane typically consists of a thick, microporous, nonselective layer formed in a first process step, subsequently overcoated with an ultrathin barrier layer on its top surface in a second process step. A base reinforcing fabric layer, typically polyester (PET) fabric, is overcoated with a layer of an anisotropic microporous polymer, such as polyethersulfone (PES). Then, the surface of the microporous polymer support is coated with an ultrathin semi-permeable barrier layer, which is responsible for contaminant rejection. While the microporous support can be varied in order to obtain improved strength and compression resistance combined with minimum resistance to permeate flow, the thin film barrier proved to be less flexible if high salt rejections are desired. In the early development of composite membranes, interfacial polymerization was proposed as approach to form a thin polymeric layer cast on the membrane support, but this approach did not succeed in industrial fabrication until Cadotte discovered a series of composite membranes with surprisingly high flux that could be made by interfacial reaction of piperazine with trimesoyl chloride (TMC)/isophthaloyl chloride mixture.[107] Subsequently, it was observed that best results could be obtained using m-phenylenediamine (MPD) as the aromatic amine in conjuction with TMC. (Fig. 92) By tweaking with the conditions and reactants, TFCs with

varying performances[108] obtained through interfacial polymerizations can be easily obtained both at the laboratory as well as at industrial scale.
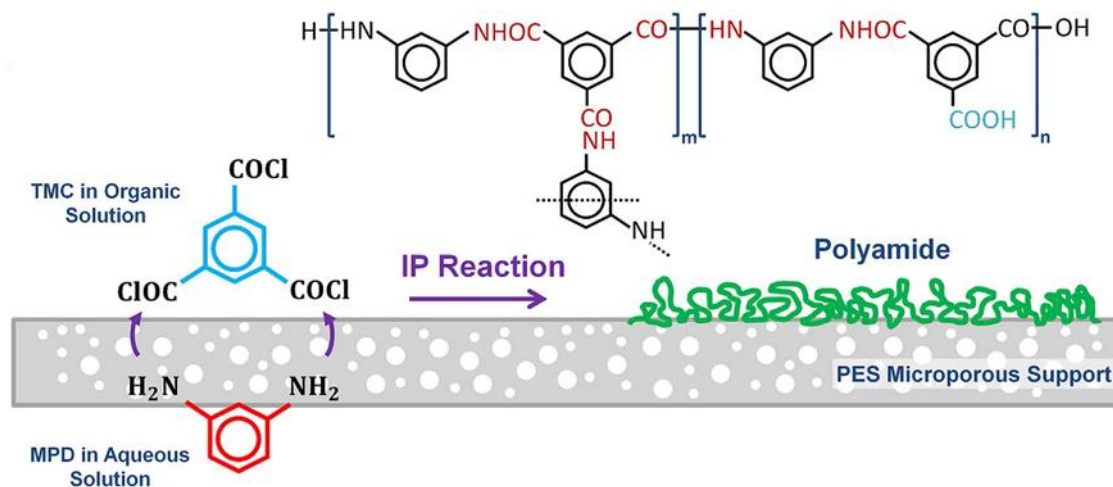
Figure 92. *TFC fabrication*: *polyamide thin film formation through interfacial polymerization (IP) using a PES support(image adapted from reference [108])*

With the development of nanomaterials, a new branch of thin film materials appeared. Thin film nanocomposites (TFNs) are the result of the incorporation of nanoparticles into the polyamide layer of the TFC membrane.[109] Several types of nanoparticles have been tried for obtaining TFNs with various performances.[110–112] One of the first pioneers of the TFN concept was Hoek, with the incorporation of zeolite nanocrystals into the polyamide matrix.[113] (Fig. 93)
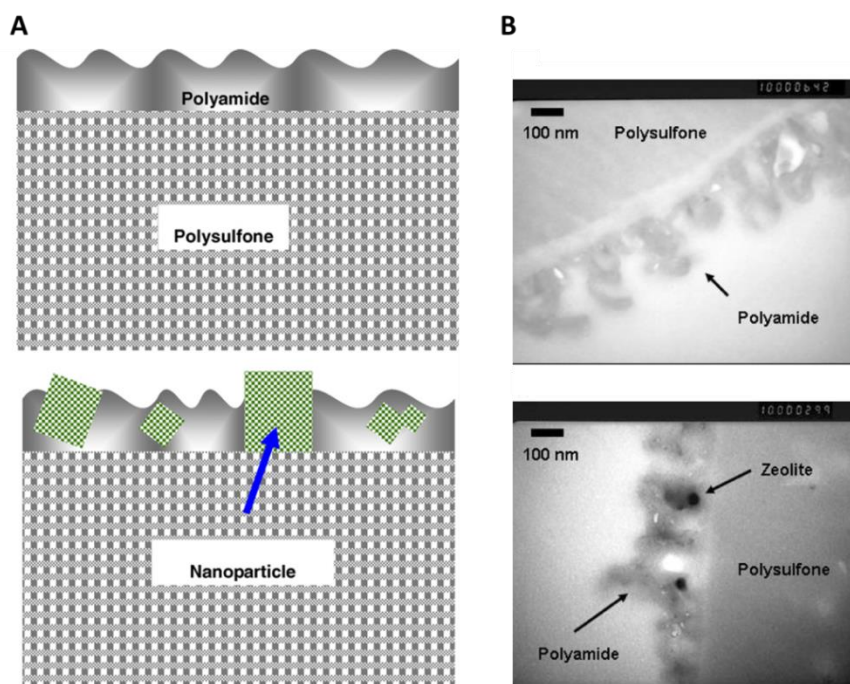
Figure 93. *(A) Polyamide TFC and TFN with zeolite nanoparticles and (B) TEM images of the membranes (image adapted from reference [113])*

The authors have proven that the obtained zeolite TFNs showed an increase of permeability as compared to the classical TFC membranes, with flux values close to the double of the control membrane. There was an issue of a slight drop of rejection, which the authors argued that could arise from the incompatibilities at the interface between the zeolite nanocrystals and the organic polymer network.

HC8-TFN membranes. Using the same principle as for the zeolite TFNs, we argued that nanocrystals of artificial water channels could be incorporated in the same fashion into the polyamide layer of a TFC membrane. For this, we first prepared nanocrystal suspensions of **HC8** in water solution, which was used later for the preparation of the TFN membrane. (Fig. 94)
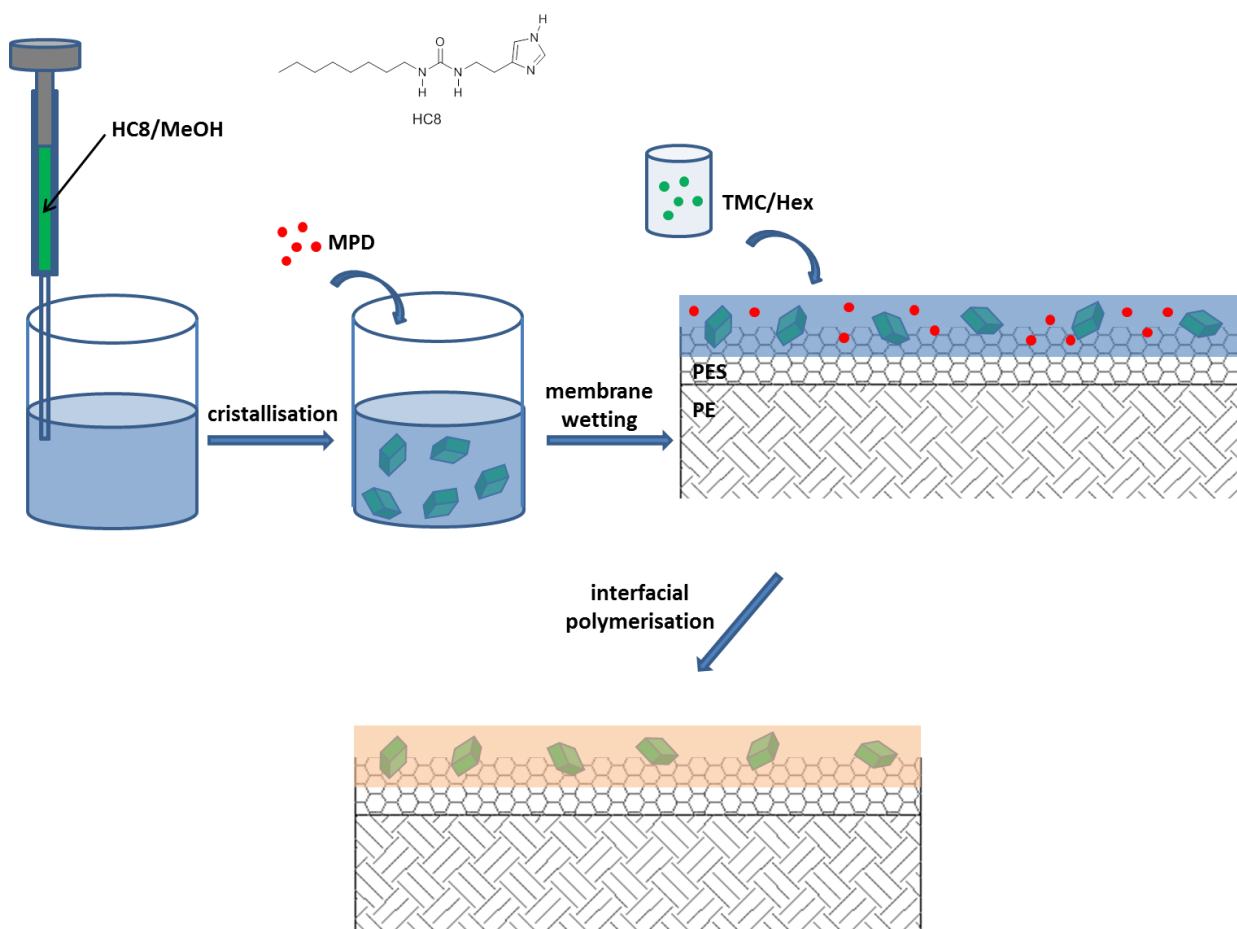
Figure 94. *TFN membrane fabrication with incorporated artificial water channels nanocrystals of **HC8***

Nanocrystallization. Nanocrystal formation for organic compounds has been previously reported.[114–116] In general, a typical experiment to obtain nanocrystals includes the injection of a small amount of highly concentrated solution of the organic compound in a solvent that is miscible with water. The diffusion of the organic solvent into the water will cause the compounds to crystallize.
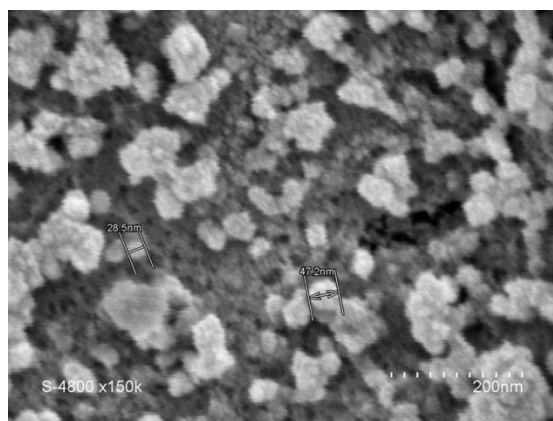
Figure 95. *SEM image of a dried **HC8** nanocrystal solution containing particles in the range 30-70 nm*

In the present case, we used **HC8** solutions in methanol and injected into water. For our experiments, we tried two different work methods for obtaining the nanocrystals. The size of the formed particles upon injection varied depending on the concentration used. When having a final concentration of 1 mM solution we obtained particles in the range of 30-70 nm while a 2 mM solution shows size variation between 200-800 nm, as proved by dynamic light scattering and Scanning Electronic Microscopy (SEM). (Fig. 95) It is noteworthy that at higher concentrations the particles start to aggregate and the solution sediments if left for a long time. In order to avoid the fast and inhomogeneous precipitation of the compounds, we tried to obtain the nanocrystals by recrystallizing from a 60°C water solution of **HC8**. MPD was then dissolved in the nanocrystal solution and subsequently poured on the PES membrane surface. After sufficient wetting time, the excess water solution is removed and the TMC in hexane is added to form the polyamide layer. Forming the thin layer in the presence of the crystals causes the entrapment of these within the polymer matrix. The formed membranes were characterized by scanning electron microscopy (SEM) and contact angle measurements. (Fig. 96) We attempted shallow angle XRD experiments in order to identify the presence of the crystalline particles in the polyamide layer, but the experiment was not sensible at the scale of the thin film layer, showing mainly peaks for the PES support membrane.

Scanning Electronic Microscopy. The obtained control membrane showed an average thickness of 250 nm, with a flaky surface morphology typical for polyamide layers. Using the nanocrystal solutions obtained at room temperature, the average thickness dropped to around 200 nm with specific changes in morphology. Significant differences have been noted when using the recrystallization technique in the presence of the PES membranes. The thickness of the obtained thin films varied largely, with the most dominant values being in the range of 100-150 nm. The surface morphology was notably different also, presenting a denser and more regular structure. (Fig. 96–C)

119
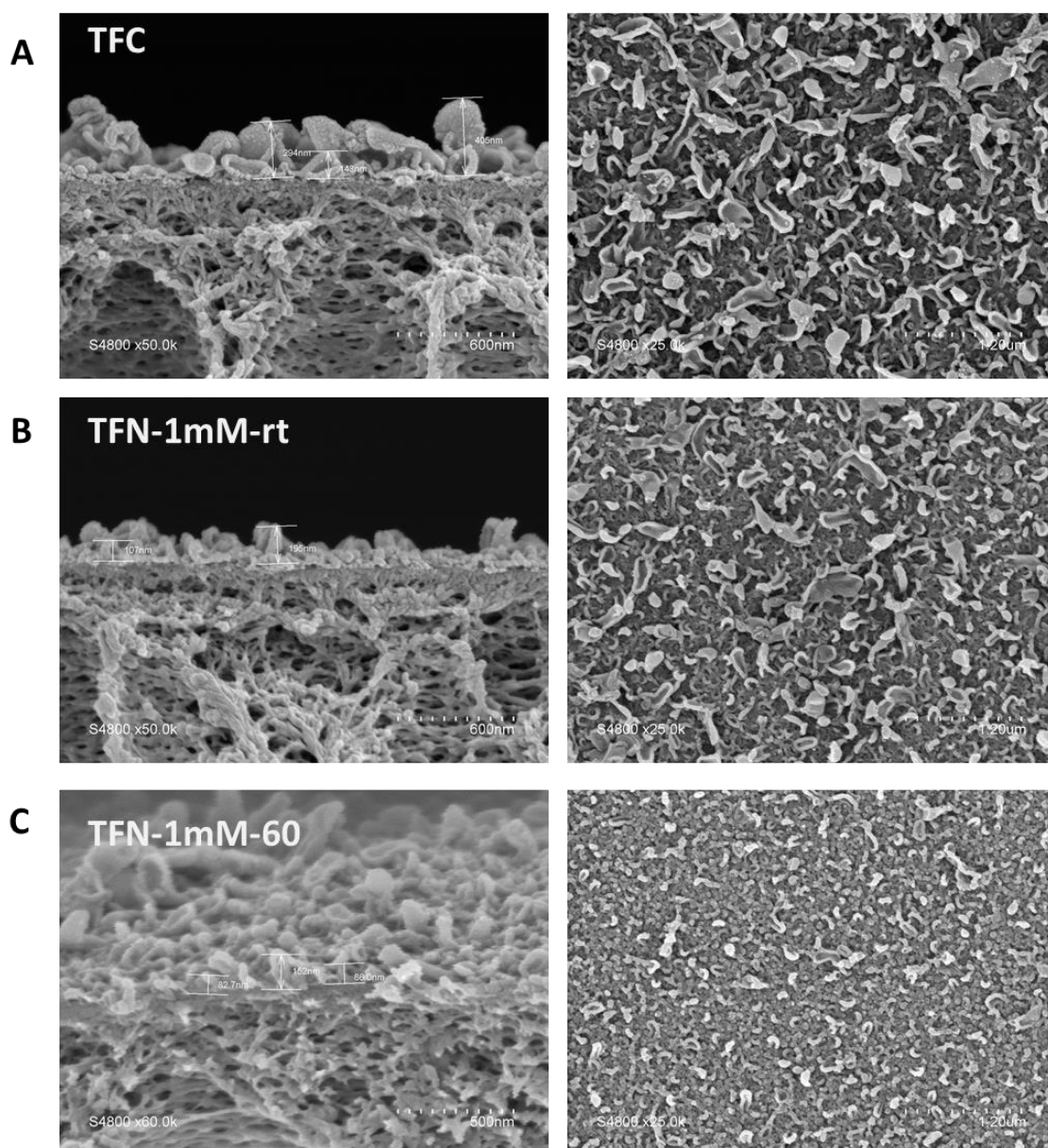
Figure 96. *Cross-section and surface SEM images of (A) TFC control membrane, (B) TFN with nanocrystal solution obtained at room temperature and (C) TFN with nanocrystal solution obtained by recrystallizing from 60^oC HC8 solution*

Contact angle. When conducting contact angle measurements between water droplets and the membrane surfaces, we have noticed a trend in the evolution of the angle. The control TFC membranes showed an average contact angle of 66°, while in the case of the TFN-1mm-rt membrane surface the angle increased to 70°. An even more pronounced increase was observed when analyzing the surface of the TFN-1mm-60 membrane, having obtained an average contact angle of 82°. These results suggest that the surface is becoming more hydrophilic. This could be due to the presence of the water binding HC8 particles in the polyamide thin film.

Reverse osmosis experiments. In order to test the performance of the membranes, we utilized a dead end reverse osmosis filtration cell. A solution of 2000 ppm NaCl was filtered through the membranes at a pressure of 10 bars. We were mainly interested in the flux rates of water and the rejection capabilities of the membranes. Water flux was determined gravimetrically and the rejection by following the conductivity of the feed/permeate. Initially, using the nanocrystal solution didn't seem to induce any change in the water permeability of the membranes, having obtained identical values both for water flux as well as for salt rejection as the control TFC membranes. This prompted a slight change in the work method. Instead of pre-crystalizing the **HC8** in the water we decided to form the crystals in the presence of the membrane. For this, we used a solution of HC8/MPD in water at 60°C and let the solution cool down to room temperature once it has been poured over the PES membrane. This way the crystals would form when to solution cools down, encouraging the adsorption of the nanocrystals onto the membrane surface. The obtained results have shown that there is indeed an influence of the nanocrystals on the performance of the membranes. (Fig. 97)
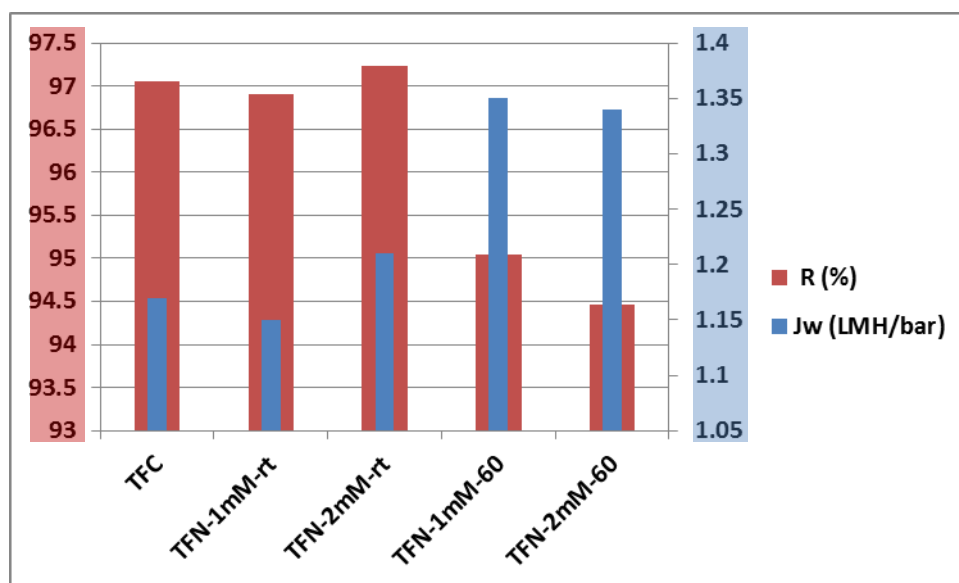
Figure 97. *Pure water flux and salt rejection of TFC and TFN membranes*

The control TFC membranes presented a pure water flux of 1.17 LMH/bar with an observed salt rejection of 97.06%. Membranes obtained by precrystallization of **HC8** (TFN-1mM-rt and TFN-2mm-rt) had very similar values, with 1.15 LMH/bar and 96.9% salt rejection respectively. By using the second work method we observed and an increase of 17.4 % of the pure water flux up to 1.35 LMH/bar while the salt rejection slightly dropped to 95.05%. Changing between the two concentrations used to obtain the nanocrystal solutions didn't change the performance of the membranes regardless of the work method used. We consider that the reduction in rejection can come from either error in the crystal network of the compound or from the incompatibility between the crystallized compound and the polyamide matrix.

Conclusions. When drawing conclusions, it is rather difficult to correlate the constitution of the membranes to their performances. While observing an increase of 15-20% in water flux in the case of the TFN-60 membranes, the slight drop in rejection might suggest that the increase in permeability could be partially due to defects induced by the compound in the polyamide layer. When taking into account the severe changes in surface morphology, this can also be considered a cause for the change in performance. Without any further experimental proof, it is difficult to draw the conclusion that the **HC8** nanocrystals function as facilitators for the selective passage of water through the polyamide layer.

4.3 Chemically grafted regenerated cellulose membranes

Membrane surface modification has been extensively applied to various types of membrane surfaces in order to induce either enhanced separation performances or to increase fouling resistance. [117,118] Depending on the nature of the membrane surface, different chemical approaches can be applied. Some of the most successful surface modifications have been achieved through surface grafting reactions using either single molecular grafting or growth of so-called polymer brushes. (Fig. 98) *Belfort el al* have used membrane surface activation by plasma treatment followed by polymer growth using acrylic compounds, having successfully grafted PES membranes with various polymer brush surfaces. [119–122]
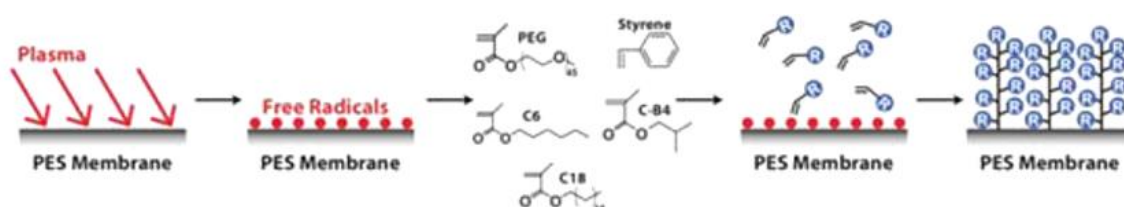
Figure 98. *Polymer brush growth on a plasma activated PES membrane surface(Image adapted from [119])*

Where the surface chemistry allows it, fully chemical approaches can be used to functionalize membrane surfaces. One of these approaches is the use of surface initiated atom transfer radical polymerization (ATRP) polymerization for obtaining finely controlled polymer brushes. [123,124] A particularly easy method was developed by Matyjaszewski et al who introduced the activator regenerated by electron transfer technique (ARGET-ATRP). [125] In short his method implied the use of a reducing agent that regenerates the activators responsible for the propagation of the polymerization reaction. Using this method the presence of air in the reaction system doesn't pose as much of a problem as in simple ATRP reactions, where even small amounts of oxygen can consume the activators, typically Cu^+ complexes. (Fig. 99)
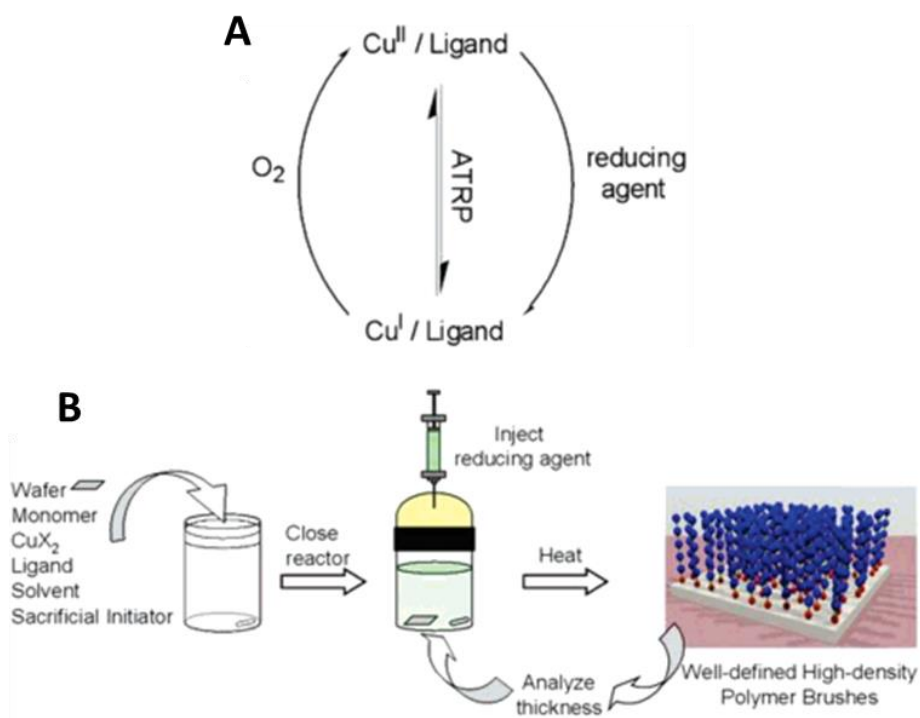
Figure 99. *(A) Mechanism of oxidation/reduction of activators during ATRP (B) ARGET-ATRP reaction setup (Image adapted from reference [125])*

Brush grafting. Based on the describe ARGET-ATRP technique we proposed to functionalize commercially available ultrafiltration membranes with polymer brushes bearing chemical moieties capable of forming water channels. For this, we synthesized custom methacrylic compounds bearing urea-imidazole and urea-diol functions, according to the moieties found in artificial water channel forming compounds described in chapter 2 and 3. As a choice for membrane substrate, we opted for regenerated cellulose (RC) as it bears hydroxyl groups that can be functionalized with molecules that would act as surface initiators and anchors for the brushes. Then polymer brush growth was attempted using different ratios of custom monomers and alkyl methacrylates in an attempt to produce a dense brush layer with attached artificial water channels. To obtain the methacrylic monomers, a simple one step reaction was used starting from commercially available compounds. (Fig. 100)
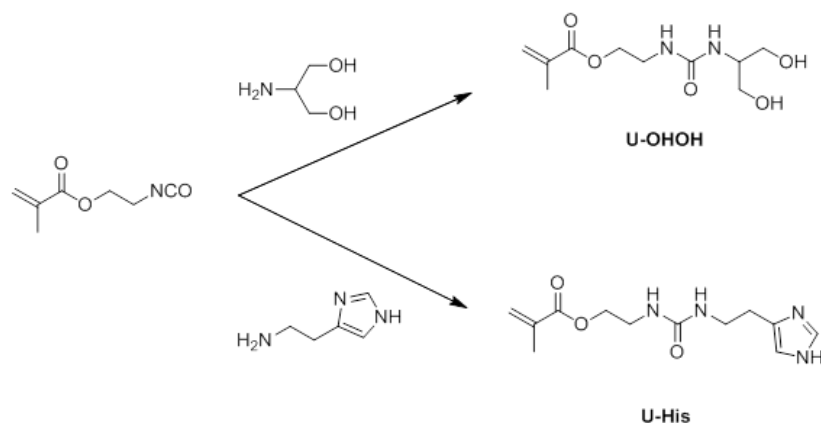
Figure 100. *Custom monomers synthesis*

Having desalination in mind, we wanted to obtain a rather dense layer of polymer brush, with a selective passage for water through formed water channel domains. For this, we used dodecyl methacrylate as the matrix for the dense polymer brush layer and we copolymerized them with two custom methacrylate compounds. In order to grow the brushes from the surface of the membrane, we attached a tertiary alkyl bromide which acts as the initiation point for the polymer chain. The functionalized membranes were then placed in a sealed vial together with all the components necessary for the reaction. (Fig. 101)
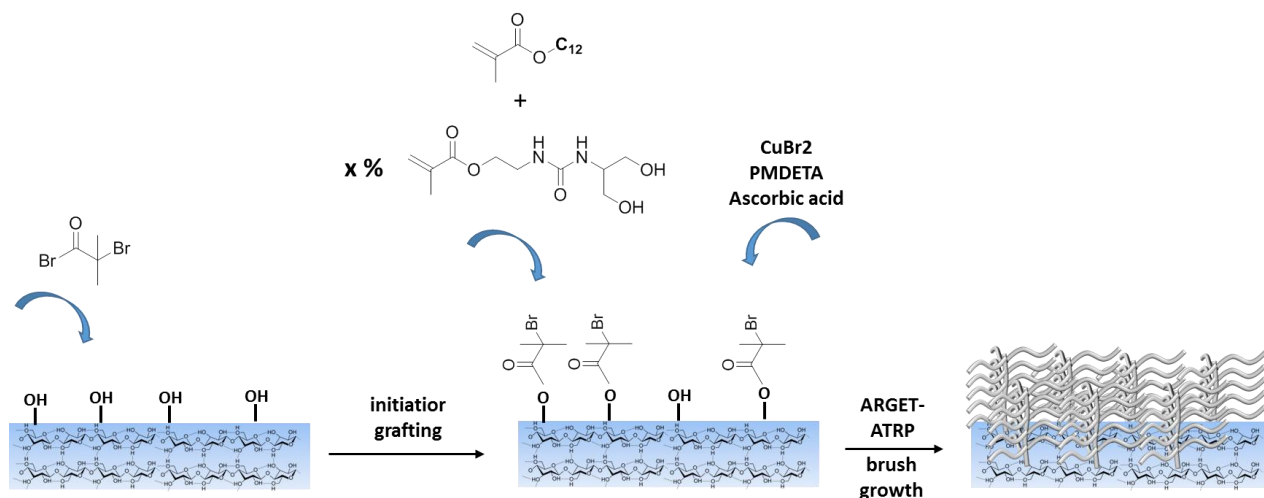
Figure 101. *Brush grafting reaction scheme*

The surface grafting was monitored by Fourier transform infrared spectroscopy (FTIR), following the appearance of the sharp carbonyl signal at ~1730 cm^{-1} attributed to the ester group present in the backbone of the polymer brush on the membrane surface. The copolymerized brushes presented and an extra set of signals for the carbonyl group present in the urea moiety of the custom monomers, found between 1500-1600 cm^{-1}. (Fig. 102) Interestingly we did not see any grafting taking place when using the **U-His** methacrylate. From the observation of the reaction mixture, it is thought that the imidazole binds to the copper in the solution, deactivating it and blocking the propagation of the polymerization.
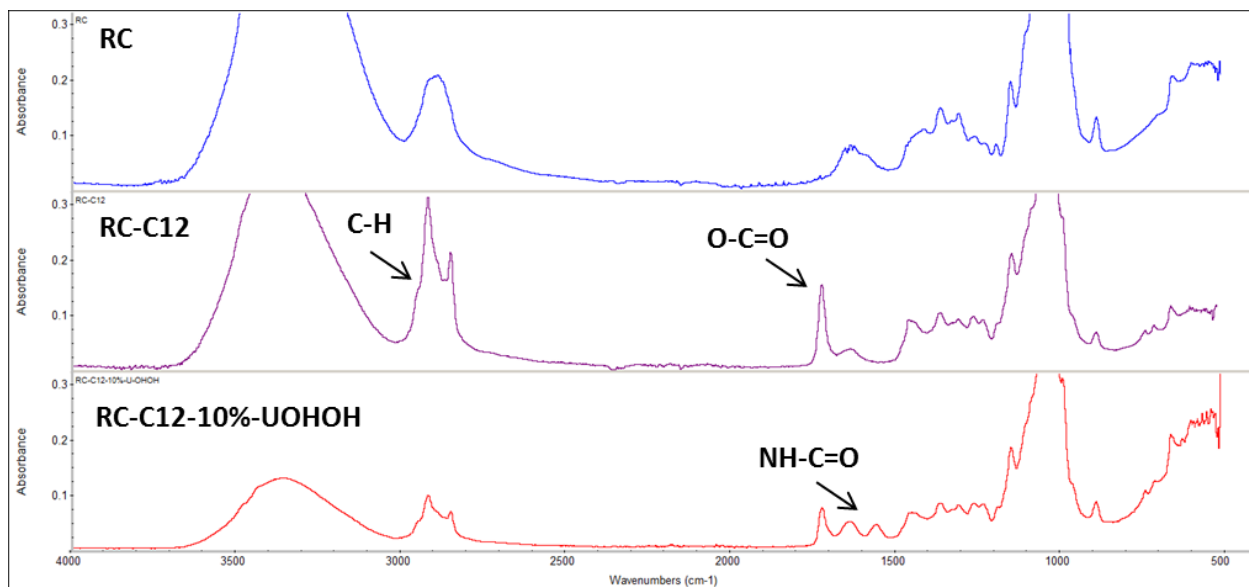
Figure 102. *ATR-FTIR spectra of regenerated cellulose (RC), dodecyl brushes (RC-C12) and mix brushes with 10% **U-OHOH** (RC-C12-10%-**U-OHOH**)*

SEM imaging. Surface and cross-section analysis reveals similar morphologies for the three obtained membranes. The thickness of the grafted layer on the RC membranes varies, decreasing from 150 nm at 5% **U-OHOH** to around 65-70 nm at 10% and 20% **U-OHOH**. (Fig. 103) This is suggesting that the increased amount of custom **U-OHOH** monomer is reducing the rate of polymer growth on the surface. Both the surface and section of each membrane shows a dense granular morphology with no particular difference between the three membranes.
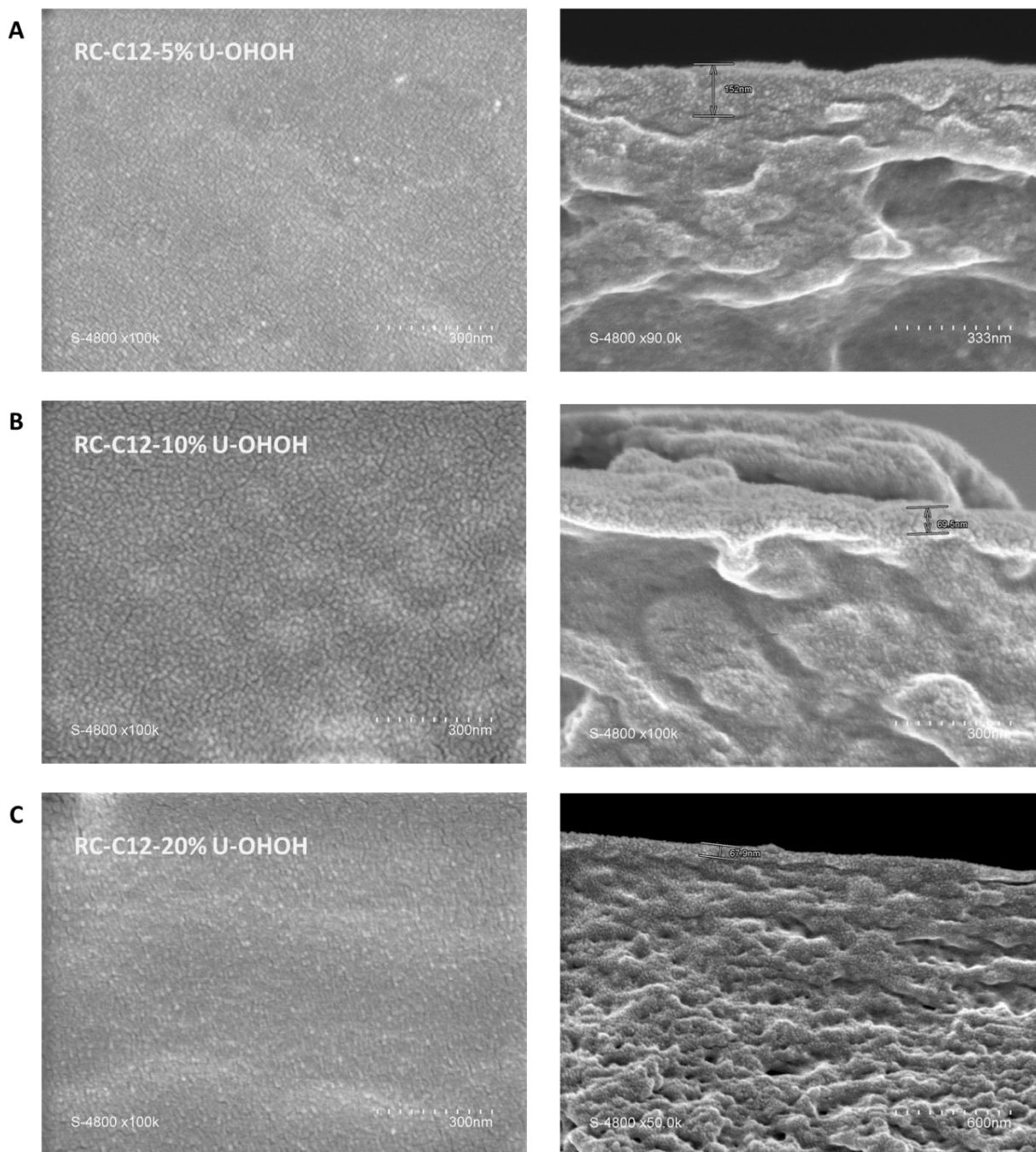
Figure 103. *Cross-section and surface SEM images of (A) RC-C12-5%* **U-OHOH** *membrane, (B) RC-C12-10%* **U-OHOH** *membrane and (C) RC-C12-20%* **U-OHOH** *membrane*

Step-by-step grafting. In a parallel work, we functionalized RC membranes using a quasi-layer by layer technique. Rationalizing that the membranes had a porosity of up to 2nm (estimated from the MWCO value), we did a step-by-step molecular functionalization of the membranes in an effort to obtain selective domains in the dense porous regions of the RC top layer. For this, we used heterogeneous reactions for the functionalization of the cellulose hydroxyl groups. (Fig. 104)
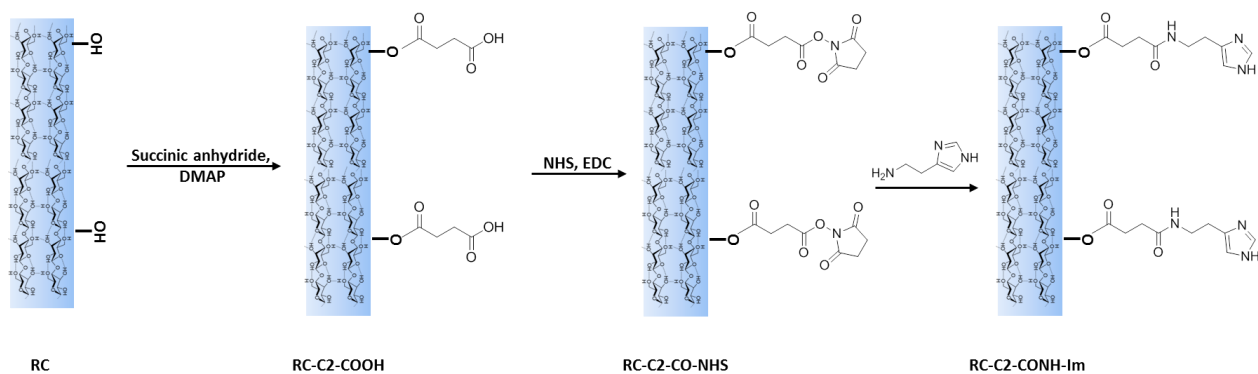
Figure 104. *Step-by-step grafting of RC membranes*

As a linker, we used succinic anhydride, which after reaction leaves a carboxylic group on the surface of the membrane. We followed with an amide coupling, linking the imidazole functional group using histamine as the coupled amine. In order for the coupling to be successful, we preliminarily activated the carboxylic group by transforming it into a N-succinate (RC-C2-CO-NHS). The reactions were followed by ATR-FTIR spectroscopy, showing the corresponding changes in vibrational signals after each reaction. (Fig. 105)
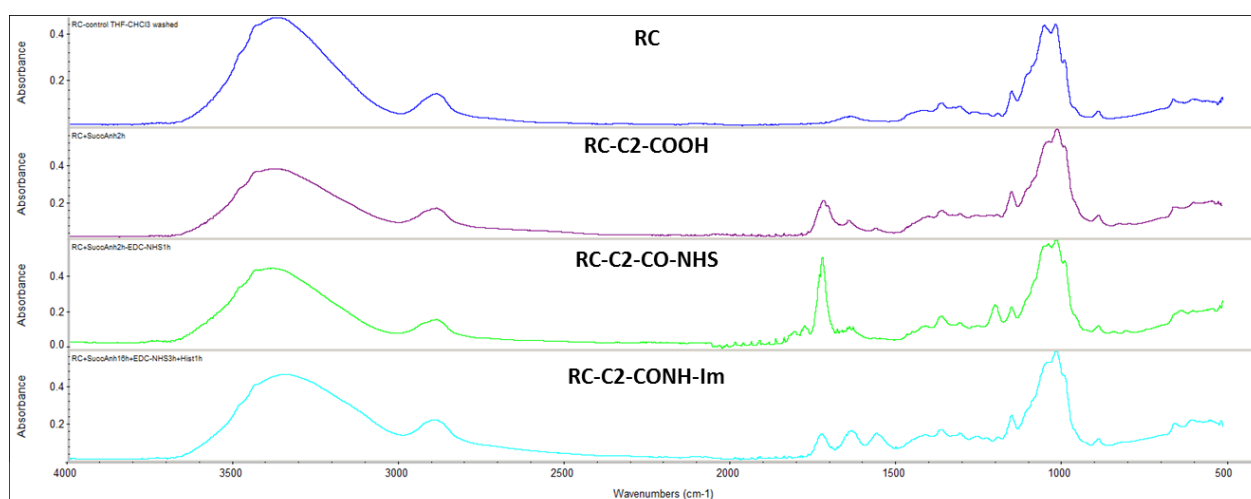
Figure 105. *ATR-FTIR spectra of step-by-step functionalization of RC membranes*

Forward osmosis experiments. Cellulose based membranes are prone to compaction under applied pressure normally used in a RO setup, as so in order to evaluate the performance of the membranes we prepared a forward osmosis setup and subsequently tested the membranes.[101–103] We tested the permeability gravimetrically and the rejection by conductivity measurements using a 1M NaCl draw solution and pure water as feed. (Fig. 106)

Membrane cell

Pump

Pump

Connectors

1M NaCl

H₂O

Support

Scale
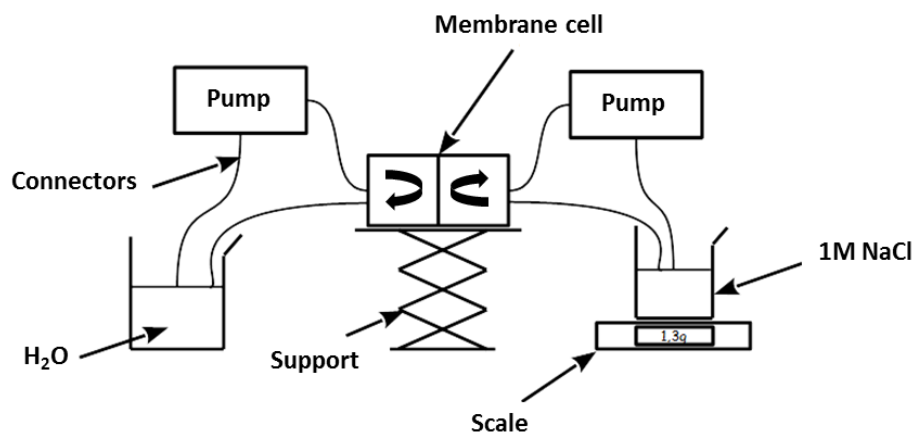
Figure 106. *Forward osmosis setup scheme*

For a typical FO experiment, the membranes were fixed between two circulation blocks with the functionalized surface towards the feed solution. Two pumps on each side ensure the mixing of solutions at the membrane interface. Due to the osmotic pressure water will tend to flow towards the concentrated solution. Measuring the weight change over time on the draw side we can determine the permeability of the membrane. In the same time, recording the conductivity on the feed side we can monitor the salt backflow, thus determining the selectivity of the membrane. The permeability of the membranes was expressed by the flux of water, J_w LMH, while the salt backflow in gMH. (Fig. 107)

Membrane	J_w (LMH)	J_s (gMH)
RC	1.92179594	87.9872286
RC-C12	-	-
RC-C12-5%-U-OHOH	-	-
RC-C12-10%-U-OHOH	-	-
RC-C12-20%-U-OHOH	1.80757	82.3781
RC-C2-COOH	5.55052864	40.2370419
RC-C2-CONH-Im	1.83823959	69.2904668

Figure 107. *Membrane performances in forward osmosis experiment*

As expected, the brush grafted membrane RC-C12 presented no water flux. The main factor for this is the hydrophobic nature of the surface from the presence of the dodecyl chains in the grafted polymer. Although the presence of the compound was confirmed by FTIR, the membranes with 5% and 10% weight ratio of **U-OHOH** remained impermeable. At 20% the membrane showed similar performances as the control RC membrane. This can suggest that at this concentration the compound is severely disrupting the formation of a dense brush layer and the performance will be mainly dictated by the underlying RC layer. Improved performance was obtained with the step-by-step grafted membranes. Interestingly, the most performing membrane obtained was the glutarate functionalized

membrane RC-C2-COOH, as opposed to the expected imidazole bearing membrane RC-C2-CONH-Im. It appears that charged surface provided by the RC-C2-COOH membrane is mainly responsible for the decrease in salt backflow and the increase in water permeability. This can be argued by the fact that the carboxyl group offers a more wettable interface with water, hence the increase in flux, while the decrease in salt flux is due to the charge repulsion between the carboxylate and the chloride anions. By coupling the imidazole group to the carboxylate we remove the charge and the flux drops back to the one obtained for the control membrane. A percentage of the salt flux reduction is preserved, which is most probably due to the added hydrogen bonding networks brought by the imidazole heads.

Conclusions. This work shows the successful functionalization of RC membranes through two different chemical grafting methods. Although regenerated cellulose membranes have been functionalized with brush polymers to obtain certain surface properties,[126–128] there have not been yet reported membranes of this type for desalination applications. Having obtained membranes with increased water flux in comparison with the blank membranes, it shows that surface modifications are a viable tool for modifying regenerated cellulose membranes in order to tailor their filtration and separation properties. Brush growth can provide a dense rejection layer for saline solutions. It remains to find the appropriate brush constitution for obtaining a selective water filtration layer.

4.4 Experimental

4.4.1 TFN membranes

Materials

Trimesoyl chloride (TMC) 98%, m-phenylenediamine (MPD) 99%, sodium chloride (NaCl) ≥ 99,5% were purchased from Sigma-Aldrich. Chemicals were dissolved in DI (deionized) water or hexane prior membrane fabrication. DI water was always obtained from a Milli-Q purification system. Polyethersulfone (PES) ultrafiltration membranes M-PS20-GPET (Nanostone Water, USA) were used as support layers for the fabrication of active thin films. All the reagents and solvents mentioned above were used without any further purifications or anhydrizations.

Nanocrystal formation

A solution of **HC8** in MeOH with a concentration of 100 mM or 200 mM was prepared and used a stock solution. 50 µL of this solution was then injected into 10 mL of DI water and sonicated for 5 min. The obtained nanocrystal solutions were used without further purification for the preparation of the TFN membranes. Dynamic light scattering (DLS) analysis was performed using Zetasizer Nano-S (Malvern Inc.).
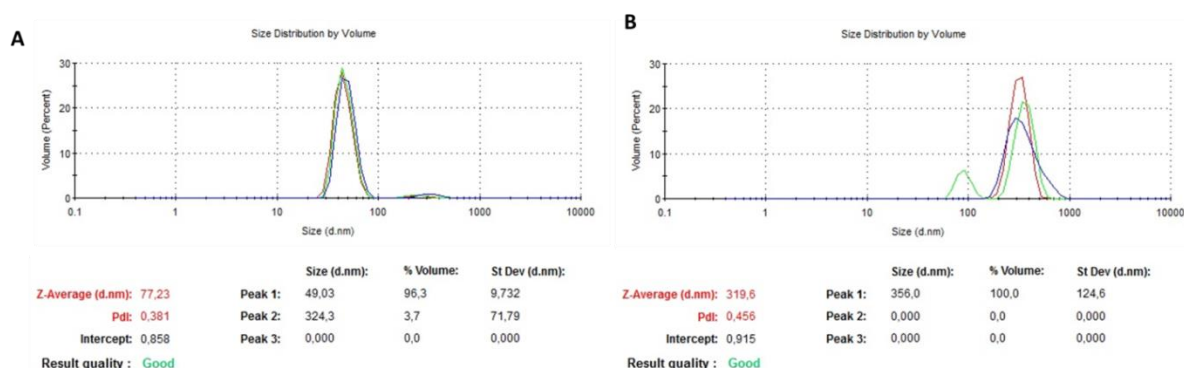
Figure 108. *Dynamic light scattering results for (A) 1 mM nanocrystal solution and (B) 2 mM nanocrystal solution*

Polyamide membranes fabrication

TFC: Thin polyamide active layers were cast on top of commercial PES support membranes via a traditional interfacial polymerization approach. The support membrane was taped onto a stainless steel plate to leave only the topmost surface available for the reaction. It was then placed in a 3 wt. % aqueous solution of MPD for 120 seconds. An air gun was used to remove the excess solution from the membrane surface. The membrane was then immersed in a 0.15 wt. % TMC hexane solution for 120 seconds. During this step, the ultra-thin polyamide layer formed. The composite membrane was then cured in DI water for 2 hours and subsequently tested in the filtration cell.

TFN-rt: A 3 wt. % MPD solution was prepared at room temperature in the respective nanocrystal solution. The excess MPD solution was removed using an air gun. The membrane was then immersed in a 0.15 wt. % TMC hexane solution for 120 seconds. The composite membrane was then cured in DI water for 2 hours and subsequently tested in the filtration cell.

TFN-60: A 3 wt. % MPD solution was prepared at 60°C in the respective HC8/water solution. The solution was immediately poured over the PES membrane and left to cool down for 5 min. The excess MPD solution was removed using an air gun. The membrane was then immersed in a 0.15 wt. % TMC hexane solution for 120 seconds. The composite membrane was then cured in DI water for 2 hours and subsequently tested in the filtration cell.

Membrane characterization

SEM imaging. Surface and cross-sectional micrographs of each membrane were imaged using a Hitachi S-4800 Scanning Electron Microscope Field Emission Gun (SEM-FEG), after drying samples overnight. A sputter coater was used to coat surface samples for 30 s and cross-sectional samples for 45 s with platinum. Hitachi S-4800 software was used to determine the average membrane thickness measured at three different locations for each membrane sample using a digital micrometer.

Contact angle. Water contact angles of TFC membranes were measured with the sessile drop method using a video contact angle system from GBX Instruments (France). Water contact angle was taken on the membrane active layers. Water drop volume was 3 μL. Room temperature was maintained at 24-25 °C during the measurements. To account for significant variations between different measurements on the same substrate, caused by surface roughness and/or chemical heterogeneities, at least three locations on three independent samples were tested, and the results were averaged for all measurements. A computer software (Digidrop) was used to determine the contact angle on both sides of a drop.

Membrane	Contact Angle
TFC	66.11±5.2
TFN-1mM-rt	70.2±1.2
TFN-1mM-60	82.54±2.5

Figure 109. *Measured contact angles of TFC – TFN membranes*

Reverse osmosis membrane filtration experiments

Pure water flux (J_w) and salt rejection (R) of the fabricated membranes were evaluated in a laboratory-scale dead-end filtration system Sterlitech, mod. HP4750. (Fig. 110) Membrane samples were clamped into the dead-end cell, where 25 °C DI water was circulated throughout the feed loop at an applied pressure (ΔP) of 10 bar) for 2 h to allow the membranes to equilibrate and the system to reach steady state.
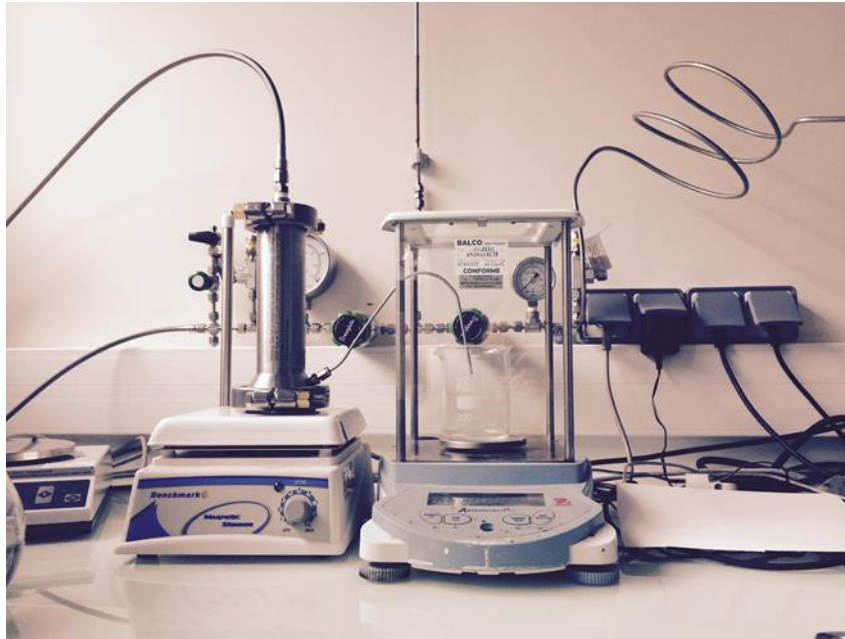
Figure 110. *Sterlitech HP4750 dead-end filtration system*

The effective membrane area was 12.56 cm^2. Pure water flux was measured gravimetrically and the intrinsic water permeability was calculated by dividing the water flow by the membrane area and by the net operating pressure applied across the membrane. Subsequently, 2000 ppm of NaCl was added to the feed, and after allowing the system to reach steady-state conditions, salt rejection was measured by keeping the applied pressure ΔP at 10 bar and measuring NaCl rejection using a conductivity meter and then converting electric conductivity into salt concentration via a calibration curve. (Fig. 111) All the conductivity measurements to determine the salt concentration were performed using an electrical conductivity meter EC/TDS/Temperature Tester DiST5, Hanna Instruments. The observed salt rejection was determined as: R(%) = 100 × (1 −(C_p/C_f)), where C_p and C_f are the salt concentration of the permeate and feed solutions, respectively.
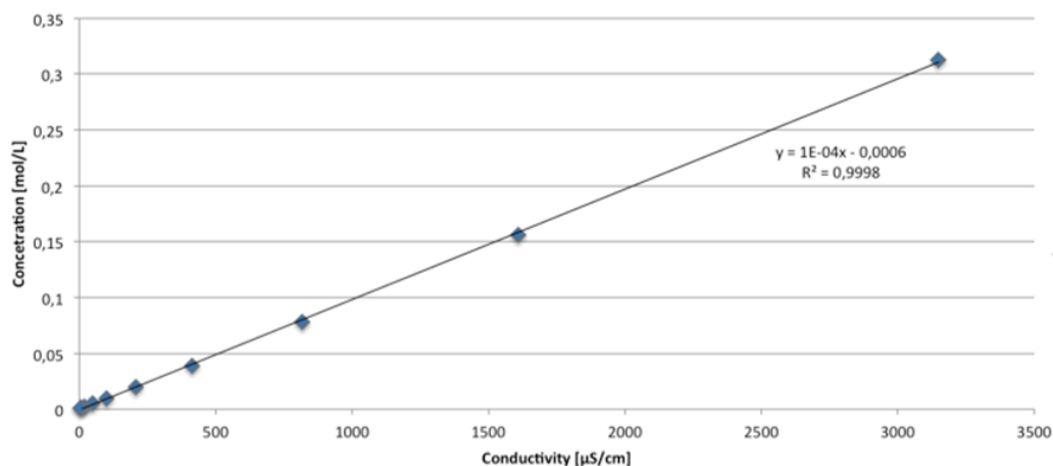
Figure 111. *Calibration curve of Hanna conductivity meter*

4.4.2   RC membranes

Materials

Regenerated cellulose membrane with a molecular weight cut-off (1 kDa MWCO) was provided by Millipore. Dodecyl methacrylate 99%, 2-Bromoisobutyryl Bromide 99% (BIBB), copper bromide (II) 99%, triethylamine 99%, N,N,N',N'',N''-Pentamethyldiethylenetriamine 99% (PMDETA), succinic anhydride 99%, N-Hydroxysuccinimide (NHS) 98%, 1-Ethyl-3-(3-dimethylaminopropyl)carbodiimide (EDC) 98%, 4-Dimethylaminopyridine (DMAP) 98% and L-ascorbic acid 99% were purchased from Sigma-Aldrich. Acetonitrile (AcCN), ethanol (EtOH) and chloroform (CHCl$_3$) were purchased from VWR. All products were used without any further purification

ARGET ATRP polymer brush grafting

Initiator immobilization: Ultrafiltration membranes (1 kDa MWCO) from for Millipore were rinsed by floating the discs with the glossy side down in a beaker containing distilled water for 1h. The membranes were washed with AcCN and an AcCN/CHCl$_3$ 1:1 v/v mixture. For the immobilization of the surface initiator, the membranes were suspending in 25 ml of AcCN/CHCl$_3$ 1:1 v/v mixture followed by the addition of 2 ml of triethylamine. After cooling the solution in an ice bath, 0.4 ml of 2-Bromoisobutyryl Bromide was added and the membranes were left to react for 15 minutes. The membranes were then washed with a mixture AcCN/CHCl$_3$ 1:1 v/v and kept in EtOH until further use.

RC-C12: For the grafting reaction, one membrane was added to a 50 ml cap screw glass container. A solution containing 5 g dodecyl methacrylate in 5 ml EtOH is added on to the membrane followed by the addition of 1 ml of CuBr2/PMDETA 0.01:0.1 mM solution in EtOH. 10 ml of EtOH containing 1 mM L-Ascorbic Acid was added and the container was

closed and kept at 60°C for 16h. The membrane was removed and rinsed with EtOH and H$_2$O and kept refrigerated in a mixture of H$_2$O/EtOH 10:1 v/v until further use.

RC-C12-U-His, RC-C12-U-OHOH: For the mixed grafting reaction, one membrane was added to a 50 ml cap screw glass container. A solution containing a mix of 5 g of dodecyl methacrylate with 5, 10 or 20 % custom methacrylate in 5 ml EtOH is added on to the membrane followed by the addition of 1 ml of CuBr2/PMDETA 0.01:0.1 mM solution in EtOH. 10 ml of EtOH containing 1 mM L-Ascorbic Acid was added and the container was closed and kept at 60°C for 16h. The membrane was removed and rinsed with EtOH and H$_2$O and kept refrigerated in a mixture of H$_2$O/EtOH 10:1 v/v until further use.

Single layer grafting of ureido-imidazole

RC-C2-COOH. Ultrafiltration membranes (1 kDa MWCO) from for Millipore were rinsed by floating the discs with the glossy side down in a beaker containing distilled water for 1h. The excess water was removed using a Kim wipe tissue and the disc was mounted into the reactor. The surface was rinsed several times with AcCN followed by an AcCN/CHCl$_3$ 1:1 v/v mixture. A solution containing 200 mg (2 mmol) of succinic anhydride and 244 mg (2 mmol) of DMAP in 30 ml CHCl$_3$ was poured into the reactor, sealed and left in a preheated oven at 60°C for 16h. After removal of the solution, the membrane was rinsed thoroughly with an AcCN/CHCl$_3$ 1:1 v/v mixture to ensure the removal of any unbound compounds followed rinsing with DI water. The membrane was kept in DI water until further use.

RC-C2-CONH-Im. The previously obtained RC-C2-COOH membrane was used without any pretreatment. A solution of 57.5 mg (0.5 mmol) NHS and 47.75 mg (0.25 mmol) EDC in 5 ml PB buffer, pH=6.4O was poured over the membrane and left to react for 2h at room temperature. The solution was removed and the membrane was thoroughly washed with DI water. A solution of 0.3% histamine in water was then poured over the membrane and left to react for 1h. The membrane was washed with DI water to remove any unreacted compounds. The membrane was kept refrigerated in a mixture of H$_2$O/EtOH 10:1 v/v until further use.

Membrane characterization

Infrared spectroscopy. FTIR-ATR measurements were performed with a Nicolet Nexus FT-IR spectrometer equipped with an ATR Diamant Golden Gate. The resolution was fixed to 4 cm^{-1} and a scan range of 500-4000 cm^{-1}. The acquisition of the spectra was made in transmittance mode with 32 scans. Membrane strips of 1 cm^2 were used for analysis, with the functional surface facing the scanning surface.

SEM imaging. Surface and cross-sectional micrographs of each membrane were imaged using a Hitachi S-4800 Scanning Electron Microscope Field Emission Gun (SEM-FEG), after drying samples overnight. A sputter coater was used to coat surface samples for 30 s and cross-sectional samples for 45 s with platinum. Hitachi S-4800 software was used to

determine the average membrane thickness measured at three different locations for each membrane sample using a digital micrometer.

Forward osmosis membrane filtration experiments

Water flux (J_w) and salt leakage (J_s) of the fabricated membranes was evaluated in a custom made laboratory-scale forward osmosis filtration system. (Fig. 112) The membranes were clamped between two rubber rings and fixed between Teflon circulation cells. Each cell contained an attached rigid net to increase turbulence near the membrane surface. The cells were connected to their respective solutions by polypropylene tubes with a 0.8 cm diameter. Circulation of the solutions was insured by two Watson-Marlow Sci-Q 300 Series peristaltic pumps. A constant flow rate of 1ml/min was maintained through all of the experiments. A solution of 1 M of NaCl in DI water was used as a draw solution and pure water as feed. In a typical experiment, the membranes are left to equilibrate for 30 min after which the water flux across the membrane is measured by registering the change in weight of the draw solution each 5 min for 45 min. The water permeation flux, Jw, was then determined based on the weight change of the feed and the effective membrane area (A) using the equation:

$$J_w = \frac{\Delta m}{\Delta t} \frac{1}{A}$$

where Δm is the weight of water permeated from the feed to the draw solution over a predetermined time Δt during the FO tests. The salt leakage, J_s, in the FO tests refers to the salt reversely permeating from the draw solution to the feed. The value of J_s was determined from the increase in the feed conductivity:

$$J_s = \frac{(C_t V_t) - (C_0 V_0)}{\Delta t} \frac{1}{A}$$

where C_0 (mol L^{-1}) and V_0 (L) are the initial salt concentration and the initial volume of the feed, respectively, while C_t (mol L^{-1}) and V_t (L) are the salt concentration and the volume of the feed at time t, respectively, during the FO tests.

Figure 112. *Custom made forward osmosis filtration system*

Conclusions

Biological systems have proved extremely efficient in their functionality, surpassing synthetic methods and becoming integrated parts of bioassisted technologies. In an effort to reduce the structural complexity yet maintain their functional efficiency, biomimetic systems have emerged. Aquaporin proteins are at present the most efficient water transporting system that is able to maintain high selectivity. This property has made it an important tool for the fabrication of desalination membranes yet issues of production and stability render them difficult to work with. Several synthetic approaches have been attempted to reproduce their high water permeability and selectivity having obtained moderate success. As described in the first chapter, there is generally a tradeoff between permeability and selectivity, the difficulty lies in bringing together these desired functions in the designed artificial systems without increasing the complexity of the systems themselves.

The work described here presented results that are both fundamental and applicative towards the design of artificial water transport systems. From a fundamental point of view, the second chapter presents detailed work towards the description of water transport mechanism in confined media. We have demonstrated that by using the appropriate design, small organic molecules can self-assemble into functional supramolecular systems. The imidazole-based compounds have proved a simple tool for obtaining an Aquaporin mimic system. Simple synthetic procedures allowed us to obtain highly selective and efficient artificial water channels. Solid state structures presented single file water wires with dipolar orientation, very similar to the structure of water molecules found in the pores of the Aquaporin. Water transport capacity was demonstrated through stopped flow experiments in vesicular systems, showing transport rates of only two orders of magnitude lower than their biological counterparts while maintaining selectivity for water in saline solutions. Molecular dynamic simulations of imidazole channels in lipid bilayers have reinforced the proposed water translocation through these assemblies. Pressure dependence and structure influence on the stability and water translocation through the channels have been correlated. The energetics of the hydrogen bonding network of water - HCx channel systems have been studied in detail, mapping the interactions for all analogs of HC8 channels, showing that in the case of the R-HC8 molecules there is almost no energy penalty for water to move in and out of the channels. Furthermore, we have provided the first physical proof of oriented water molecules inside the lipid-embedded channels, through the use of sum frequency generated experiments. This has proved that the channels indeed exist in an active form in the bilayer, ordering water molecules into a preferential dipolar structure.

In the third chapter, we have presented alternatives for the formation of novel artificial water channels, proving that the concept of self-assembly can be extended through several designs in order to obtain functional artificial water channels. By exploring several

moieties that are capable of providing a favorable donor-acceptor network, we have found that the 1,3 – propylene diol functionality can act as water binder, show channel-like structures in solid state and present water transport activity in stopped flow experiments. Even more, the DC8 channels proved to be selective for water against both NaCl and protons. Even though we have obtained a channel-like structure with the pyridine-based compounds, no water transport activity could be recorded. On the other hand, we managed to obtain huge increases in water transport when using the DOTAx compounds. Although the systems are not selective for water, the magnitude of induced water permeability in vesicular systems is remarkable. With the early results from the molecular dynamics simulations, we have proposed a mechanism of water transport, having observed that water translocation takes place between the stacks of the DOTA compounds. A rather special scaffold for water channels, the triarylamines are a viable approach for the design of self-assembling channels, having observed incubation time-dependent water permeability increases.

The fourth chapter of the thesis presented work that was directed more towards the applicative side. In a first attempt to valorize the artificial water channels, thin film nanocomposite membranes using integrated HC8 particles and modified regenerated cellulose membranes with either imidazole or diol compounds were designed and fabricated. In the case of nanocomposite membranes, the transition from molecular assemblies to functional materials was attempted through the use of nanocrystals. Membranes based on polyamide selective layers incorporating HC8 particles were prepared. The obtained early filtration results show that there is indeed an effect of incorporating the channels into the thin layer polymer. We observed an increase of water permeability for the membranes obtained with HC8 nanoparticles recrystallized from high temperature, although the slight decrease in rejection reduces the final performance of these membranes. In the case of the modified cellulose membranes, two different approaches have been used. Reconstruction of water channel domains was attempted through the growth of surface polymer brushes and through the step-by-step chemical modification of the pores of the membranes. The chemical grafting was proved by both SEM imaging as well as through ATR-FTIR analysis. The membranes were tested in a forward osmosis setup, having obtained increase permeability for the step-by-step modified membranes. The polymer brush membranes proved either impermeable, at low custom monomer content, or inefficient for water transport and salt rejection.

The work done here opens up perspectives for future development in the field of artificial water channels. From a fundamental point of, even more in-depth studies should be conducted on the imidazole channels in order to determine the relationship between the orientation of the water wires and the constitution of the lipid bilayer. The influence of bilayer polarization, hydrophobic pressure, and ionic strength could be determined. For the novel artificial water channels, similar sum frequency generation experiments and more complex molecular dynamics simulations can be conducted in order to determine an

accurate mechanism for the water transport. Chemical modifications, such as quaternary amine formation can be envisaged for the DOTAx compounds in order to remove their cation binding capability, while suitable pending arms can be used for the pyridine compounds to make them compatible with the lipid bilayer while still preserving their water transport properties. For the fabrication of efficient membrane materials, adjustments to the work methods can be brought. The nanocrystal formation can be controlled by varying both the solvents used as well as the temperature, in order to obtain smaller homogenous particles that could be better inserted into the thin polyamide layer. For the brush grafted membranes, various custom monomers could be tried, introducing more moieties that could direct the formation of the water channels domain.

Overall, the field of artificial water channels is still in its early ages. We have successfully described several designs that function, on a nanomolecular scale, as selective water transporters. Further developing the molecular design of the building blocks for the formation of the channels could result in even more efficient and stable water channels. Thus research in this area is important if we intend to expand our knowledge on biomimetic systems. As mentioned at the beginning of this thesis, my personal belief is that research should be conducted towards the benefit of humanity, as so I believe that the next step for development in this field of research should be the fabrication of functional desalination membranes. Using the principle of artificial water channels to obtain membranes that are cost-effective, new biomimetic membrane materials could provide fresh water for the entire population of the globe.

References

1. Guo, Z., Zhou, F., Hao, J. & Liu, W. Stable Biomimetic Super-Hydrophobic Engineering Materials. *J. Am. Chem. Soc.* **127,** 15670–15671 (2005).
2. Ahn, B. K. *et al.* High-performance mussel-inspired adhesives of reduced complexity. *Nat. Commun.* **6,** 8663 (2015).
3. Agre, P. Aquaporin Water Channels (Nobel Lecture). *Angew. Chem. Int. Ed.* **43,** 4278–4290 (2004).
4. Benga, G. Water channel proteins (later called aquaporins) and relatives: Past, present, and future. *IUBMB Life* **61,** 112–133 (2009).
5. de Groot, B. L. & Grubmüller, H. The dynamics and energetics of water permeation and proton exclusion in aquaporins. *Curr. Opin. Struct. Biol.* **15,** 176–183 (2005).
6. Savage, D. F., Egea, P. F., Robles-Colmenares, Y., Iii, J. D. O. & Stroud, R. M. Architecture and Selectivity in Aquaporins: 2.5 Å X-Ray Structure of Aquaporin Z. *PLoS Biol.* **1,** 72 (2003).
7. Tajkhorshid, E. Control of the Selectivity of the Aquaporin Water Channel Family by Global Orientational Tuning. *Science* **296,** 525–530 (2002).
8. Agmon, N. The Grotthuss mechanism. *Chem. Phys. Lett.* **244,** 456–462 (1995).
9. Akbarzadeh, A. *et al.* Liposome: classification, preparation, and applications. *Nanoscale Res. Lett.* **8,** 102 (2013).
10. Patil, Y. P. & Jadhav, S. Novel methods for liposome preparation. *Chem. Phys. Lipids* **177,** 8–18 (2014).
11. Tong, J., Briggs, M. M. & McIntosh, T. J. Water Permeability of Aquaporin-4 Channel Depends on Bilayer Composition, Thickness, and Elasticity. *Biophys. J.* **103,** 1899–1908 (2012).
12. Mathai, J. C., Tristram-Nagle, S., Nagle, J. F. & Zeidel, M. L. Structural Determinants of Water Permeability through the Lipid Membrane. *J. Gen. Physiol.* **131,** 69–76 (2008).
13. Eliasson, J. The rising pressure of global water shortages. *Nature* **517,** 6–7 (2015).
14. Mekonnen, M. M. & Hoekstra, A. Y. Four billion people facing severe water scarcity. *Sci. Adv.* **2,** 1500323–1500323 (2016).
15. Schewe, J. *et al.* Multimodel assessment of water scarcity under climate change. *Proc. Natl. Acad. Sci.* **111,** 3245–3250 (2014).
16. Geise, G. M. *et al.* Water purification by membranes: The role of polymer science. *J. Polym. Sci. Part B Polym. Phys.* **48,** 1685–1718 (2010).
17. Tang, C. Y., Zhao, Y., Wang, R., Hélix-Nielsen, C. & Fane, A. G. Desalination by biomimetic aquaporin membranes: Review of status and prospects. *Desalination* **308,** 34–40 (2013).
18. Habel, J. *et al.* Aquaporin-Based Biomimetic Polymeric Membranes: Approaches and Challenges. *Membranes* **5,** 307–351 (2015).
19. Ding, W. *et al.* Fabrication of an aquaporin-based forward osmosis membrane through covalent bonding of a lipid bilayer to a microporous support. *J Mater Chem A* **3,** 20118–20126 (2015).
20. Kumar, M., Habel, J. E. O., Shen, Y., Meier, W. P. & Walz, T. High-Density Reconstitution of Functional Water Channels into Vesicular and Planar Block Copolymer Membranes. *J. Am. Chem. Soc.* **134,** 18631–18637 (2012).
21. Kumar, M., Grzelakowski, M., Zilles, J., Clark, M. & Meier, W. Highly permeable polymeric membranes based on the incorporation of the functional water channel protein Aquaporin Z. *Proc. Natl. Acad. Sci.* **104,** 20719–20724 (2007).

22. Zhao, Y. *et al.* Synthesis of robust and high-performance aquaporin-based biomimetic membranes by interfacial polymerization-membrane preparation and RO performance characterization. *J. Membr. Sci.* **423–424,** 422–428 (2012).

23. Gerstein, M. & Levitt, M. Simulating water and the molecules of life. *Sci. Am.* **279,** 100–105 (1998).

24. Yoshizawa, M. *et al.* Endohedral Clusterization of Ten Water Molecules into a 'Molecular Ice' within the Hydrophobic Pocket of a Self-Assembled Cage. *J. Am. Chem. Soc.* **127,** 2798–2799 (2005).

25. Mitra, T. *et al.* Gated and Differently Functionalized (New) Porous Capsules Direct Encapsulates' Structures: Higher and Lower Density Water. *Chem. - Eur. J.* **15,** 1844–1852 (2009).

26. Hu, X.-B., Chen, Z., Tang, G., Hou, J.-L. & Li, Z.-T. Single-Molecular Artificial Transmembrane Water Channels. *J. Am. Chem. Soc.* **134,** 8384–8387 (2012).

27. Shen, Y. *et al.* Highly permeable artificial water channels that can self-assemble into two-dimensional arrays. *Proc. Natl. Acad. Sci.* **112,** 9810–9815 (2015).

28. Sun, X., Su, X., Wu, J. & Hinds, B. J. Electrophoretic Transport of Biomolecules through Carbon Nanotube Membranes. *Langmuir* **27,** 3150–3156 (2011).

29. Majumder, M., Zhan, X., Andrews, R. & Hinds, B. J. Voltage Gated Carbon Nanotube Membranes. *Langmuir* **23,** 8624–8631 (2007).

30. Sanip, S. M. *et al.* Gas separation properties of functionalized carbon nanotubes mixed matrix membranes. *Sep. Purif. Technol.* **78,** 208–213 (2011).

31. Thomas, J. A. & McGaughey, A. J. H. Water Flow in Carbon Nanotubes: Transition to Subcontinuum Transport. *Phys. Rev. Lett.* **102,** (2009).

32. Pascal, T. A., Goddard, W. A. & Jung, Y. Entropy and the driving force for the filling of carbon nanotubes with water. *Proc. Natl. Acad. Sci.* **108,** 11794–11798 (2011).

33. Liu, L., Yang, C., Zhao, K., Li, J. & Wu, H.-C. Ultrashort single-walled carbon nanotubes in a lipid bilayer as a new nanopore sensor. *Nat. Commun.* **4,** (2013).

34. Lopez, C. F., Nielsen, S. O., Moore, P. B. & Klein, M. L. Understanding nature's design for a nanosyringe. *Proc. Natl. Acad. Sci. U. S. A.* **101,** 4431–4434 (2004).

35. Kim, K. *et al.* Osmotically-Driven Transport in Carbon Nanotube Porins. *Nano Lett.* **14,** 7051–7056 (2014).

36. Geng, J. *et al.* Stochastic transport through carbon nanotubes in lipid bilayers and live cell membranes. *Nature* **514,** 612–615 (2014).

37. Tunuguntla, R. H., Allen, F. I., Kim, K., Belliveau, A. & Noy, A. Ultrafast proton transport in sub-1-nm diameter carbon nanotube porins. *Nat. Nanotechnol.* **11,** 639–644 (2016).

38. Peter, C. & Hummer, G. Ion Transport through Membrane-Spanning Nanopores Studied by Molecular Dynamics Simulations and Continuum Electrostatics Calculations. *Biophys. J.* **89,** 2222–2234 (2005).

39. Corry, B. Designing Carbon Nanotube Membranes for Efficient Water Desalination. *J. Phys. Chem. B* **112,** 1427–1434 (2008).

40. Holt, J. K. Fast Mass Transport Through Sub-2-Nanometer Carbon Nanotubes. *Science* **312,** 1034–1037 (2006).

41. Fornasiero, F. *et al.* Ion exclusion by sub-2-nm carbon nanotube pores. *Proc. Natl. Acad. Sci.* **105,** 17250–17255 (2008).

42. Koshland, D. E. The Key–Lock Theory and the Induced Fit Theory. *Angew. Chem. Int. Ed. Engl.* **33,** 2375–2378 (1995).

43. Lehn, J.-M. Supramolecular chemistry - Scope and perspectives: Molecules, Supermolecules, and Molecular devices. *Angew. Chem. Int. Ed. Engl.* **27,** 89-112 (1988).

44. Pedersen, C. J. Cyclic polyethers and their complexes with metal salts. *J. Am. Chem. Soc.* **89,** 7017–7036 (1967).

45. Lehn, J.-M. *Supramolecular Chemistry: Concepts and Perspectives*. (Wiley-VCH Verlag GmbH & Co. KGaA, 1995). doi:10.1002/3527607439

46. Mattia, E. & Otto, S. Supramolecular systems chemistry. *Nat. Nanotechnol.* **10,** 111–119 (2015).

47. Gale, P. A. Supramolecular chemistry: from complexes to complexity. *Philos. Trans. R. Soc. Math. Phys. Eng. Sci.* **358,** 431–453 (2000).

48. Erbas-Cakmak, S., Leigh, D. A., McTernan, C. T. & Nussbaumer, A. L. Artificial Molecular Machines. *Chem. Rev.* **115,** 10081–10206 (2015).

49. Richards, V. 2016 Nobel Prize in Chemistry: Molecular machines. *Nat. Chem.* **8,** 1090–1090 (2016).

50. Stupp, S. I. & Palmer, L. C. Supramolecular Chemistry and Self-Assembly in Organic Materials Design. *Chem. Mater.* **26,** 507–518 (2014).

51. Kang, Y. *et al.* Controllable Supramolecular Polymerization Promoted by Host-Enhanced Photodimerization. *ACS Macro Lett.* **5,** 1397–1401 (2016).

52. Palmer, L. C. & Stupp, S. I. Molecular Self-Assembly into One-Dimensional Nanostructures. *Acc. Chem. Res.* **41,** 1674–1684 (2008).

53. Huo, Y. & Zeng, H. 'Sticky'-Ends-Guided Creation of Functional Hollow Nanopores for Guest Encapsulation and Water Transport. *Acc. Chem. Res.* **49,** 922–930 (2016).

54. Zhou, X. *et al.* Self-assembling subnanometer pores with unusual mass-transport properties. *Nat. Commun.* **3,** 949 (2012).

55. Le Duc, Y. *et al.* Imidazole-Quartet Water and Proton Dipolar Channels. *Angew. Chem. Int. Ed.* **50,** 11366–11372 (2011).

56. Ball, P. Water as an Active Constituent in Cell Biology. *Chem. Rev.* **108,** 74–108 (2008).

57. Zhong, D., Pal, S. K. & Zewail, A. H. Biological water: A critique. *Chem. Phys. Lett.* **503,** 1–11 (2011).

58. Barrett, A., Imbrogno, J., Belfort, G. & Petersen, P. B. Phosphate Ions Affect the Water Structure at Functionalized Membrane Surfaces. *Langmuir* **32,** 9074–9082 (2016).

59. Cheng, J.-X., Pautot, S., Weitz, D. A. & Xie, X. S. Ordering of water molecules between phospholipid bilayers visualized by coherent anti-Stokes Raman scattering microscopy. *Proc. Natl. Acad. Sci.* **100,** 9826–9830 (2003).

60. Hummer, G. & Tokmakoff, A. Preface: Special Topic on Biological Water. *J. Chem. Phys.* **141,** 22D101 (2014).

61. Ma, C. D., Wang, C., Acevedo-Vélez, C., Gellman, S. H. & Abbott, N. L. Modulation of hydrophobic interactions by proximally immobilized ions. *Nature* **517,** 347–350 (2015).

62. Allen, T. W., Andersen, O. S. & Roux, B. Energetics of ion conduction through the gramicidin channel. *Proc. Natl. Acad. Sci.* **101,** 117–122 (2004).

63. Barboiu, M. *et al.* An artificial primitive mimic of the Gramicidin-A channel. *Nat. Commun.* **5,** (2014).

64. Custelcean, R. Crystal engineering with urea and thiourea hydrogen-bonding groups. *Chem Commun* 295–307 (2008). doi:10.1039/B708921J

65. Mihai, S. *et al.* Supramolecular self-organization in constitutional hybrid materials. *New J. Chem.* **33,** 2335 (2009).

66. Mihai, S., Le Duc, Y., Cot, D. & Barboiu, M. Sol–gel selection of hybrid G-quadruplex architectures from dynamic supramolecular guanosine libraries. *J. Mater. Chem.* **20,** 9443 (2010).

67. Hu, F., Luo, W. & Hong, M. Mechanisms of Proton Conduction and Gating in Influenza M2 Proton Channels from Solid-State NMR. *Science* **330,** 505–508 (2010).

68. Sharma, M. *et al.* Insight into the Mechanism of the Influenza A Proton Channel from a Structure in a Lipid Bilayer. *Science* **330,** 509–512 (2010).

69. Cherezov, V., Clogston, J., Papiz, M. Z. & Caffrey, M. Room to Move: Crystallizing Membrane Proteins in Swollen Lipidic Mesophases. *J. Mol. Biol.* **357,** 1605–1618 (2006).

70. Caffrey, M. A comprehensive review of the lipid cubic phase or *in meso* method for crystallizing membrane and soluble proteins and complexes. *Acta Crystallogr. Sect. F Struct. Biol. Commun.* **71,** 3–18 (2015).

71. Höfer, N., Aragão, D. & Caffrey, M. Crystallizing Transmembrane Peptides in Lipidic Mesophases. *Biophys. J.* **99,** L23–L25 (2010).

72. Thiyagarajan, P. & Tiede, D. M. Detergent micelle structure and micelle-micelle interactions determined by small-angle neutron scattering under solution conditions used for membrane protein crystallization. *J. Phys. Chem.* **98,** 10343–10351 (1994).

73. Hosamani, B. *et al.* Membrane protein crystallization in micelles conjugated by nucleoside base-pairing: A different concept. *J. Struct. Biol.* **195,** 379–386 (2016).

74. Newby, Z. E. R. *et al.* A general protocol for the crystallization of membrane proteins for X-ray structural investigation. *Nat. Protoc.* **4,** 619–637 (2009).

75. Schmitt, C., Lippert, A. H., Bonakdar, N., Sandoghdar, V. & Voll, L. M. Compartmentalization and Transport in Synthetic Vesicles. *Front. Bioeng. Biotechnol.* **4,** (2016).

76. Elani, Y., Law, R. V. & Ces, O. Vesicle-based artificial cells as chemical microreactors with spatially segregated reaction pathways. *Nat. Commun.* **5,** 5305 (2014).

77. Chen, I. A. & Szostak, J. W. A Kinetic Study of the Growth of Fatty Acid Vesicles. *Biophys. J.* **87,** 988–998 (2004).

78. Eisenthal, K. B. Liquid interfaces probed by second-harmonic and sum-frequency spectroscopy. *Chem. Rev.* **96,** 1343–1360 (1996).

79. Nomura, K. *et al.* Water structure at the interfaces between a zwitterionic self-assembled monolayer/liquid water evaluated by sum-frequency generation spectroscopy. *Colloids Surf. B Biointerfaces* **135,** 267–273 (2015).

80. Perakis, F. *et al.* Vibrational Spectroscopy and Dynamics of Water. *Chem. Rev.* **116,** 7590–7607 (2016).

81. Licsandru, E. *et al.* Salt-Excluding Artificial Water Channels Exhibiting Enhanced Dipolar Water and Proton Translocation. *J. Am. Chem. Soc.* **138,** 5403–5409 (2016).

82. Cho, N.-J., Frank, C. W., Kasemo, B. & Höök, F. Quartz crystal microbalance with dissipation monitoring of supported lipid bilayers on various substrates. *Nat. Protoc.* **5,** 1096–1106 (2010).

83. Mahon, E., Aastrup, T. & Barboiu, M. Dynamic glycovesicle systems for amplified QCM detection of carbohydrate-lectin multivalent biorecognition. *Chem. Commun.* **46,** 2441 (2010).

84. Briand, E., Zäch, M., Svedhem, S., Kasemo, B. & Petronis, S. Combined QCM-D and EIS study of supported lipid bilayer formation and interaction with pore-forming peptides. *The Analyst* **135,** 343–350 (2010).

85. Cremer, P. S. & Boxer, S. G. Formation and Spreading of Lipid Bilayers on Planar Glass Supports. *J. Phys. Chem. B* **103,** 2554–2559 (1999).

86. Palatinus, L. & Chapuis, G. *SUPERFLIP* – a computer program for the solution of crystal structures by charge flipping in arbitrary dimensions. *J. Appl. Crystallogr.* **40,** 786–790 (2007).

87. Betteridge, P. W., Carruthers, J. R., Cooper, R. I., Prout, K. & Watkin, D. J. *CRYSTALS* version 12: software for guided crystal structure analysis. *J. Appl. Crystallogr.* **36,** 1487–1487 (2003).

88. Patra, M. *et al.* Molecular Dynamics Simulations of Lipid Bilayers: Major Artifacts Due to Truncating Electrostatic Interactions. *Biophys. J.* **84,** 3636–3645 (2003).

89. Kučerka, N., Tristram-Nagle, S. & Nagle, J. F. Structure of Fully Hydrated Fluid Phase Lipid Bilayers with Monounsaturated Chains. *J. Membr. Biol.* **208,** 193–202 (2006).

90. Barboiu, M. Artificial water channels – incipient innovative developments. *Chem Commun* **52,** 5657–5665 (2016).

91. Mani, T., Tircsó, G., Zhao, P., Sherry, A. D. & Woods, M. Effect of the Regiochemistry of Butyl Amide Substituents on the Solution-State Structures of Lanthanide(III) DOTA-Tetraamide Complexes. *Inorg. Chem.* **48,** 10338–10345 (2009).

92. Pasha, A., Tircsó, G., Benyó, E. T., Brücher, E. & Sherry, A. D. Synthesis and Characterization of DOTA-(amide)4 Derivatives: Equilibrium and Kinetic Behavior of Their Lanthanide(III) Complexes. *Eur. J. Inorg. Chem.* **2007,** 4340–4349 (2007).

93. Vipond, J. *et al.* A bridge to coordination isomer selection in lanthanide (III) DOTA-tetraamide complexes. *Inorg. Chem.* **46,** 2584–2595 (2007).

94. Hubert, J.-F. *et al.* Pore selectivity analysis of an aquaglyceroporin by stopped-flow spectrophotometry on bacterial cell suspensions. *Biol. Cell* **97,** 675–686 (2005).

95. Smart, O. S., Breed, J., Smith, G. R. & Sansom, M. S. A novel method for structure-based prediction of ion channel conductance properties. *Biophys. J.* **72,** 1109–1126 (1997).

96. Moulin, E. *et al.* The Hierarchical Self-Assembly of Charge Nanocarriers: A Highly Cooperative Process Promoted by Visible Light. *Angew. Chem. Int. Ed.* **49,** 6974–6978 (2010).

97. Nyrkova, I. *et al.* Supramolecular Self-Assembly and Radical Kinetics in Conducting Self-Replicating Nanowires. *ACS Nano* **8,** 10111–10124 (2014).

98. Licsandru, E.-D. *et al.* Self-assembly of supramolecular triarylamine nanowires in mesoporous silica and biocompatible electrodes thereof. *Nanoscale* **8,** 5605–5611 (2016).

99. Mazlan, N. M., Peshev, D. & Livingston, A. G. Energy consumption for desalination - A comparison of forward osmosis with reverse osmosis, and the potential for perfect membranes. *Desalination* **377,** 138–151 (2016).

100. Phillip, W. A., Yong, J. S. & Elimelech, M. Reverse Draw Solute Permeation in Forward Osmosis: Modeling and Experiments. *Environ. Sci. Technol.* **44,** 5170–5176 (2010).

101. Sato, N., Sato, Y. & Yanase, S. Forward osmosis using dimethyl ether as a draw solute. *Desalination* **349,** 102–105 (2014).

102. Zhao, S., Zou, L., Tang, C. Y. & Mulcahy, D. Recent developments in forward osmosis: Opportunities and challenges. *J. Membr. Sci.* **396,** 1–21 (2012).

103. Shaffer, D. L., Werber, J. R., Jaramillo, H., Lin, S. & Elimelech, M. Forward osmosis: Where are we now? *Desalination* **356,** 271–284 (2015).

104. Lee, K. P., Arnot, T. C. & Mattia, D. A review of reverse osmosis membrane materials for desalination - Development to date and future potential. *J. Membr. Sci.* **370,** 1–22 (2011).

105. Li, D. & Wang, H. Recent developments in reverse osmosis desalination membranes. *J. Mater. Chem.* **20,** 4551 (2010).

106. Mitchell, G. E., Mickols, B., Hernandez-Cruz, D. & Hitchcock, A. Unexpected new phase detected in FT30 type reverse osmosis membranes using scanning transmission X-ray microscopy. *Polymer* **52,** 3956–3962 (2011).

107. Cadotte, J. E., Petersen, R. J., Larson, R. E. & Erickson, E. E. A new thin-film composite seawater reverse osmosis membrane. *Desalination* **32,** 25–31 (1980).

108. Khorshidi, B., Thundat, T., Fleck, B. A. & Sadrzadeh, M. A Novel Approach Toward Fabrication of High Performance Thin Film Composite Polyamide Membranes. *Sci. Rep.* **6,** (2016).

109. Lau, W. J. *et al.* A review on polyamide thin film nanocomposite (TFN) membranes: History, applications, challenges and approaches. *Water Res.* **80,** 306–324 (2015).

110. Yin, J., Kim, E.-S., Yang, J. & Deng, B. Fabrication of a novel thin-film nanocomposite (TFN) membrane containing MCM-41 silica nanoparticles (NPs) for water purification. *J. Membr. Sci.* **423–424,** 238–246 (2012).

111. Zhao, H. *et al.* Improving the performance of polyamide reverse osmosis membrane by incorporation of modified multi-walled carbon nanotubes. *J. Membr. Sci.* **450,** 249–256 (2014).

112. Zhu, B. *et al.* Application of robust MFI-type zeolite membrane for desalination of saline wastewater. *J. Membr. Sci.* **475,** 167–174 (2015).

113. Jeong, B.-H. *et al.* Interfacial polymerization of thin film nanocomposites: A new concept for reverse osmosis membranes. *J. Membr. Sci.* **294,** 1–7 (2007).

114. Baba, K., Kasai, H., Nishida, K. & Nakanishi, H. Functional Organic Nanocrystals. in *Nanocrystal* (InTech, 2011).

115. Fateminia, S. M. A. *et al.* Nanocrystallization: A Unique Approach to Yield Bright Organic Nanocrystals for Biological Applications. *Adv. Mater.* **29,** 1604100 (2017).

116. Rosenne, S. *et al.* Self-Assembled Organic Nanocrystals with Strong Nonlinear Optical Response. *Nano Lett.* **15,** 7232–7237 (2015).

117. Wandera, D., Wickramasinghe, S. R. & Husson, S. M. Modification and characterization of ultrafiltration membranes for treatment of produced water. *J. Membr. Sci.* **373,** 178–188 (2011).

118. Wandera, D., Himstedt, H. H., Marroquin, M., Wickramasinghe, S. R. & Husson, S. M. Modification of ultrafiltration membranes with block copolymer nanolayers for produced water treatment: The roles of polymer chain density and polymerization time on performance. *J. Membr. Sci.* **403–404,** 250–260 (2012).

119. Grimaldi, J., Imbrogno, J., Kilduff, J. (Chip) & Belfort, G. New Class of Synthetic Membranes: Organophilic Pervaporation Brushes for Organics Recovery. *Chem. Mater.* **27,** 4142–4148 (2015).

120. Gu, M., Kilduff, J. E. & Belfort, G. High throughput atmospheric pressure plasma-induced graft polymerization for identifying protein-resistant surfaces. *Biomaterials* **33,** 1261–1270 (2012).

121. Imbrogno, J., Williams, M. D. & Belfort, G. A New Combinatorial Method for Synthesizing, Screening, and Discovering Antifouling Surface Chemistries. *ACS Appl. Mater. Interfaces* **7,** 2385–2392 (2015).

122. Zonca, M. R., Yune, P. S., Heldt, C. L., Belfort, G. & Xie, Y. High-Throughput Screening of Substrate Chemistry for Embryonic Stem Cell Attachment, Expansion, and Maintaining Pluripotency: High-Throughput Screening of Substrate Chemistry *Macromol. Biosci.* **13,** 177–190 (2013).

123. Kang, C., Crockett, R. M. & Spencer, N. D. Molecular-Weight Determination of Polymer Brushes Generated by SI-ATRP on Flat Surfaces. *Macromolecules* **47,** 269–275 (2014).

124. Tugulu, S. *et al.* Synthesis of Poly(methacrylic acid) Brushes via Surface-Initiated Atom Transfer Radical Polymerization of Sodium Methacrylate and Their Use as Substrates for the Mineralization of Calcium Carbonate. *Macromolecules* **40,** 168–177 (2007).

125. Matyjaszewski, K., Dong, H., Jakubowski, W., Pietrasik, J. & Kusumo, A. Grafting from Surfaces for "Everyone" : ARGET ATRP in the Presence of Air. *Langmuir* **23,** 4528–4531 (2007).

126. Feng, Q. *et al.* Electrospun Regenerated Cellulose Nanofibrous Membranes Surface-Grafted with Polymer Chains/Brushes via the Atom Transfer Radical Polymerization Method for Catalase Immobilization. *ACS Appl. Mater. Interfaces* **6,** 20958–20967 (2014).

127. Wei, Y.-T., Zheng, Y.-M. & Chen, J. P. Functionalization of Regenerated Cellulose Membrane via Surface Initiated Atom Transfer Radical Polymerization for Boron Removal from Aqueous Solution. *Langmuir* **27,** 6018–6025 (2011).

128. Hansson, S., Östmark, E., Carlmark, A. & Malmström, E. ARGET ATRP for Versatile Grafting of Cellulose Using Various Monomers. *ACS Appl. Mater. Interfaces* **1,** 2651–2659 (2009).